DISSERTATION

Correlated Wind Turbulence and Aeroelastic Instability Modeling for 3-D Time-Domain Analysis of Slender Structural Systems

Submitted by

Jonathan S. Goode

Department of Civil and Environmental Engineering

In partial fulfillment of the requirements

For the Degree of Doctor of Philosophy

Colorado State University

Fort Collins, Colorado

Spring 2007

ProQuest Information and Learning Company
300 North Zeeb Road
P.O. Box 1346
Ann Arbor, MI 48106-1346

COLORADO STATE UNIVERSITY

March 30, 2007

WE HEREBY RECOMMEND THAT THE DISSERTATION PREPARED UNDER OUR SUPERVISION BY JONATHAN S. GOODE ENTITLED CORRELATED WIND TURBULENCE AND AEROELASTIC INSTABILITY MODELING FOR 3-D TIME-DOMAIN ANALYSIS OF SLENDER STRUCTURAL SYSTEMS BE ACCEPTED AS FULFILLING IN PART REQUIREMENTS FOR THE DEGREE OF DOCTOR OF PHILOSOPHY.

Committee on Graduate Work

Bogusz J. Bienkiewicz

Marvin E. Criswell

Paul R. Heyliger

Donald W. Radford

Adviser: John W. van de Lindt

Department Head: Luis Garcia

ABSTRACT OF DISSERTATION

CORRELATED WIND TURBULENCE AND AEROELASTIC INSTABILITY MODELING FOR 3-D TIME-DOMAIN ANALYSIS OF SLENDER STRUCTURAL SYSTEMS

Slender structural systems, such as high-mast lighting structural supports, are known to be sensitive to natural wind fluctuations. In particular, these systems are also prone to produce aeroelastic instabilities as a result of the structural motion and wind flow. This in turn can result in poor fatigue performance of these structures. In order to accurately determine this fatigue performance, numerical time-domain solution techniques are needed to estimate the fatigue life of a structure due to a probabilistically described loading event. Time-domain solutions, however, require accurate modeling of the fluid/structure interaction and the structural system since all vibration modes are inherently present. This requirement can often be a central problem to the use of time-domain solutions in engineering analyses. Furthermore, because these structural systems interact with the wind flow, this modeling complexity is exacerbated due to the modeling complexities associated with the wind flow and corresponding aeroelastic instabilities induced as a result of relative motion. To date, very little work has been attempted outside of physical modeling studies to form a comprehensive numerical modeling technique for slender structural systems in naturally occurring wind flows. Thus, this study seeks to incorporate existing models for wind flow and vortex shedding into a time-domain analysis solution procedure that simultaneously resolves the three-dimensional equation of motion.

The objectives of this study are focused on three modeling techniques that are incorporated into a comprehensive time-domain numerical analysis algorithm. Modeling of the approach wind flow to generate a simulated wind speed time history for use in the time-domain structural analysis algorithm is the first objective. Included in this objective is the use of random field theory to model the inherent spatial correlation of the approach wind flow. The approach used is empirical in nature and, thus, a numerical investigation was conducted to determine the effects of varying the spatial correlation of the wind flow on the response of the slender structural system. The second modeling objective of this study includes the incorporation of an existing vortex shedding model into the time-domain structural analysis routine. Again, the model considered is empirical in nature and a second numerical investigation was conducted to determine the effects of varying parameters within the vortex shedding model on the response of the structure. Finally, the last modeling objective of this study considers the fatigue performance of a structural system with respect to a probabilistically described lifetime wind speed statistical distribution that describes the natural wind fluctuations over the lifetime of the structure. The spatially correlated wind flow and vortex shedding models are subsequently included to determine their effects on the fatigue performance of the system.

The results and contributions of this study are derived from the numerical investigations of spatial correlation, vortex shedding and fatigue performance. Primary among these is the integration of the models into a comprehensive numerical analysis procedure. As a consequence a greater understanding of the effects of the spatial correlation of the wind flow and vortex shedding on the response, loading and fatigue performance of the structural system is also achieved. As expected, fully correlated wind turbulence flows produce the maximum response of the structure. Decreases in the spatial correlation subsequently produce decreases in the response of the structure. The vortex shedding model is dominated by the forced vibration quasi-sinusoidal term. However, the vortex shedding model only considers the first natural frequency of the structure in the determination of the critical wind velocity for which the effects of aerodynamic damping are nearly negligible. Finally, fatigue performance of the structure in the across-wind direction is dramatically reduced due to the incorporation of the vortex shedding model. Lowest fatigue life estimates are produced in the along-wind direction and are primarily due to the buffeting of the structure. Recommendations for future study and improvement are also made so that other studies can extend the work contained herein to obtain further understanding and potential improvements in design standards and mitigation techniques to improve performance.

Jonathan S. Goode
Department of Civil and Environmental Engineering
Colorado State University
Fort Collins, CO 80523
Spring 2007

Dedication

To the One

"There are many things to think about,

but nothing to worry about."

\- Matt Koepke

Acknowledgements

I would like to acknowledge the assistance, support and advice of many people without whom this work would not have been possible. Dr. John van de Lindt, my dissertation advisor, provided assistance, support, advice and patience. Dr. van de Lindt always pushed me to achieve and explore further. My appreciation is beyond words. I would also like to thank the other members of my graduate committee, Dr. Bogusz Bienkiewicz, Dr. Marvin Criswell, Dr. Paul Heyliger and Dr. Donald Radford. Their guidance and assistance is deeply appreciated. I would also like to thank my fellow graduate students at Colorado State University for their support, encouragement, assistance, and friendship.

I would like to thank several people over the last few years that encouraged me to pursue my dreams and goals. Dr. John Schramski, Dr. Sid Thompson, and Dr. Garrett Van Wicklen provided assistance and guidance during my undergraduate studies at the University of Georgia. Mansour Alipour-fard, Mindy Schaefer-Zarske, Janet Yowell, and Professor Dan Frangopol provided assistance and guidance during my graduate studies at the University of Colorado at Boulder. I would also like to thank Mike and Rebecca Groves, Katie France, Danielle Crail, Emily Lown, Sarah Proctor, Fernando Ramirez, CJ Riley, Stephanie Pinon, Mae Benvenga, Shiling Pei, Hongyan Liu, and John Halstead for their friendship, love, and support during my studies. In particular, I would like to thank Heather Zacharias for her patience, support, friendship, and love. I would have not begun this long journey without her encouragement.

I would like to extend many thanks to my parents, sister, and the rest of my family for their guidance, sacrifices, support, love, and advice. They have always been the bedrock that keeps me standing. Anything that I have ever or will ever accomplish is due to them.

Table of Contents

List of Figures

List of Tables

Chapter One

Introduction

1.1 Background and Problem Definition

A recent study conducted by van de Lindt and Goode (2006) considered the development of a reliability-based selection method for fatigue performance of high-mast lighting (HML) structural supports in the State of Colorado. HML structural supports are slender structures that are considered to be sensitive to wind fluctuations. They are considered wind sensitive because natural wind flow patterns in the atmosphere can lead to the dynamic excitation of these structures, which in turn produce relatively large stresses at the base of the structure. Because of the natural variations of the wind flow, these time-varying stresses form fatigue damaging stress cycles. Depending on the magnitude of the stress cycles, the fatigue life of the structure can be severely inhibited.

These HML structural supports as well as other slender structural systems have traditionally been analyzed using equivalent static methods (ASCE 7, 2005; AASHTO, 2001) or by using frequency domain analyses. Using these methods, the description of the motion caused by natural wind variations is not captured. Furthermore, the limited response of the structure that is determined is decoupled in the orthogonal directions of the response. As such it is difficult to predict the behavior and performance of these structures. In order to fully describe the structural behavior of the system, numerical time-domain techniques are needed to determine the response of the system to naturally occurring wind flows. Time-domain solutions are becoming increasingly popular due to the computational capacity of today's computer systems.

The focus of this study centers on the incorporation of multiple models into a time-domain analysis solution. In this solution, the equation of motion is integrated with respect to time. Time-domain solutions, however, require accurate models for the structural system because of all structural vibration modes being inherently present. To accomplish this task, a three-dimensional finite element framework is utilized to model the structural system and becomes the focal point for the incorporation of fluid/structure interaction models. Time-domain solutions also require accurate models for the forcing function. This can often be a central problem to their use in engineering analyses involving fluid/structure interaction such as wind flow. Slender structures also tend to introduce aeroelastic instabilities driven by the relative motion between the wind flow and the motion of the structure.

The study completed by van de Lindt and Goode (2006) provides the motivation and foundation for this dissertation. This dissertation research builds upon the concepts used in the previous study particularly in the area of modeling the approach wind flow and vortex shedding that is a result of alternating vortices (localized areas of low pressure) being shed in the wake of the wind flow. Hence, it is the goal of this study to incorporate existing models for improving the modeling of the wind flow and vortex shedding potentially leading to aeroelastic instabilities into a time-domain analysis solution procedure and determine their effects on the response and performance of the structural system.

The work presented herein centers on the use of two particular wind flow and fluid/structure interaction models. These models are investigated to determine their effect on the response and performance of a slender structural system. In order to keep observations in a general context based on the investigations illustrated later in this study, a structural system similar to the HML structural support is considered. As such, the numerical algorithm written by the student/author was developed with this general context in mind. This generality provides substantial flexibility with regards to future development or the incorporation of further refined models.

The two models considered in this study consider the spatial correlation of wind turbulence in the approach wind flow and vortex shedding in the wake of the structure causing additional across-wind buffeting of the structure. An existing model for spatial correlation will be integrated into a frequency dependent random field model to emulate the naturally occurring characteristics of the approach wind flow as it passes the structure imparting a force on it. The model considered is empirical in-nature and thus a numerical investigation study is implemented to determine its effects on the response and performance of the structural system considered in this study. Vortex shedding caused by the alternating vortices shed in the wake of the wind flow may actually intensify based on the motion of the structure and the wind flow in a condition known as lock-in. The model incorporated into this study considers this phenomenon based on an empirical model developed to determine the response of similar, yet, more rigid structure. Similar to the study based on the spatial correlation model, a numerical investigation study is also conducted on the vortex shedding model to determine its effects on the response and performance of the structural system.

1.2 Current State of Art/Practice

Two design code bodies dictate the current state of practice for the design of structural systems and structures similar to HML structural supports subjected to wind loading. First, the American Society of Civil Engineers (ASCE) Standard *Minimum Design Loads for Buildings and Other Structures* (ASCE 7, 2005) is primarily adopted by many of the building code authorities throughout the nation. Second, the American Association of State Highway and Transportation Officials (AASHTO) *Standard Specifications for Structural Supports for Highway Signs, Luminaires and Traffic Signals* (AASHTO, 2001) governs the design of transportation-related structures. Both of these specifications use a similar equivalent static approach for the design of structures for an extreme wind event or design wind speed. Typically, this design wind speed has an annual probability of exceedance of 0.02, which represents a wind event with a 50-year return period. Using the design wind speed, the design wind pressure can be determined for the structure. A simple static structural analysis is then used to determine the adequacy of the structure.

In using the equivalent static approach in both specifications, wind turbulence fluctuations are not directly considered in the analysis. Thus, the spatial correlation of the wind turbulence is not needed. As a result of this approach, neither specification directly addresses time-domain analyses or more complex computer simulations. This limitation can be primarily attributed to time-domain analysis capabilities still being in their (relative) infancy for routine design use due to the tremendous computational requirements for accurate and meaningful analyses. Recently, however, several studies employing this state-of-the-art procedure have used time-domain analysis to better analyze the response of a structure. These studies, primarily done for cable-supported bridges such as suspension and cable-stayed, have considered perfect correlation and partial correlation of wind turbulence in a horizontal, parallel to the ground, direction only.

Vortex shedding is only addressed in the AASHTO Specification for the design of transportation-related structures for fatigue performance. The procedure for determining the equivalent static force caused by vortex shedding at a minimum wind speed requires knowledge of the structural system such as the first mode or lowest natural frequency. Tapering of the structure with a minimum taper of 0.14 in/ft (11.67 mm/m), however, often alleviates this requirement from a codified perspective. As noted in the AASHTO Commentary, "structures composed of tapered members do not appear susceptible to vortex-induced vibrations when tapered at least 0.14 in/ft [11.67 mm/m]". Furthermore, AASHTO Commentary states that "the dimensions of most tapered members result in critical wind velocities below the threshold velocity" for vortex shedding lock-in and "any vortices that may form are correlated over a short length of the member, and they consequently generate insignificant vortex-shedding forces". Indeed, as was reported by Goode and van de Lindt (2006) for the HML structural supports they studied, as-built construction documents procured from a prior project conducted in the State of Colorado indicate that this minimum taper is used and thus vortex shedding may be neglected during the design process according to the AASHTO provisions. However, van de Lindt and Goode (2006) were able to demonstrate in a limited fashion that lock-in can occur at low wind speeds for first mode vibrations, at moderate wind speeds for second mode vibrations, and at somewhat higher wind speeds for third mode vibrations. These results may indicate that consideration of only the fundamental frequency of a slender structure is not sufficient when considering higher mode lock-in.

As noted by Simiu and Scanlan (1996), no completely successful analytical (i.e. mechanistic model) method has yet been developed for vortex shedding. Slender structures, as considered in the present study, will deflect in some manner that influences the local wind flow. Simiu and Scanlan (1996) also note that this has not been studied in detail.

Several more recent studies have considered slender structural systems in regards to their response and fatigue performance. These studies, however, have often not considered these systems in the time-domain. Quite often, these systems, as well as many other systems within the context of wind engineering, are considered in the frequency domain. As previously discussed, this limits the capability of the analysis. For example, time-domain techniques allow for complex stress processes at the base of the structure affecting the fatigue performance of the system to be utilized in a non-linear fatigue damage accumulation model coupled within the algorithm. This and other more complex modeling techniques are not always possible in the frequency domain. Alternatively, wind tunnel studies have also been quite extensively used to determine the response of structural systems. Recent studies (Harrison and Roschke, 2000; Bosch and Guterres, 2001) have considered similar slender structural systems in experimental investigations. In these studies, they have determined the response of slender structural elements from an experimental perspective. These studies, however, require substantial time and capital investment to conduct.

Other recent studies have begun to consider a time-domain approach to determine the response of slender structural systems. Dul and Pietrucha (1996) considered the response of a flexible chimney in their time-marching approach. Stoyanoff (2001) also considered a time-domain approach to determine the response of a structural system. In this work, Stoyanoff considered the response of an elastic pedestrian bridge primarily focused on the galloping stability and buffeting response of the structure. Kondo et al (1997) and Asa-Jakobsen and Strømmen (2001) presented methods by which spatially correlated wind velocity fluctuations could be generated. Mann (1998) extended some of this work in wind field simulation using an efficient algorithm to simulate turbulent, atmospheric wind fields including three-dimensional wind flows.

As discussed previously, frequency-domain approaches have been consistently used in wind engineering to determine the response of a structure system. With frequency-domain being the traditional approach, several recent papers have considered the response of slender structural systems using this approach. Most notably, Piccardo and Solari (1998) developed closed-form response predictions for three-dimensionally wind-excited slender structures. In there predictions, only the mean and peak responses are developed. Modal analysis techniques have also been employed by Chen and Kareem (2001) to determine the aeroelastic response of structural systems under multi-correlated winds. Solari and Piccardo (2001) also considered modal analysis to determine a probabilistic approach for the gust buffeting of structures.

Recent studies in vortex shedding due to wind flow past a cylindrical structural system have focused on experimental and numerical studies in smooth, non-turbulent wind flows. The work done by Vickery and Basu (1983) to date still produces one of the more robust semi-empirical models for slender, flexible structures. Goswami, Scanlan, and Jones (1993) conducted wind tunnel investigations to further develop the model by Vickery and Basu. This study outlined procedures to determine the parameters of the model but not necessarily how to incorporate the model into a numerical response scheme. D'Asdia and Noe (1998) developed simplified models specific to their case study of reinforced concrete chimneys, but demonstrated the capability of their model in the time-domain response of the system. A more generalized perspective of vortex shedding was considered by Yamamoto et al (2004) in their investigation on flexible cylinders in fluid flow. Their study considered fluid flow having a relatively high mass density compared to air, i.e., water. Finally, Fujisawa et al (2005) considered the use of advanced computational fluid dynamic (CFD) models to confirm experimental results of fluid flow past a circular cylinder in a uniform flow.

Repetto and Solari (2001; 2002; 2004; 2006) considered the fatigue performance of slender structural systems. In each of their studies, Repetto and Solari considered linear elastic behavior of the structural system. Fatigue damage was a result of the bending stress in the direction considered. Deoliya and Datta (2001) employed the method outlined by Holmes (2001) and developed by Wirsching and Light (1980) to determine the fatigue damage due to a wide-band stress process based on the same characteristics defining a narrow-band stress process. In this procedure, an empirical parameter based on the spectral bandwidth of the stress process is determined to correct the expected damage due to the stress process based on the assumption of it being narrow-banded. In their latest paper, Repetto and Solari (2006) develop a refined procedure based on the work done in their previous studies and by Wirsching and Light. The primary difference between the procedures is that of the cycle counting method utilized to determine the expected damage of the stress process.

1.3 Objectives

This dissertation study is focused on the incorporation of three modeling techniques into a numerical time-domain finite element analysis framework. These three modeling techniques represent a "comprehensive" approach to three-dimensional time-domain analysis of slender structural systems. As defined, this approach represents the most inclusive use of several models to determine the response of the structural system with respect to fluid/structure interaction causing the motion of the system.

First, the approach wind flow is generated to simulate the wind speed time history for use in the numerical algorithm. Included in this first objective is the use of random field theory to model the inherent spatial correlation of the approach wind flow. Second, the effects of vortex shedding on the resultant loading and response of the structure is incorporated into the numerical algorithm. The model for vortex shedding considered in this study, like the model to incorporate the spatial correlation of wind turbulence, is also empirical but presents itself as the most applicable to a finite element framework. Finally, the last modeling objective of this study considers the fatigue performance of the structural system considered in this study with respect to a probabilistically described lifetime wind speed statistical distribution that describes the natural wind fluctuations over the lifetime of the structure. The spatially correlated wind flow and vortex shedding models are subsequently included to determine their effects on the fatigue performance of the structural system.

1.4 Approach

The approach considered in this study is centered on the use of a generalized finite element framework to model the slender structural system. This framework provides substantial flexibility with regards to the ability to easily change parameters of the structural model or refine the incorporated models for the approach wind flow and vortex shedding in the fluid/structure interaction domain. A numerical integration scheme is employed to integrate the equation of motion in time to capture the three-dimensional response of the structural system. A well-known approach to determine the force imparted by the fluid flow past the structure is used within a procedure to determine the relative motion of the structure with respect to the wind flow. This results in a non-linear forcing function that must be resolved within each step of the time-domain solution procedure.

There are several approaches by which the spatial correlation of wind turbulence can be incorporated into the wind flow model. Primary among these is a method proposed by Simiu and Scanlan (1996) and subsequently demonstrated by Asa-Jakobsen and Strømmen (2001). The approach consists of the use of a frequency-dependent random field model or narrow-band cross correlation. This model uses a frequency-dependent exponential decay function to determine the spatial correlation structure of wind turbulence. To integrate this model into the traditional spectral analysis, simulated wind speed time series are generated that are correlated at multiple locations.

Contained within this random field model approach is an empirical constant, namely an exponential decay constant, that has been traditionally obtained experimentally. Simiu and Scanlan (1996) suggest a value of ten (10) for spatial correlation of wind turbulence with respect to height above ground that produces a relatively strong spatially correlated wind flow. However, they also note that this empirical constant depends strongly on the height above ground and wind speed, among other factors. A fairly substantial investment in equipment and time would be required to determine the empirical constant from field measurements. This dissertation study does not seek to determine the correct empirical constant for any given situation such as terrain. Rather, this study seeks to understand it, model it with the necessary accuracy, and determine its potential effects on structural response. As such, a numerical investigation study will be conducted using the random field model by varying the empirical constant value to determine the sensitivity of the three-dimensional response of a structure to this constant. Furthermore, fatigue life estimates of the structure will also be produced based on the characteristics of the structure-to-foundation connection where fatigue problems are most evident in this type of structure.

The vortex shedding model is derived from the work of Vickery and Basu (1983). As Simiu and Scanlan (1996) note, however, vortex shedding models have not been extensively studied for slender structures such as those considered in this study. Nor have these models been incorporated into a finite element framework for time-domain analyses. The model derived by Vickery and Basu was developed to estimate the response of chimneys and towers. Contained within the model are two nonlinear forcing function components: forced vibration and aerodynamic damping. Both of these components are functions of the natural frequency of the structure and semi-empirical constants developed by Vickery and Basu. Incorporation of this type of model, although semi-empirical, into this study of slender structural systems will help to provide substantial insight into the incorporation of vortex shedding models into a dynamic, time-domain finite element analysis of structural systems. Additional insights into the across-wind response and reduction of fatigue life caused by vortex shedding will also be determined.

1.5 Overview

The next four chapters of this dissertation lead the reader through the theoretical development of the numerical modeling of slender structural systems, spatial correlation of wind turbulence, vortex shedding, and the estimation of fatigue life using a random vibration approach. Subsequent chapters provide the results and discussion of the numerical investigations conducted for this research on the effects of spatial correlation and vortex shedding on response and fatigue life. Finally, conclusions and recommendations resulting from this study are collectively offered for the reader, along with recommendations for potential future research avenues.

The following chapter summaries provide a brief overview of the remaining chapters in this study:

Chapter 2: Dynamic Modeling of Slender Members in Fluid Flow

Chapter Two presents the fundamental theories for the dynamic modeling of slender structural systems in wind flow. The slender structural system identified as the example structure used in the numerical investigation studies of Chapters 6 – 8 is presented. The methods by which the example structure is modeled are also identified. Finally, the fundamental basis for transforming a fluid flow past a structure into an applied force is presented. Included in this chapter is the capability for considering a nonlinear, relative motion concept for fluid flow.

Chapter 3: Spatial Correlation and Wind Turbulence Modeling

Chapter Three presents the fundamental theories for the modeling of wind turbulence and its inherent spatial correlation along the height of a structure. Contained within this presentation is the review of a concept to introduce spatial correlation into the simulation of wind speed time series; namely, the random field theory.

Chapter 4: Vortex Shedding Modeling

Chapter Four presents the fundamental theories for the modeling of vortex shedding associated with slender, flexible structural systems in fluid flow. The development of the semi-empirical model used in this study is the focus of this chapter.

Chapter 5: Fatigue Life Modeling

Chapter Five presents the fundamental theories for the estimation of fatigue life following a random vibration approach. The development of this method follows the assumption that the stress process that induces the fatigue loading is a well-behaved narrow-band random process. A method by which the estimated damage caused by a wide-band stress process can be determined using the assumption of narrow-band stress process is also presented. Finally, a statistical description of the loading event causing the fatigue loading over the lifetime of the structure is discussed.

Chapter 6: Spatial Correlation

Chapter Six presents the results of a numerical investigation study considering changes in spatial correlation, properties of the example structure as outlined in Chapter Two, and wind speed. The results of the study including the spatial- and cross-correlation of the wind speed, loading resultant, and motion of the structure are discussed in detail.

Chapter 7: Vortex Shedding

Chapter Seven presents the results of a numerical investigation study considering changes in vortex shedding parameters, properties of the example structure as outlined in Chapter Two, and wind speed. The results of the study including the effects of vortex shedding on the loading resultant and motion of the structure are discussed in detail.

Chapter 8: Fatigue Life

Chapter Eight presents the results of a numerical investigation study considering changes in spatial correlation, vortex shedding parameters, properties of the example structure as outlined in Chapter Two, and the lifetime statistical distribution of wind speed. The results of the study focus on the effects of these changes on the estimated fatigue life of the structure for each of two detail categories directly affecting the fatigue performance for the connection at the base of the structure.

Chapter 9: Summary, Conclusions, and Recommendations

Chapter Nine provides the overall summary of the conclusions and recommendations resulting from this study. These are based on the incorporation of the spatial correlation and vortex shedding models into a dynamic time-domain finite element analysis of slender structural systems. Also presented are further comments on the behavior of the example structure based on the numerical investigations of Chapters 6 – 8, along with recommendations for further research.

Chapter Two

Dynamic Modeling of Slender Members in Fluid Flow

2.1 Slender Structural Systems

The focus of this study is on slender structural systems that are sensitive to wind fluctuations. Some examples of these types of systems include flagpoles, utility poles, cantilevered transportation-related structural supports, and, to some extent, high-rise buildings. All of these structures are related in that natural wind flow patterns in the atmosphere can lead to the dynamic excitation of these structures which in turn produce relatively large stresses at the base of the structure.

This study focuses on one type of slender structural system only. Following the study by van de Lindt and Goode (2006) concerning high-mast lighting (HML) structural supports in the state of Colorado, a similar type of transportation-related structure will be utilized for this study. This structure, herein referred to as the example structure, is characterized as having some total vertical height above the ground and is constructed using a prefabricated structural steel tubing having constant outside diameter and constant wall thickness. Whereas typical HML structural supports are tapered based on AASHTO specifications referenced in Section 1.2, the example structure in this study is considered to have a constant cross-section throughout its height for the purposes of generalization. Figure 2-1 illustrates the example structure used in this study. The vertical height, outside diameter, and wall thickness given in Figure 2-1 are typical ranges for an HML structural support and are used as the basis in later numerical investigations.

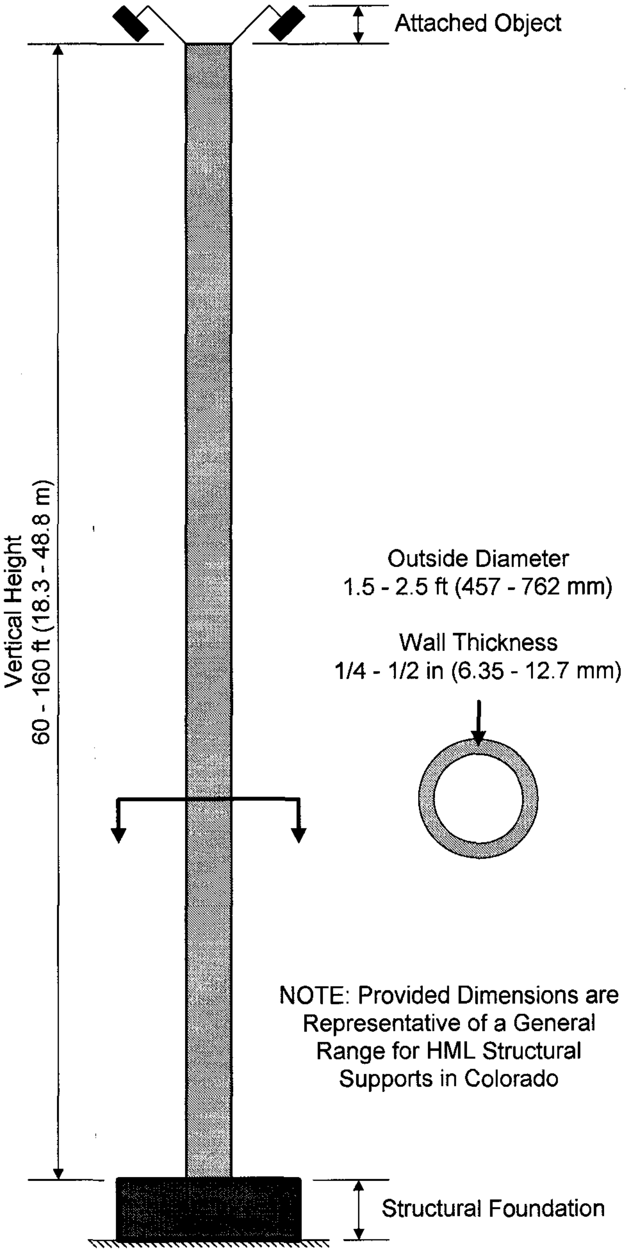

Figure 2-1: Example Structure

As noted previously, the example structure serves as the basis for numerical investigations later in this study. Based on the general range of values provided for the vertical height, outside diameter, and wall thickness given in Figure 2-1 as being representative for HML structural supports in the state of Colorado, Table 2-1 provides the various properties of the example structure considered in this study. Table 2-1 provides all of the values that are considered in this study. In some analyses, not all of these values/combinations will be used exhaustively. Thus, a summary will be provided for in later such analyses.

Property	Value
Vertical Height	60, 80, 100, 120, 140 ft (18.3, 24.4, 30.5, 36.6, 42.7 m)
Outside Diameter	2.0 and 2.5 ft (610 and 762 mm)
Wall Thickness	¼ and ½ in (6.35 and 12.7 mm)

Table 2-1: Example Structure Properties

Similar to a typical HML structure, the example structure is comprised of structural steel and has an attached object (or a luminaire system in the case of an HML structure) having mass and surface area affixed to its top as shown in Figure 2-1. Table 2-2 provides the material properties for the example structure. Table 2-3 provides a summary of the object (luminaire) attached to the top of the example structure.

Property	Value
Material Type	Structural Steel
Modulus of Elasticity	29,000 ksi (200 GPa)
Poisson's Ratio	0.30
Volumetric Weight	490.1 lb/ft^3 (7,850 kg/m^3)

Table 2-2: Example Structure Material Properties

Property	Value
Type of Object	Luminaire System
Object Weight	600 lb (272 kg)
Projected Area: Along-Wind / Across-Wind	10 ft^2 (0.93 m^2) / 10 ft^2 (0.93 m^2)

Table 2-3: Example Structure Attached Object Properties

The base of the example structure is attached to a rigid foundation in a similar fashion as the previously studied HML structure that can be simply described as the welding of the structural steel tubing to a rigid base plate. The details of the connection are not as important as the classification of the connection type per AASHTO specifications. In this study two AASHTO classification types, or detail categories, will be assumed for the base connection: E and E′. These detail categories are only of importance in the determination of the estimated fatigue life outlined further in Chapter 5. At this point, it is only important to note that the base connection is conservatively assumed to be rigid. Table 2-4 provides a summary of the base connection classification per AASHTO specifications along with further details concerning these connections as they relate to a typical HML structural support base connection.

Classification	Construction & Application	Detail
E	Groove-Welded Connection & Column-to-Base-Plate	Full-penetration groove-welded tube-to-transverse plate connections with the backing ring attached to the plate with a full-penetration weld, or with a continuous fillet weld around interior face of backing ring. The thickness of the backing ring shall not exceed 0.375 in (10 mm) with fillet weld attachment to plate. Full penetration groove-welded tube-to-transverse plate connections welded from both sides with back gouging (without backing ring).
E′		Full penetration groove-welded tube-to-transverse plate connections with the backing ring not attached to the plate with a continuous full-penetration weld, or with a continuous interior fillet weld.

Table 2-4: Example Structure Base Connection Classification (Excerpted from AASHTO, 2001)

2.2 Structural Modeling

The example structure outlined in Section 2.1 is modeled using a finite element framework. Twelve degree-of-freedom beam elements are used to determine the properties of the structure in a discretized manner and to capture the three-dimensional motion of the structure. These properties are then directly related to determining the dynamic motion of the system using the equation of motion, which can be expressed as

$$\mathbf{M}\ddot{\mathbf{x}} + \mathbf{C}\dot{\mathbf{x}} + \mathbf{K}\mathbf{x} = \mathbf{F}(t) \tag{2-1}$$

where the three matrices, **M**, **C**, and **K**, are the mass, damping, and stiffness matrices, respectively. The mass and stiffness matrices are as given by traditional structural analysis texts such as Paz (2004). The damping matrix is derived from a linear combination of the structure stiffness and mass matrices (Chopra, 2001). This type of damping matrix is also known as Rayleigh damping. The critical damping ratio (ξ) is assumed to be 1% following experimental results of similar structures. The forcing function, $\mathbf{F}(t)$, is nonlinear due to the relative motion between the wind flow and the structure, and is discussed further in Sections 2.3 and 2.4. The vectors, $\mathbf{x}$, $\dot{\mathbf{x}}$, and $\ddot{\mathbf{x}}$, represent the position, velocity, and acceleration, respectively, of the nodal points, or discretized points representing the continuous system, of the structure.

Boundary support conditions are applied to model the attachment of the structure to its foundation. These support conditions are represented by linear translational and rotational springs placed at the base of the structure and are a function of the foundation type and soil properties under the foundation. The springs that model the boundary support condition are considered to have no mass. As stated in Section 2.1, for this study the foundation is conservatively modeled as a rigid support.

Existing capabilities within the analysis routine written by Goode and van de Lindt (2006) allow for the inclusion of a luminaire structure, or any other object having mass and surface area, to be attached to the top of the structure. The mass of the object is evenly distributed to translational degrees-of-freedom at the top of the structure. The projected-area of the object is used for determining additional drag force caused by wind flow past the attached object.

After assembly of the structural properties and generation of the simulated wind speed time series (see Chapter Three) the equation of motion can be solved. The method chosen by van de Lindt and Goode (2006) and subsequently used in this study is the Newmark-Beta method (Newmark, 1959; Paz, 2004). This method provides a means to numerically integrate the equation of motion incrementally over a very small time interval, Δt. It is assumed that the deformations of the system remain in the linear range for the material of the structure (steel for this study) and thus relatively small. Because of this assumption, a time step of 0.1 seconds is assumed. However, as will be discussed in Section 2.4, the forcing function due to wind speed becomes nonlinear as the structure begins to move with some velocity. Therefore, a procedure is included to check for unstable solutions. If a specified number of peak displacements continue to grow, an unstable condition is noted and the dynamic analysis procedure is repeated with a time step equal to half of the previous time step. This assumes proper convergence and subsequently accurate results at all wind velocities.

2.3 Fluid Flow Modeling

The forcing function, $\mathbf{F}(t)$, in the equation of motion requires that a force must be specified at all nodal points for all points in time, or at all time steps. The study by

Goode and van de Lindt (2006) made use of a well-known equation relating fluid flow past a stationary object to determine the resulting force. In this case, the wind speed time series generated by the procedure outlined in Chapter Three is the fluid flow defined at all nodal points and at all time steps. Thus, neglecting the inertial term due to the relatively low mass density of air, the forcing function obtained from Morison's equation is given as (Morison, 1950)

$$\mathbf{F} = \frac{1}{2}\rho_{air}\mathbf{A}\mathbf{C}_d\mathbf{U}_{wind}\left|\mathbf{U}_{wind}\right| \qquad (2\text{-}2)$$

where ρ_{air} is the mass density of air. All other variables are vectors of length equal to the number of nodal points. **A** is the tributary projected area for each nodal point, $\mathbf{C}_d$ is the drag coefficient, $\mathbf{U}_{wind}$ is the wind speed for each nodal point at time t, and **F** is the force produced by the wind speed past the stationary structure at time t.

The drag coefficient for each nodal point, C_d, is determined experimentally and is, in general, a function of the Reynolds number, projected area of the object normal to flow, and other factors such as surface roughness. For flow past a smooth cylinder, C_d can be obtained from Figure 2-2. This figure was a result of experimental tests for flow past a stationary smooth cylinder.

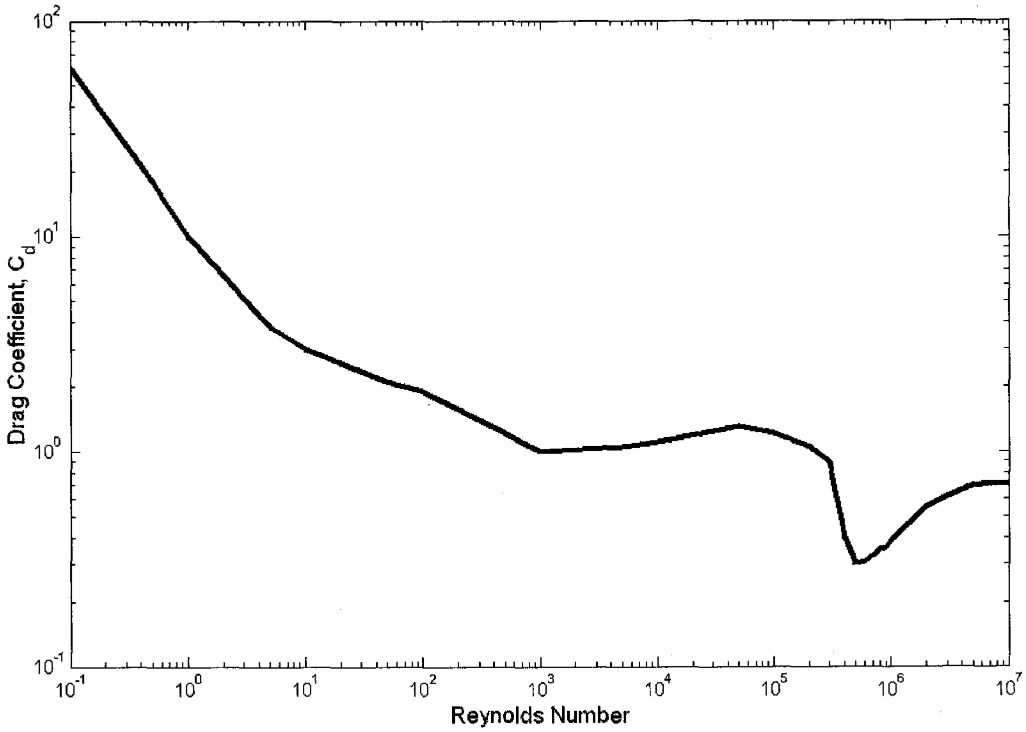

Figure 2-2: Drag Coefficient for a Smooth Cylinder (Excerpted from Wilcox, 2000)

2.4 Non-Linear Fluid Flow Modeling

As noted in Section 2.2, a procedure is necessary for resolving the nonlinear wind loading forcing function. The cause for this nonlinearity is due to Morison's equation that is used to determine the drag force from the wind flow past the structure in Equation (2-2). This equation, however, is valid only for fluid flow past a stationary object. Within the time-domain approach used by Goode and van de Lindt (2006) and again here in this study, the structure moves along with the wind flow. As the structure moves, each point on it has some velocity positive or negative with regards to the reference coordinate system depending on the motion. The wind flow, as noted, is also moving with some velocity positive or negative with regards to the same reference coordinate system. Thus, the true forcing function must be determined from the relative velocity between the structure and the wind at that instant in time during the solution process.

In order to check the forcing function value at an instant in time, a procedure such that the structure velocity at each nodal point before and after the forcing function is updated is checked for convergence. To update the forcing function, the structure velocity at each nodal point is extracted. These structure velocities, obtained at the end of the time step being considered, are combined with the wind velocity at the appropriate time to obtain the relative velocity given as

$$\mathbf{U}_{rel} = \mathbf{U}_{wind} - \mathbf{U}_{structure} \tag{2-3}$$

where $\mathbf{U}_{rel}$ is the vector of relative velocity at each nodal point between the wind velocity, $\mathbf{U}_{wind}$, and the structure velocity, $\mathbf{U}_{structure}$, all at time t. Figure 2-3 illustrates the use of Equation (2-3). Here, positive velocities are assumed to be in the positive x-direction. The wind velocity is moving with some velocity, $\mathbf{U}_{wind}$, in the positive direction. The structure is also moving with some velocity, $\mathbf{U}_{structure}$, in the positive direction. Thus, the net or relative velocity, $\mathbf{U}_{rel}$, is the difference between the wind velocity and the structure velocity.

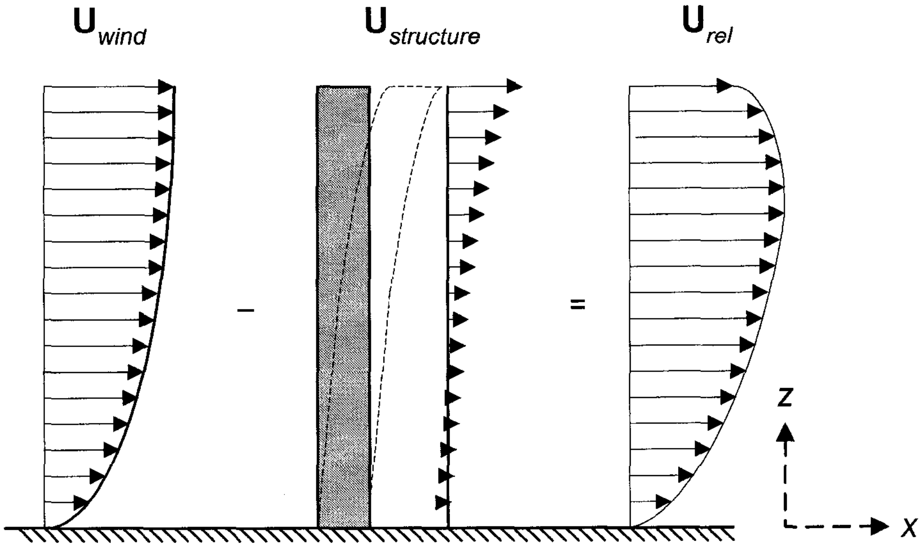

Figure 2-3: Relative Velocity of Wind and Structure

Using the relative velocity between the structure and wind, an updated forcing function using a modified version of Morison's equation is determined as

$$\mathbf{F} = \frac{1}{2}\rho_{air}\mathbf{A}\mathbf{C}_d\mathbf{U}_{rel}\left|\mathbf{U}_{rel}\right| \tag{2-4}$$

where $\mathbf{U}_{rel}$ is the relative velocity determined from equation (2-3). Dynamic analysis using the Newmark-Beta method from Section 2.2 is completed to reevaluate the position, velocity, and acceleration of each node of the structure at the end of the time step. Structure velocities are again extracted. Comparisons are made between the previously extracted structure velocities and these new structure velocities at each node. If a set tolerance is exceeded, this procedure is repeated until convergence is reached. If the tolerance is not exceeded, convergence is achieved and the relative motion for the particular time step is completed.

A sensitivity analysis was conducted to determine the necessity of considering the relative velocity in the determination of the buffeting force due to turbulent wind flow. In each case, only a few iterations were required to resolve the relative velocity within 10^{-5} ft/s (3×10^{-6} m/s). Changes in the response of the structure were particularly evident at the peaks of the response. Inclusion of the relative velocity term produced larger buffeting forces and hence larger response displacements. Higher wind velocities produced larger discrepancies between the use of the relative velocity term and the use of Morison's equation without relative velocity. This relative term was included to allow the model (1) to be as general as possible, and (2) to have application in other fluid flow fields.

Chapter Three

Spatial Correlation and Wind Turbulence Modeling

3.1 Wind Turbulence Modeling

It is well known that the variation of wind speeds in time is due to the natural turbulent characteristics of the wind flow. Accurate modeling of wind turbulence is useful in structural engineering applications for several reasons. Simiu and Scanlan (1996) note that fluctuations caused by wind turbulence may induce resonant amplification effects such as vortex shedding in flexible structures (see Chapter Four). In order to mathematically describe wind turbulence, the spectral density function is used. The spectral density describes the distribution of turbulence as a function of frequency, or how rapidly the magnitude of the wind speed varies with time (Holmes, 2001).

Consider a Cartesian coordinate system defined with its x-axis parallel to the mean wind velocity $\overline{U}$ and its z-axis in the vertical direction. Following Asa-Jakobsen and Strømmen (2001), the turbulence components, or fluctuations, in the x, y and z-directions are denoted as u', v' and w' such that the wind velocity vector may be described by

$$\mathbf{U}\{x,y,z,t\}=\begin{Bmatrix}\overline{U}+u'\\ v'\\ w'\end{Bmatrix} \tag{3-1}$$

These three orthogonal components are often referred to as the along-wind (or longitudinal) turbulence component in the x-coordinate direction, the across-wind (or lateral) turbulence component in the y-coordinate direction, and the vertical turbulence component in the z-coordinate direction. Asa-Jakobsen and Strømmen (2001) also state that the wind field properties are fully defined by the mean wind velocity profiles and a 3 x 3 matrix containing the relevant cross-spectra of the turbulence components as

$$\mathbf{S}\{x,y,z,n\}=\begin{bmatrix}S_{uu} & S_{uv} & S_{uw}\\ S_{vu} & S_{vv} & S_{vw}\\ S_{wu} & S_{wv} & S_{ww}\end{bmatrix} \tag{3-2}$$

They then specify that the variation of cross-spectra in space may be expressed by the separation distance $s = |s_i - s_j|$ between two arbitrary points s_i and s_j. Thus, the cross-spectra $S_{ij}\{s,n\}$ may then be expressed in terms of the single-point spectra S_i and S_j and the corresponding normalized co-spectra as

$$S_{ij}\{s,n\}=\sqrt{S_i\{n\}S_j\{n\}}\sqrt{\mathrm{Coh}_{ij}\{s,n\}} \tag{3-3}$$

where the last term of this equation is the root-coherence function.

The wind turbulence spectra for the three directions, u', v' and w', are obtained from Simiu and Scanlan (1996). The along-wind (longitudinal) turbulence spectra is given as

$$\frac{nS_{uu}(z,n)}{u_*^2} = \frac{200f}{(1+50f)^{5/3}} \tag{3-4}$$

where the non-dimensional quantity

$$f = \frac{nz}{\overline{U}(z)} \tag{3-5}$$

is the Monin (or similarity) coordinate and the friction velocity u_* can be determined from the logarithmic law defining the mean wind velocity profile as

$$\overline{U}(z) = \frac{u_*}{k}\ln\left(\frac{z}{z_0}\right) \tag{3-6}$$

where k is von Kármán's constant (generally assumed to be ≈ 0.4), z_0 is the roughness length, and $\overline{U}(z)$ is the mean wind speed at height z.

Similarly, the across-wind (lateral) and vertical wind turbulence spectral equations provided by Simiu and Scanlan (1996) are given as

$$\frac{nS_{vv}(z,n)}{u_*^2} = \frac{15f}{(1+9.5f)^{5/3}} \tag{3-7}$$

$$\frac{nS_{ww}(z,n)}{u_*^2} = \frac{3.36f}{1+10f^{5/3}} \tag{3-8}$$

A simplification of Equation (3-2) is made in Section 3.4 such that the cross-covariance between u', v', and w' are not needed and the 3 x 3 matrix is reduced to a diagonal matrix. This simplification is a consequence of the off-diagonal cross-covariance terms tending to be very small in comparison to the diagonal terms of Equation (3-2) and therefore can be neglected (Asa-Jakobsen and Strømmen, 2001). As such, the cross-covariance components are not presented nor considered in this study.

3.2 Spatial Correlation of Wind Turbulence

The spatial covariance between the fluctuating wind velocities at two different heights z_1 and z_2 for longitudinal fluctuations over an averaging dimension T is defined as (Holmes, 2001)

$$\overline{u'(z_1)u'(z_2)} = \frac{1}{T}\int_0^T u'(z_1,t)u'(z_2,t)dt \tag{3-9}$$

and for lateral fluctuations is defined as

$$\overline{v'(z_1)v'(z_2)} = \frac{1}{T}\int_0^T v'(z_1,t)v'(z_2,t)dt \tag{3-10}$$

From statistics, the spatial correlation coefficient for longitudinal fluctuations can be written as

$$\rho_{u'} = \frac{\overline{u'(z_1)u'(z_2)}}{\sigma_u(z_1)\sigma_u(z_2)} \tag{3-11}$$

and for lateral fluctuations as

$$\rho_{v'} = \frac{\overline{v'(z_1)v'(z_2)}}{\sigma_v(z_1)\sigma_v(z_2)} \tag{3-12}$$

The spatial correlation of fluctuating wind velocities at two different heights can be modeled using the exponential decay function for longitudinal fluctuations as (Holmes, 2001)

$$\rho_{u'} \approx \exp[-C_{u'}|z_1 - z_2|] \tag{3-13}$$

and for lateral fluctuations as

$$\rho_{v'} \approx \exp[-C_{v'}|z_1 - z_2|] \tag{3-14}$$

Vanmarcke (1983) introduced several correlation and variance functions to be applied in the context of random fields. The exponential correlation function associated with a first-order (Markov) auto-regressive process and its variance function are given as (Vanmarcke, 1983)

$$\rho(\tau) = \exp\left[-\left|\tau\right| / b\right] \tag{3-15}$$

and

$$\gamma(T) = 2\left(\frac{b}{T}\right)^2\left(\frac{T}{b} - 1 + e^{-T/b}\right) \tag{3-16}$$

Noting that the correlation functions in Equations (3-13) and (3-14) are similar to Equation (3-15), then the following observations may be made

$$\tau = z_1 - z_2 \tag{3-17}$$

where τ is the lag vector, and

$$1/b = C_i \tag{3-18}$$

Hence, using Holmes' (2001) notation, the variance functions for a one-dimensional random field considering spatial correlation of wind velocity fluctuations are

$$\gamma_{u'}(T)=2\left(\frac{1}{C_{u'}T}\right)^2\left(C_{u'}T-1+\mathrm{e}^{-C_{u'}T}\right) \tag{3-19}$$

for longitudinal fluctuations and

$$\gamma_{v'}(T)=2\left(\frac{1}{C_{v'}T}\right)^2\left(C_{v'}T-1+\mathrm{e}^{-C_{v'}T}\right) \tag{3-20}$$

for lateral fluctuations.

Consider a structure with an arbitrary vertical height and defined by finite elements and nodal points as illustrated in Figure 3-1.

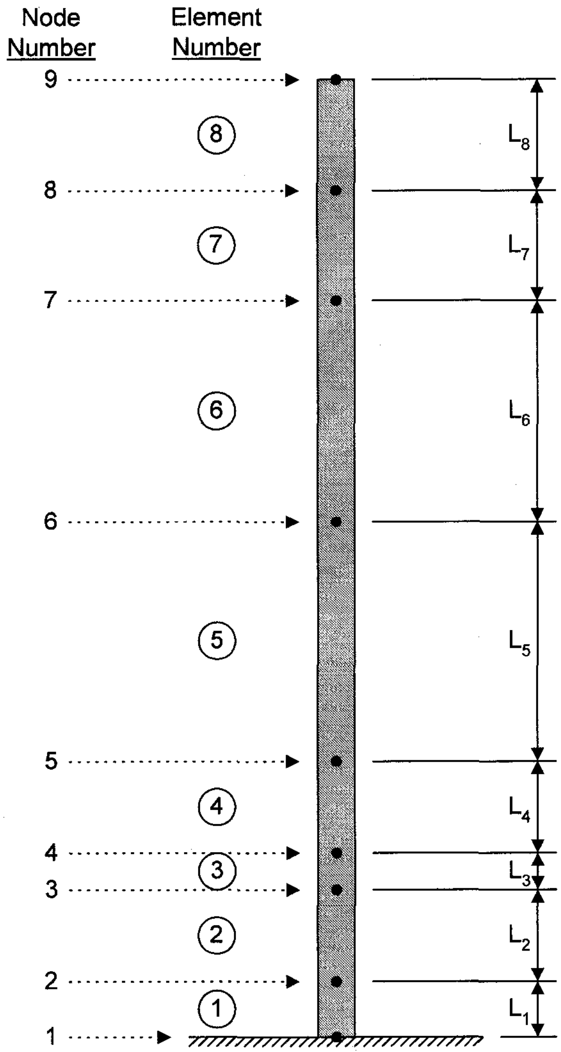

Figure 3-1: Generalized Finite Element Model of a Structure

The correlation of wind velocity fluctuations between any two nodes averaged over the tributary length of the elements above and below the nodal points are

$$\rho_{u'_i,u'_j} = \frac{h_0^2\gamma_{u'}(h_0) - h_1^2\gamma_{u'}(h_1) + h_2^2\gamma_{u'}(h_2) - h_3^2\gamma_{u'}(h_3)}{2D_iD_j\sqrt{\gamma_{u'}(D_i)\gamma_{u'}(D_j)}} \qquad (3\text{-}21)$$

for longitudinal fluctuations and

$$\rho_{v'_i,v'_j}=\frac{h_0^2\gamma_{v'}(h_0)-h_1^2\gamma_{v'}(h_1)+h_2^2\gamma_{v'}(h_2)-h_3^2\gamma_{v'}(h_3)}{2D_iD_j\sqrt{\gamma_{v'}(D_i)\gamma_{v'}(D_j)}} \tag{3-22}$$

for lateral fluctuations where D_i and D_j are given as

$$\begin{aligned} D_i &= \frac{1}{2}(L_{i-1}+L_i) \\ D_j &= \frac{1}{2}(L_{j-1}+L_j) \end{aligned} \tag{3-23}$$

and h_i are the distances defining the location of the averaging processes illustrated in Figure 3-2.

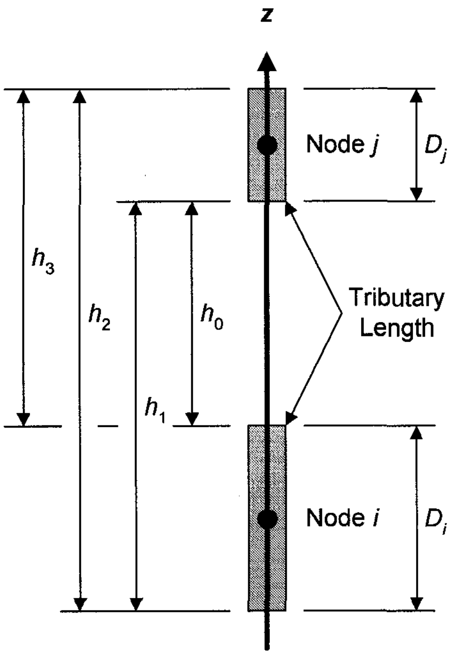

Figure 3-2: Generalized Distances for Spatial Correlation with Finite Element Model

The root-coherence function given in Equation (3-3) is the necessary component in the generation of the simulated wind speed time series to apply the random field model. As proposed by Simiu and Scanlan (1996), a frequency dependent random field model (also known as narrow-band cross-correlation), can be defined as

$$\sqrt{\mathrm{Coh}(s,n)} = e^{-\hat{f}} \tag{3-24}$$

which is simply an exponential decay function where the decay variable, $\hat{f}$, can be defined as

$$\hat{f} = \frac{n\left[C_z^2(z_1 - z_2)^2 + C_y^2(y_1 - y_2)^2\right]^{1/2}}{\frac{1}{2}\left[\bar{U}(z_1) + \bar{U}(z_2)\right]} \tag{3-25}$$

where n is the frequency and C_y and C_z are exponential decay coefficients. This study only considers spatial correlation along the vertical z-axis. Thus, $y_1 = y_2$ and Equation (3-25) reduces to

$$\hat{f} = \frac{nC_z\left|z_1 - z_2\right|}{\frac{1}{2}\left[\bar{U}(z_1) + \bar{U}(z_2)\right]} \tag{3-26}$$

which produces

$$\sqrt{\mathrm{Coh}(s,n)} = e^{-|z_1 - z_2|\left[\frac{nC_z}{\overline{U}(z_1,z_2)}\right]} \tag{3-27}$$

where the average wind speed between heights z_1 and z_2 is given as

$$\overline{U}(z_1,z_2) = \frac{1}{2}\left[\overline{U}(z_1) + \overline{U}(z_2)\right] \tag{3-28}$$

Simiu and Scanlan (1996) suggest that the exponential decay coefficient C_z be given a value of 10 based on experimental results. However, the dependence of the exponential decay coefficient upon terrain roughness, height above ground, and wind speed is insufficiently documented and therefore represents a source of uncertainty (Simiu and Scanlan, 1996).

3.3 Simulation of Wind Speed Time Series

From Section 3.1, the wind field properties are fully defined by the mean wind velocity profiles and a 3 x 3 matrix given in Equation (3-2). The computational efforts are greatly reduced in a simulation if the cross-covariance between u', v' and w' are insignificant and may be neglected as (Asa-Jakobsen and Strømmen, 2001)

$$\mathbf{S}\{s,n\} \approx \begin{bmatrix} S_{uu} & 0 & 0 \\ 0 & S_{vv} & 0 \\ 0 & 0 & S_{ww} \end{bmatrix} \tag{3-29}$$

in which case the simulations of $u'\{t\}$, $v'\{t\}$ and $w'\{t\}$ may be performed independently of one another. The use of Equation (3-29) is a commonly adopted assumption, as sufficient information regarding the off-diagonal terms is often difficult to compute/determine (Asa-Jakobsen and Strømmen, 2001).

In order to generate simulated wind speed time series that are correlated, a method proposed by Asa-Jakobsen and Strømmen (2001) is employed. In their study, they assumed that the approaching wind flow was unidirectional in reference to the mean velocity flow. This implies that the mean velocity flow is in the along-wind (longitudinal) direction and to complete the simulated wind speed time series for this direction, the mean wind velocity is added as given by Equation (3-1). The mean velocity flow is modeled using the logarithmic law given in Equation (3-6). Similar to Goode and van de Lindt (2006), Asa-Jakobsen and Strømmen (2001) also assumed that the wind field behaves as a stationary Gaussian random process. This implies that over the period for which the simulation is considered, the statistical variation of the wind does not change. Finally, Asa-Jakobsen and Strømmen (2001) assumed that the wind field was homogenous ensuring that in all regions in space, similar statistical properties exist.

A traditional spectral approach can then be used to generate simulated wind speed time series that are correlated. The spectral approach begins by subdividing the frequency range into N segments and the spatial representation of the flow fields into M points corresponding to the number of nodal points in the finite element representation of the structure (see Section 2.2). An M-by-M cross-spectral density matrix may be established for each frequency setting $\omega_n(n = 1 \rightarrow N)$ as (Asa-Jakobsen and Strømmen, 2001)

$$\mathbf{S}\{\omega_n\} = \begin{bmatrix} S_{11}\{\omega_n\} & S_{12}\{\omega_n\} & \cdots & S_{1M}\{\omega_n\} \\ S_{21}\{\omega_n\} & S_{22}\{\omega_n\} & \cdots & S_{2M}\{\omega_n\} \\ \vdots & \vdots & \ddots & \vdots \\ S_{M1}\{\omega_n\} & S_{M2}\{\omega_n\} & \cdots & S_{MM}\{\omega_n\} \end{bmatrix} \tag{3-30}$$

for each turbulence component u', v' and w' where $S_{ij}\{\omega_n\}$ is determined from the normalized co-spectra given in Equation (3-3). Cholesky decomposition may then be performed, such that $\mathbf{S}\{\omega_n\}$ may be written as the product of a lower triangular matrix $\mathbf{G}\{\omega_n\}$ and its transposed complex conjugate as

$$\mathbf{S}\{\omega_n\} = \mathbf{G}\{\omega_n\} \cdot \mathbf{G}^{*\mathrm{T}}\{\omega_n\} \tag{3-31}$$

where

$$\mathbf{G}\{\omega_n\}=\begin{bmatrix} G_{11}\{\omega_n\} & 0 & \cdots & 0 & \cdots & 0 \\ G_{21}\{\omega_n\} & G_{22}\{\omega_n\} & & 0 & & 0 \\ \vdots & \vdots & \ddots & \vdots & & \\ G_{m1}\{\omega_n\} & G_{m2}\{\omega_n\} & \cdots & G_{mm}\{\omega_n\} & & 0 \\ \vdots & \vdots & & \vdots & \ddots & \\ G_{M1}\{\omega_n\} & G_{M2}\{\omega_n\} & \cdots & G_{Mm}\{\omega_n\} & \cdots & G_{MM}\{\omega_n\} \end{bmatrix} \qquad (3\text{-}32)$$

Finally, a time domain simulated version of the process ($f = u'$, v', or w') at a point m in space may then be established from

$$f_m\{t\}=\sum_{k=1}^{m}\sum_{n=1}^{N-1}\left|G_{mk}\{\omega_n\}\right|\sqrt{2\Delta\omega}\cos\left[\omega_n t+\theta_{mk}\{\omega_n\}+\phi_{kn}\right] \qquad (3\text{-}33)$$

where θ_{mk} is zero if the cross-covariance between u', v' and w' are insignificant and neglected as assumed in Equation (3-29) and φ_{kn} is a random phase uniformly distributed on the interval $[0, 2\pi]$.

As noted, the use of Equation (3-33) allows for the independent generation of all three components of wind turbulence u', v' and w'. This study, however, will not consider the vertical turbulence component w' as contributions to structural response are negligible. Along-wind (longitudinal) and across-wind (lateral) turbulence components will be generated to determine the structural response. Figure 3-3 provides an example of the correlated wind speed time series for along-wind (longitudinal) components, u', at five points along a structure for two cases: a) full correlation, and b) no correlation. Note in

Figure 3-3a that gusts at one height correspond with gusts at other heights at the same time. This does not hold for Figure 3-3b.

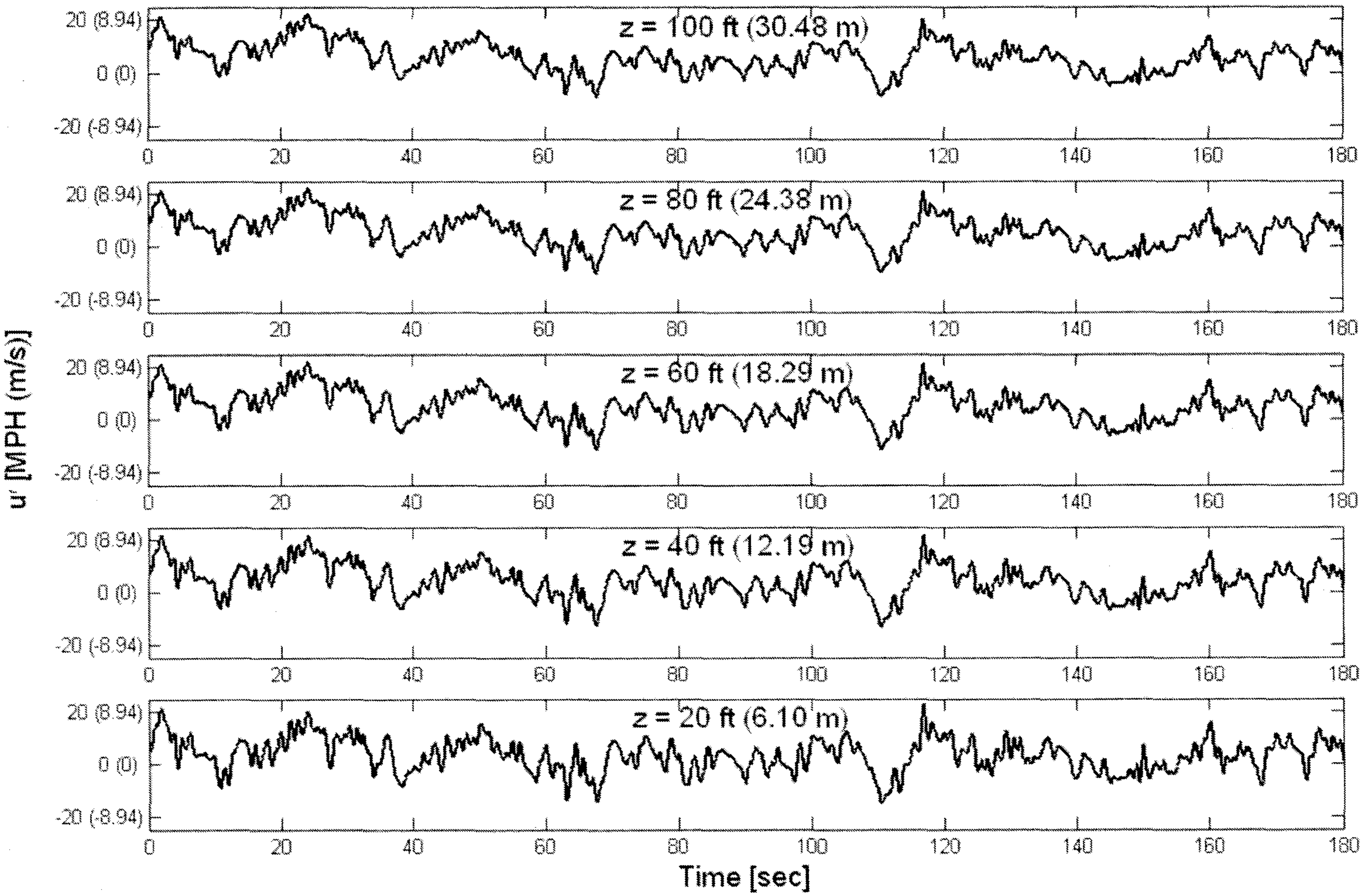

(a): Full Correlation

Figure 3-3: Spatially Correlated Wind Speed Time Series Example

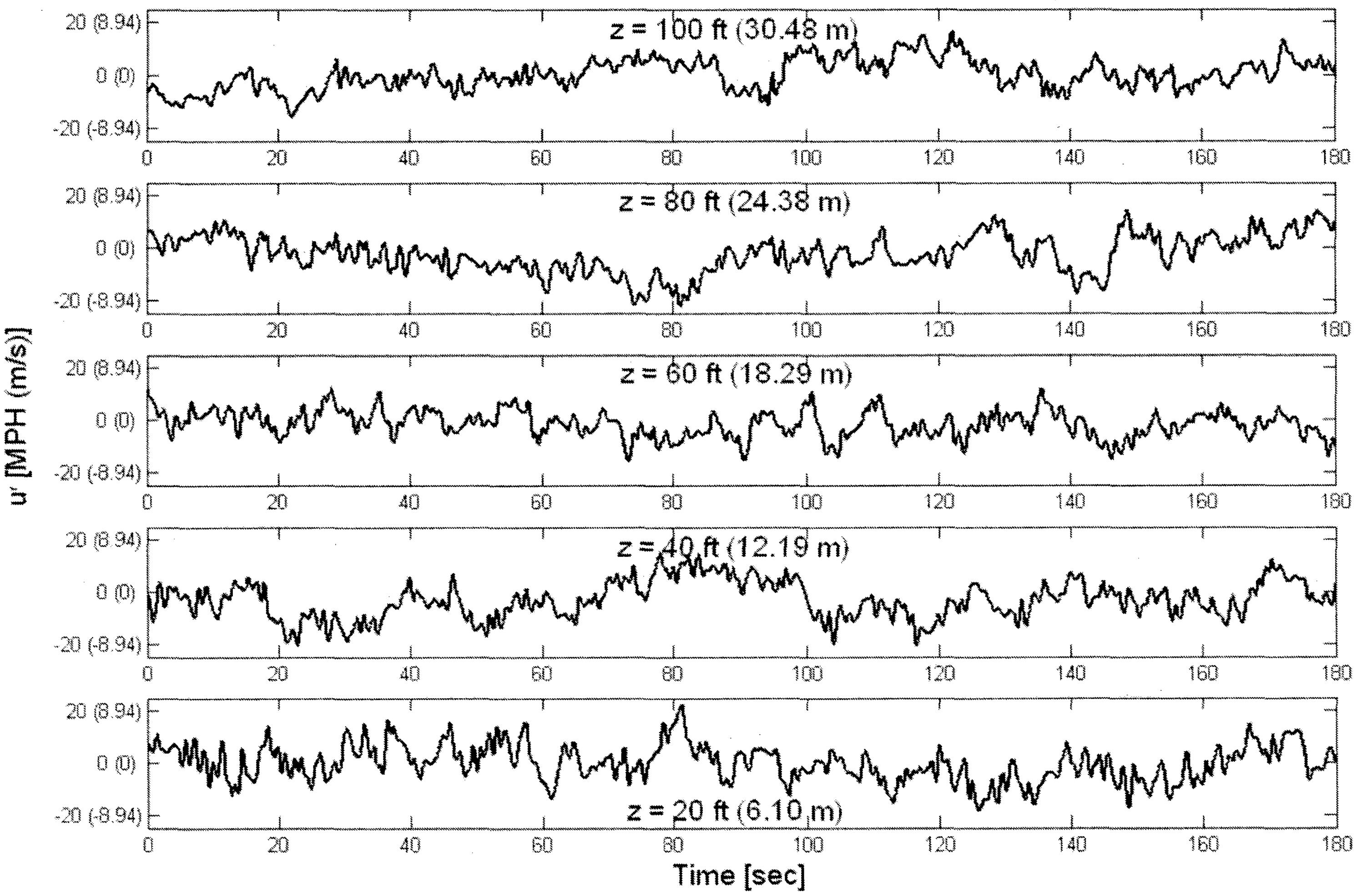

(b): No Correlation

Figure 3-3 (cont.): Spatially Correlated Wind Speed Time Series Example

Chapter Four

Vortex Shedding Modeling

4.1 Vortex Shedding

Aeroelasticity is the study of the interaction of aerodynamic forces and structural motions (Simiu and Scanlan, 1996). Aerodynamic forces that are caused or induced by structural motions, also known as self-excited forces, represent aeroelastic instabilities that are the focus of this chapter. Vortex shedding, common in slender, flexible structures particularly with a circular cross-section, can lead to aeroelastic instabilities caused by the aerodynamic forces and the motion of the structure. Vortex shedding, also called vortex-induced-vibration, is depicted in Figure 4-1 and occurs when vortices are formed and alternatively shed in the wake just behind the structure. As each vortex is shed, an across-wind force is induced towards the side of the shed vortex (Holmes, 2001). The alternative shedding induces a nearly harmonic across-wind force variation on the structure (Holmes, 2001).

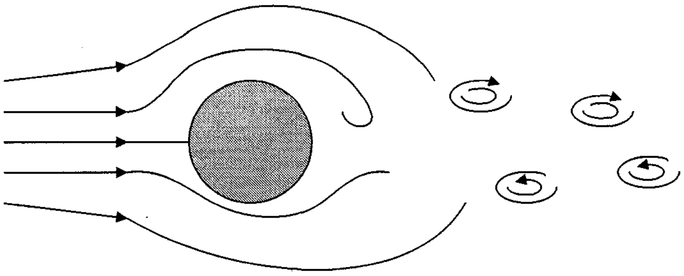

Figure 4-1: Vortex Shedding (Excerpted from Simiu and Scanlan, 1996)

The primary frequency of the alternating vortices shed from the structure, n_s, is related to the non-dimensional Strouhal number, St, as (Simiu and Scanlan, 1996; Holmes, 2001)

$$\mathrm{St} = \frac{n_s D}{\overline{U}} \tag{4-1}$$

where D is the cross-wind structure width, or diameter of the circular cross-section used in this study, and $\overline{U}$ is the mean wind speed acting on the structure. The Strouhal number varies with the shape of the cross-section. In addition, the Strouhal number for circular cross-sections varies with the Reynolds number as (Holmes, 2001)

$$\mathrm{Re} = \frac{\rho_{air}\overline{U}D}{\mu_{air}} = \frac{\overline{U}D}{\nu_{air}} \tag{4-2}$$

where ρ_{air} is the density of air, μ_{air} is the viscosity of air, and ν_{air} is the kinematic viscosity of air.

The vibration of the structure may also enhance the vortex intensity. Additionally, the vortex shedding frequency may change to the frequency of vibration of the structure due to structural motions in a phenomenon known as lock-in (Holmes, 2001). Near this frequency, mechanical frequency controls vortex shedding and greater movement is elicited producing stronger interaction even if the vortex shedding frequency is changed within a few percent because of flow velocity as shown in Figure 4-2 (Simiu and Scanlan, 1996). During lock-in, the amplitude of oscillations attains some fraction, rarely exceeding half, of the across-wind dimension (Simiu and Scanlan, 1996). Otherwise, the amplitude of oscillations caused by vortex shedding is relatively small.

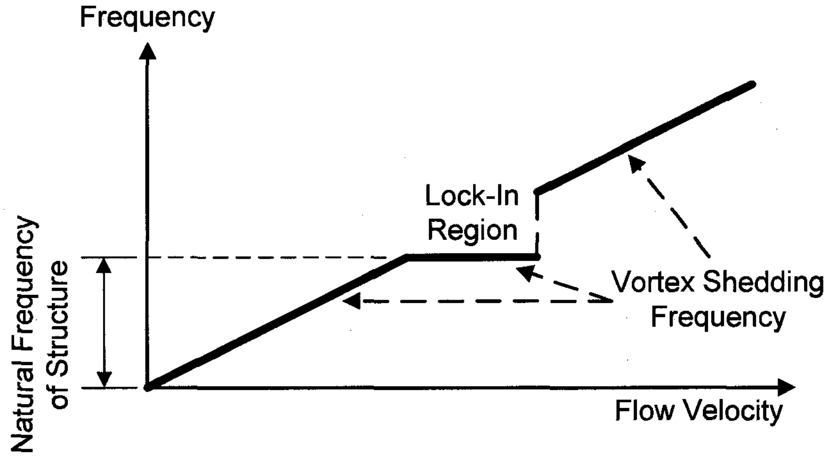

Figure 4-2: Vortex Shedding Lock-In (Excerpted from Simiu and Scanlan, 1996)

As discussed in Chapter One of this dissertation, no completely successful analytical (i.e. mechanistic model) method has yet been developed for vortex shedding (Simiu and Scanlan, 1996). Flexible structures, as considered in the present study, will deflect in some manner thus influencing the local flow. Simiu and Scanlan (1996) note that this has not been studied in detail. Thus, this is considered in the present study and incorporated into a time-domain finite element analysis framework as presented in latter sections of this chapter.

4.2 Modeling

Simiu and Scanlan (1986) proposed a useful empirical model for determining the effects of vortex shedding in the across-wind (lateral) direction, which is incorporated into the present study. In single degree-of-freedom form, the equation of motion of this model is given as

$$m\left[\ddot{y}+2\xi\omega_1\dot{y}+\omega_1^2 y\right]=\frac{1}{2}\rho_{air}U^2D\left[Y_1(k)\left(1-\varepsilon\frac{y^2}{D^2}\right)\frac{\dot{y}}{U}+Y_2(k)\frac{y}{D}+C_L(k)\sin(\omega_s t+\phi)\right] \quad (4\text{-}3)$$

where m is the structure mass, y, $\dot{y}$, and $\ddot{y}$ are the displacement, velocity, and acceleration, respectively, in the across-wind direction of the structure, ξ is the structure damping ratio, ω_1 is the structure natural frequency, ρ_{air} is the density of air, U is the along-wind (longitudinal) direction wind velocity, D is the frontal dimension or diameter of the pole, t is time in seconds, and φ is a random phase angle. As noted by Simiu and Scanlan (1986), this model exhibits characteristics of a Van der Pol oscillator or a non-conservative oscillator with nonlinear damping. Most importantly, however, as observed in experimental tests, this model contains aspects of being nonlinear and self-limiting in amplitude. Simiu and Scanlan (1986) note that at low amplitudes, this model produces fluid instigated negative damping that is reversed at higher amplitudes. The parameters Y_1, ε, Y_2, and C_L are empirically determined and are functions of the parameter k that is defined as

$$k = \frac{D\omega_s}{U} \tag{4-4}$$

where ω_s in Equations (4-3) and (4-4) satisfies the Strouhal relation as

$$\frac{\omega_s D}{U} = 2\pi \mathrm{St} \tag{4-5}$$

Based on the work of Vickery and Basu (1983), at lock-in where $\omega = \omega_1$ the second and third terms on the right-hand side of Equation (4-3) may be neglected since $Y_2 \approx 0$ and $C_L \approx 0$. This observation is based upon their relative magnitudes in comparison to the first term on the right-hand side reflecting the aerodynamic damping effects. In this study, however, only the second term on the right-hand side will be neglected reflecting that $Y_2 \approx 0$ as additional information concerning this parameter has not been published in detail. Thus, the first term and the third term on the right-hand side of Equation (4-3), herein referred to as the aerodynamic damping term and the forced vibration term, respectively, will be considered in this study for modeling vortex shedding effects on a slender, flexible structure.

Vickery and Basu (1983) developed this model for the application of the design of chimney and towers with circular cross-sections. Although the procedure presented by Vickery and Basu is conceptually advanced, it can yield results that may be uncertain to within at least 30%. This may be an undesirable consequence of this model, but, to date, this model is the most appropriate for incorporation into a time-domain finite element analysis framework. Other more comprehensive approaches to vortex shedding modeling, such as computational fluid dynamic (CFD) models, may produce more accurate results but are beyond the scope of this study. These models focus on the modeling of the entire wind flow field as opposed to the modeling of the wind flow field that only the structure "experiences". It should also be noted that until recently, CFD models have only considered rigid, non-flexible structures. However, more recent CFD studies have considered flexible structures as is considered in this study, but they have also only been focused on the effects of the wind field due to vortex shedding and not necessarily on the effects of the structure.

Aerodynamic Damping

The vortex-induced aerodynamic term contains the nonlinear and self-limiting aspects of the model given in Equation (4-3) and is triggered purely based on the response of the structure or its motion. This term, a function of the displacement and velocity of the pole and the empirical parameters Y_1 and ε, is given as

$$\frac{1}{2}\rho_{air}U^2 DY_1(k)\left(1-\varepsilon\frac{y^2}{D^2}\right)\frac{\dot{y}}{U} \tag{4-6}$$

Following Simiu and Scanlan (1986), the following substitution is made as

$$\varepsilon\frac{y^2}{D^2} \Rightarrow \left(\frac{y}{\lambda D}\right)^2 \leq 1 \tag{4-7}$$

where λ is the parameter defining the limiting displacement. For the case when the displacement, y, equals or exceeds λD the aerodynamic damping vanishes. Substituting Equation (4-7) into (4-6) results in

$$2\omega_1\rho_{air}D^2 K_{a0}\left(\frac{U}{U_{cr}}\right)\left[1-\left(\frac{y}{\lambda D}\right)^2\right]\dot{y} \tag{4-8}$$

where the term

$$K_{a0}\left(\frac{U}{U_{cr}}\right) \tag{4-9}$$

is defined as an aerodynamic coefficient and is addressed later in this section.

For this study, Equation (4-8), representing the aerodynamic damping term on the right-hand side of Equation (4-3), remains on the forcing function side of the equation of motion. It is, however, possible to equate Equation (4-8) to ($-2m\zeta_a\omega_1$) where the aerodynamic damping ratio is given as

$$\xi_a = \frac{-\rho_{air}D^2}{m}K_{a0}\left(\frac{U}{U_{cr}}\right)\left[1-\left(\frac{y}{\lambda D}\right)^2\right] \tag{4-10}$$

such that it may be moved to the left-hand side of the equation of motion. Then the total damping ratio of the system can be calculated as

$$\xi_t = \xi + \xi_a \tag{4-11}$$

where ξ is the structural damping ratio.

Forced Vibration

The vortex-induced forced vibration term, a function of the empirical parameter C_L, or lift coefficient, and the vortex shedding frequency, is given as

$$\frac{1}{2}\rho_{air}U^2DC_L(k)\sin(\omega_s t+\phi) \tag{4-12}$$

where ω_s is determined from the Strouhal relation given in Equation (4-5). The Strouhal number, St, and the lift coefficient are also detailed later in this section.

Following Vickery and Basu (1983), in a turbulent flow the structure would experience a superposition of two across-wind loads. First, the vortex-induced forced vibration term given in Equation (4-12). Second, the buffeting of the lateral turbulence in the approach flow given as

$$\frac{1}{2}\rho C_D(z,t)D(z)U^2(z)\left[\frac{v'(z,t)}{U(z)}\right] \tag{4-13}$$

where C_D is the drag coefficient and $v'(z,t)$ is the across-wind (lateral direction) turbulence component both as previously defined in Chapters Two and Three, respectively.

Parameters for Vortex Shedding Model

To determine the parameters for the vortex shedding model, a critical elevation height must be selected to determine the properties such as critical wind velocity, Reynolds number, and Strouhal number. From Simiu and Scanlan (1986), the critical elevation, z_{ei}, is suggested to be

$$z_{ei} = \begin{cases} h \\ \frac{2}{3}h \rightarrow \frac{5}{6}h \end{cases} \tag{4-14}$$

where Vickery and Basu (1983) use $(^5/_6)h$. Because a finite element procedure is used to discretize the structural system, all nodes of the finite element system will be used in this study to determine the properties for each individual node in relation to updates in the forcing function caused by vortex shedding. Thus, parameters will be checked at all nodes to determine critical wind velocities, Reynolds number, and Strouhal number for each node.

The Reynolds number is determined as

$$\mathrm{Re} = \frac{\rho U D}{\mu} = \frac{UD}{v} \tag{4-15}$$

where μ is the viscosity of air, v is the kinematic viscosity of air, U is the relative velocity between the along-wind (longitudinal) velocity and the structure velocity at a particular nodal height, and D is the outside diameter of the structure also at a particular nodal height. Thus, for a structure composed of M nodal points, there are M Reynolds numbers, one for each nodal height. The Strouhal number, based on an empirical relationship with the Reynolds number, can be determined for each nodal height as (Simiu and Scanlan, 1986)

$$\mathrm{St} = \begin{cases} 0.20 & \mathrm{Re} < 2\times10^5 \\ 0.22 \le \mathrm{St} \le 0.45 & 2\times10^5 \le \mathrm{Re} \le 2\times10^6 \\ c\left\{0.23 - 0.007\left[\log_{10}\left(\frac{k}{D}\right) + 5\right]\right\} & \mathrm{Re} > 2\times10^6 \end{cases} \tag{4-16}$$

where c is determined as

$$c = \begin{cases} 1.00 & \frac{h}{D(h)} \ge 30 \\ 0.736 + 0.012\left[\frac{h}{D(h)} - 8.0\right] & 8 < \frac{h}{D(h)} < 30 \end{cases} \tag{4-17}$$

and k is the grain size of the sand or surface roughness. In this study the structure is considered to be smooth. For $2 \times 10^5 \le \mathrm{Re} \le 2 \times 10^6$ in Equation (4-16) the vortex shedding is considered random in nature, and the Strouhal number given corresponds to the predominant frequency of the flow in the wake of the structure (Simiu and Scanlan, 1986).

The critical wind velocity, $U(z_{ei})$, occurring at an elevation z_{ei} produce vortex shedding frequencies equal to the natural frequencies of the structure as

$$U(z_{ei}) = \frac{1}{\mathrm{St}} n_i D(z_{ei}) \tag{4-18}$$

where n_i is the i^{th} natural frequency of the structure. For purposes of simplicity in this study, only the first natural frequency of the structure will be used. This assumption produces the lowest critical wind speed for which the vortex shedding model will lock-in. It is, however, possible to update the algorithm of the analysis to account for higher modes of structural vibration in the application of this vortex shedding model. Using the critical wind velocity for each nodal height, the aeroelastic parameter K_{a0} for the aerodynamic damping term given in Equations (4-8) and (4-9) is determined as (Simiu and Scanlan, 1986)

$$K_{a0}\left(\frac{U}{U_{cr}}\right)=\begin{cases} 0 & \dfrac{U}{U_{cr}}<0.85 \\ a_t\left(3.5\dfrac{U}{U_{cr}}-2.95\right) & 0.85\le\dfrac{U}{U_{cr}}<1.0 \\ 0.55a_t & 1.0\le\dfrac{U}{U_{cr}}<1.1 \\ a_t\left(2.75-2\dfrac{U}{U_{cr}}\right) & 1.1\le\dfrac{U}{U_{cr}}<1.3 \\ a_t\left(0.46-0.25\dfrac{U}{U_{cr}}\right) & 1.3\le\dfrac{U}{U_{cr}}<1.84 \\ 0 & 1.84\le\dfrac{U}{U_{cr}} \end{cases} \tag{4-19}$$

where

$$a_t=a_1a_2a_3a_4 \tag{4-20}$$

and

$$a_1 = \begin{cases} 1.0 & \mathrm{Re} < 10^4 \\ 1.8 & 10^4 \le \mathrm{Re} < 10^5 \\ 1.0 & 10^5 \le \mathrm{Re} \end{cases} \tag{4-21}$$

$$a_2 = \begin{cases} 2.0 & U(z_{ei}) \le 26.8\,\mathrm{MPH}\left(12\,{}^{m}\!/\!_{s}\right) \\ 1.0 & U(z_{ei}) > 26.8\,\mathrm{MPH}\left(12\,{}^{m}\!/\!_{s}\right) \end{cases} \tag{4-22}$$

$$a_3 = 0.9 + 0.2\left[\log_{10}\left(\frac{k}{D}\right) + 5\right] \tag{4-23}$$

$$a_4 = \begin{cases} 1.0 & \dfrac{h}{D(h)} > 12.5 \\ 1.0 - 0.04\left(12.5 - \dfrac{h}{D(h)}\right) & \dfrac{h}{D(h)} \le 12.5 \end{cases} \tag{4-24}$$

The parameter a_2 accounts for the fact that if the wind speed is relatively low the atmospheric turbulence may be weak thus leading to an enhancement of the aeroelastic effects of the aerodynamic damping term.

Finally, the drag coefficient, C_D, is as determined from Chapter Two and the lift coefficient, C_L, is determined for each nodal height as (Simiu and Scanlan, 1986)

$$C_L = \begin{cases} 0.45 & \mathrm{Re} < 2\times10^5 \\ 0.14 & 2\times10^5 \le \mathrm{Re} \le 2\times10^6 \\ d\left\{0.15 + 0.035\left[5 + \log_{10}\left(\frac{k}{D}\right)\right]^2\right\} & \mathrm{Re} > 2\times10^6 \end{cases} \tag{4-25}$$

where d is determined as

$$d = \begin{cases} 1.00 & \frac{h}{D(h)} \ge 12 \\ 0.8 + 0.05\left[\frac{h}{D(h)} - 8.0\right] & 8 < \frac{h}{D(h)} < 12 \end{cases} \tag{4-26}$$

Due to the nonlinear aerodynamic damping term of Equation (4-8) in the forcing function for the vortex shedding model used in this study, an iterative procedure similar to the procedure for relative velocity in Section 2.4 is employed within the analysis algorithm. As before, convergence is achieved when the difference between the nodal velocities of the structure before and after the updating of the forcing function are within a set tolerance. This iteration procedure for the vortex shedding forcing function including both the aerodynamic damping and forced vibration terms occurs within the relative motion iterative procedure.

Chapter Five

Fatigue Life Modeling

5.1 Narrow-Band Fatigue Life Estimation

A procedure outlined by Goode and van de Lindt (2006) is used in this study to estimate the fatigue life of a structure due to natural wind variations. The fatigue analysis assumes that the response of the structure is linear elastic, i.e., the loading of the structure causes no permanent deformations. The derivation to calculate or estimate the fatigue life of the structure follows the random vibration approach developed by Crandall and Mark (1963). According to the Palmgren-Miner rule, each stress cycle causes some amount of damage over some time duration. At some point, the accumulated damage reaches a value of unity, indicating (numerical) failure of the system.

The derivation of the procedure to estimate fatigue life assumes that the stress process is characterized as being a narrow-band stress process. A narrow-band stress process means that the resulting stress variations can be regarded as quasi-sinusoidal with randomly varying amplitudes (Holmes, 2001). The main feature of a narrow-band stress process is a zero or mean-level stress crossing between peaks. Figure 5-1 illustrates an example of a narrow-band stress process. Notice that the stress process crosses the mean-level denoted by the dashed line between each peak.

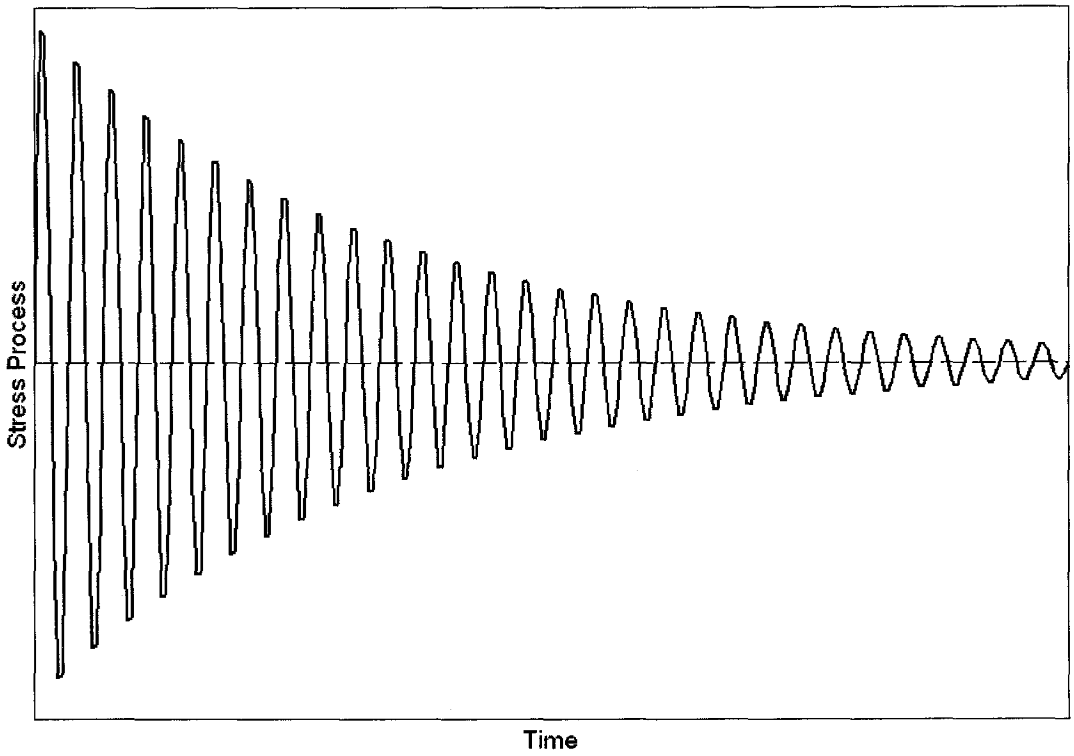

Figure 5-1: Narrow-Band Stress Process

First, it is assumed that v_0^+ is the mean up-crossing rate (i.e., the number of mean stress crossings with a positive slope over one second for the stress time history) such that during a time period the number of stress cycles is v_0^+. The fraction of these cycles that would have amplitudes between some value a and $a+da$ would be $p(a)da$ where $p(a)$ is the probability density function (PDF) of the peaks of the stress time history. The expected number of peaks, $n(a)$, between these values is then calculated as

$$n(a) = v_0^+ T p(a) da \tag{5-1}$$

where T is the time duration of the stress time history. According to the Palmgren-Miner rule, a single peak a causes an incremental damage of

$$dD = \frac{1}{N(a)} \tag{5-2}$$

where $N(a)$ is the number of cycles to failure at the stress amplitude a for that material from test data. For all cycles between a and $a+da$ over time, the expected damage is determined as

$$\frac{n(a)}{N(a)} = \frac{v_0^+ T p(a) da}{N(a)} \tag{5-3}$$

To account for all possible values of a and to determine the total expected damage, integration over the entire possible range from zero to infinity yields

$$E[D(T)] = v_o^+ T \int_0^\infty \frac{p(a)}{N(a)} da \tag{5-4}$$

where $E[D(T)]$ is the total expected damage. Assuming that the stress process is a Gaussian process, a process that fits a normal distribution, then the peaks follow a special case of the Weibull distribution known as the Rayleigh distribution (shape parameter = 2.0). The probability density function (PDF) for the Rayleigh distribution is given as

$$p(a) = \frac{a}{\sigma_y^2} \exp\left(-\frac{a^2}{2\sigma_y^2} \right) \qquad (5\text{-}5)$$

where a is the stress amplitudes and σ_y^2 is the variance of the stress process as a function of time. Substitution of Equation (5-5) into (5-4) produces

$$E[D(T)] = \frac{v_0^+ T}{c\sigma_y^2} \int_0^\infty a^{b+1} \exp\left(-\frac{a^2}{2\sigma_y^2} \right) da \qquad (5\text{-}6)$$

where b and c are fatigue constants related to the material of the structure. These constants, b and c, are determined from

$$NS^b = c \qquad (5\text{-}7)$$

where N is the number of cycles at stress amplitude S. As noted, b and c are the parameters that define the fatigue (S-N) curve for a particular stress category. Integrating the expected damage from Equation (5-6) yields

$$E[D(T)] = \frac{v_0^+}{c} \left(2\sqrt{2}\sigma_y \right)^b \Gamma\left(1 + \frac{b}{2} \right) \qquad (5\text{-}8)$$

where σ_y is the standard deviation of the stress process as a function of time and the gamma function is defined as

$$\Gamma(x) = \int_0^{\infty} t^{x-1} e^{-1} dt \tag{5-9}$$

Finally, setting $F_i = E[D(T)]_i$ for the i^{th} wind speed (from the PDF of wind speed; see Section 5.3) the fatigue life can be calculated according to the Palmgren-Miner rule as

$$F_{life} = \frac{1}{\sum_{i=1}^{n} F_i P_{0i}} \tag{5-10}$$

where P_{0i} is the probability of occurrence of the wind force for the i^{th} wind speed and causing the associated damage in Equation (5-8).

5.2 Wind-Band Fatigue Life Estimation

The damage resulting from the random stress process is determined based upon the assumption that the stress process is narrow-banded. A narrow-band assumption of the stress process means that the resulting stress variations can be regarded as quasi-sinusoidal with randomly varying amplitudes (Holmes, 2001). Indeed, however, this is usually not the case for wind-induced loading particularly when multi-mode excitation of the structure is induced by the loading function. The stress process is then characterized by a wide-band random process that is defined as random vibrations consisting of contributions over a broad range of frequencies (Holmes, 2001). Figure 5-2 illustrates an example of a wide-band stress process. Notice that the stress process does not necessarily cross the mean-level denoted by the dashed line between each peak.

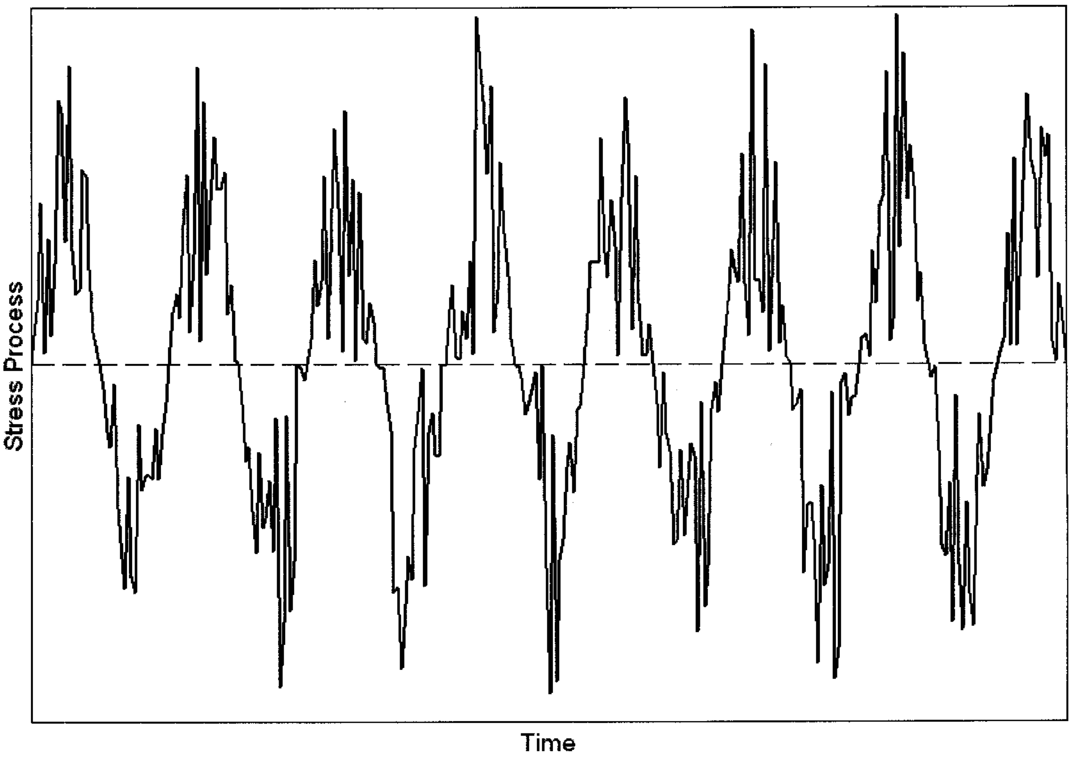

Figure 5-2: Wide-Band Stress Process

As such, Holmes (2001) outlines an empirical approach proposed by Wirsching and Light (1980) to determine the fractional fatigue damage due to a wide-band stress process. This damage is determined as

$$D = \lambda D_{nb} \qquad (5\text{-}11)$$

where D is the fatigue damage, D_{nb} is the damage calculated for a narrow-band stress process assumption as given by Equation (5-8), and λ is an empirical parameter. Based on the work of Wirsching and Light (1980), the empirical parameter is estimated based on the fatigue parameters of the S-N curve and a spectral bandwidth parameter, ε, given as

$$\varepsilon = 1 - \frac{\mu_2^2}{\mu_0 \mu_4} \tag{5-12}$$

where μ_k is the k^{th} moment of the spectral density of the wide-band stress process and is calculated as

$$\mu_k = \int_0^{\infty} n^k S(n) dn \tag{5-13}$$

where n is the frequency and $S(n)$ is the spectral density function of the stress process. It follows that the empirical parameter, λ, can be determined as

$$\lambda = a_\lambda + (1 - a_\lambda)(1 - \varepsilon)^{b_\lambda} \tag{5-14}$$

where the constants a_λ and b_λ are functions of the fatigue constants of the S-N curve given in Equation (5-7) as

$$\begin{aligned} a_\lambda &\approx 0.926 - 0.033b \\ b_\lambda &\approx 1.587b - 2.323 \end{aligned} \tag{5-15}$$

Finally, it should be noted that the variation in the spectral bandwidth parameter, ε, produces upper and lower limits on the estimated fatigue damage and, hence, the estimated fatigue life. For a purely narrow-banded stress process, the spectral bandwidth parameter will approach zero and thus the empirical parameter will approach one. This is given symbolically as

$$\varepsilon \to 0 \therefore \lambda \to 1 \tag{5-16}$$

This scenario produces an upper limit on the fatigue damage and a lower limit on the estimated fatigue life. Considering the other extreme, as the spectral bandwidth parameter approaches one, the empirical parameter will approach the value determined by the constant a in Equation (5-15) that is a function of the fatigue constants of the S-N curve. This is also given symbolically as

$$\varepsilon \to 1 \therefore \lambda \to a \tag{5-17}$$

This scenario produces a lower limit on the fatigue damage and an upper limit on the estimated fatigue life.

The approach used within this study will determine both the lower and upper limits of the estimated fatigue life. Then the estimated fatigue life as determined from Equation (5-11) utilizing Equations (5-12) – (5-15) will also be computed. As illustrated by Holmes (2001), it is envisioned that these results will further demonstrate the sensitivity of fatigue damage estimates based on the characteristics of the random stress process.

5.3 Lifetime Wind Speed Distributions

In order to estimate the fatigue life using Crandall and Mark's (1963) method, it is necessary to procure the wind speed statistical distribution information. Statistics for specific locations are not easily accessible and thus it is often difficult to determine the appropriate distribution to use in the determination of fatigue life. A recent project, however, at Colorado State University has procured NOAA (2006) data of recorded wind speeds in the state of Colorado and throughout the United States. Thus, using this set of data, these lifetime wind speed distributions, also called parent wind speed distributions, are being developed for the state of Colorado. For this study, however, two lifetime wind speed distributions will be utilized in the numerical investigation study for fatigue life in Chapter Eight.

The first lifetime wind speed distribution utilized in this study is an assumed distribution based on a reasonable fit for data developed by the National Oceanographic and Atmospheric Administration (NOAA) for the contiguous United States. The distribution utilized for this fit is the two-parameter lognormal distribution. The probability density function (PDF) for the lognormal distribution of wind speed, u, can be expressed as

$$f_U(u)=\frac{1}{\sqrt{2\pi}\,\zeta\,u}\exp\left[-\frac{1}{2}\left(\frac{\ln u-\lambda}{\zeta}\right)^2\right] \tag{5-18}$$

where the shape and scale parameters are ζ and λ, respectively, and are defined as

$$\begin{aligned}\zeta^2 &= \ln\left(1+\frac{\sigma^2}{\mu^2}\right)\\ \lambda &= \ln\mu-\frac{1}{2}\zeta^2\end{aligned} \tag{5-19}$$

and the parameters μ and σ are defined as the mean wind speed and standard deviation of wind speed, respectively. The mean wind speed and standard deviation of wind speed are related by the coefficient of variation (COV) as

$$\mathrm{COV}=\frac{\sigma}{\mu} \tag{5-20}$$

The second lifetime wind speed distribution utilized in this study makes use of some of the preliminary results from the project referenced above at Colorado State University. Traditionally the parent wind speed distribution is assumed to behave according to a two-parameter Weibull distribution in wind engineering literature (Holmes, 2001). The PDF for the Weibull distribution of wind speed, u, can be expressed as

$$f_U(u) = \frac{\kappa u^{\kappa-1}}{\lambda^\kappa} \exp\left[-\left(\frac{u}{\lambda} \right)^\kappa \right] \tag{5-21}$$

where the shape and scale parameters are κ and λ, respectively. The shape and scale parameters are determined by fitting the data obtained from the referenced project above to a Weibull distribution. The data chosen for this study is based on a site location near the Denver Metropolitan Area at the site of the former airport called Stapleton. The characteristics of this data are provided with the numerical investigation in Chapter Eight of this study. Finally, the mean and variance (square of the standard deviation) of the Weibull distribution are related to the shape and scale parameters as

$$\begin{gathered} \mu = \lambda \Gamma\left(1 + \frac{1}{\kappa}\right) \\ \sigma^2 = \lambda^2 \Gamma\left(1 + \frac{2}{\kappa}\right) - \mu^2 \end{gathered} \tag{5-22}$$

For example, consider Figure 5-3 that illustrates Equation (5-18), the lognormal PDF, for a mean wind speed of 20 MPH (8.94 m/s) and coefficient of variation equal to 25%.

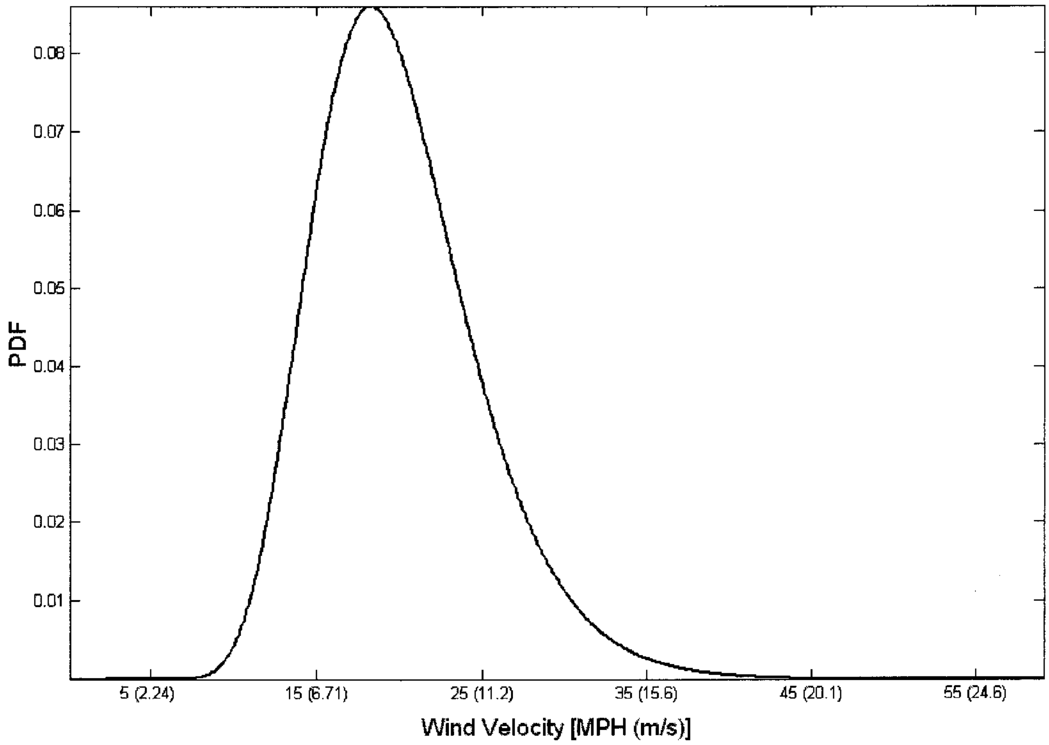

Figure 5-3: Lifetime PDF of Wind Speed

As given by Section 5.1, the fatigue life is estimated by dividing the PDF describing the wind speed over the life of the structure into bins of equal width each having a probability of occurrence, P_{0i}. The area under each bin represents the probability of occurrence of a wind speed having a magnitude between the upper and lower bounds of the bin. The probability of occurrence is paired with the wind speed occurring at the midpoint of that bin for fatigue analysis. Following Goode and van de Lindt (2006), twenty-five bins of equal width are used to estimate the fatigue life. Figure 5-4 illustrates the bins denoted by dashed lines that would be used for the PDF in Figure 5-3.

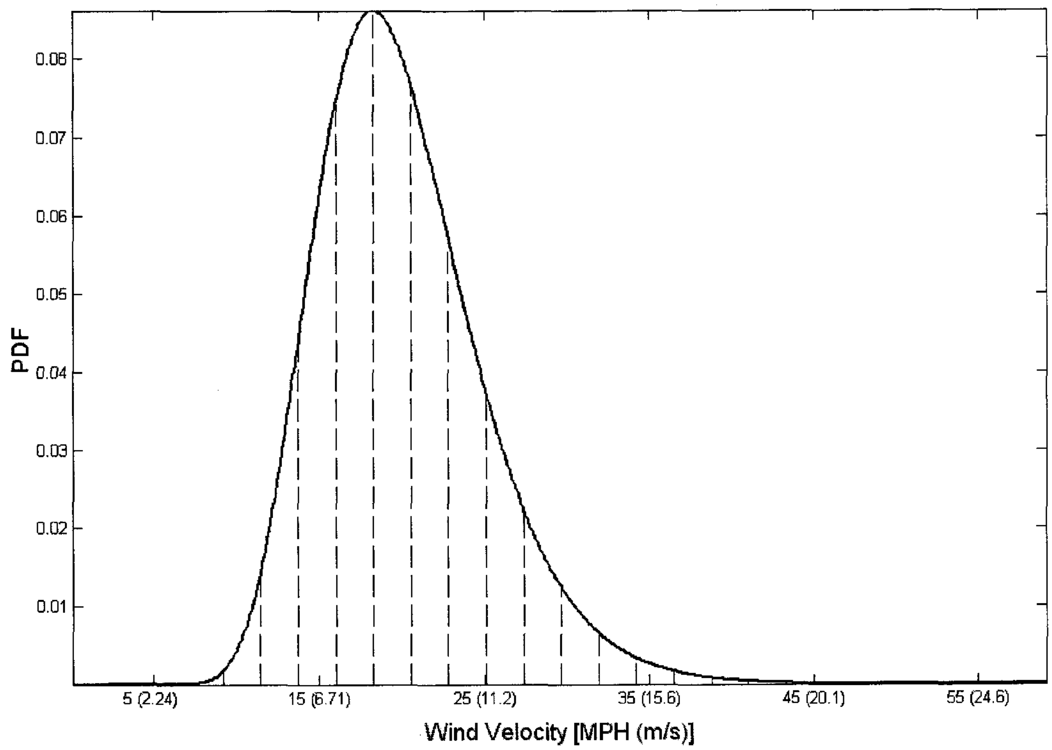

Figure 5-4: Lifetime PDF of Wind Speed with Bins

As the wind speed increases beyond the mean value, the area within each bin typically decreases. Although their occurrence probability is very small, high wind speeds must be considered as they may cause extensive damage to the structure, decreasing its fatigue life even with a relatively low probability of occurrence.

Chapter Six

Spatial Correlation

6.1 Setup and Procedure

This study of spatial correlation considers several variations in wind speed, structure properties such as vertical height, outside diameter, and wall thickness, and the spatial correlation of wind turbulence. The primary goal of this portion of the study is to determine the effects of the spatial correlation of wind turbulence on slender structural systems. A consequence of this study will result in the spatial correlation of the resulting load and response of the structure with respect to the assumed spatial correlation of wind turbulence. Cross-correlation parameters between these results are also of interest.

As given in Chapter Three, the spatial correlation of wind turbulence is derived from the root-coherence function contained within the cross-spectra of wind turbulence. Expressed in terms of the single-point spectra S_i and S_j as given in Equation (3-3), the normalized co-spectra is (Asa-Jakobsen and Strømmen, 2001)

$$S_{ij}\{s,n\} = \sqrt{S_i\{n\}S_j\{n\}}\sqrt{\mathrm{Coh}_{ij}\{s,n\}} \tag{6-1}$$

As proposed by Simiu and Scanlan (1996), a frequency dependent random field model (also known as narrow-band cross-correlation), can be defined as

$$\sqrt{\mathrm{Coh}(s,n)} = e^{-\hat{f}} \tag{6-2}$$

which is simply an exponential decay function where the decay variable, $\hat{f}$, is simplified by only considering points with vertical variations, z, as

$$\hat{f} = \frac{nC_z\left|z_1 - z_2\right|}{\frac{1}{2}\left[\overline{U}(z_1)+\overline{U}(z_2)\right]} \tag{6-3}$$

where n is the frequency and C_z is an exponential decay coefficient. Substituting Equation (6-3) into (6-2) produces

$$\sqrt{\mathrm{Coh}(s,n)} = e^{-\left|z_1 - z_2\right|\left[\frac{nC_z}{\overline{U}(z_1,z_2)}\right]} \tag{6-4}$$

where the average wind speed between heights z_1 and z_2 is given as

$$\overline{U}(z_1,z_2) = \frac{1}{2}\left[\overline{U}(z_1)+\overline{U}(z_2)\right] \tag{6-5}$$

Simiu and Scanlan (1996) suggest that the exponential decay coefficient C_z be given a value of 10 based on experimental results. However, the dependence of the exponential decay coefficient upon terrain roughness, height above ground, and wind speed is insufficiently documented and therefore represents a source of uncertainty (Simiu and Scanlan, 1996). Thus, the exponential decay coefficient is considered as the primary variable in determining the spatial correlation of wind turbulence in the generation of simulated wind speed time series for this numerical investigation.

Here, both two-dimensional and three-dimensional wind flows will be considered separately. Two-dimensional wind flow is comprised of only the along-wind (longitudinal) turbulence component u' and the mean wind velocity $\overline{U}$. The turbulence component u' is generated for each nodal point of the structure over a time duration of 3 minutes or 180 seconds. The mean wind velocity $\overline{U}$ is constant in time but varies along the height of the structure according to the logarithmic law defining the mean wind velocity profile given in Equation (3-6) as

$$\overline{U}(z) = \frac{u_*}{k} \ln\left(\frac{z}{z_0}\right) \tag{6-6}$$

where the parameters are defined in Section 3.1. Three-dimensional wind flow is comprised of both the along-wind (longitudinal) and across-wind (lateral) turbulence components u' and v', respectively, and the mean wind velocity $\overline{U}$. Both turbulence components u' and v' are generated independently for each nodal point of the structure over a time duration of 3 minutes or 180 seconds. As for two-dimensional wind flow, the mean wind velocity $\overline{U}$ in three-dimensional wind flow is constant in time but varies along the height of the structure according to the logarithmic law given in Equation (6-6).

Both cases of two-dimensional and three-dimensional wind flow will consider the same variations in the properties of the example structure first presented in Chapter Two. The variations in the properties of the example structure are outlined in Table 6-1. There are five vertical height variations, two outside diameter variations, and two wall thickness variations representing 20 total variations in the example structure properties. Each structure variation is discretized using finite elements of 2 ft (610 mm) in length. Thus, the structures having a vertical height of 60 ft (18.3 m) are composed of 30 elements; 80 ft (24.4 m) structures have 40 elements; and so on.

Property	Value
Vertical Height	60, 80, 100, 120, 140 ft (18.3, 24.4, 30.5, 36.6, 42.7 m)
Outside Diameter	2.0 and 2.5 ft (610 and 762 mm)
Wall Thickness	¼ and ½ in (6.35 and 12.7 mm)

Table 6-1: Variations in Example Structure Properties for Spatial Correlation

The variations in spatial correlation are outlined in Sections 6.2 and 6.3 for two-dimensional and three-dimensional wind flows, respectively.

6.2 2-D Wind Flow Results

The first numerical investigation of spatial correlation considers only two-dimensional wind flow in the along-wind (longitudinal) direction. In this case, only simulated wind speed time series are generated for the u' turbulence component. The mean wind velocity profile is added to this time series to derive the total wind speed time series for the along-wind (longitudinal) direction for dynamic analysis within the time-domain finite element analysis routine.

Variations in the exponential decay coefficient, C_z, within the root-coherence function of Chapter Three and Section 6.1 represent changes to the assumed spatial correlation of wind turbulence for the u' turbulence component. Table 6-2 provides a summary of the changes to the exponential decay coefficient $C_{z(long)}$ for the u' turbulence component considered for the two-dimensional flow analysis. The example structure property variations of Table 6-1 are also considered to vary for each of the variations listed in Table 6-2. Also as noted in Table 6-2, variations in the mean wind speed at 32.8 ft (10 m) above the ground are considered. There are 10 variations in mean wind speed, nine variations in the assumed spatial correlation of wind turbulence, and from Section 6.1 there are 20 variations in the example structure properties. Thus, there are 1,800 separate analyses for two-dimensional wind flow that are considered for this investigation.

Property	Value
Mean Wind Speed at 32.8 ft (10 m)	10, 20, 30, 40, 50, 60, 70, 80, 90, 100 MPH (4.47, 8.94, 13.4, 17.9, 22.4, 26.8, 31.3, 35.8, 40.2, 44.7 m/s)
Along-Wind (Longitudinal) Exponential Decay Coefficient, $C_{z(long)}$	0, 2.5, 5.0, 7.5, 10, 20, 100, 1000, $+\infty$

Table 6-2: Variations in Wind Flow Properties for 2-D Wind Flow

Results of Analysis

The results for the two-dimensional wind flow numerical investigation are presented and discussed using two primary components. First, complete time-domain examples of the wind flow, wind loading, and response of the structure are presented graphically. Limitations require that only a few examples may be presented, but these offer a representative description of all the analyses conducted for this first study. Supplementing these examples are maximum response figures for select analyses considered for this study. The second component presents an overall effect of the spatial correlation of the wind flow on the resultant loading, response, and other parameters of the resulting analysis. Particular attention is given to the spatial correlation and cross-correlation of certain processes.

Figures 6-1 through 6-5 provide an illustrative representation of the resulting time-domain dynamic analysis of the structure considered. Sub-figure's (a), (b), and (c) provide the time history for along-wind speed, resulting along-wind load, and along-wind displacement, respectively. Comparisons between the various assumed spatial correlation parameter are given for values of $C_{z(long)} = C_z = 0$, 10, and $+\infty$ representing full, strong and very weak spatial correlation of the wind flow, respectively. Each figure also provides the respective time history at different heights along the structures. These heights are roughly at the ⅓, ⅔, and top points of the structure. Each figure also considers a set of common parameters such that comparisons are easily observed. The mean wind speed for each figure is considered to be 50 MPH (22.4 m/s) at 32.8 ft (10 m). Furthermore, the structure cross-section properties for each figure provided have an outside diameter of 2.0 ft (610 mm) and a wall thickness of ¼ in (6.35 mm). Note, however, that far more variations in mean wind speed and structure properties were considered as given in Tables 6-1 and 6-2, but are not fully provided for by Figures 6-1 through 6-5 in the interest of brevity.

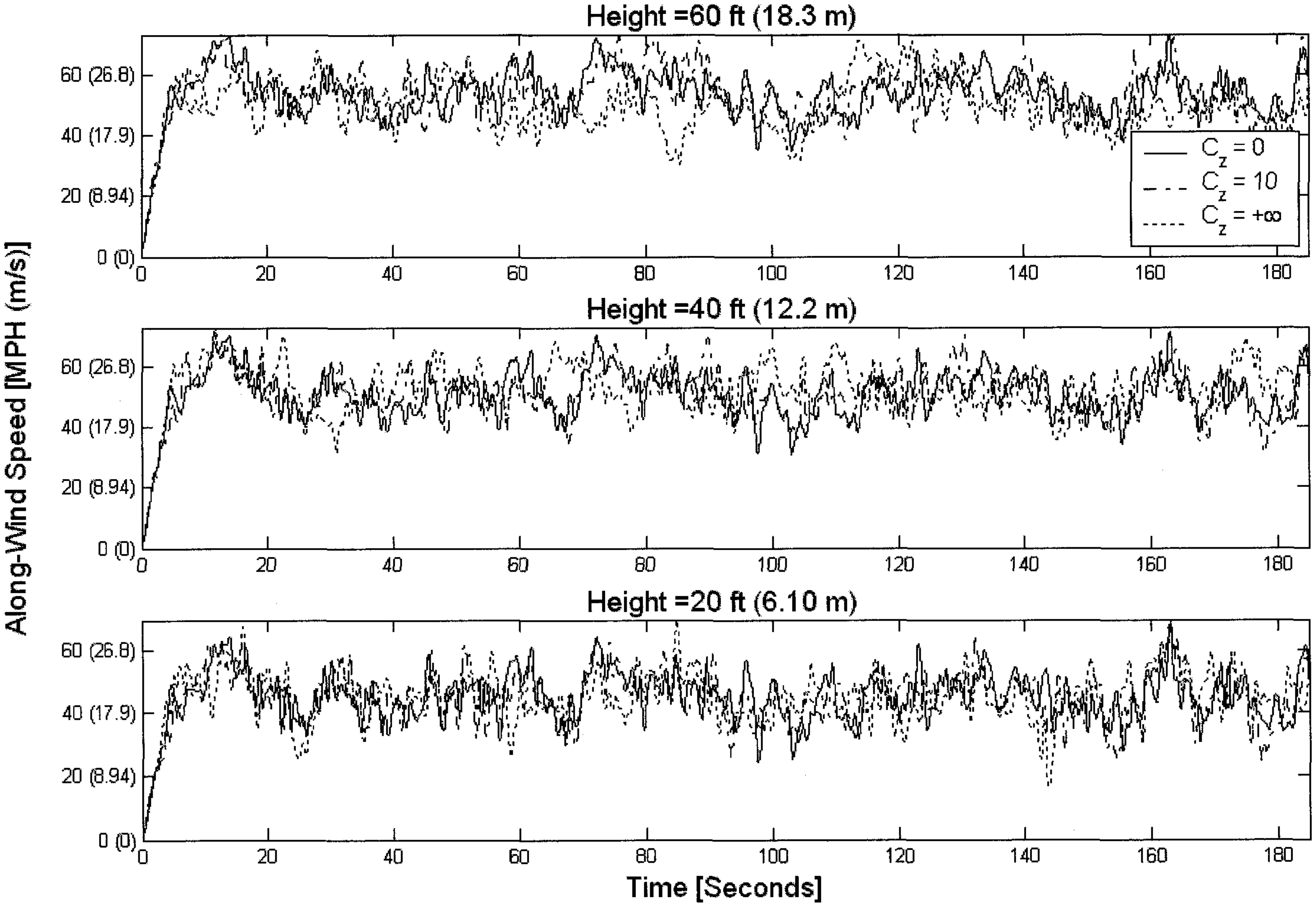

(a): Wind Speed Time History

Figure 6-1: 2-D Wind Flow Time History of Analysis – Vertical Height = 60 ft (18.3 m)

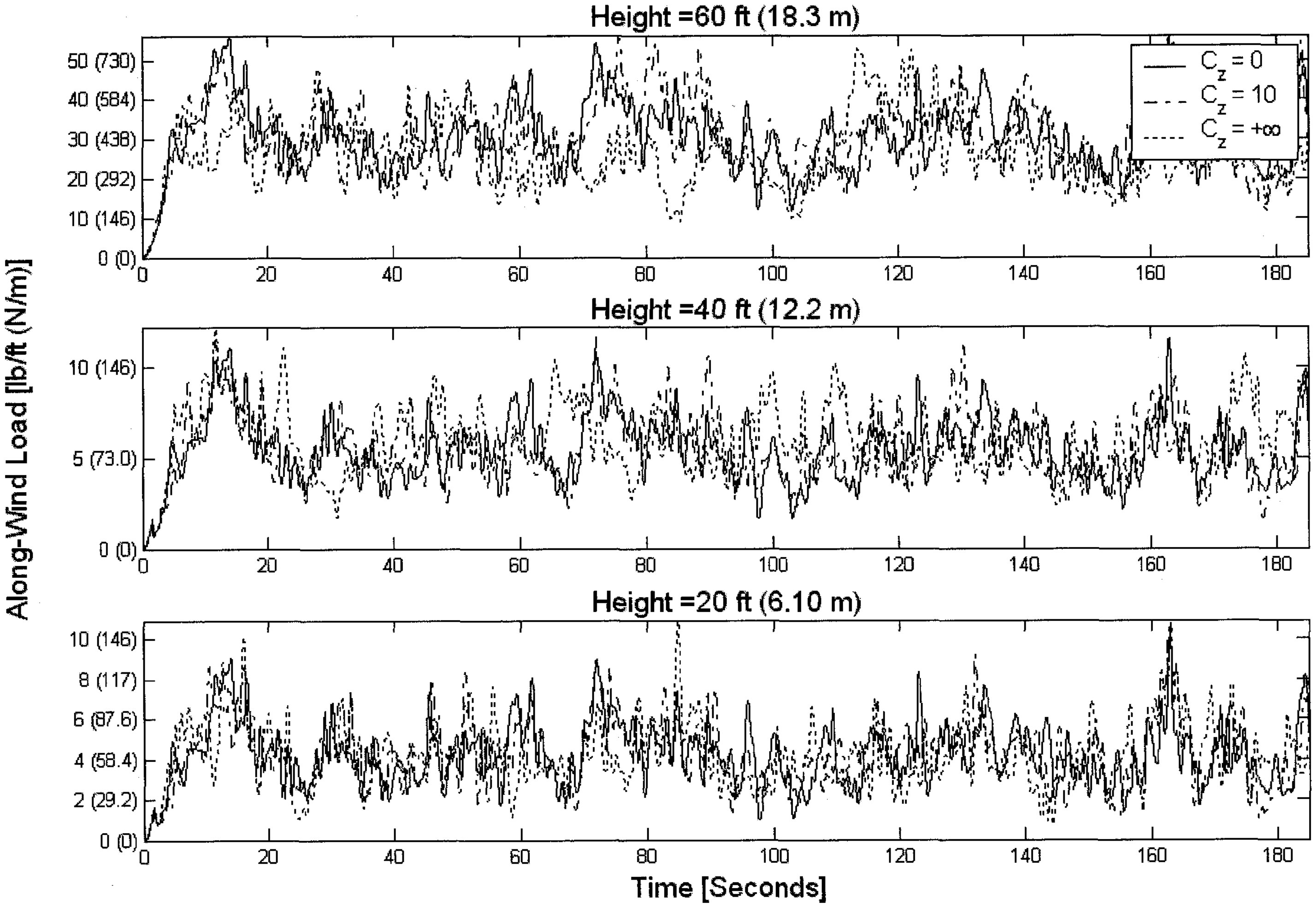

(b): Wind Load Time History

Figure 6-1 (cont.): 2-D Wind Flow Time History of Analysis – Vertical Height = 60 ft (18.3 m)

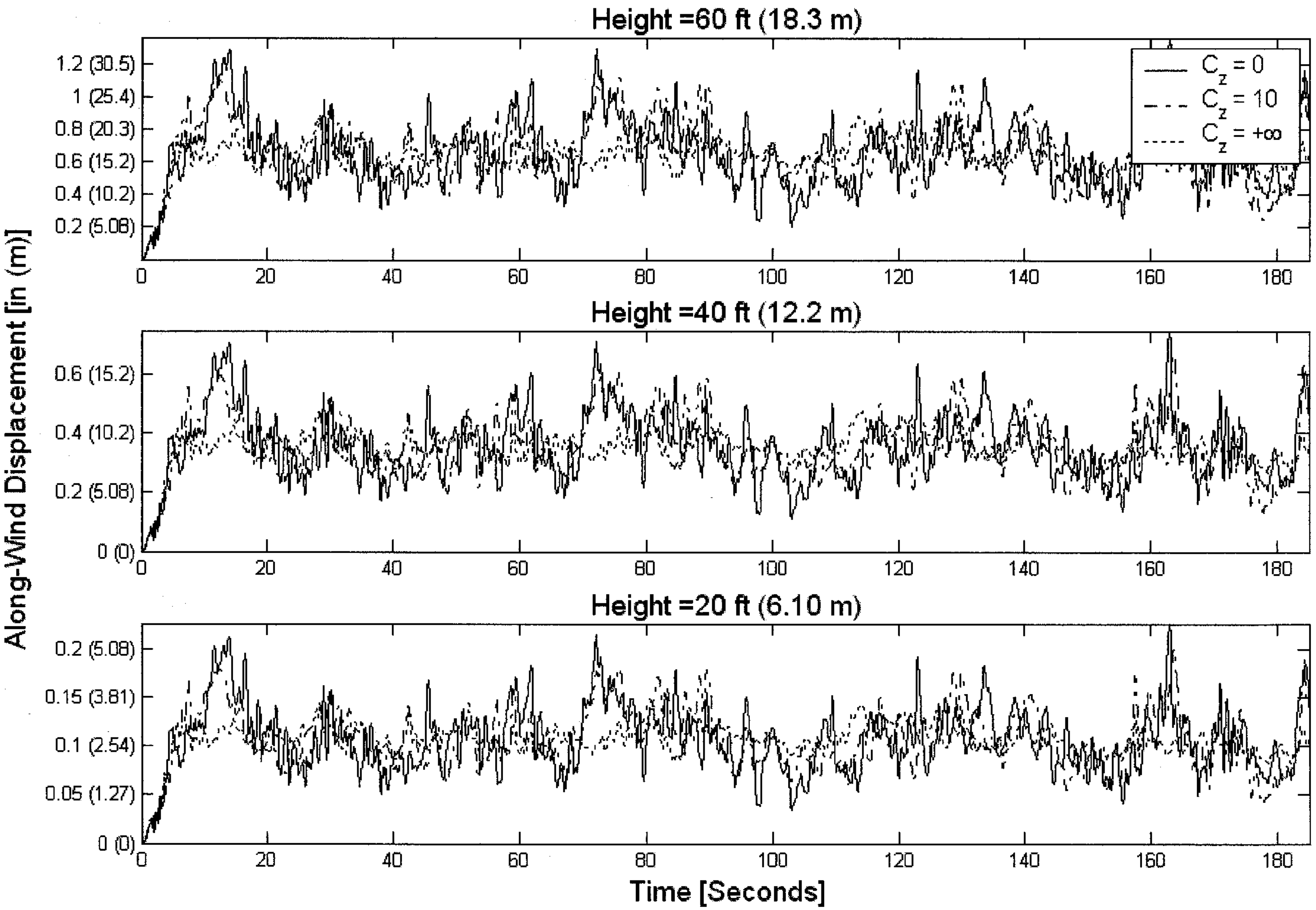

(c): Along-Wind Displacement Time History

Figure 6-1 (cont.): 2-D Wind Flow Time History of Analysis – Vertical Height = 60 ft (18.3 m)

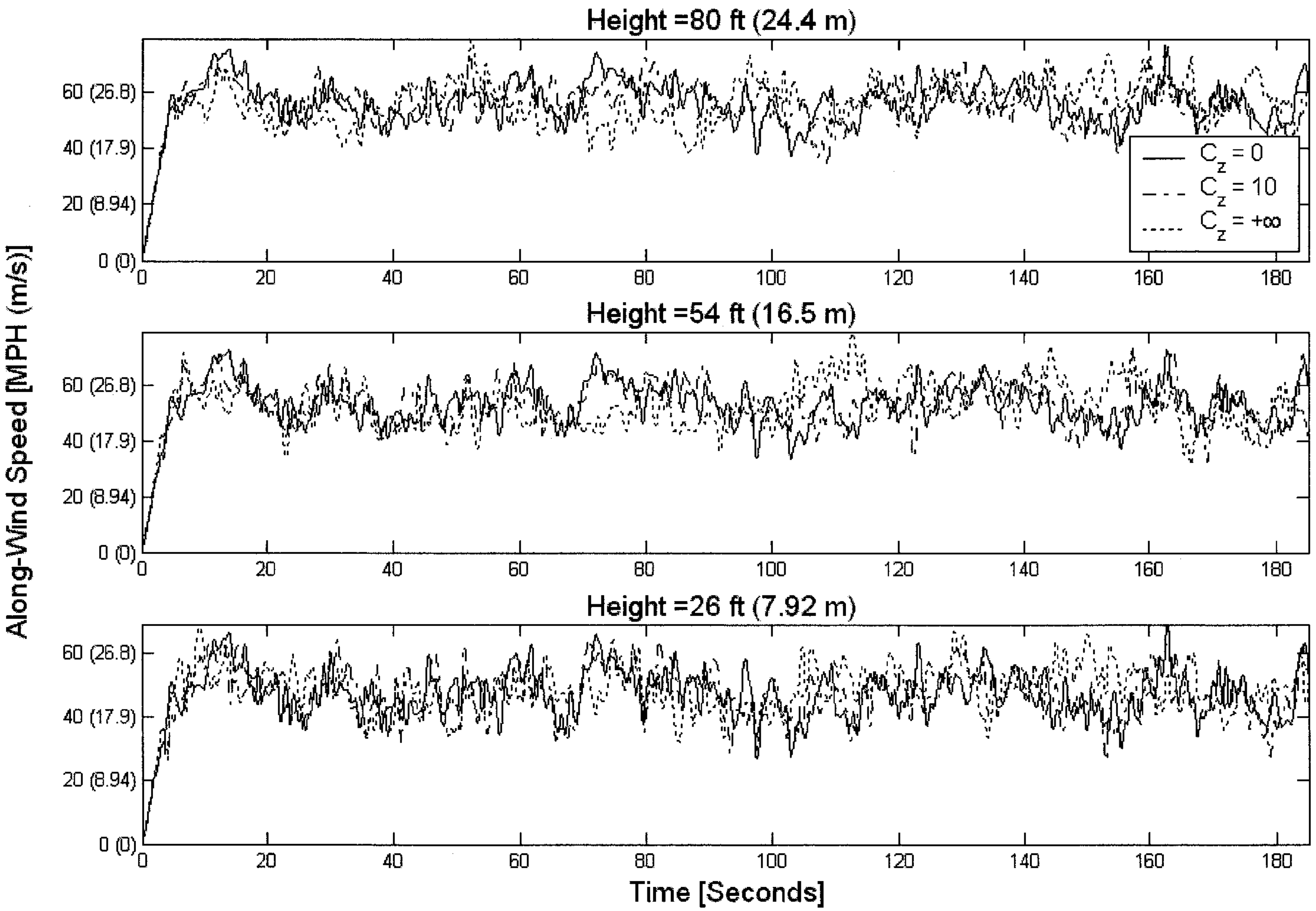

(a): Wind Speed Time History

Figure 6-2: 2-D Wind Flow Time History of Analysis – Vertical Height = 80 ft (24.4 m)

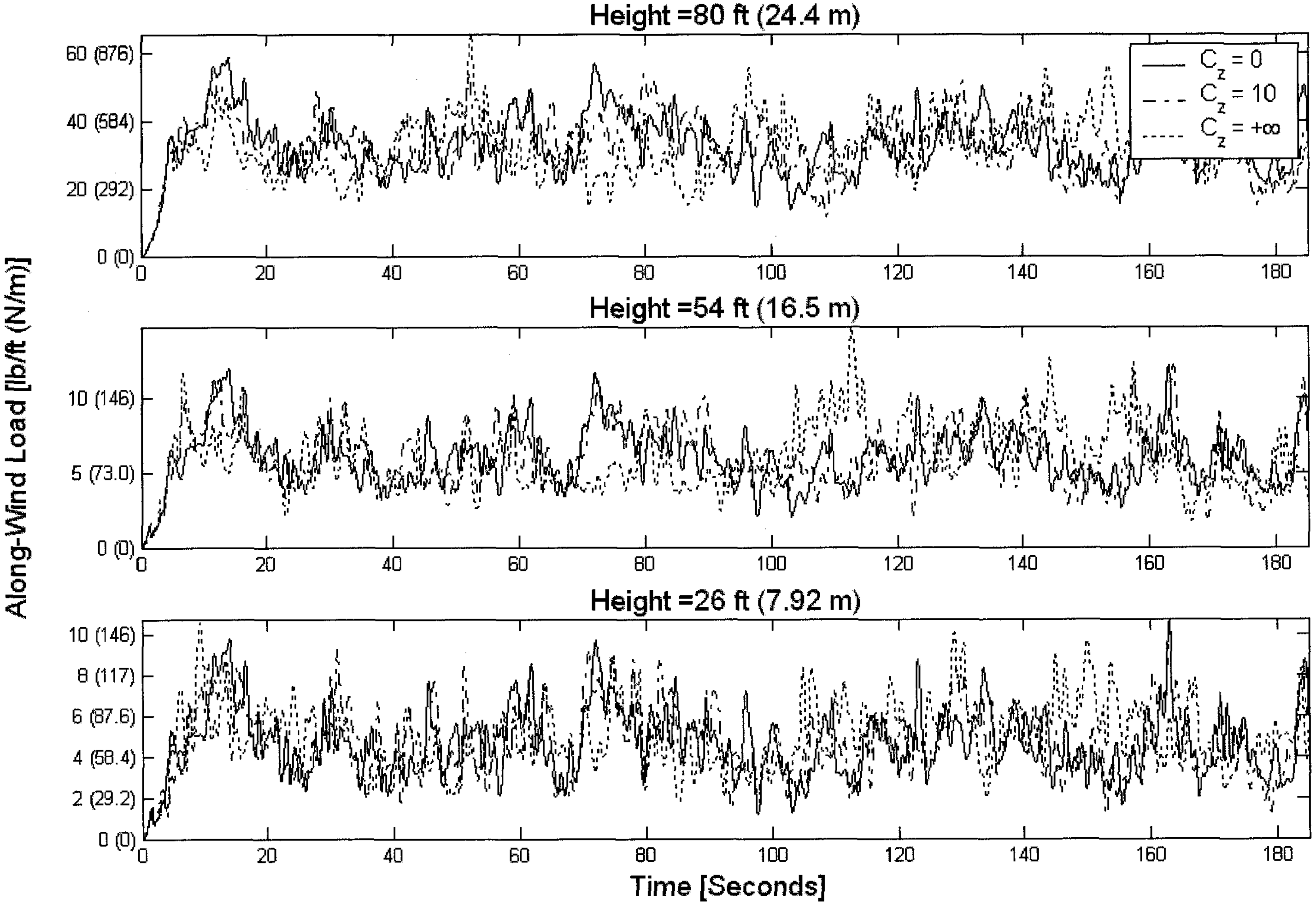

(b): Wind Load Time History

Figure 6-2 (cont.): 2-D Wind Flow Time History of Analysis – Vertical Height = 80 ft (24.4 m)

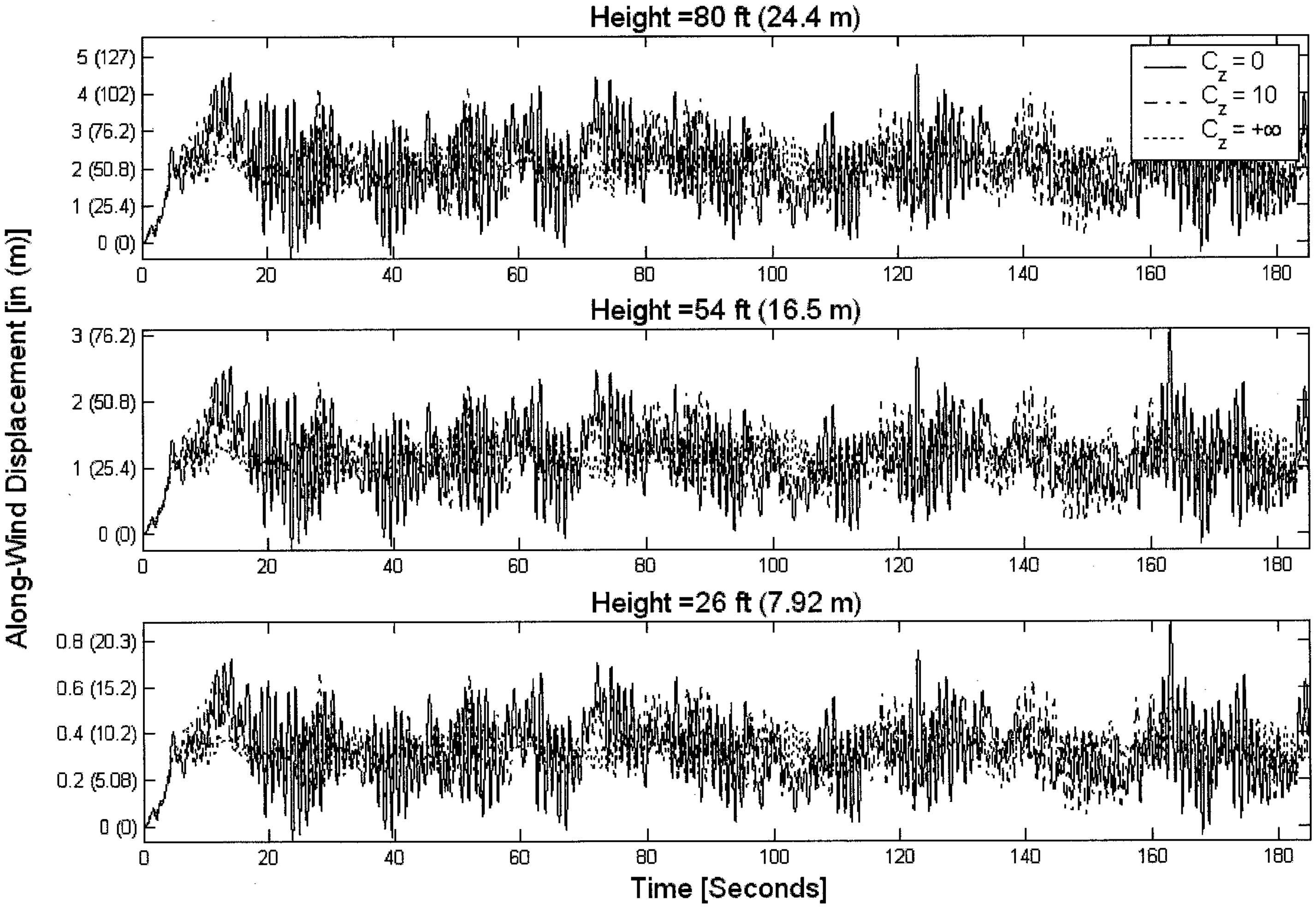

(c): Along-Wind Displacement Time History

Figure 6-2 (cont.): 2-D Wind Flow Time History of Analysis – Vertical Height = 80 ft (24.4 m)

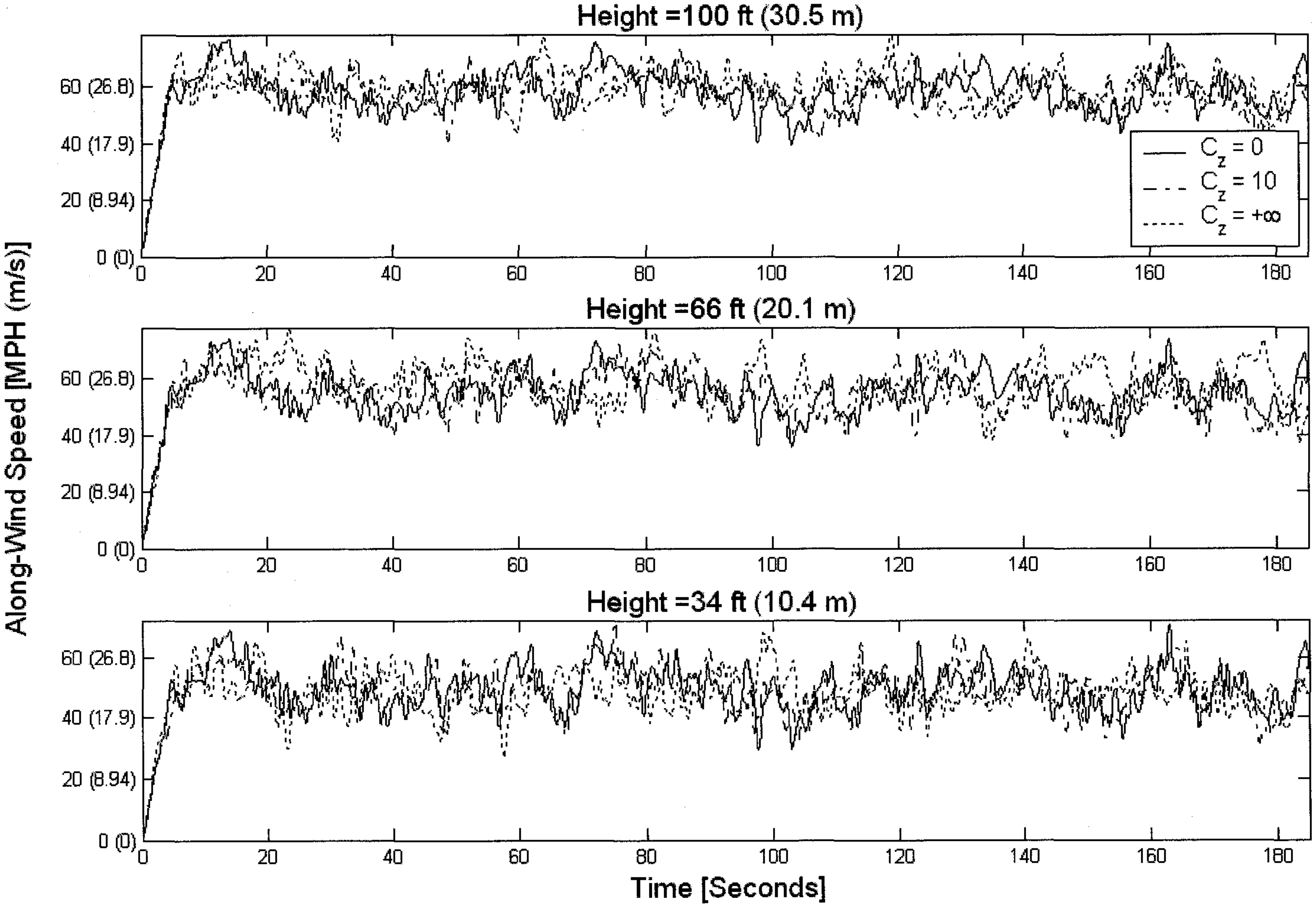

(a): Wind Speed Time History

Figure 6-3: 2-D Wind Flow Time History of Analysis – Vertical Height = 100 ft (30.5 m)

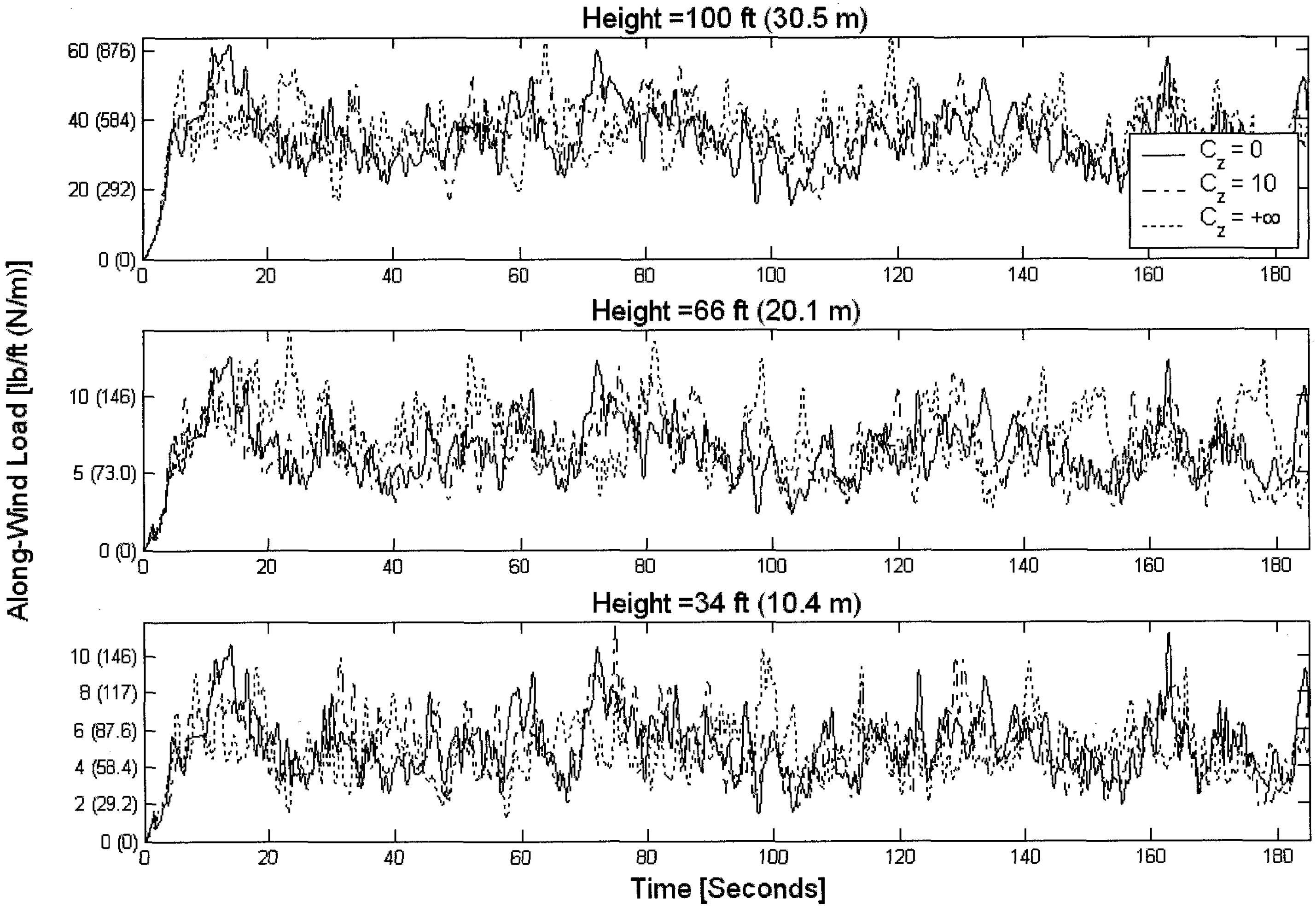

(b): Wind Load Time History

Figure 6-3 (cont.): 2-D Wind Flow Time History of Analysis – Vertical Height = 100 ft (30.5 m)

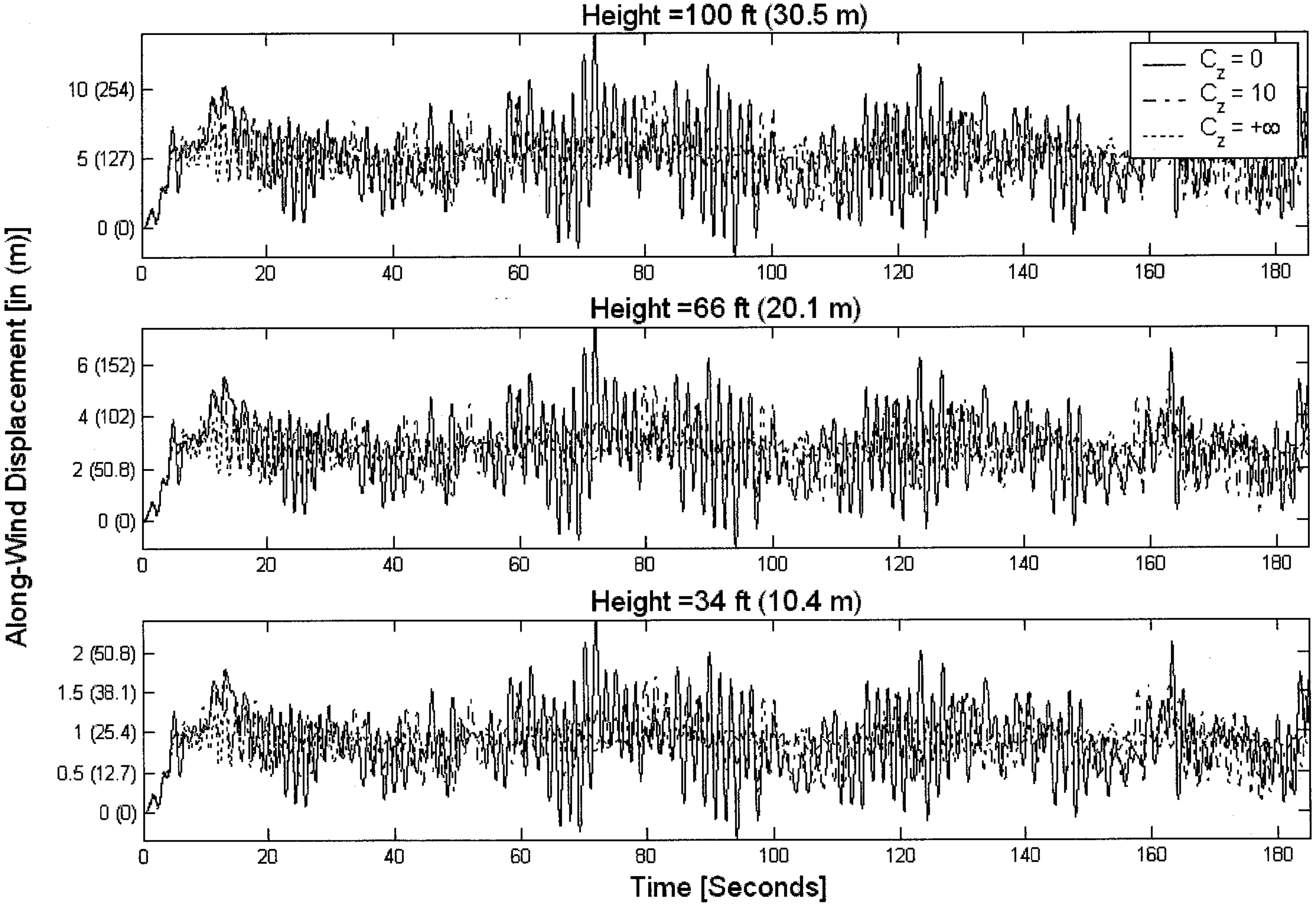

(c): Along-Wind Displacement Time History

Figure 6-3 (cont.): 2-D Wind Flow Time History of Analysis – Vertical Height = 100 ft (30.5 m)

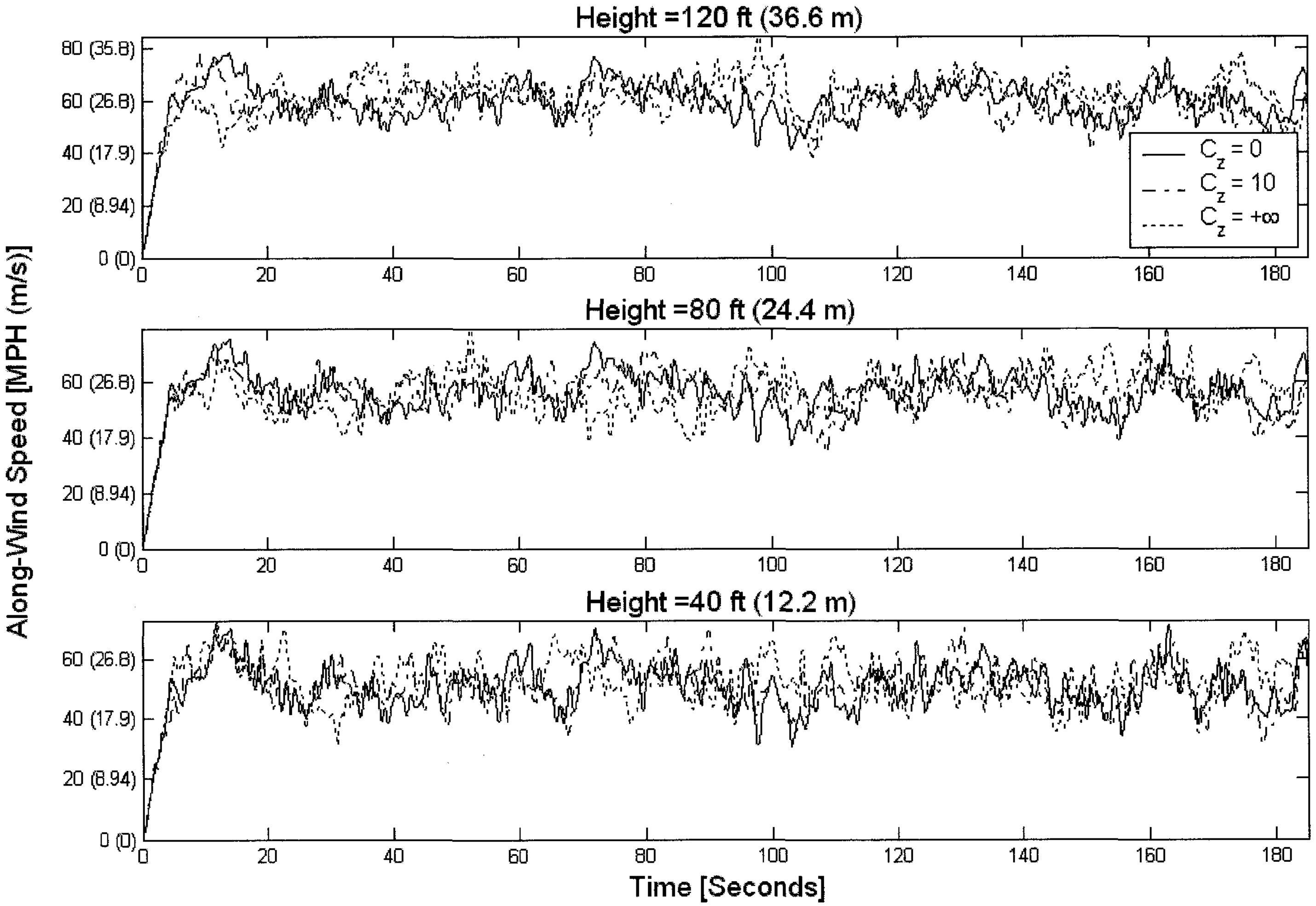

(a): Wind Speed Time History

Figure 6-4: 2-D Wind Flow Time History of Analysis – Vertical Height = 120 ft (36.6 m)

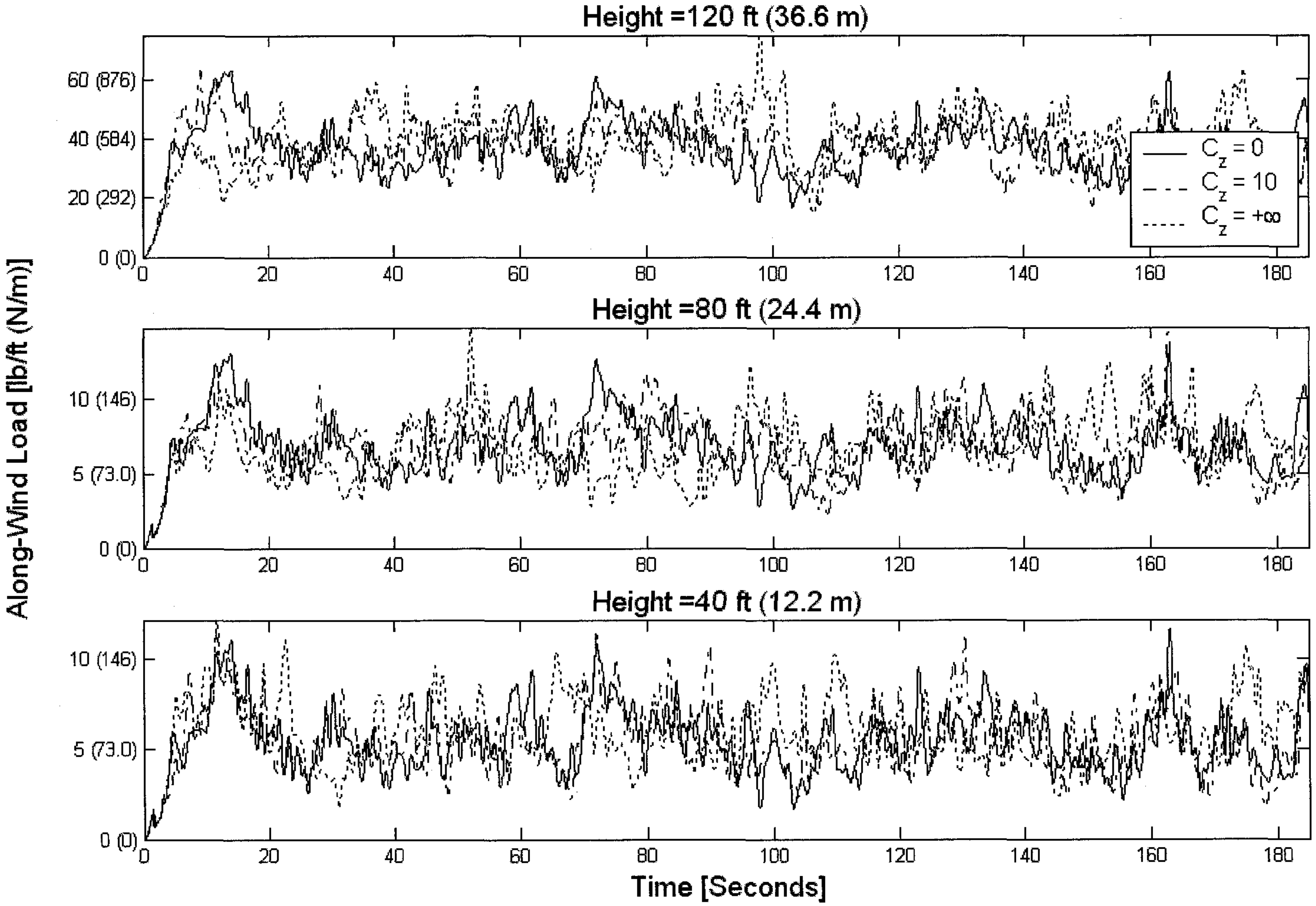

(b): Wind Load Time History

Figure 6-4 (cont.): 2-D Wind Flow Time History of Analysis – Vertical Height = 120 ft (36.6 m)

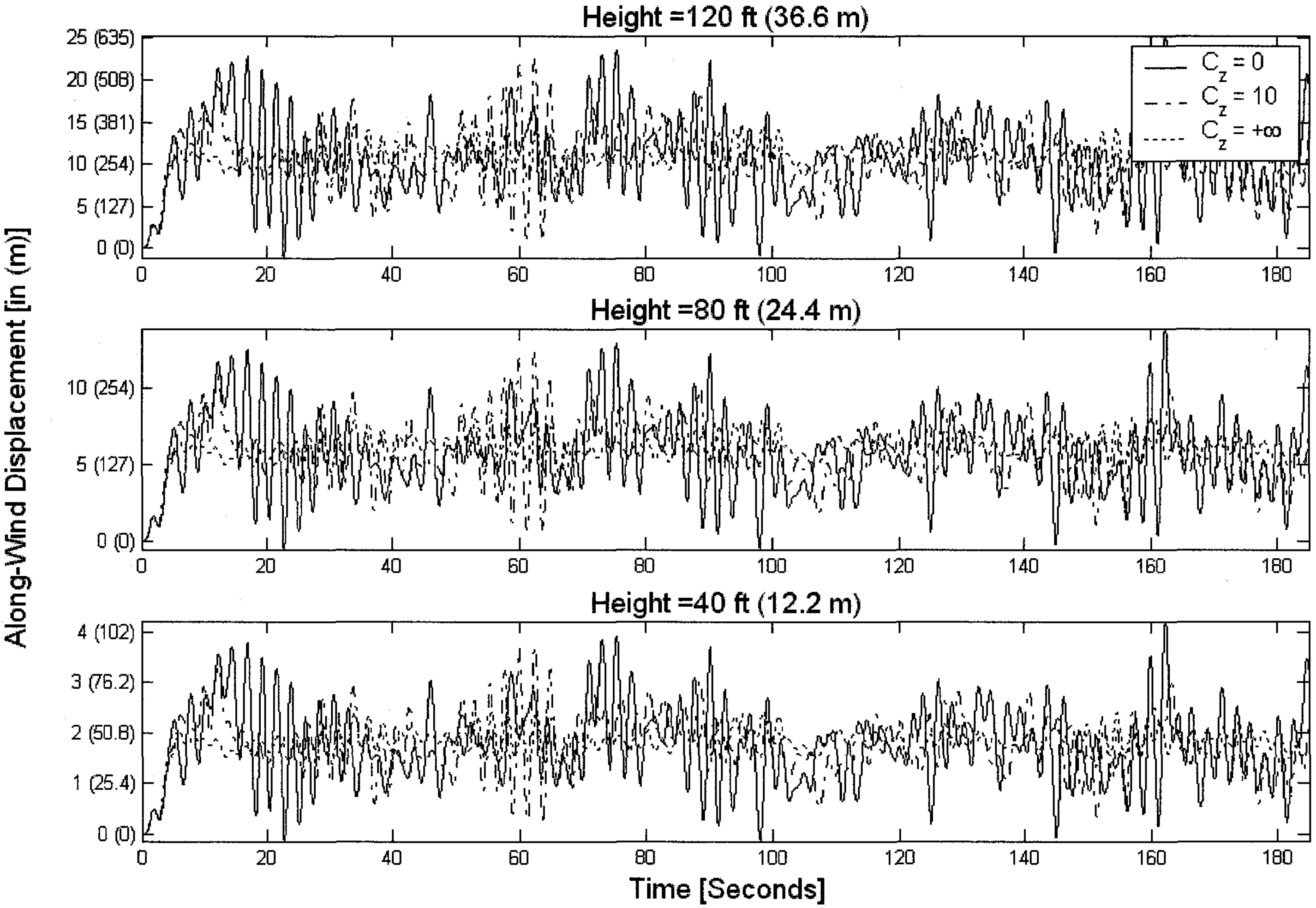

(c): Along-Wind Displacement Time History

Figure 6-4 (cont.): 2-D Wind Flow Time History of Analysis – Vertical Height = 120 ft (36.6 m)

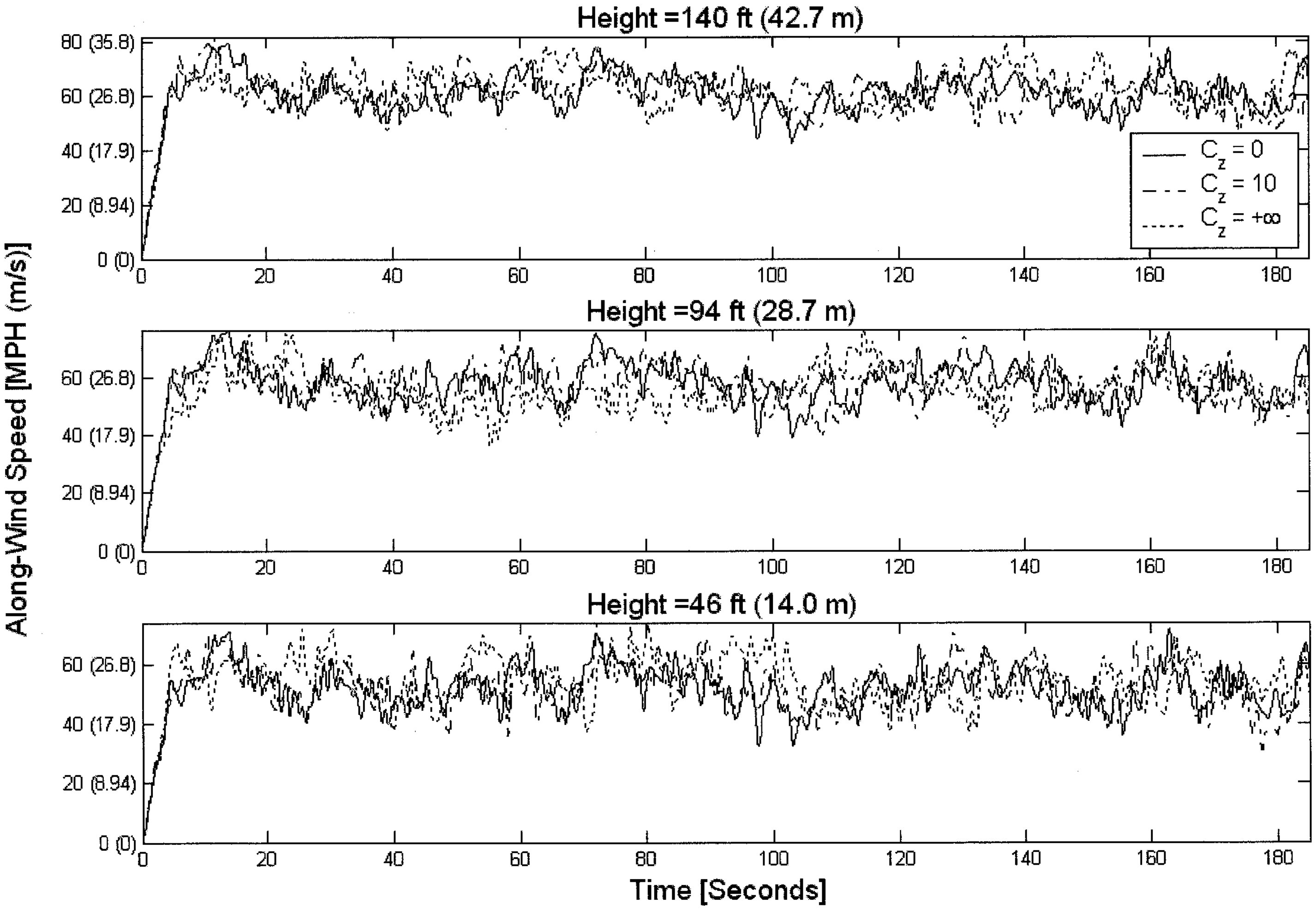

(a): Wind Speed Time History

Figure 6-5: 2-D Wind Flow Time History of Analysis – Vertical Height = 140 ft (42.7 m)

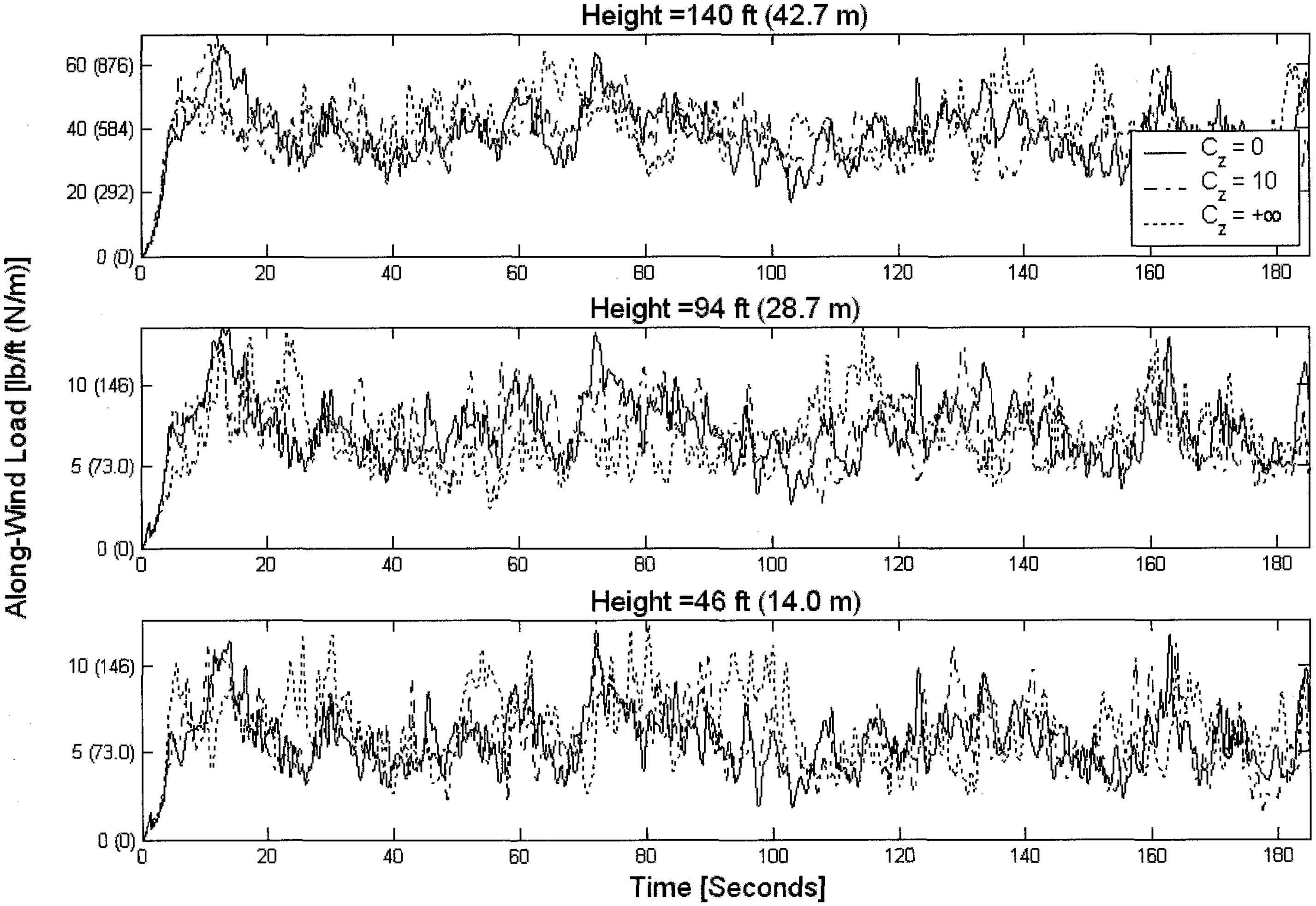

(b): Wind Load Time History

Figure 6-5 (cont.): 2-D Wind Flow Time History of Analysis – Vertical Height = 140 ft (42.7 m)

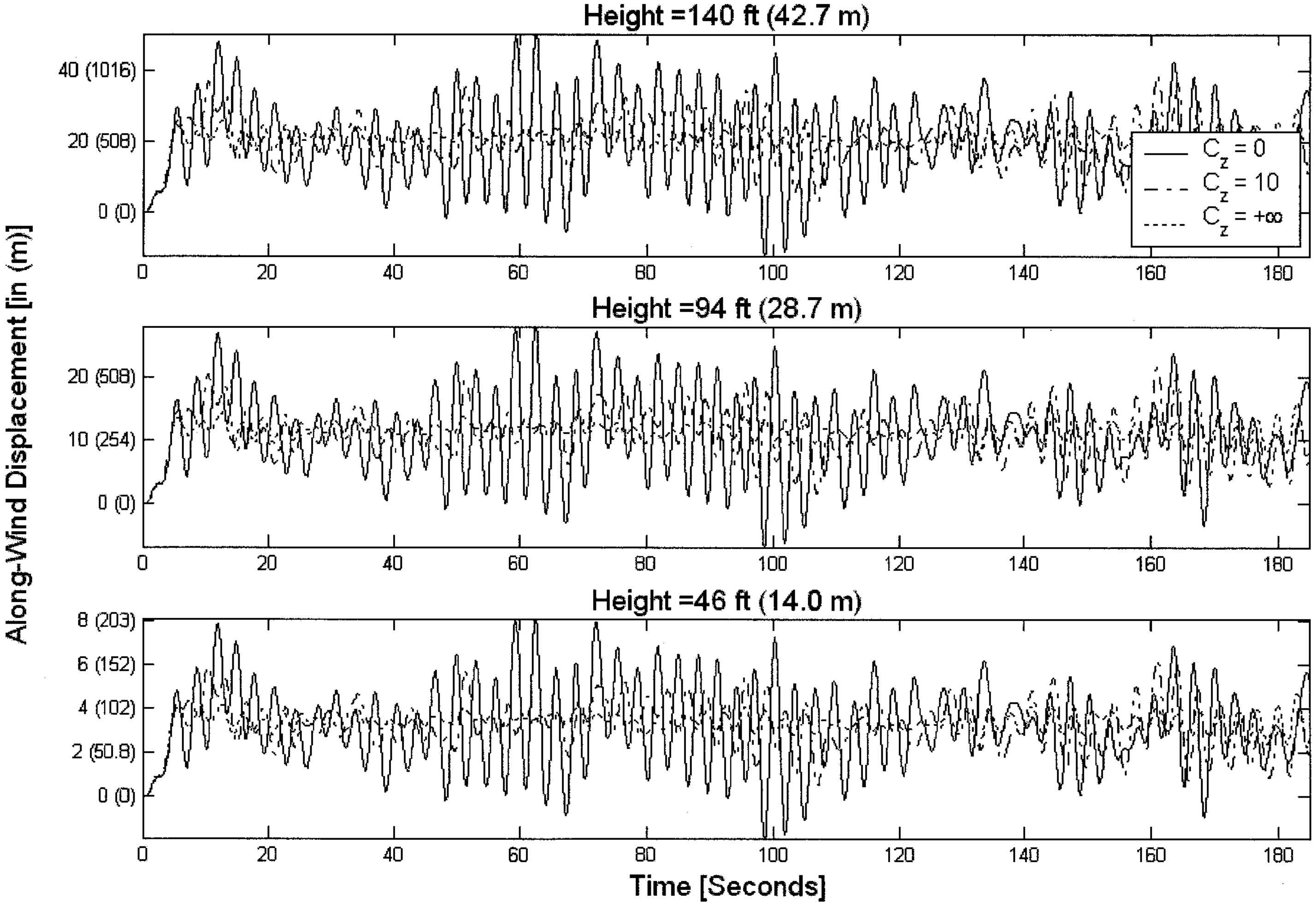

(c): Along-Wind Displacement Time History

Figure 6-5 (cont.): 2-D Wind Flow Time History of Analysis – Vertical Height = 140 ft (42.7 m)

Observe the first five seconds of each figure presented. During this time period, a linear ramp-up in wind speed fro all locations along the height of the structure was implemented. This ramp-up minimizes any numerical instability associated with the immediate application of the full resultant wind loading at the beginning of the time-domain analysis. In order to gain a substantial record length for the response of the structure, all analyses consider a three-minute or 180-second time range. Hence, due to the ramp-up in simulated wind speed as noted above, all analyses considered a total record length of 185 seconds.

After the initial ramp-up, when the response is due to the full simulated wind speed and resultant loading, the wind speed time history with full spatial correlation consistently produces the maximum response of the structure. This result is as expected because the gusts and lulls, maximum and minimum peaks of the wind speed, act in unison. Thus, the loading of the structure during a strong wind gust occurs simultaneously at all points along the height of the structure. This produces a maximum drag force loading on the structure thus producing the maximum response of the structure as well.

Considering the response from a more generalized perspective, the along-wind (longitudinal) displacements due to the two-dimensional wind flow with varying degrees of spatial correlation follow a pattern depending on mean wind speed and vertical height of the structure. As expected, all response displacements increase with higher mean wind speeds and increased vertical heights. Decreases in the cross-sectional properties, outside diameter and wall thickness, produce more flexible structures and corresponding increases in response displacements.

The maximum response characteristics, considering the entire time-domain, for all structure variations again follow the previous comments regarding fully correlated wind speed time histories producing the absolute maximum response of the structure. Figure 6-6 illustrates this for vertical heights of 60 ft (18.3 m) and 140 ft (42.7 m) with cross-sectional properties of 2.0 ft (610 mm) for the outside diameter and ½ in (12.7 mm) for the wall thickness.

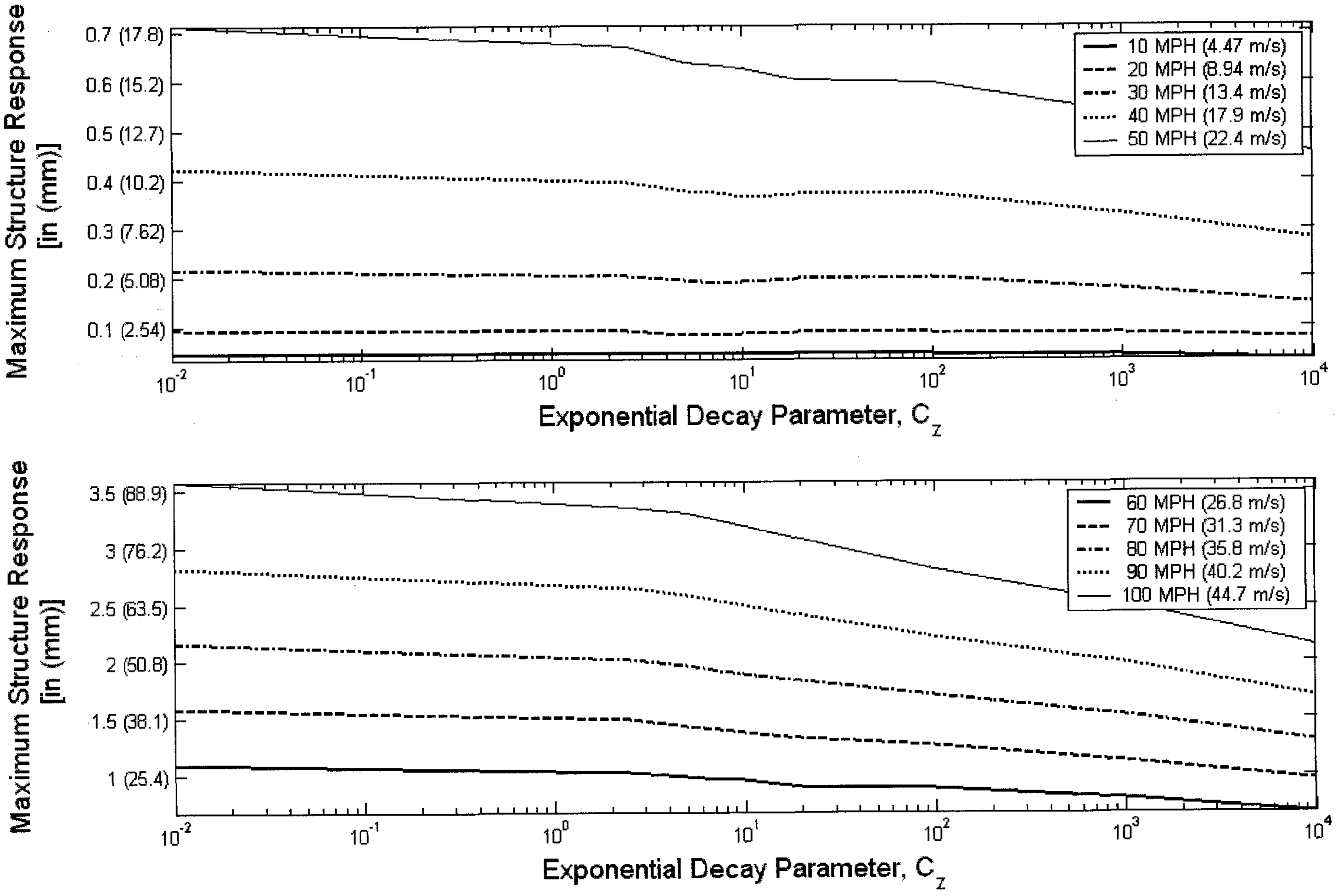

(a): Vertical Height = 60 ft (18.3 m)

Figure 6-6: 2-D Wind Flow Maximum Response Characteristics

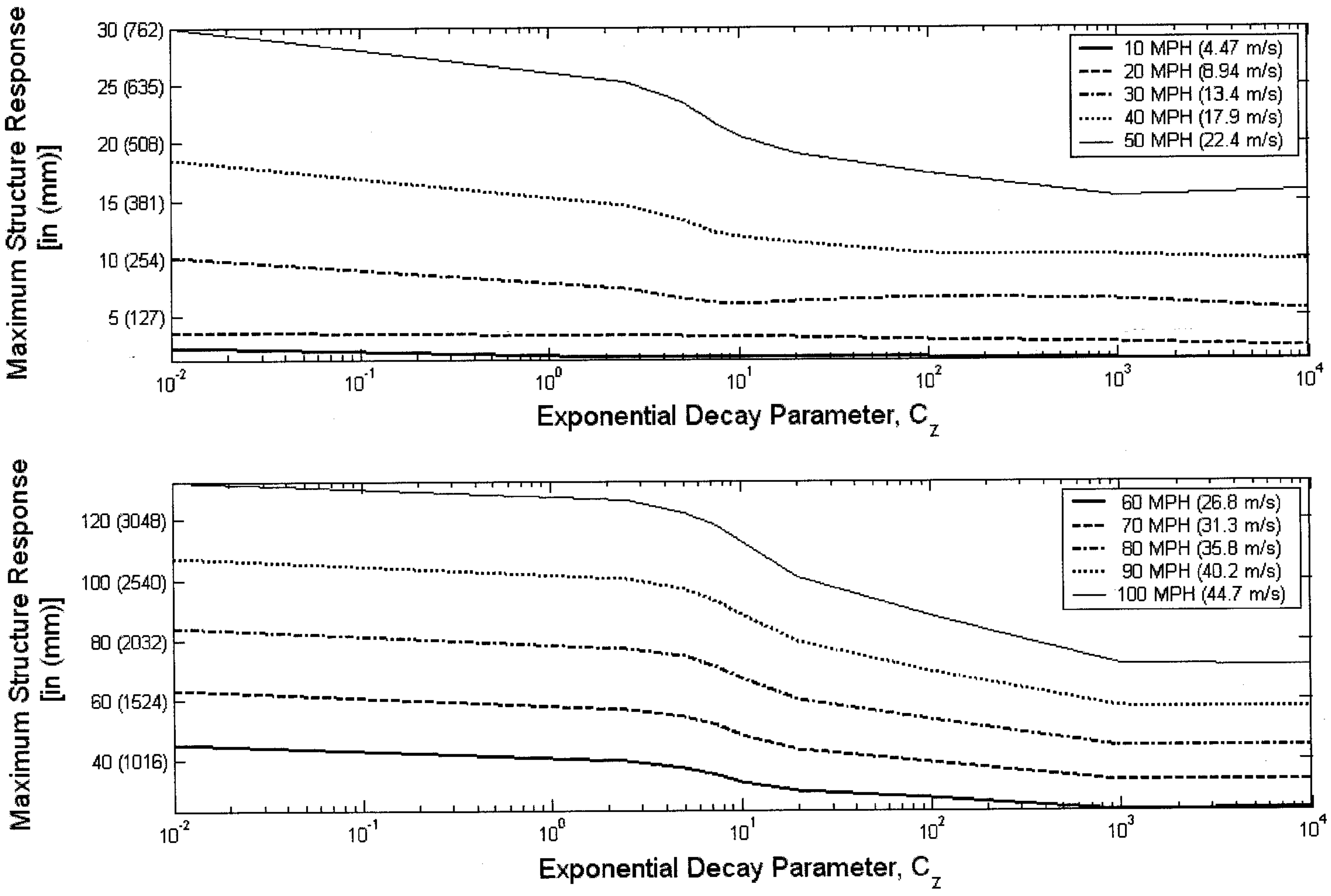

(b): Vertical Height = 140 ft (42.7 m)

Figure 6-6 (cont.): 2-D Wind Flow Maximum Response Characteristics

The maximum structure response for both vertical heights illustrated follow a particular pattern unique to each. However, for both cases, fully correlated wind flows where the exponential decay parameter $C_z = C_{z(long)}$ approaches zero produces the maximum structure response. Increases in C_z correspond to lower maximum structure responses for both cases. Though, the decrease in response is relatively steady for the 60 ft (18.3 m) structure for an increase in C_z. While, the decrease in response for the 140 ft (42.7 m) structure is more dramatic near the range of $C_z = 5 - 10$. Thus, the height of the structure plays an important role in the deviation of the maximum response for various spatial correlation properties of the wind flow. Finally, the mean wind speed also produces an effect on the variation of the structure response for changes in C_z. As shown in Figure 6-6, higher wind speeds also produce more dramatic changes in the response for increases in C_z and, thus, a decrease in the spatial correlation of the wind flow.

The final component of the two-dimensional wind flow investigation considers statistical quantities of the wind flow and resulting response of the structure. Specifically, the statistical quantities of interest are the resulting spatial correlation of the time histories for wind flow, resulting wind-induced loading, and response of the structure. Cross-correlation quantities between these time histories are also briefly discussed.

Within the context of this study, three time histories are investigated in relation to the assumed exponential decay parameter $C_{z(long)}$ of the simulated wind speed time series. Recall that when $C_{z(long)} = 0$, the spatial correlation of the resulting wind speed time series is fully correlated. This is due to the exponential function of Equation (6-4) degenerating to unity, producing a fully correlated time series with respect to multiple heights along the structure. Alternatively, when $C_{z(long)} = +\infty$, the spatial correlation of the resulting wind speed time series has no correlation producing an exponential function value of zero in the limit.

The three time histories investigated within this study consider all time series for each node of the structure. First, the wind speed time history due to the simulated wind flow is considered. Second, the resulting wind-induced drag force time history caused by the wind flow is considered. The drag force considered is due to the relative motion of the wind flow and response of the structure as given by Equation (2-4). Finally, the response of the structure in the along-wind (longitudinal) direction is considered.

An *m*-by-*m* symmetric correlation matrix where *m* is the total number of nodes discretized within the finite element analysis framework provides the spatial correlation of these time histories. In the interest of brevity, these correlation matrices are not presented in full detail. Rather, specific columns (or rows due to the symmetric nature of these matrices) are provided graphically. Figure 6-7 provides the spatial correlation of the 60 ft (18.3 m) structure for various values of the assumed spatial correlation of the two-dimensional wind flow. The spatial correlation of the wind flow, wind-induced load, and response of the structure are considered in sub-figures (a), (b), and (c), respectively. For comparison purposes, sub-figure (d) combines sub-figures (a) and (b) into one figure. In Figure 6-7 (d) the wind speed time histories are indicated by the lines marked "W" and the wind-induced load time histories are indicated by the data points marked "L". For all figures, the spatial correlation of each time history is considered with respect to three heights on the structure: ⅓ total height, ⅔ total height, and at the top of the structure. At these points, notice that the spatial correlation is at unity for all cases of $C_{z(long)} = C_z$ as expected and required mathematically. One additional figure, sub-figure (e), is provided to illustrate the effects of changing the exponential decay parameter $C_{z(long)} = C_z$. Figure 6-7 (e) considers only the spatial correlation at the ⅓ total height in relation to the top of the structure for the wind flow, wind-induced load, and response of the structure time histories. Note that only figures are provided for the structure with a vertical height of 60 ft (18.3 m), outside diameter of 2.0 ft (610 mm), and wall thickness of ¼ in (6.35 mm). Other cross-section properties and vertical height variations produced similar results.

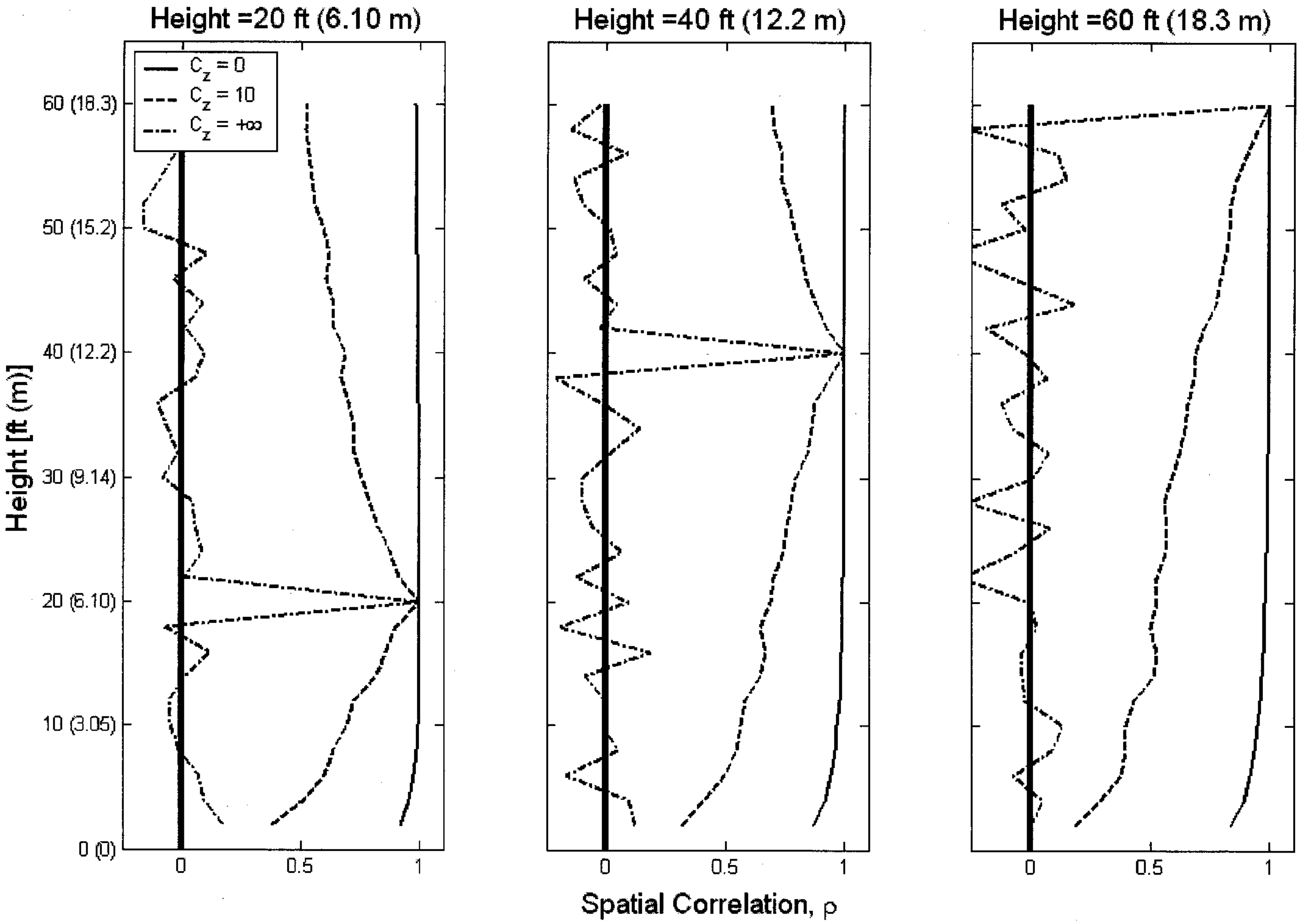

(a): Wind Speed Time History

Figure 6-7: 2-D Wind Flow Spatial Correlation

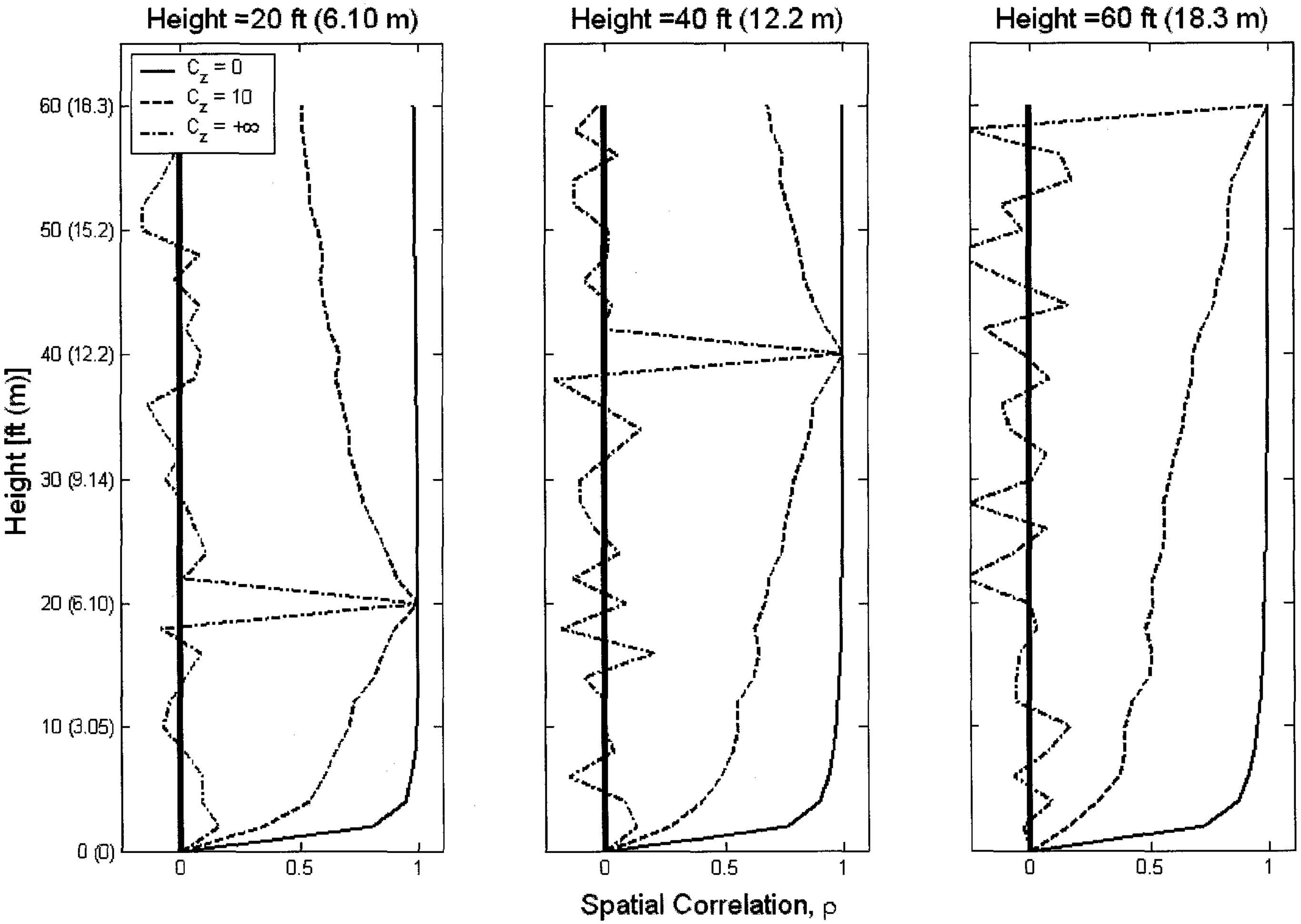

(b): Wind-Induced Load Time History

Figure 6-7 (cont.): 2-D Wind Flow Spatial Correlation

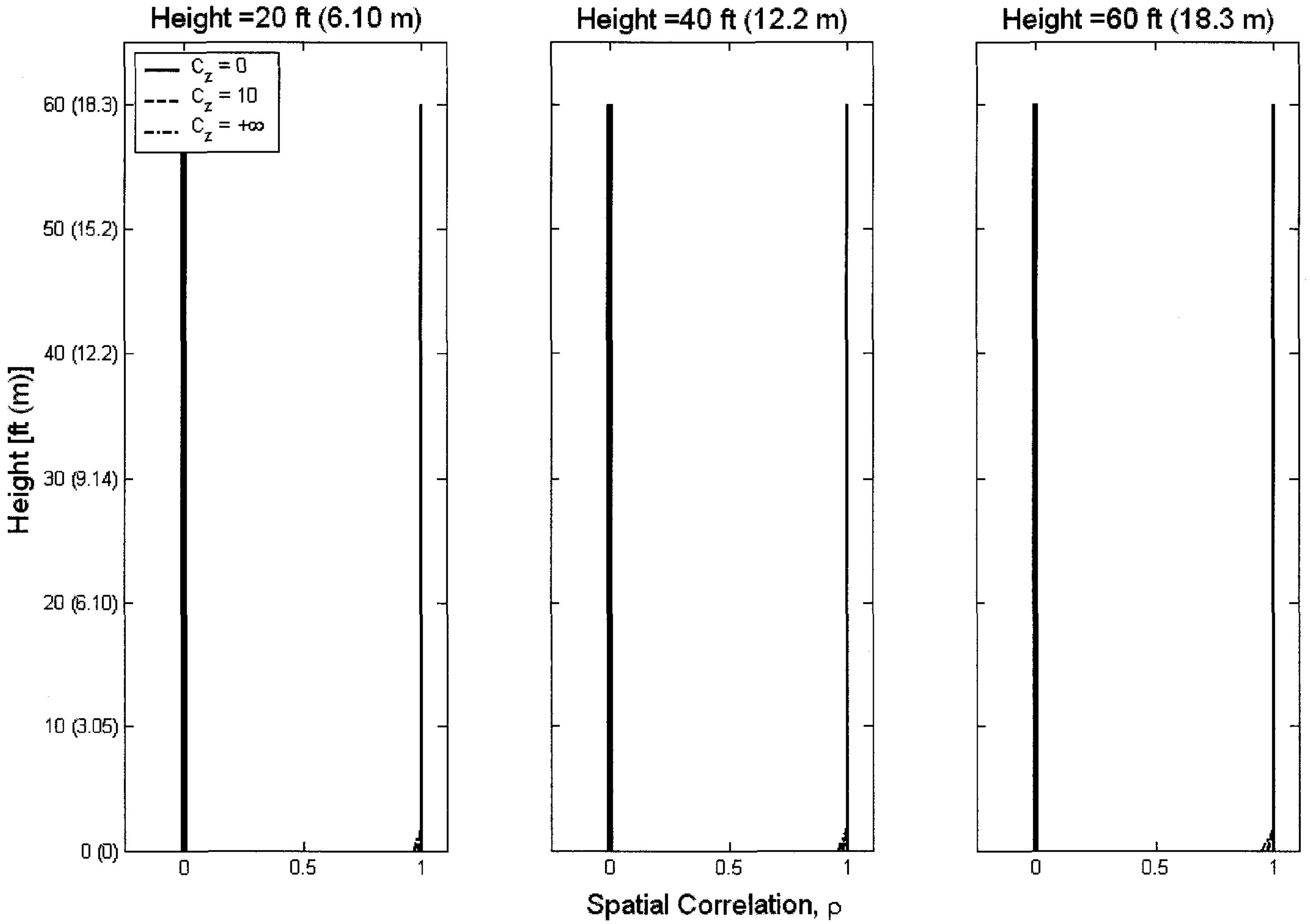

(c): Displacement Time History

Figure 6-7 (cont.): 2-D Wind Flow Spatial Correlation

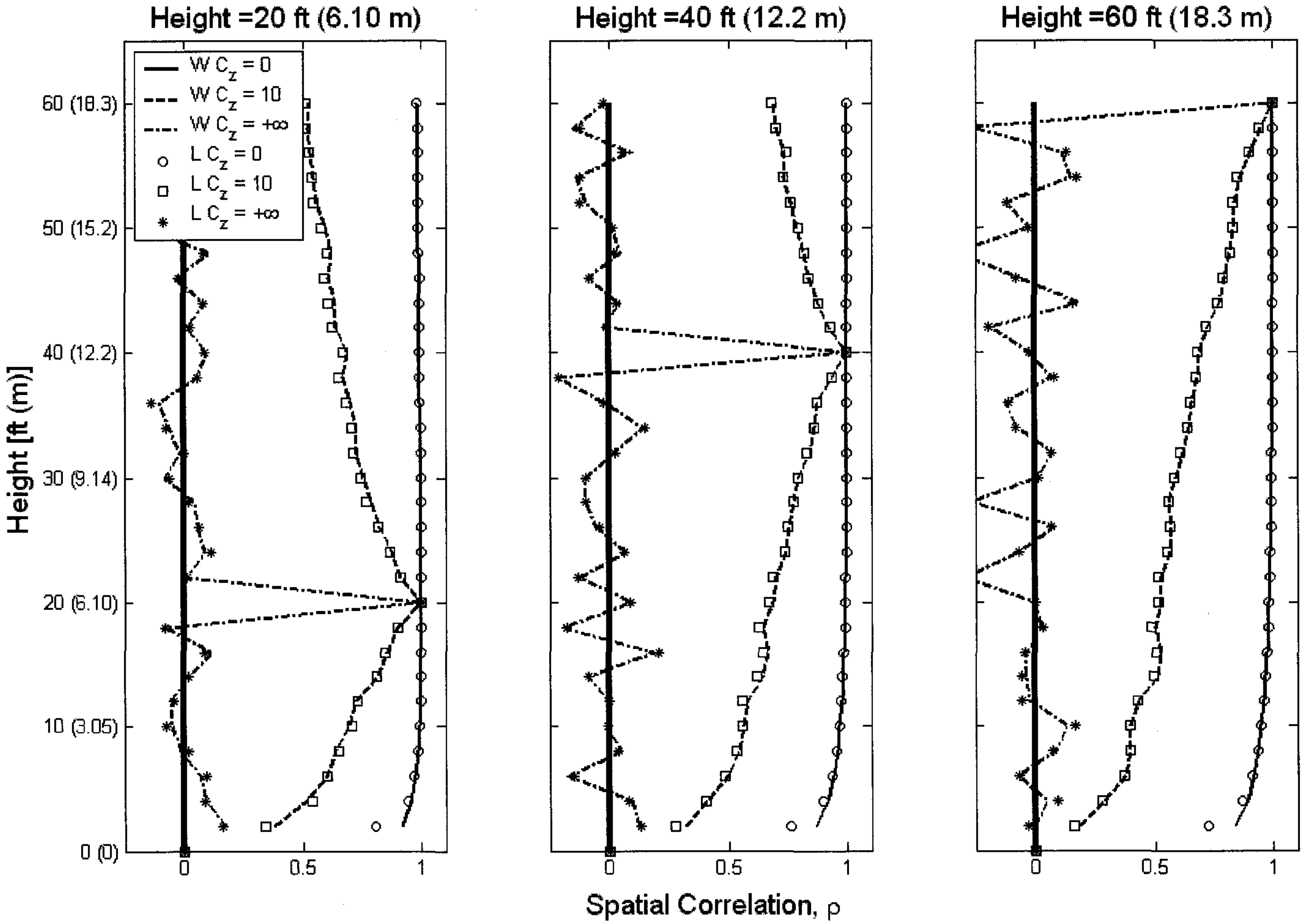

(d): Wind Speed and Wind-Induced Load Time Histories

Figure 6-7 (cont.): 2-D Wind Flow Spatial Correlation

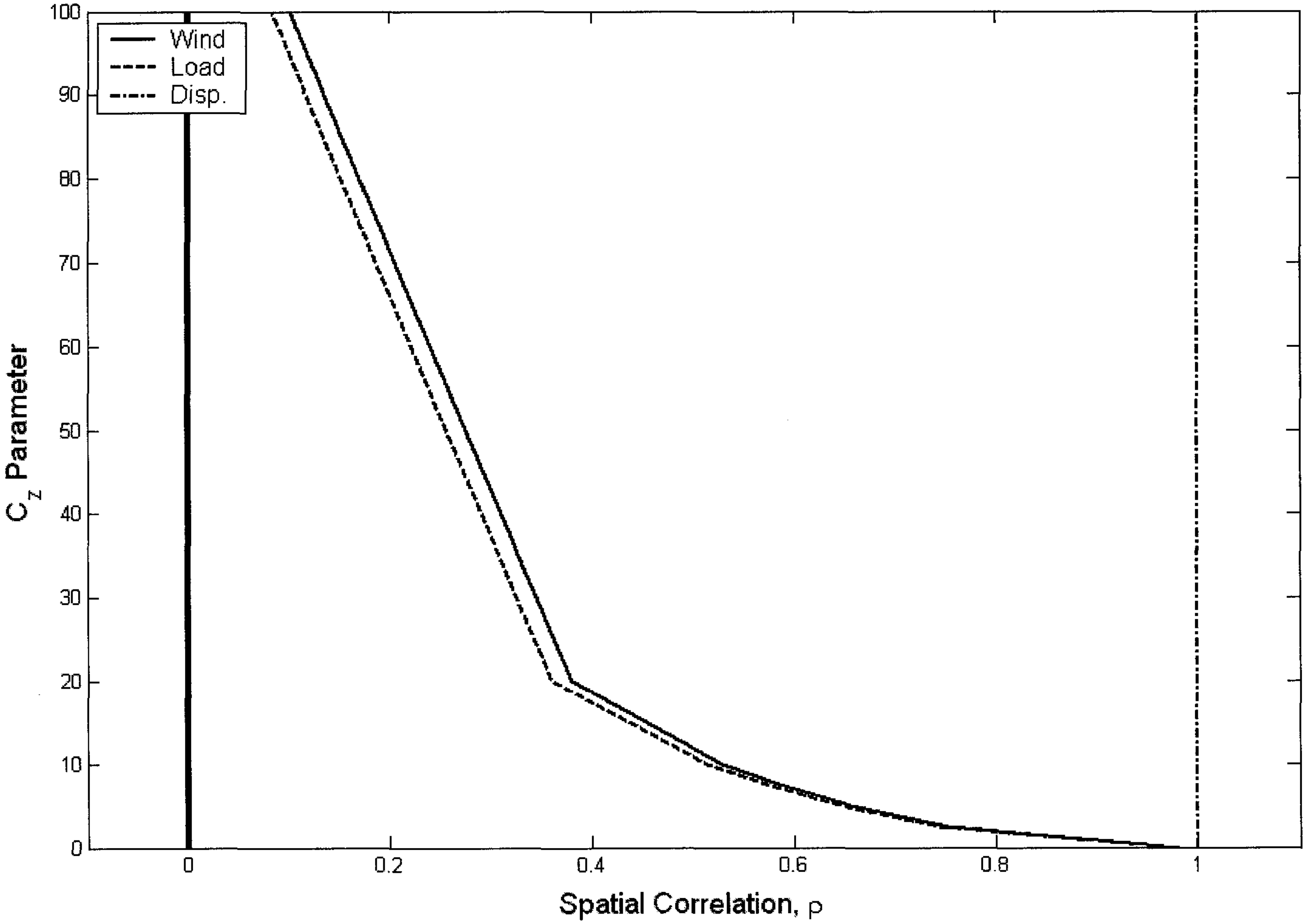

(e): Spatial Correlation Parameter

Figure 6-7 (cont.): 2-D Wind Flow Spatial Correlation

Based on the results provided in Figure 6-7 (a), spatial correlation of the wind speed time history, variations in the assumed spatial correlation used to simulate the wind flow produce similar variations in the measured spatial correlation. For example, when $C_{z(long)} = 0$ the simulated wind flow is assumed to be fully correlated. Based on the measured spatial correlation that indicates nearly full correlation of the wind flow for $C_{z(long)} = 0$, these results are comparable. On average, when $C_{z(long)} = +\infty$ the measured spatial correlation is near zero indicating no correlation between nodal points along the height of the structure.

The same results given by Figure 6-7 (a) are also given in Figure 6-7 (b) where the spatial correlation of the wind-induced load is considered. Based on the function used to derive this load, Equation (2-4), only the drag coefficient and relative velocity terms vary from one node to the next. However, all of these terms are directly related to the wind flow that has some type of spatial correlation. Thus, the resulting spatial correlation of the wind-induced load and wind speed time histories are quite similar as shown in Figure 6-7 (d).

The results of the spatial correlation of the along-wind (longitudinal) displacement time history, Figure 6-7 (c), provide results that are to be expected. The structure is composed of a series of interconnected finite elements and thus moves in tandem. Fully-correlated time histories between nodes of the structure are reproduced for all values of the assumed parameter $C_{z(long)}$. Any other value would indicate a structural modeling error and lack of continuity within the finite element analysis framework.

Finally, the effects of varying the spatial correlation parameter, $C_{z(long)} = C_z$, are most evident in Figure 6-7 (e). Low values (less than 10) of $C_{z(long)}$ correspond well with strong spatial correlation characteristics of the time histories considered. Alternatively, higher values (greater than 50) correspond well with relatively weak spatial correlation characteristics of the time histories considered. As previously discussed, the spatial correlation of the wind flow and wind-induced load time histories are comparable. Furthermore, the spatial correlation of the displacement time history is always fully correlated at unity.

The final consideration for the two-dimensional wind flow study is the cross-correlation between particular time histories generated as a result of the time-domain analyses. In this case, however, all five vertical height variations of the structure are presented for investigation. As before, variations in the assumed spatial correlation of the along-wind (longitudinal) wind flow are the basis for comparisons. Table 6-3 presents the cross-correlation quantities considered. First, the cross-correlation between the wind speed (U_h) and displacement (x_h) time histories at the top of the structure are presented. Second, the cross-correlation between the wind speed and wind-induced load (L_h) time histories at the top of the structure are presented. Third, the cross-correlation between the wind-induced load and displacement time histories at the top of the structure are presented. Finally, the cross-correlation between the wind speed at the top of the structure and the bending stress (σ_y) at the bottom of the structure are presented in Table 6-8. The bending stress time history will be an important quantity in the numerical investigation of fatigue life considered in Chapter Eight of this study. A large number of cross-correlation quantities exist for investigation, but these four are of particular interest and provide a general overview of the cross-correlation properties between time histories of slender structures.

Vertical Height ft (m)	$C_{z(long)} = C_z$	Cross-Correlation			
		$U_h - x_h$	$U_h - L_h$	$L_h - x_h$	$U_h - \sigma_y$
60 (18.3)	0	0.931	0.996	0.937	0.935
	10	0.834	0.996	0.837	0.820
	$+\infty$	0.613	0.994	0.621	0.552
80 (24.4)	0	0.652	0.995	0.657	0.671
	10	0.662	0.995	0.668	0.655
	$+\infty$	0.475	0.996	0.478	0.424
100 (30.5)	0	0.546	0.994	0.550	0.572
	10	0.571	0.995	0.575	0.570
	$+\infty$	0.372	0.997	0.378	0.337
120 (36.6)	0	0.587	0.993	0.588	0.617
	10	0.516	0.994	0.517	0.519
	$+\infty$	0.282	0.995	0.286	0.245
140 (42.7)	0	0.386	0.979	0.397	0.415
	10	0.485	0.991	0.490	0.487
	$+\infty$	0.180	0.995	0.181	0.149

Table 6-3: 2-D Wind Flow Cross-Correlation

The cross-correlation quantities provided in Table 6-3 yield interesting results. Generally, as the height of the structure increases, the cross-correlation between all time series decreases with the exception being the cross-correlation between the wind speed and the wind-induced loading at the top of the structure. As for Figure 6-7, this result is expected based on the equation used to derive the wind-induced load. The assumed parameter $C_{z(long)} = +\infty$ also consistently produces the lowest cross-correlation between the time series of interest. Perhaps most interesting is the comparison of the cross-correlation quantities of the 60 ft (18.3 m) and 140 ft (42.7 m) structures. For the 60 ft (18.3 m) structure, all cross-correlation quantities are above 0.55. Thus, the response of the structure is well correlated with the wind flow and wind-induced loading. However, for the 140 ft (42.7 m) structure, all cross-correlation quantities are below 0.49 with the exception of the wind speed and wind-induced load at the top of the structure. Thus, the difference in height significantly reduces the cross-correlation between the response of the structure and the wind speed or wind-induced load.

6.3 3-D Wind Flow Results

The second numerical investigation of spatial correlation considers three-dimensional wind flow in the along-wind (longitudinal) and across-wind (lateral) directions. In this case, both simulated wind speed time series are generated for the u' and v' turbulence components. The mean wind velocity profile is added only to the u' turbulence component time series to derive the total wind speed time series for the along-wind (longitudinal) direction for dynamic analysis within the time-domain finite element analysis routine.

Variations in the exponential decay coefficient, C_z, within the root-coherence function of Chapter Three and Section 6.1 represent changes to the assumed spatial correlation of wind turbulence for the u' and v' turbulence components separately. Table 6-4 provides a summary of the changes to the exponential decay coefficients $C_{z(long)}$ and $C_{z(lat)}$ for the u' and v' turbulence components, respectively, considered for the three-dimensional flow analysis. The example structure property variations of Table 6-1 are also considered to vary for each of the variations listed in Table 6-4. Also as noted in Table 6-4, variations in the mean wind speed at 32.8 ft (10 m) above the ground are considered. There are 10 variations in mean wind speed, three variations in the assumed spatial correlation of the *u'* wind turbulence component, three variations in the assumed spatial correlation of the *v'* wind turbulence component, and from Section 6.1 there are 20 variations in the example structure properties. Thus, there are also 1,800 separate analyses for three-dimensional wind flow that are considered in this study.

Property	Value
Mean Wind Speed at 32.8 ft (10 m)	10, 20, 30, 40, 50, 60, 70, 80, 90, 100 MPH (4.47, 8.94, 13.4, 17.9, 22.4, 26.8, 31.3, 35.8, 40.2, 44.7 m/s)
Along-Wind (Longitudinal) Exponential Decay Coefficient, $C_{z(long)}$	0, 10, +∞
Across-Wind (Lateral) Exponential Decay Coefficient, $C_{z(lat)}$	0, 10, +∞

Table 6-4: Variations in Wind Flow Properties for 3-D Wind Flow

Results of Analysis

The results for the three-dimensional wind flow numerical investigation are presented and discussed again using two primary components similar to the two-dimensional wind flow study. First, complete time-domain examples of the wind flow, wind loading, and response of the structure are presented graphically. Maximum response figures are again used to supplement the complete time-domain examples. As for the two-dimensional wind flow study, the second component presents an overall effect of the spatial correlation of the wind flow on the resultant loading, response, and other parameters from the dynamic analysis. Particular attention is again given to the spatial correlation and cross-correlation of certain processes.

Figures 6-8 through 6-12 provide an illustrative representation of the resulting time-domain analysis of the structure considered. Sub-figure's (a), (b), and (c) provide the time history for along- and across-wind speeds, resulting along- and across-wind loading, and along- and across-wind displacements, respectively. Comparisons between the various assumed spatial correlation parameters $C_{z(long)}$ and $C_{z(lat)}$ are given for matched ($C_{z(long)} = C_{z(lat)}$) values of 0, 10, and $+\infty$ representing full, strong, and very weak spatial correlation of the wind flow, respectively. Each figure provides the respective time history at the top of each structure while also considering a set of common parameters such that comparisons are easily observed. The mean wind speed for each figure is considered to be 50 MPH (22.4 m/s) at 32.8 ft (10 m). Furthermore, the structure cross-section properties for each figure provided have an outside diameter of 2.0 ft (610 mm) and a wall thickness of ¼ in (6.35 mm). Note, however, that far more variations in mean wind speed and structure properties were considered as given in Tables 6-1 and 6-4, but again are not fully provided for by Figures 6-8 through 6-12 in the interest of brevity.

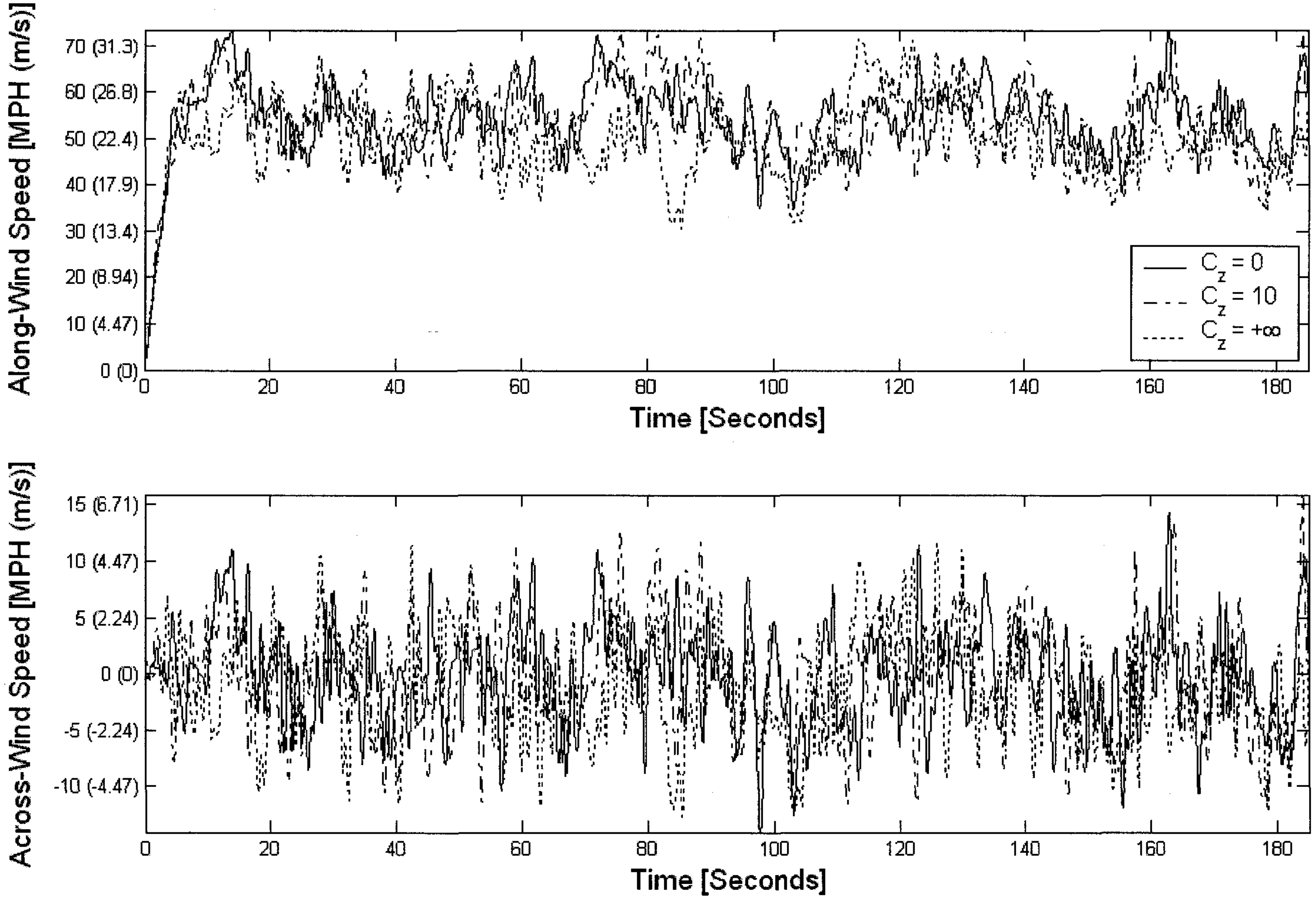

(a): Wind Speed Time History

Figure 6-8: 3-D Wind Flow Time History of Analysis – Vertical Height = 60 ft (18.3 m)

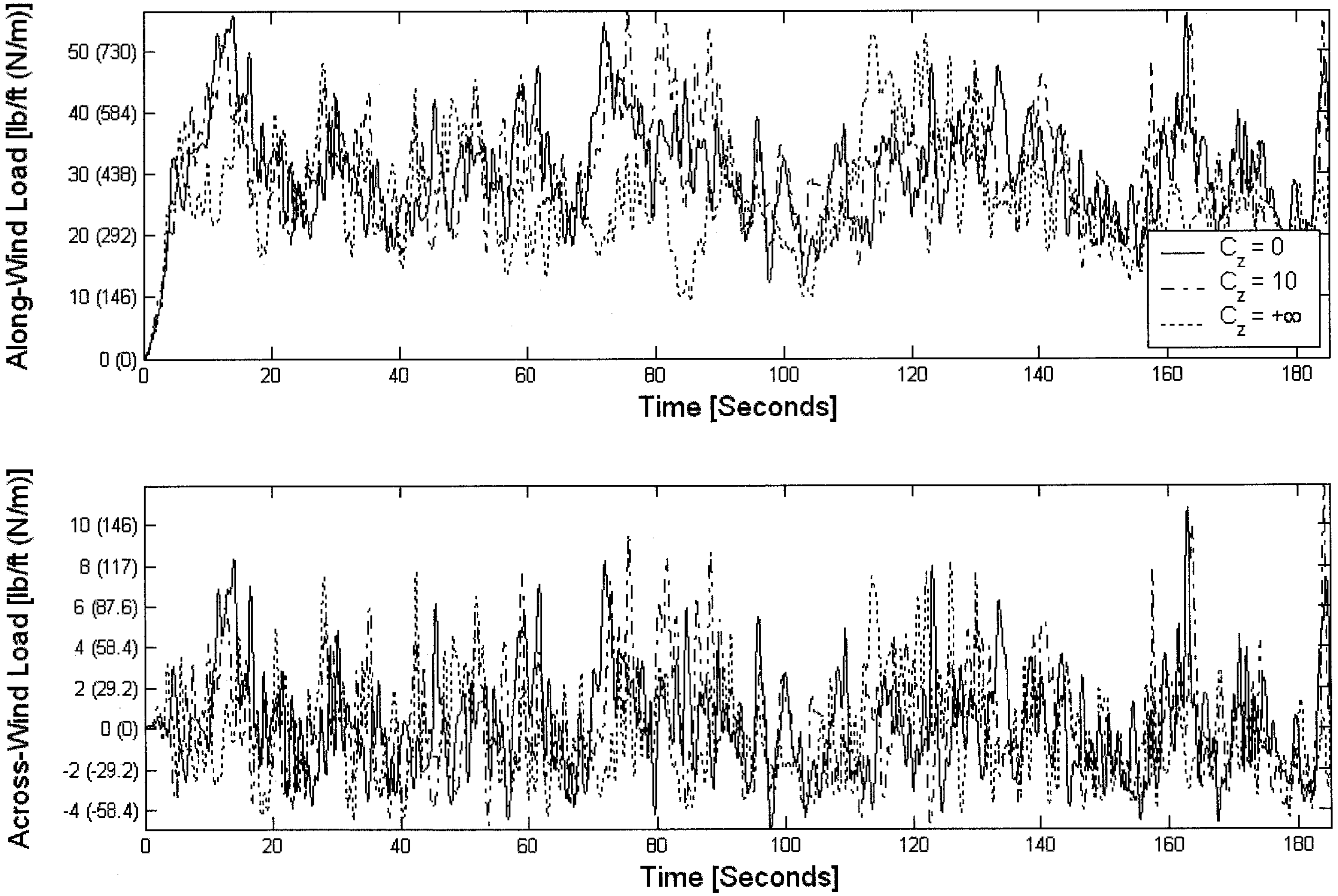

(b): Wind Load Time History

Figure 6-8 (cont.): 3-D Wind Flow Time History of Analysis – Vertical Height = 60 ft (18.3 m)

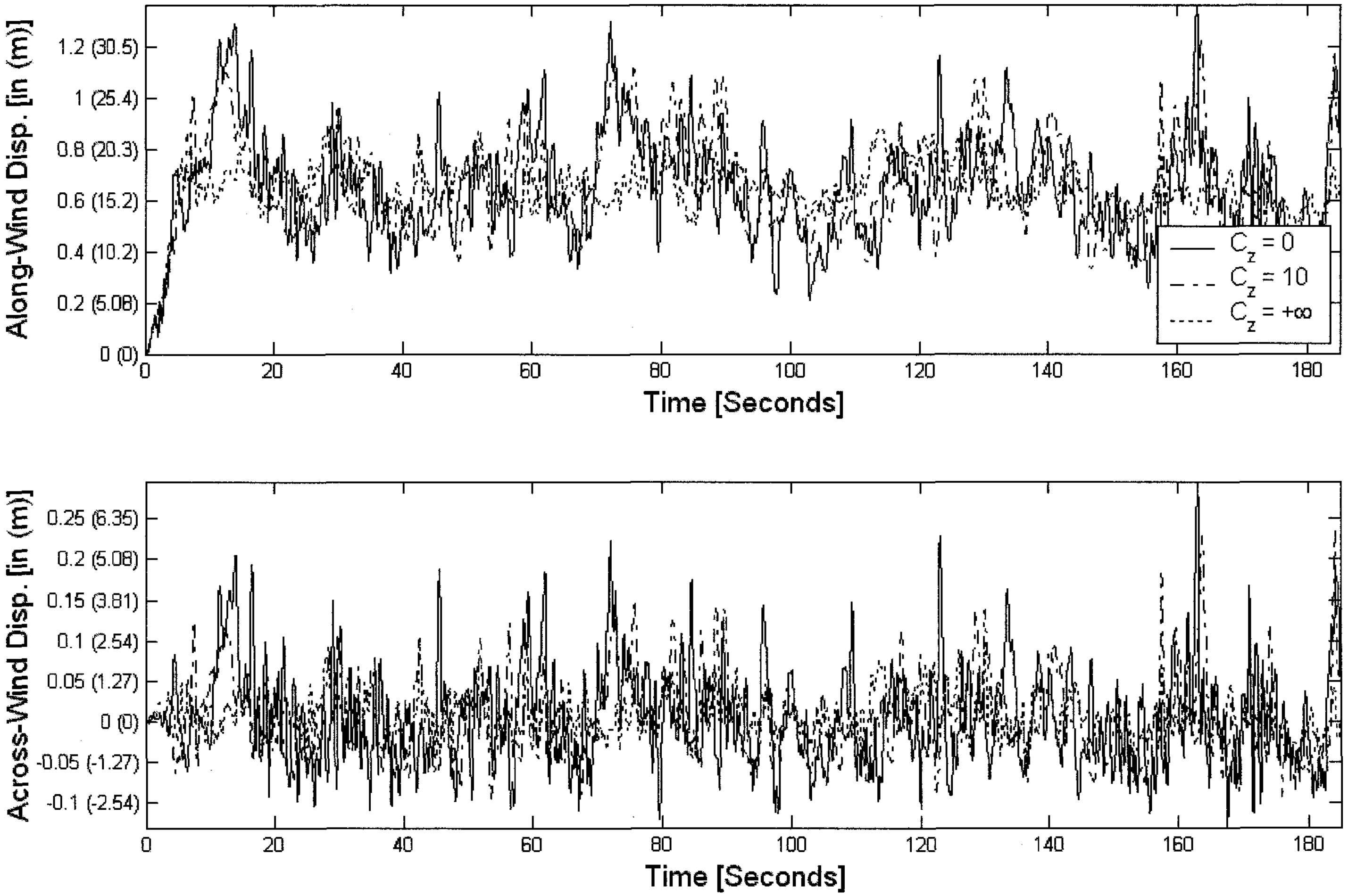

(c): Displacement Time History

Figure 6-8 (cont.): 3-D Wind Flow Time History of Analysis – Vertical Height = 60 ft (18.3 m)

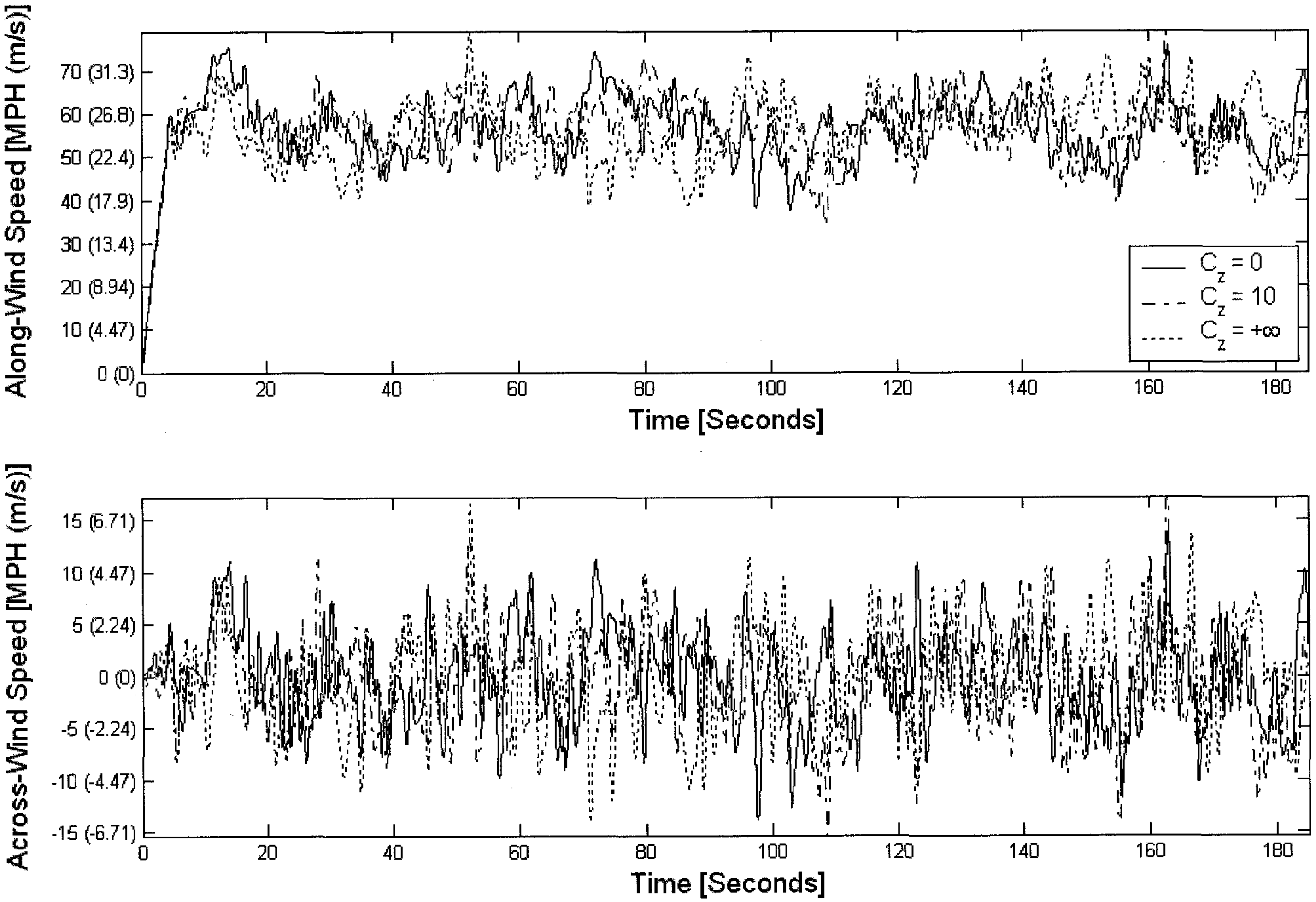

(a): Wind Speed Time History

Figure 6-9: 3-D Wind Flow Time History of Analysis – Vertical Height = 80 ft (24.4 m)

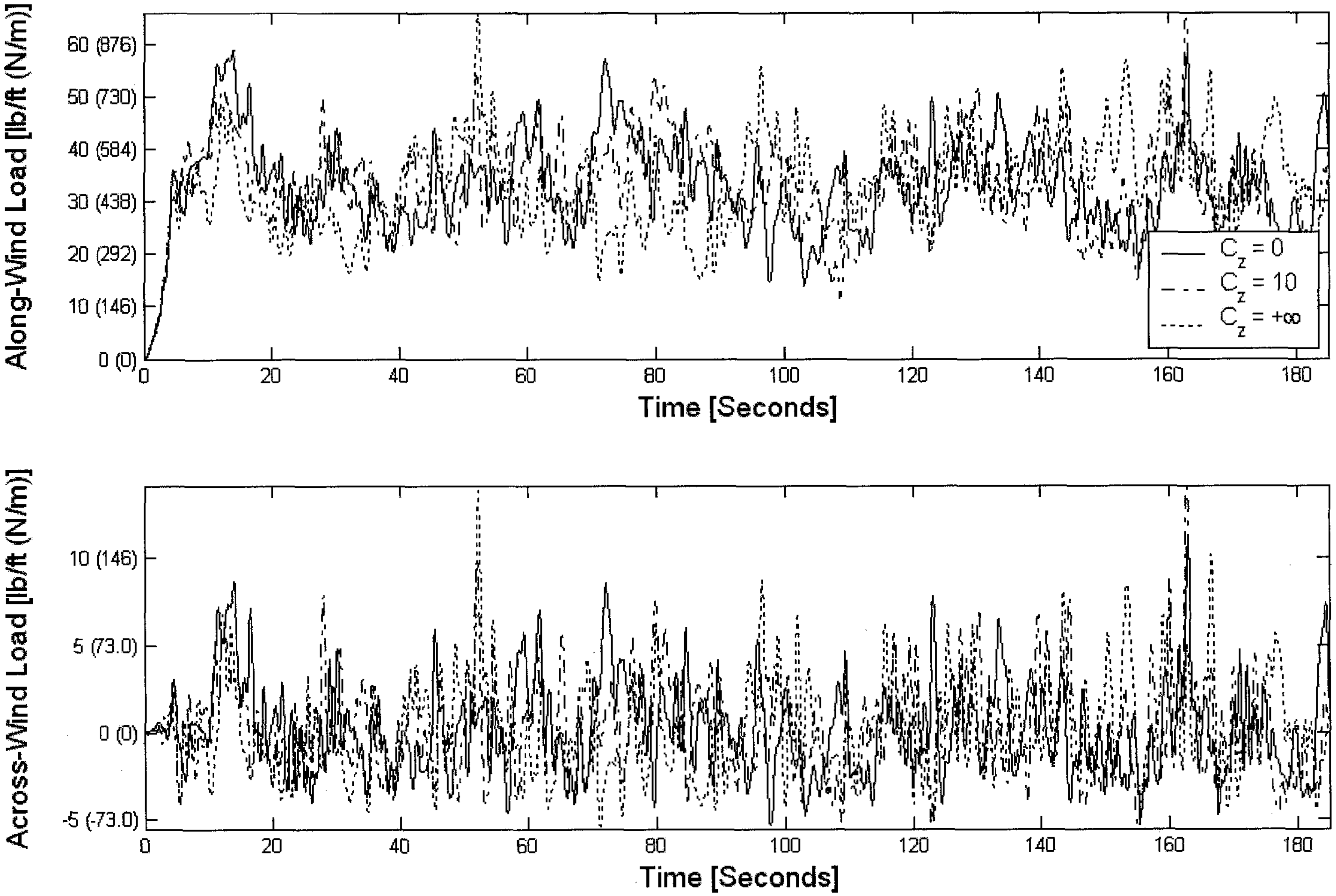

(b): Wind Load Time History

Figure 6-9 (cont.): 3-D Wind Flow Time History of Analysis – Vertical Height = 80 ft (24.4 m)

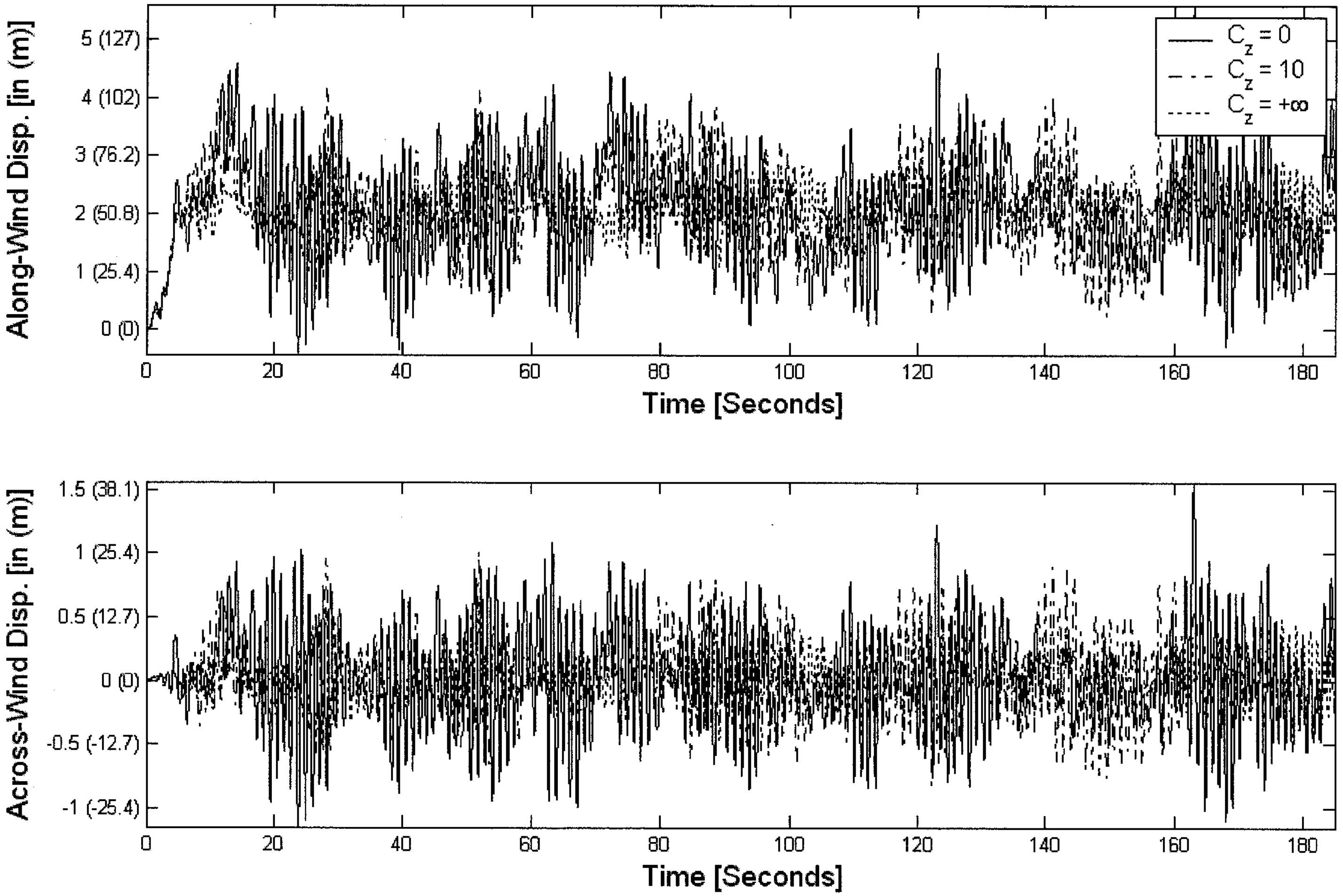

(c): Displacement Time History

Figure 6-9 (cont.): 3-D Wind Flow Time History of Analysis – Vertical Height = 80 ft (24.4 m)

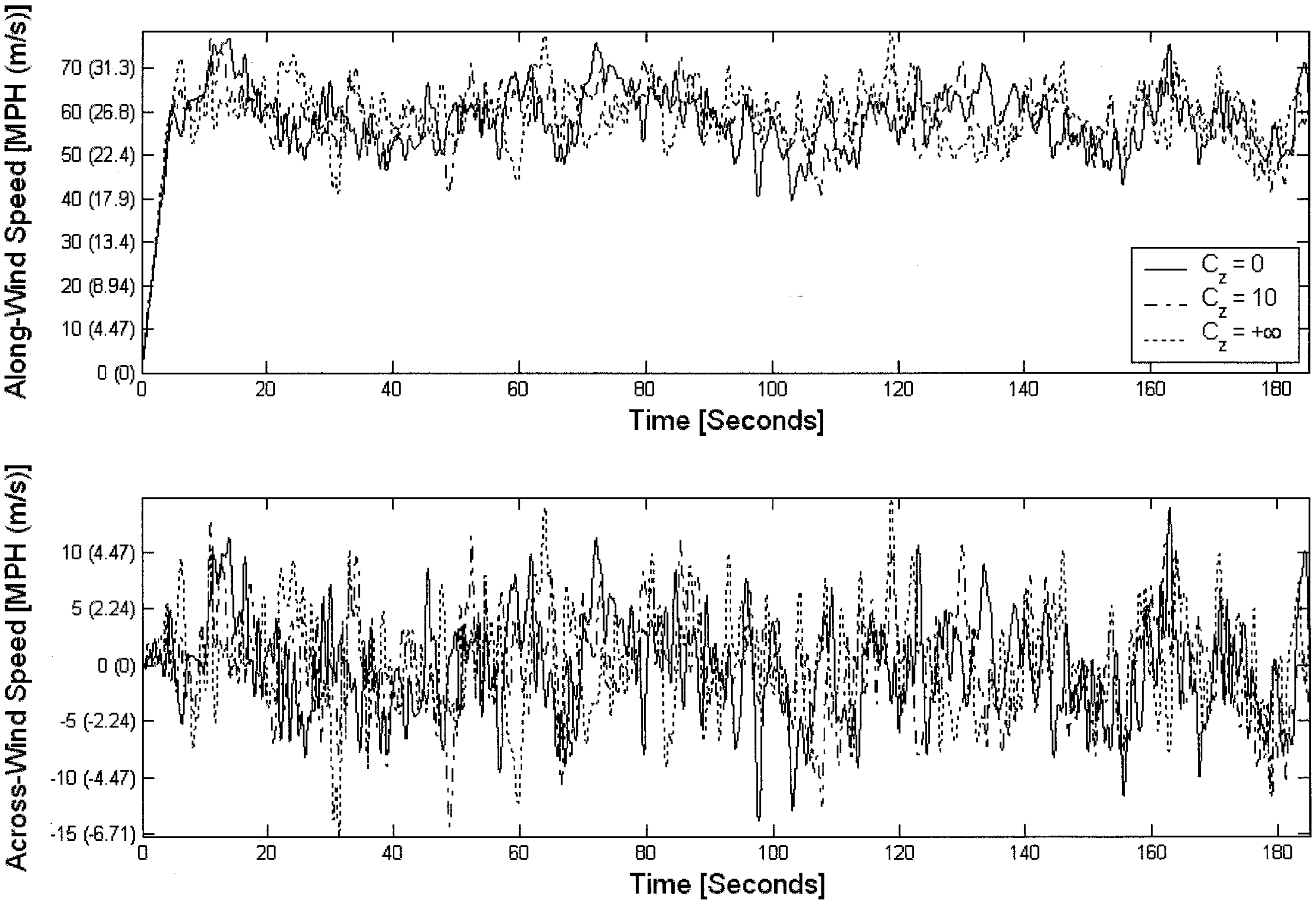

(a): Wind Speed Time History

Figure 6-10: 3-D Wind Flow Time History of Analysis – Vertical Height = 100 ft (30.5 m)

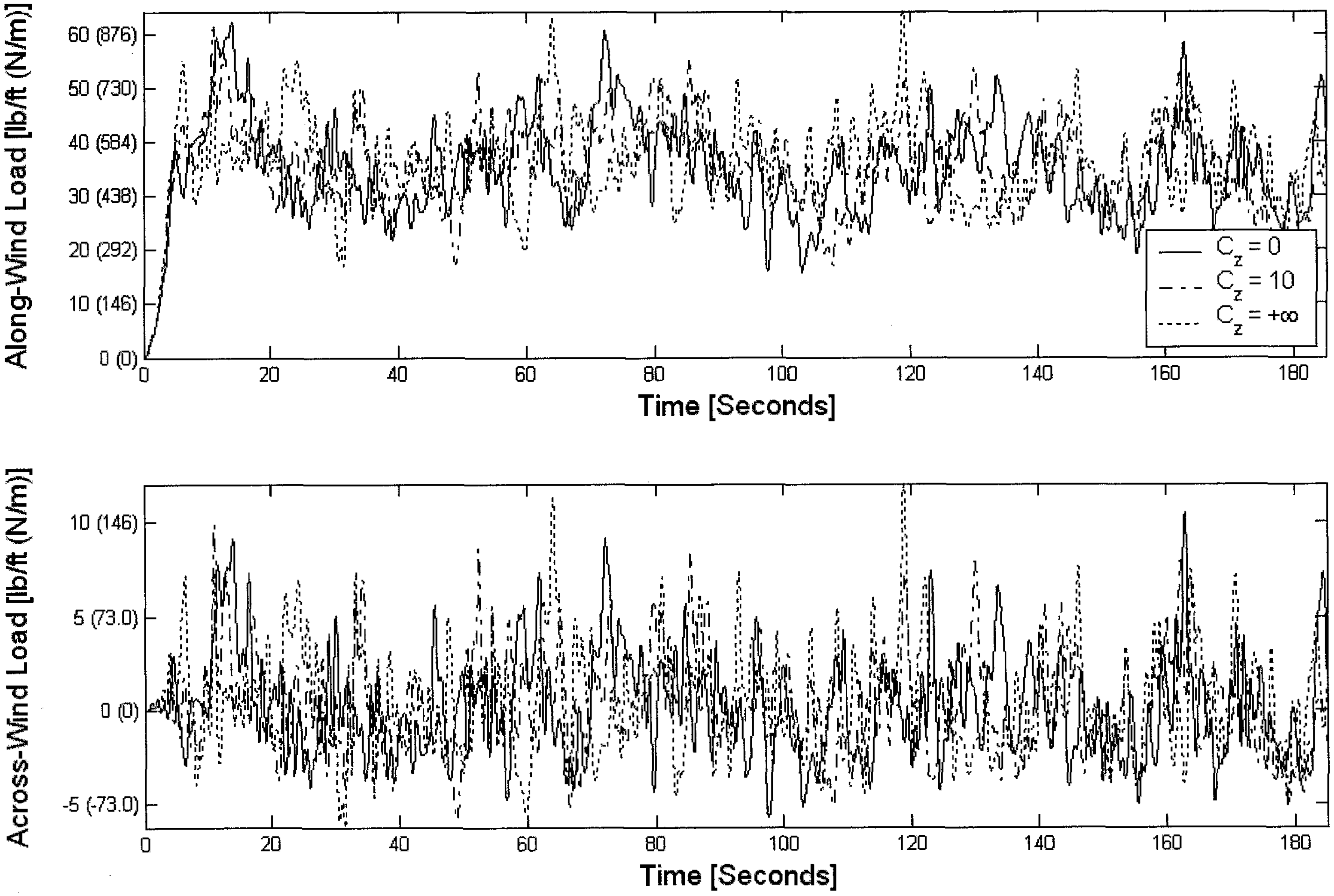

(b): Wind Load Time History

Figure 6-10 (cont.): 3-D Wind Flow Time History of Analysis – Vertical Height = 100 ft (30.5 m)

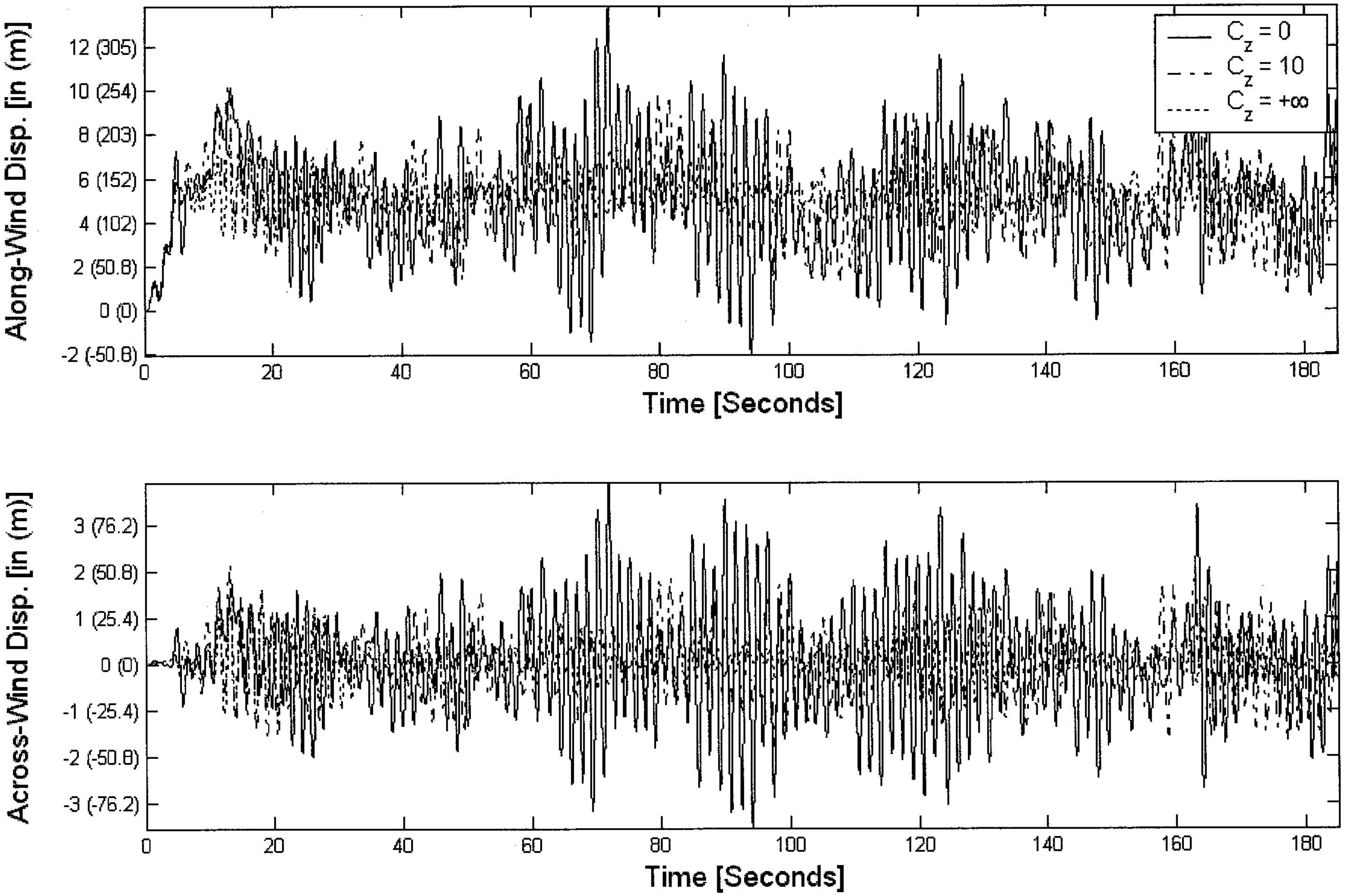

(c): Displacement Time History

Figure 6-10 (cont.): 3-D Wind Flow Time History of Analysis – Vertical Height = 100 ft (30.5 m)

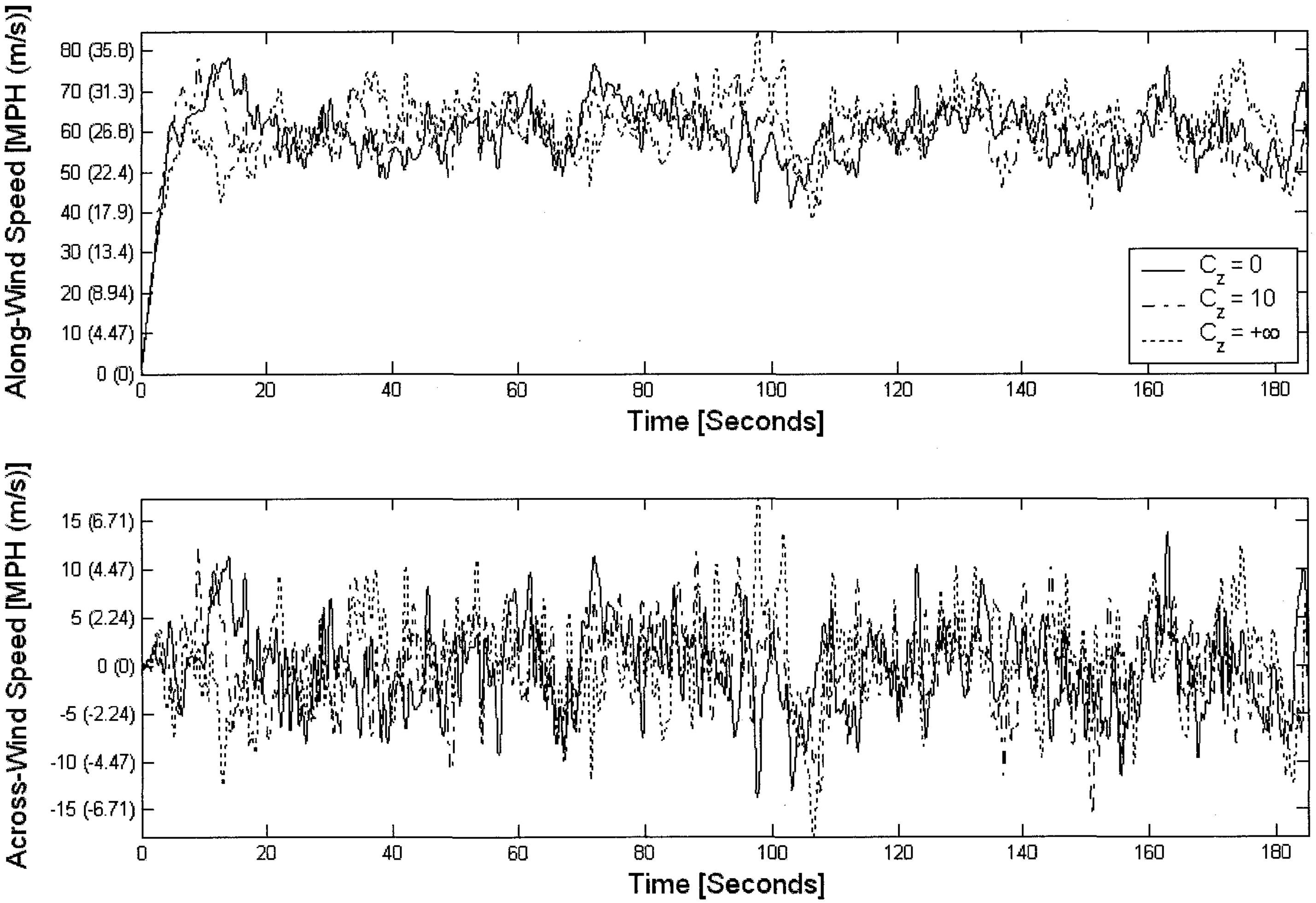

(a): Wind Speed Time History

Figure 6-11: 3-D Wind Flow Time History of Analysis – Vertical Height = 120 ft (36.6 m)

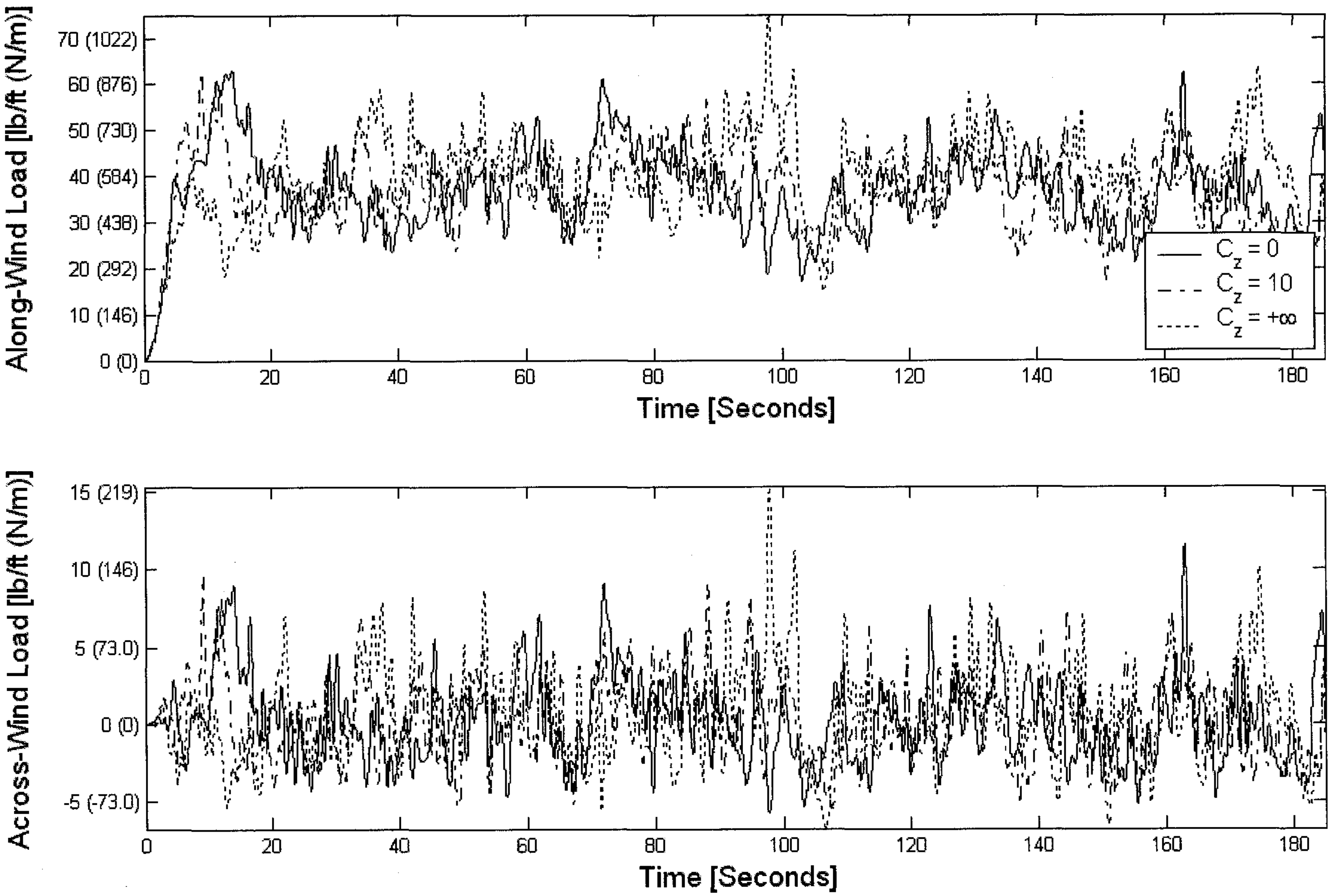

(b): Wind Load Time History

Figure 6-11 (cont.): 3-D Wind Flow Time History of Analysis – Vertical Height = 120 ft (36.6 m)

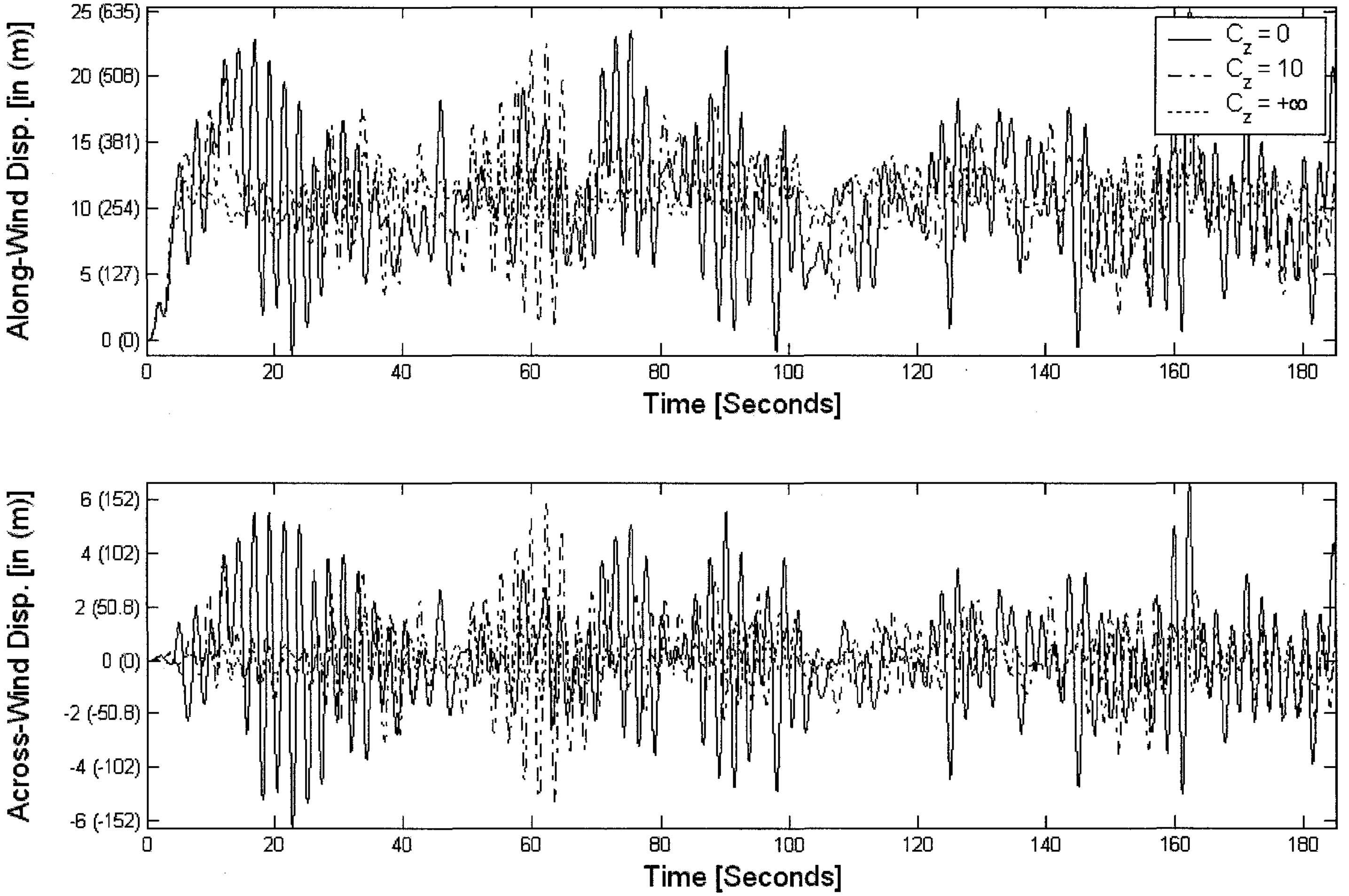

(c): Displacement Time History

Figure 6-11 (cont.): 3-D Wind Flow Time History of Analysis – Vertical Height = 120 ft (36.6 m)

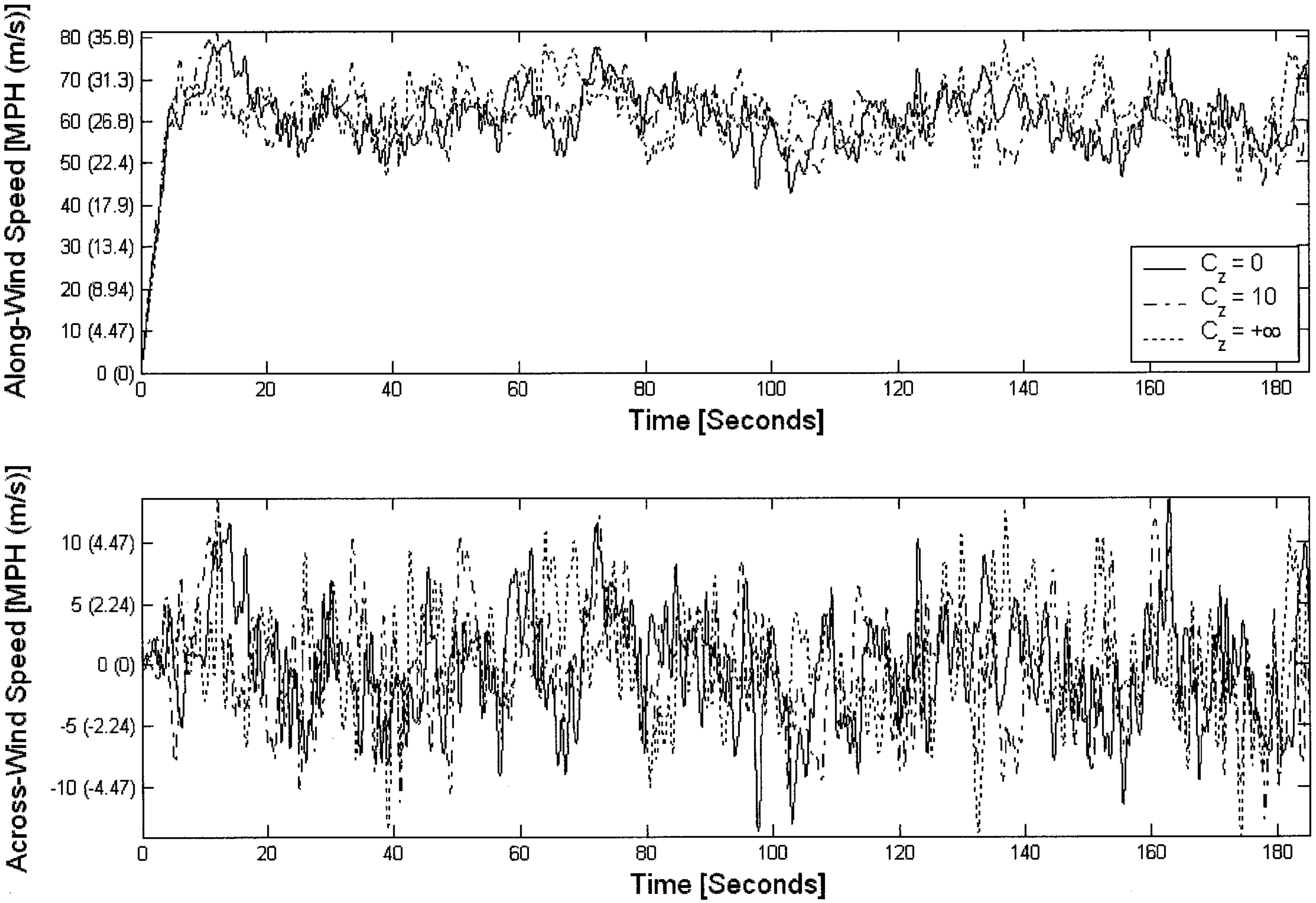

(a): Wind Speed Time History

Figure 6-12: 3-D Wind Flow Time History of Analysis – Vertical Height = 140 ft (42.7 m)

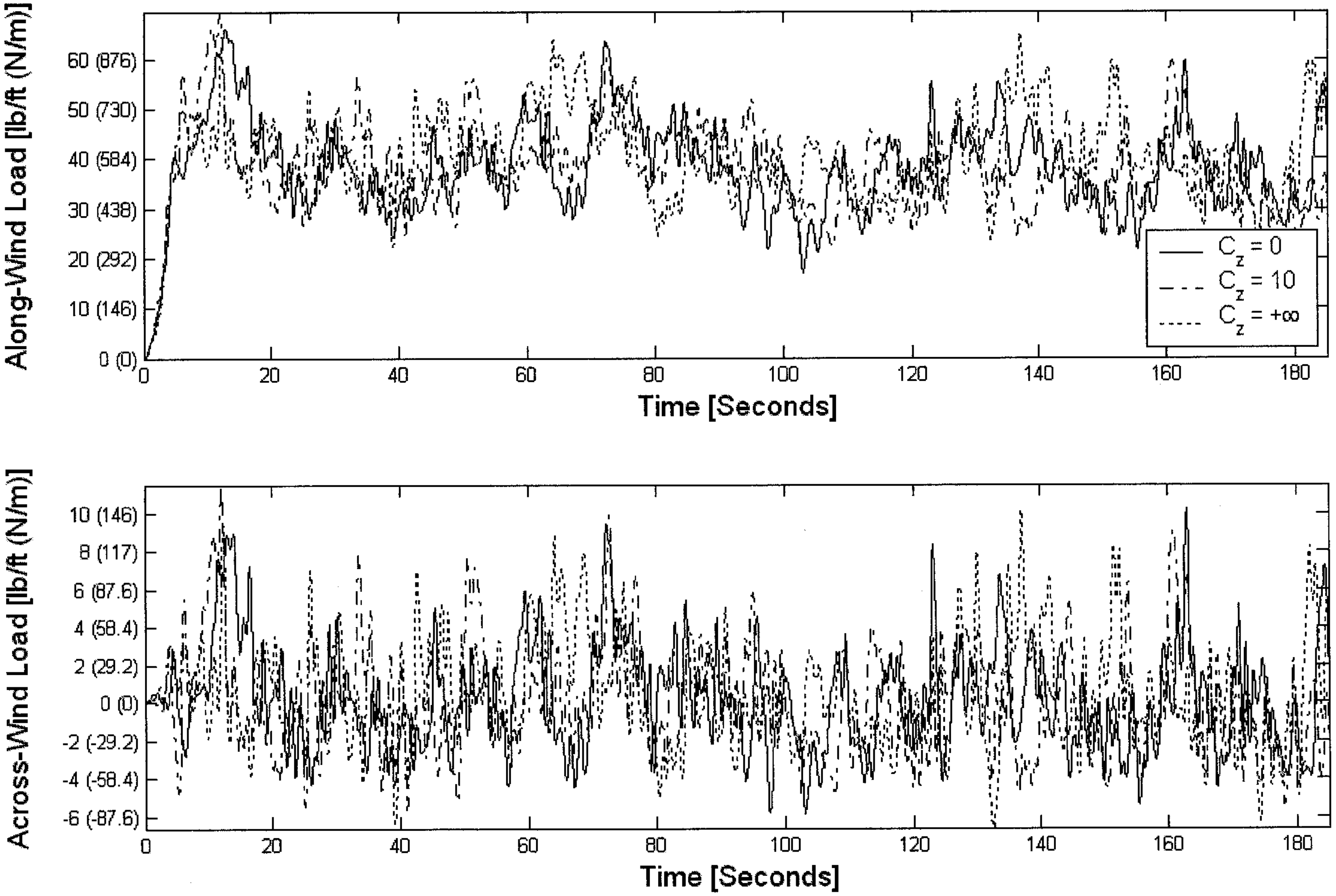

(b): Wind Load Time History

Figure 6-12 (cont.): 3-D Wind Flow Time History of Analysis – Vertical Height = 140 ft (42.7 m)

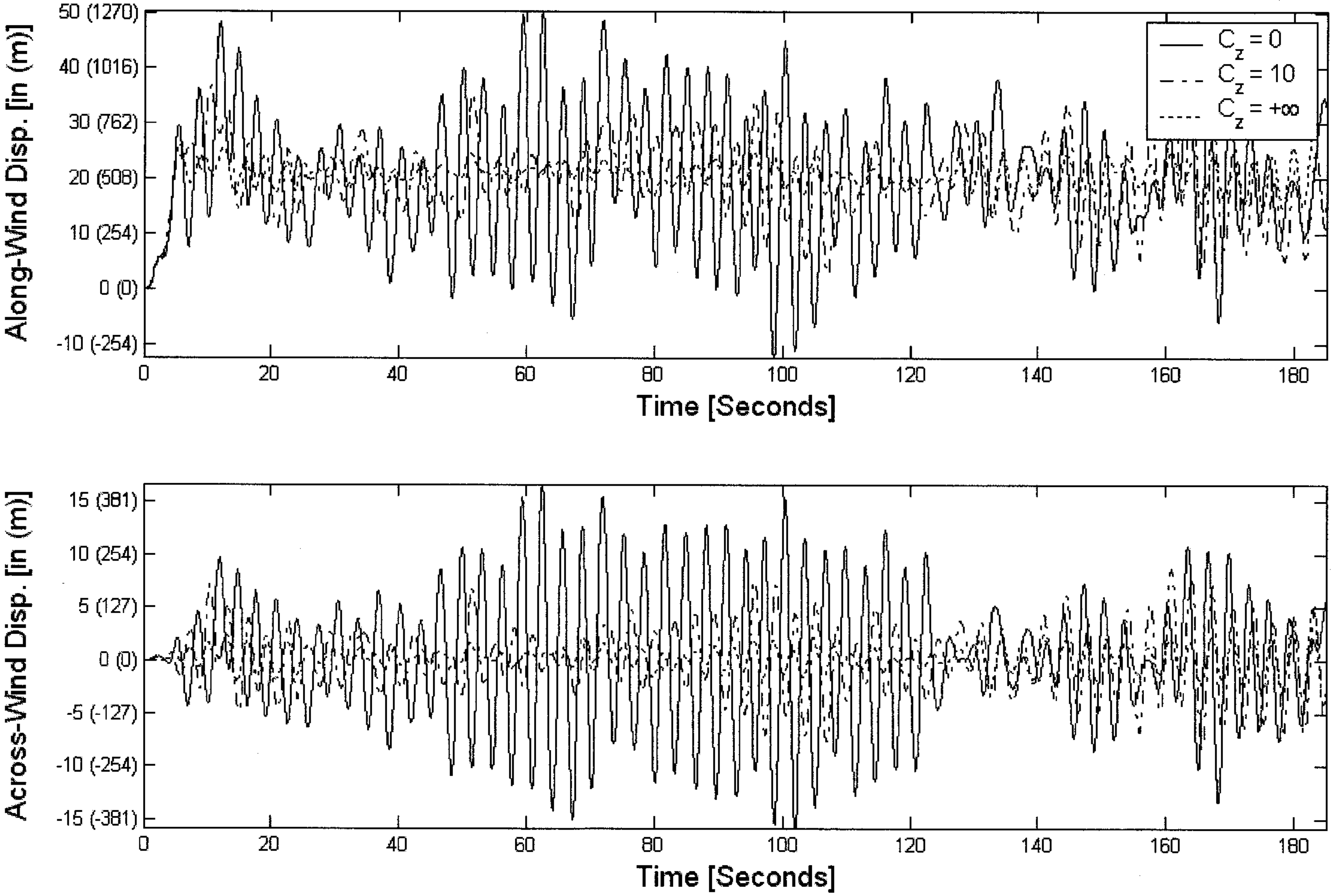

(c): Displacement Time History

Figure 6-12 (cont.): 3-D Wind Flow Time History of Analysis – Vertical Height = 140 ft (42.7 m)

The peaks of all the spatially correlated along- and across-wind speed time histories match well as expected. In the generation of these time series, even though they were generated independently, all parameters were kept constant thus generating similar characteristics. As for the two-dimensional wind flow numerical investigation, a second observation can be made with respect to the first five seconds of all analyses. For the two-dimensional wind flow study, the linear ramp-up was only applied to the simulated along-wind (longitudinal) time history. The across-wind (lateral) flow was not considered and thus was set to zero. However, this three-dimensional study does consider the across-wind (lateral) time history. Thus, the linear ramp-up was applied to both the along- and across-wind time histories before the time-domain structural analysis was conducted.

As for the two-dimensional wind flow study, the effects of changing the physical properties of the structure such as vertical height and cross-sectional dimensions also follow a general pattern. More flexible structures, as expected, produce larger response displacements. Increases in mean wind speed also produce larger responses.

The maximum response characteristics for the along-wind (longitudinal) and across-wind (lateral) directions are considered separately in this study. The along-wind (longitudinal) maximum response displacements, like the two-dimensional wind flow, also follow the conclusions of fully correlated wind flows producing the absolute maximum response of the structure. The across-wind (lateral) maximum response displacements depend on the selection of the spatial correlation of the along-wind (longitudinal) flow. Thus, these maximum displacements are considered with respect to mean wind speed and the along-wind (longitudinal) exponential decay parameter $C_{z(long)}$ used to set the spatial correlation of the wind flow. Figure 6-13 illustrates both the maximum response displacements for along- and across-wind directions for vertical heights of 60 ft (18.3 m) and 140 ft (42.7 m) with cross-sectional properties of 2.0 ft (610 mm) for the outside diameter and ½ in (12.7 mm) for the wall thickness. These are the same properties that were considered for illustrative purposes of the maximum along-wind (longitudinal) response displacements in the two-dimensional wind flow study.

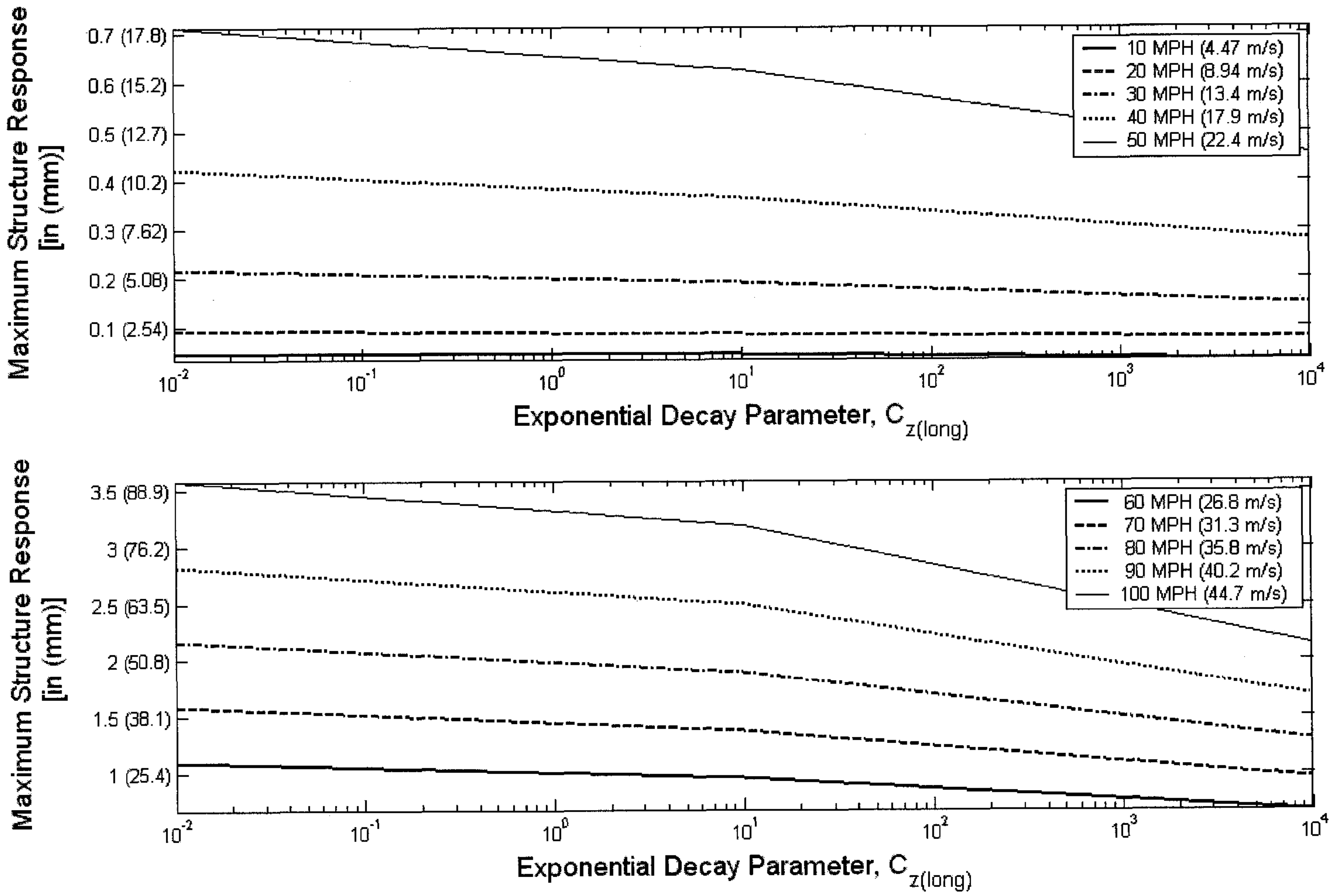

(a): Vertical Height = 60 ft (18.3 m) – Along-Wind Direction

Figure 6-13: 3-D Wind Flow Maximum Response Characteristics

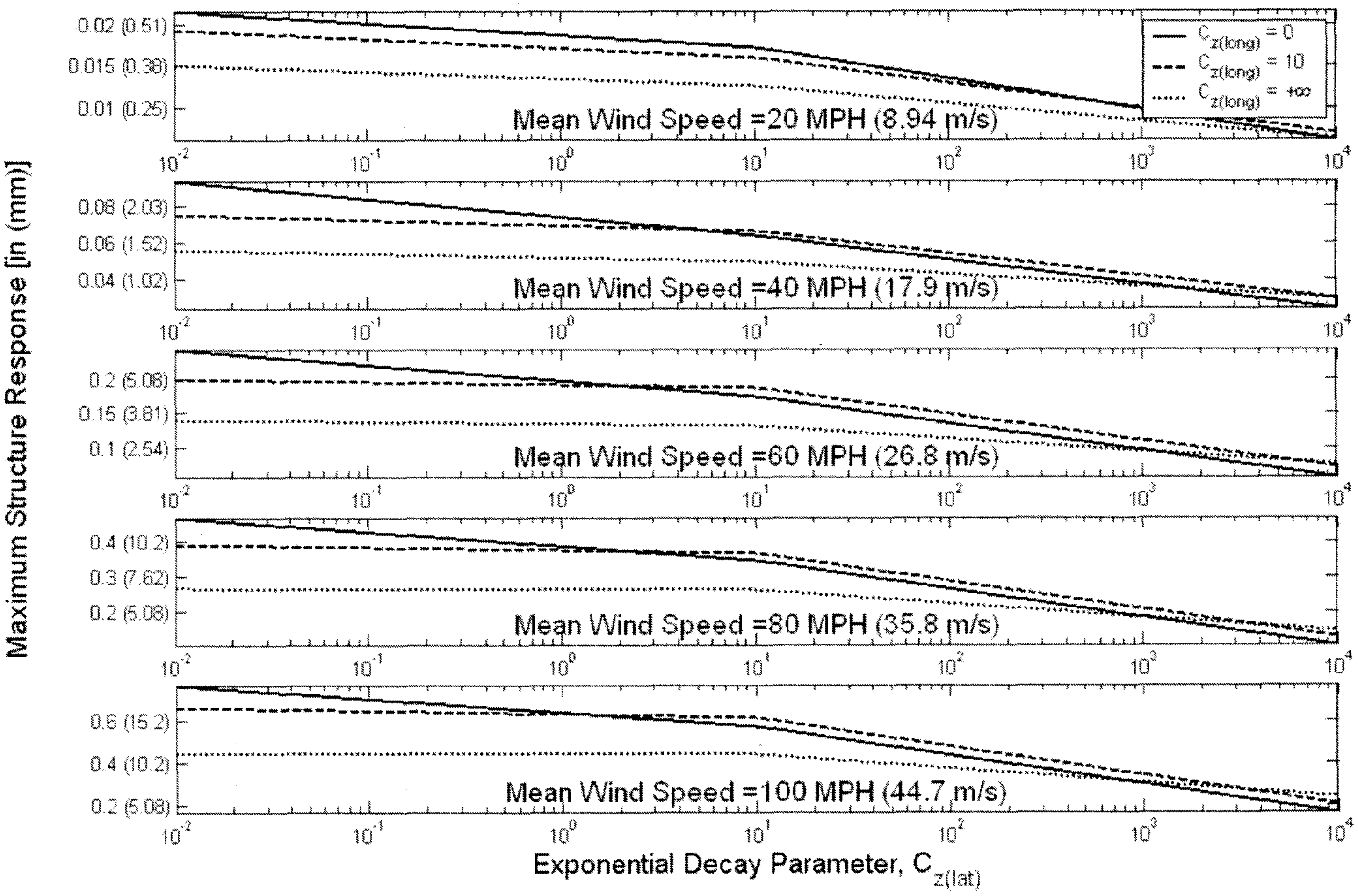

(b): Vertical Height = 60 ft (18.3 m) – Across-Wind Direction

Figure 6-13 (cont.): 3-D Wind Flow Maximum Response Characteristics

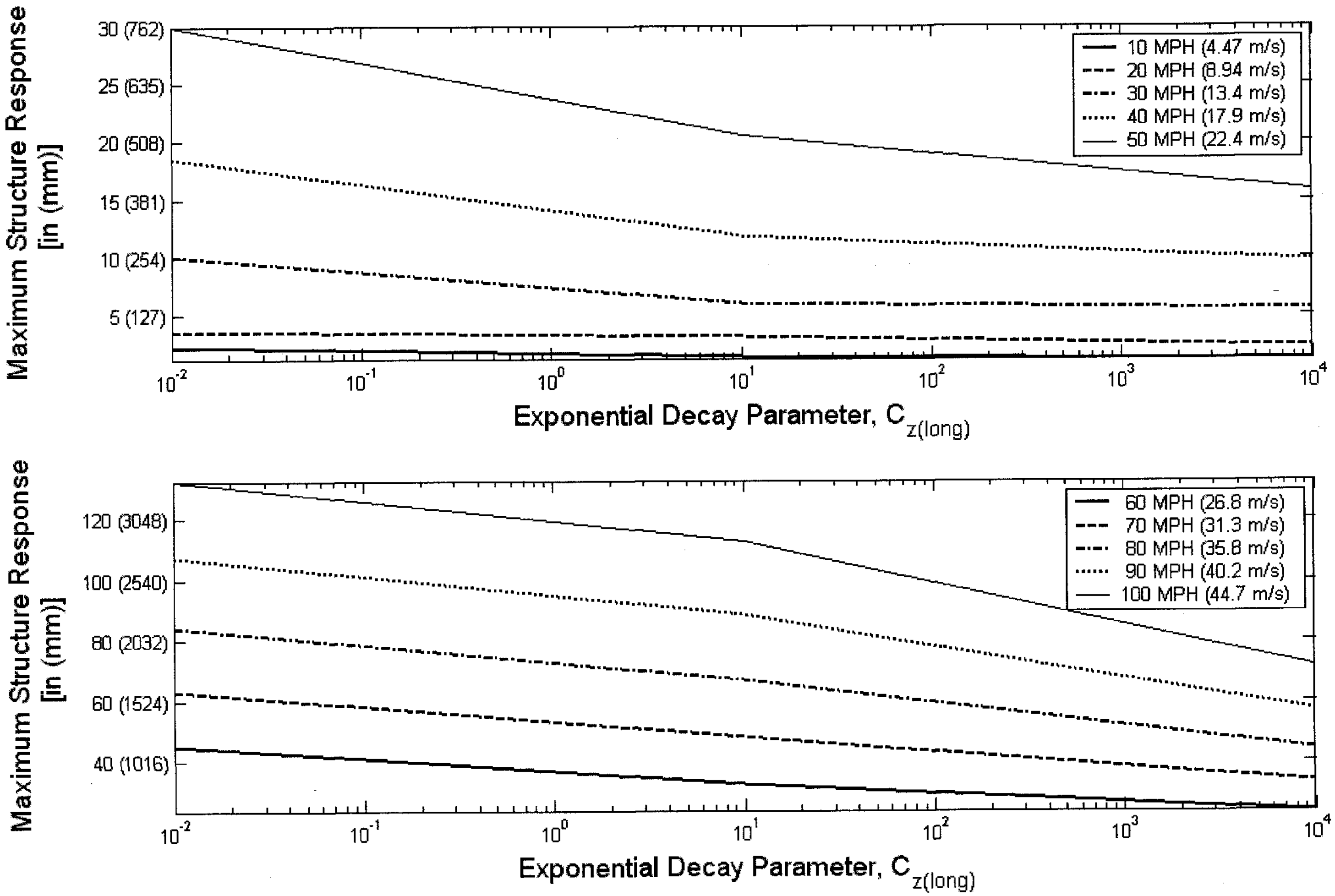

(c): Vertical Height = 140 ft (42.7 m) – Along-Wind Direction

Figure 6-13 (cont.): 3-D Wind Flow Maximum Response Characteristics

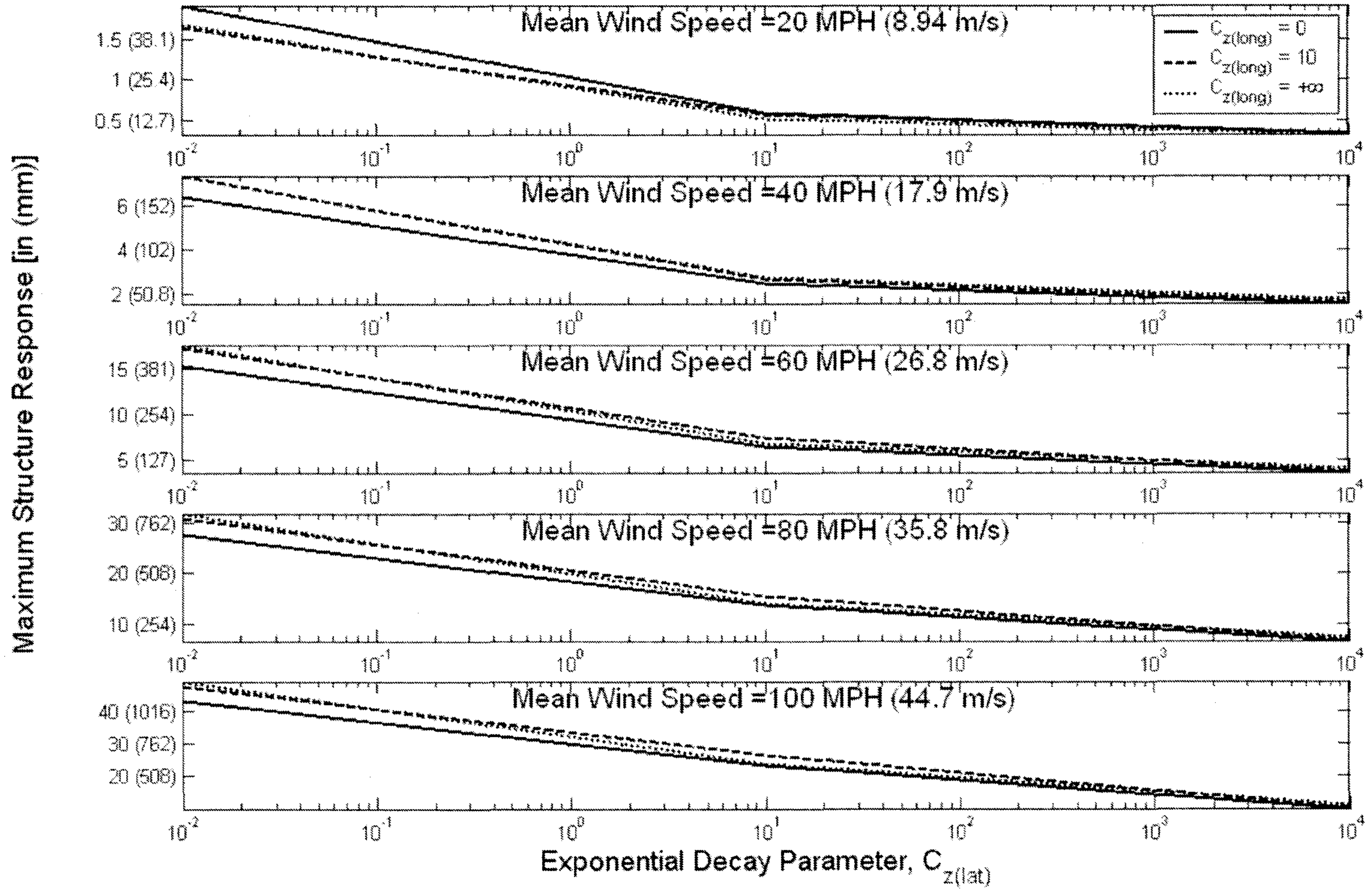

(d): Vertical Height = 140 ft (42.7 m) – Across-Wind Direction

Figure 6-13 (cont.): 3-D Wind Flow Maximum Response Characteristics

The maximum along-wind (longitudinal) displacements for all variations in vertical height of the structure and mean wind speed occurred for a spatial correlation parameter $C_{z(long)}$ approaching zero providing full spatial correlation of the wind flow. These results, as expected, correspond well with the results from the two-dimensional wind flow study. However, the changes in the maximum response of the structure appear to be less dramatic for this study. This can be primarily attributed to a coarser selection of the exponential decay parameter $C_{z(long)}$. Whereas the two-dimensional study considered nine variations of $C_{z(long)}$, this three-dimensional study considers nine combinations of $C_{z(long)}$ and $C_{z(lat)}$ but only three total variations of $C_{z(long)}$.

The maximum across-wind (lateral) response displacements also follow a general pattern. The overall maximum response is elicited for full spatial correlation of both the along- and across-wind flows. However, if each across-wind (lateral) variation of the spatial correlation is considered separately, then the maximum displacement for that particular $C_{z(lat)}$ value occurs when the along-wind (longitudinal) spatial correlation parameter $C_{z(long)}$ is equal or matched.

Recall from Chapter Three that the along-wind (longitudinal) and across-wind (lateral) turbulence components u' and v', respectively, are generated independently. The forcing function for the along-wind (longitudinal) direction is determined from Equation (2-4) that relates the relative velocity and the resulting drag force. This forcing function contains only the along-wind (longitudinal) velocity components of the wind flow and motion of the structure. It does not depend on any velocity terms in the across-wind (lateral) direction. Finally, the structure motion in the along-wind (longitudinal) direction is decoupled from the across-wind (lateral) direction based on the use of the twelve degree-of-freedom beam elements used to analyze the structure in the finite element routine. Thus, for a constant exponential decay coefficient $C_{z(long)}$, the response displacements are equivalent even for changes in the across-wind (lateral) spatial correlation parameter $C_{z(lat)}$.

Independency between changes in the along-wind (longitudinal) flow and the across-wind (lateral) forcing function, however, does not exist. The forcing function for the across-wind (lateral) direction is determined from Equation (4-13) that relates the relative velocity and the resulting drag force. This second forcing function contains both the along-wind (longitudinal) and across-wind (lateral) velocity components of the wind flow and motion of the structure. Thus, changes in the along-wind (longitudinal) spatial correlation effect the across-wind (lateral) displacements.

The final component of the three-dimensional wind flow study considers statistical quantities of the wind flow and resulting response of the structure. Specifically, the statistical quantities of interest are the resulting spatial correlation of the time histories for the along-wind (longitudinal) and across-wind (lateral) wind flows, resulting wind-induced loadings, and response of the structure. Cross-correlation quantities between these time histories are also briefly discussed.

Within the context of this study, six time histories are investigated in relation to the assumed exponential decay parameters $C_{z(long)}$ and $C_{z(lat)}$ of the simulated wind speed time series. Recall that when $C_{z(long)} = C_{z(lat)} = 0$, the spatial correlation of the resulting wind speed time series is fully correlated. This is due to the exponential function of Equation (6-4) degenerating to unity thus producing a fully correlated time series with respect to multiple heights along the structure. Alternatively, when $C_{z(long)} = C_{z(lat)} = +\infty$, the spatial correlation of the resulting wind speed time series has no correlation producing an exponential function value of zero in the limit.

The six time histories investigated within this study consider all time series for each node of the structure. First, the along-wind (longitudinal) and across-wind (lateral) wind speed time histories due to the simulated wind flow are considered. Second, the resulting along-wind (longitudinal) and across-wind (lateral) wind-induced drag force time histories caused by the wind flow are considered. The drag force considered is due to the relative motion of the wind flow and response of the structure as given by Equations (2-4) and (4-13). Finally, the response of the structure in the along-wind (longitudinal) and across-wind (lateral) directions is considered.

In the interest of brevity, complete *m*-by-*m* correlation matrices are not presented in full detail. Rather, as was done in the two-dimensional wind flow study, specific columns (or rows due to the symmetric nature of these matrices) are provided graphically. Figure 6-14 provides the spatial correlation of the 60 ft (18.3 m) structure for various values of the assumed spatial correlation of the three-dimensional wind flow. The spatial correlation of the wind flow, wind-induced load, and response of the structure are considered in sub-figures (a), (b), and (c), respectively. For comparison purposes, sub-figure (d) combines sub-figures (a) and (b) into one figure where the wind speed time histories are indicated by the lines marked "W" and the wind-induced load time histories are indicated by the data points marked "L". For all figures, the spatial correlation of each time history is considered with respect to the third-point heights of the structure. One additional figure, sub-figure (e), is provided to illustrate the effects of changing the exponential decay parameters $C_{z(long)}$ and $C_{z(lat)}$ with respect to the measured spatial correlation at the ⅓ height point. Changes to the across-wind (lateral) spatial correlation do not affect the spatial correlation characteristics in the along-wind (longitudinal) direction. However, based on the loading function for the across-wind (lateral) direction given by Equation (4-13), changes to the spatial correlation in the along-wind (longitudinal) direction do affect the spatial correlation characteristics in the across-wind direction. Note that only figures are provided for the structure with a vertical height of 60 ft (18.3 m), outside diameter of 2.0 ft (610 mm), and wall thickness of ¼ in (6.35 mm). Other cross-section properties and vertical height variations produce similar results.

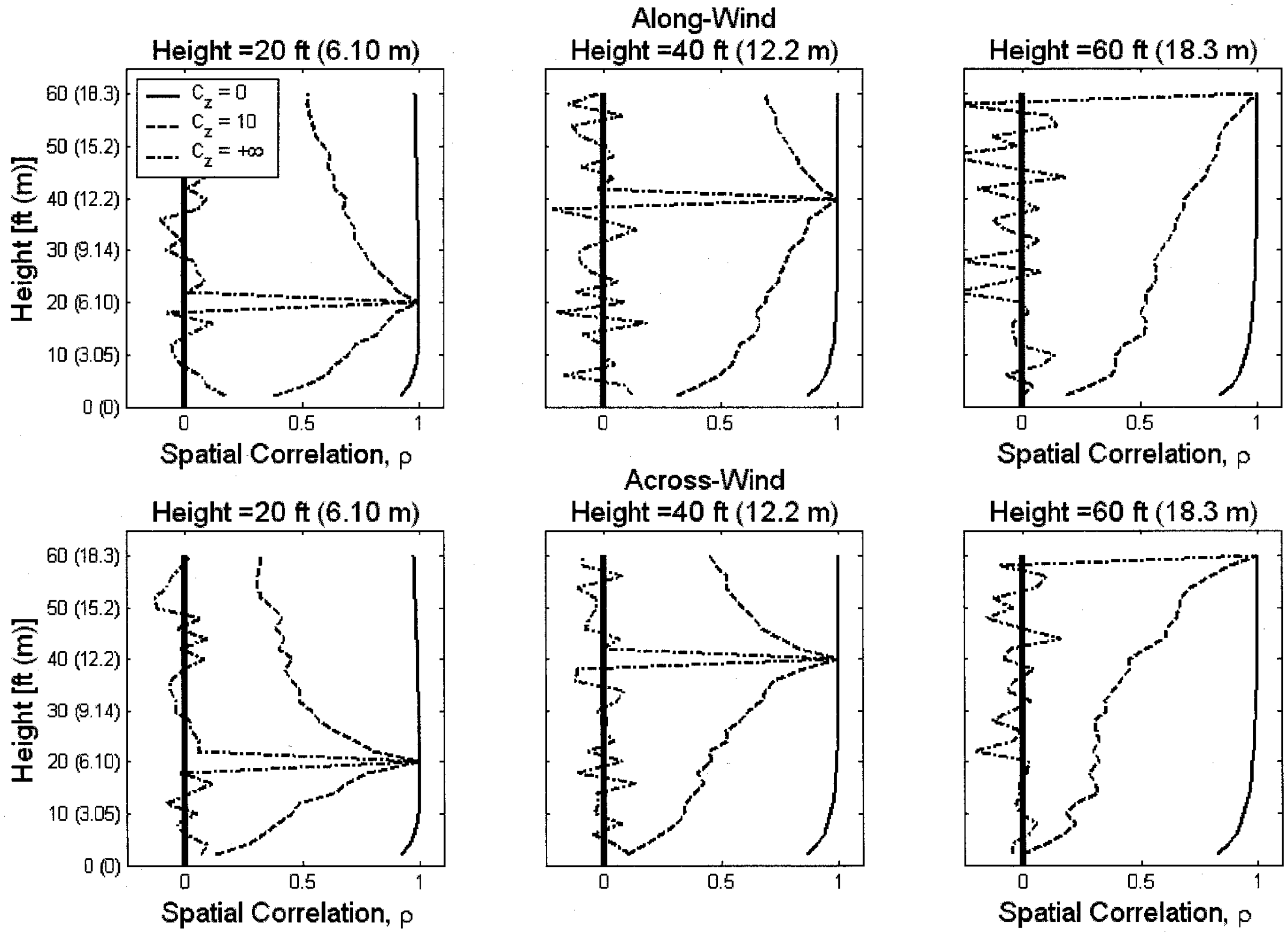

(a): Wind Speed Time History

Figure 6-14: 3-D Wind Flow Spatial Correlation

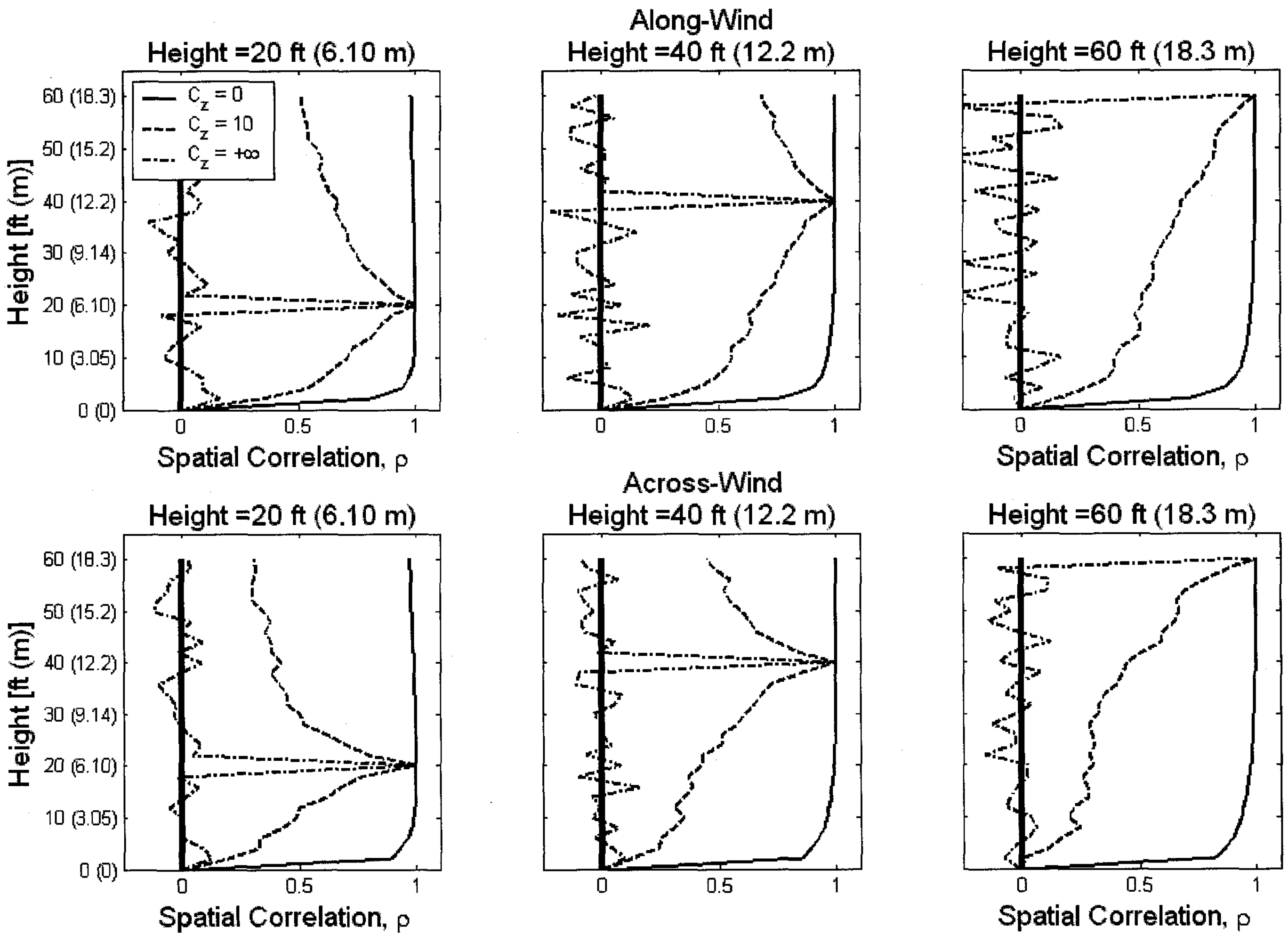

(b): Wind-Induced Load Time History

Figure 6-14 (cont.): 3-D Wind Flow Spatial Correlation

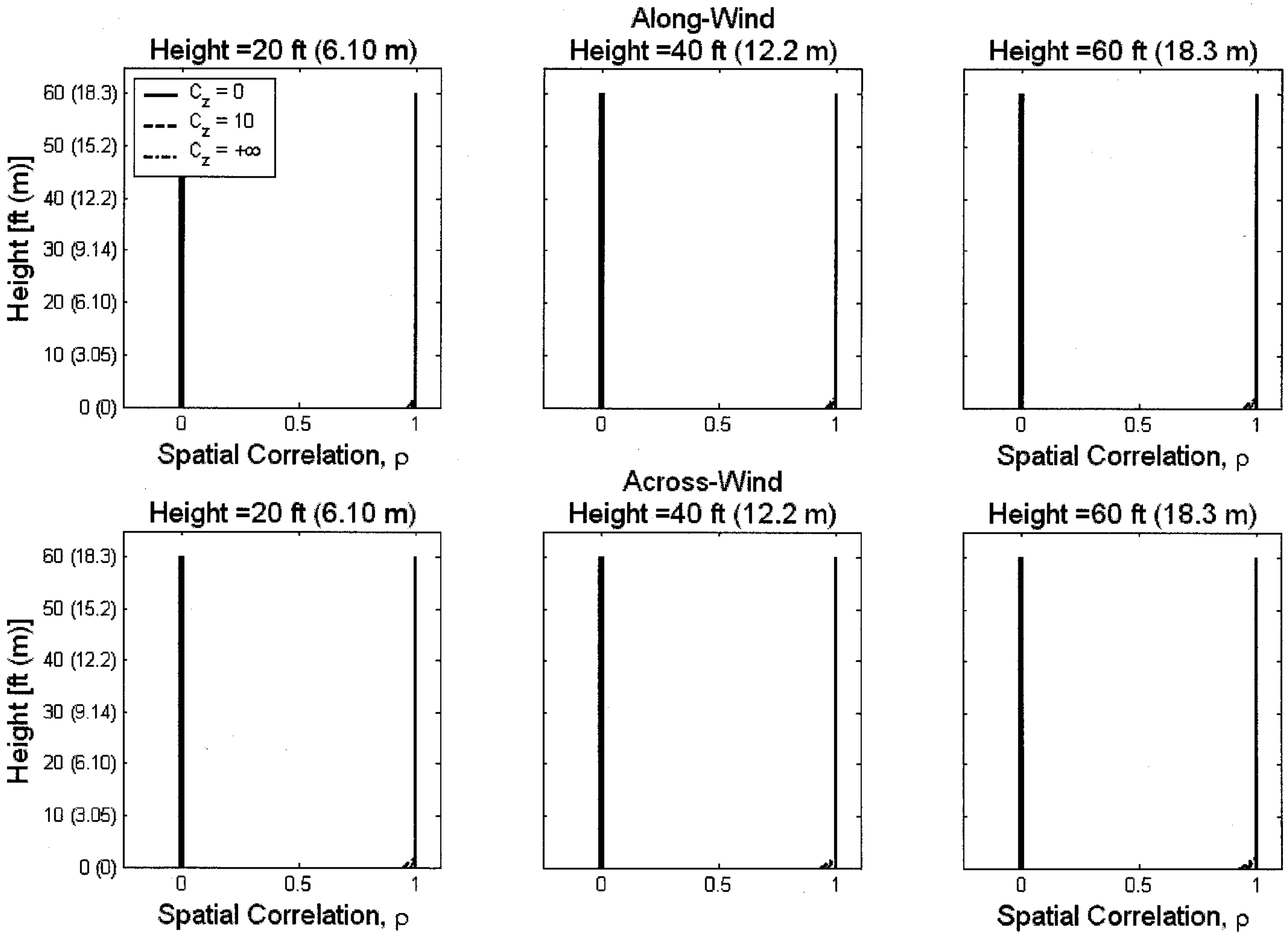

(c): Displacement Time History

Figure 6-14 (cont.): 3-D Wind Flow Spatial Correlation

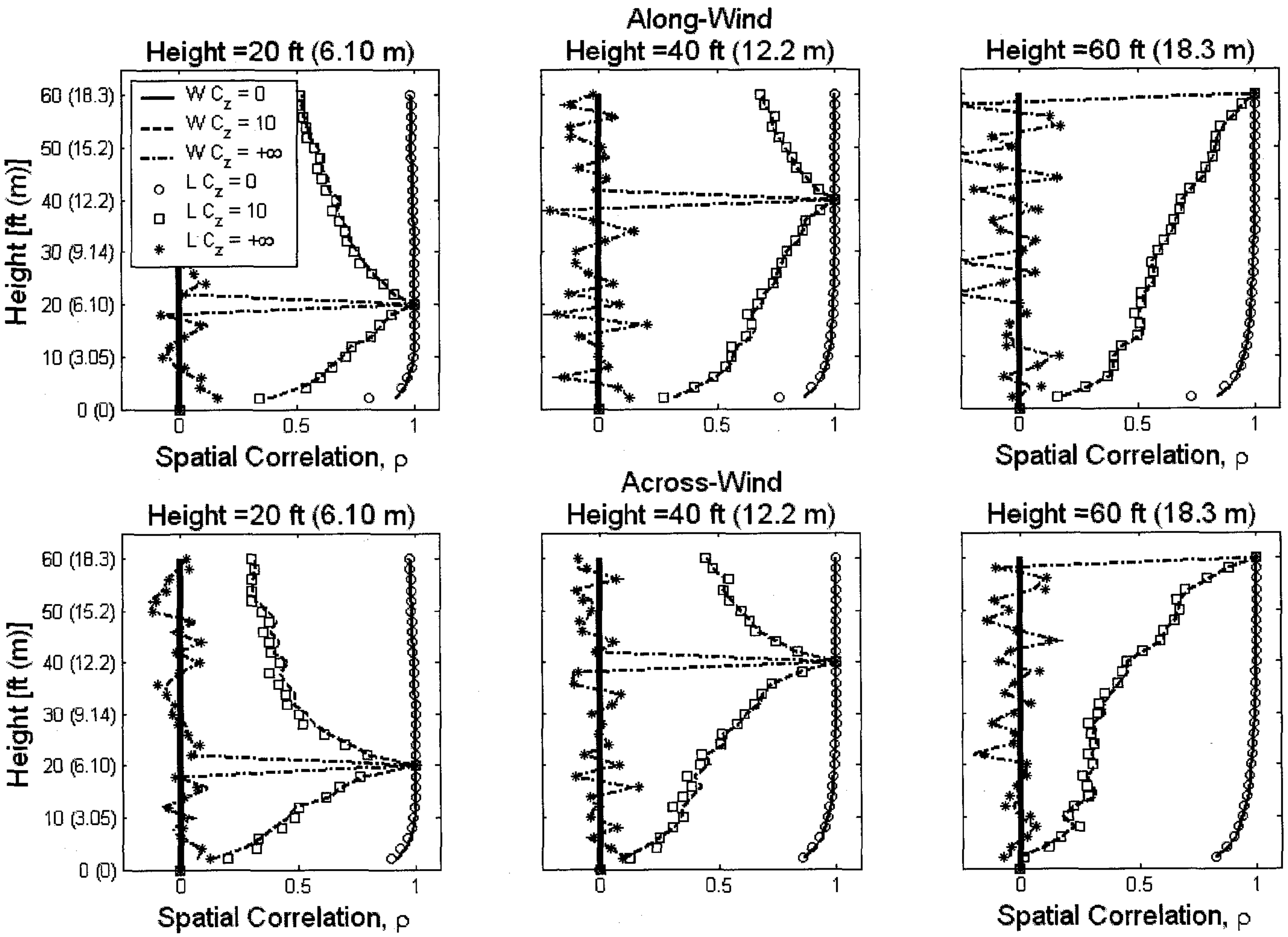

(d): Wind Speed and Wind-Induced Load Time Histories

Figure 6-14 (cont.): 3-D Wind Flow Spatial Correlation

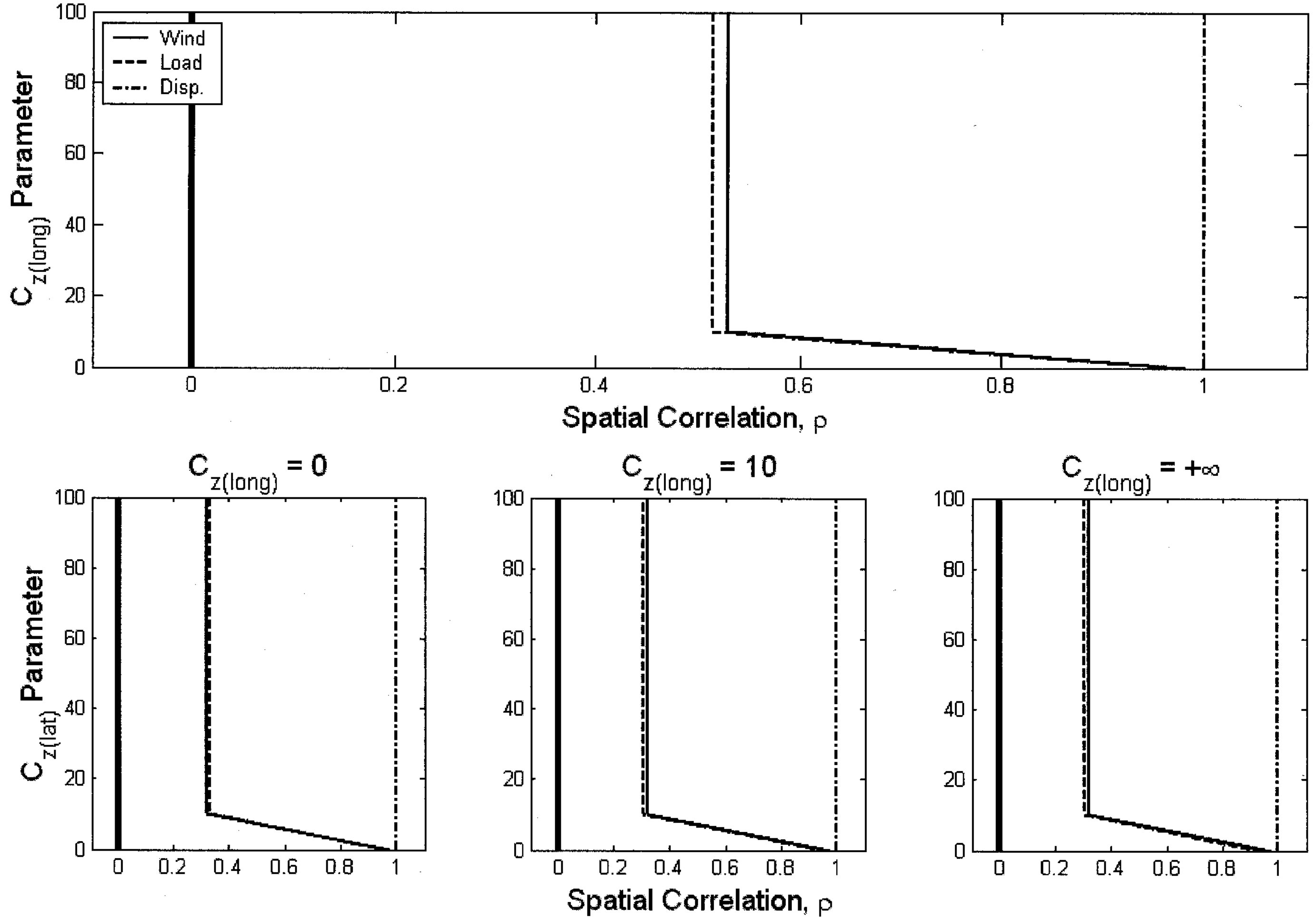

(e): Spatial Correlation Parameter

Figure 6-14 (cont.): 3-D Wind Flow Spatial Correlation

Based on the results provided in Figure 6-14 (a), spatial correlation of the wind speed time history, variations in the assumed spatial correlation used to simulate the wind flow produce similar variations in the measured spatial correlation. For example, when $C_{z(long)} = C_{z(lat)} = 0$ the simulated wind flow is assumed to be fully correlated. Based on the measured spatial correlation that indicates nearly full correlation of the wind flow for $C_{z(long)} = C_{z(lat)} = 0$, these results are comparable. On average, when $C_{z(long)} = C_{z(lat)} = +\infty$ the measured spatial correlation is near zero indicating no correlation between nodal points along the height of the structure.

The same results given by Figure 6-14 (a) are also given in Figure 6-14 (b) where the spatial correlation of the wind-induced load is considered. Based on the function used to derive this load, Equation (2-4) for the along-wind (longitudinal) load and Equation (4-13) for the across-wind (lateral) load, only the drag coefficient and relative velocity terms vary from one node to the next. However, all of these terms are directly related to the wind flow that has some type of spatial correlation. Thus, the resulting spatial correlation of the wind-induced load and wind speed time histories are quite similar as shown in Figure 6-14 (d).

The results of the spatial correlation of the along-wind (longitudinal) and across-wind (lateral) displacement time histories, Figure 6-14 (c), provide results that are to be expected. The structure is composed of a series of interconnected finite elements and thus moves in tandem. Fully-correlated time histories between nodes of the structure are reproduced for all values of the assumed parameters $C_{z(long)}$ and $C_{z(lat)}$. Any other value would indicate a structural modeling error and lack of continuity within the finite element analysis framework.

Finally, the effects of varying the spatial correlation parameters, $C_{z(long)}$ and $C_{z(lat)}$, are most evident in Figure 6-14 (e). As for two-dimensional wind flow, low values (less than 10) of C_z correspond well with strong spatial correlation of the time histories considered. Changes in the across-wind (lateral) direction parameter $C_{z(lat)}$ produced no changes in the spatial correlation characteristics of the along-wind (longitudinal) time histories. This, again, is due to the independent generation of the three-dimensional wind flow and the decoupled structural analysis finite element method incorporated in this study. For time histories in the across-wind (lateral) direction, however, small changes in the spatial correlation in the along-wind (longitudinal) direction can be seen to affect the time histories considered. For all cases and in both directions, however, the spatial correlation of the displacement time history is always fully correlated at unity.

The final consideration for the three-dimensional wind flow study is the cross-correlation between particular time histories generated as a result of the time-domain analyses. In this case, however, all five vertical height variations of the structure are presented for investigation. As before, variations in the assumed spatial correlation of the along-wind (longitudinal) and across-wind (lateral) flows are the basis for comparisons. Table 6-5 presents the cross-correlation quantities considered. Table 6-5 (a) presents the cross-correlation between the along-wind (U_h) and across-wind (V_h) wind speed time series at the top of the structure. Tables 6-5 (b) and (c) present the results for the along-wind (longitudinal) and across-wind (lateral) directions, respectively. Within each of these tables, first, the cross-correlation between the wind speed (U_h or V_h) and displacement (x_h or y_h) time histories at the top of the structure are presented. Second, the cross-correlation between the wind speed and wind-induced load (L_{Uh} or L_{Vh}) time histories at the top of the structure are presented. Third, the cross-correlation between the wind-induced load and displacement time histories at the top of the structure are presented. Finally, the cross-correlation between the wind speed at the top of the structure and the bending stress (σ_y or σ_x) at the bottom of the structure are presented. These bending stress time histories will be an important quantity in the numerical investigation of fatigue life considered in Chapter Eight of this study. A large number of cross-correlation quantities exist for investigation, but these nine total are of particular interest and provide a general overview of the cross-correlation properties between time histories of slender structures.

Vertical Height ft (m)	$C_{z(long)} = C_{z(lat)} = C_z$	Cross-Correlation
		$U_h - V_h$
60 (18.3)	0	0.939
	10	0.943
	$+\infty$	0.931
80 (24.4)	0	0.942
	10	0.942
	$+\infty$	0.936
100 (30.5)	0	0.945
	10	0.947
	$+\infty$	0.968
120 (36.6)	0	0.948
	10	0.945
	$+\infty$	0.962
140 (42.7)	0	0.950
	10	0.940
	$+\infty$	0.954

(a): Along- and Across-Wind Time Histories Cross Correlation

Vertical Height ft (m)	$C_{z(long)} = C_z$	Cross-Correlation			
		$U_h - x_h$	$U_h - F_{Uh}$	$F_{Uh} - x_h$	$U_h - \sigma_y$
60 (18.3)	0	0.931	0.996	0.937	0.935
	10	0.834	0.996	0.837	0.820
	$+\infty$	0.613	0.994	0.621	0.552
80 (24.4)	0	0.652	0.995	0.657	0.671
	10	0.662	0.995	0.668	0.655
	$+\infty$	0.475	0.996	0.478	0.424
100 (30.5)	0	0.546	0.994	0.550	0.572
	10	0.571	0.995	0.575	0.570
	$+\infty$	0.372	0.997	0.378	0.337
120 (36.6)	0	0.587	0.993	0.588	0.617
	10	0.516	0.994	0.517	0.519
	$+\infty$	0.282	0.995	0.286	0.245
140 (42.7)	0	0.386	0.979	0.397	0.415
	10	0.485	0.991	0.490	0.487
	$+\infty$	0.180	0.995	0.181	0.149

(b): Longitudinal Time Histories Cross-Correlation

Table 6-5: 3-D Wind Flow Cross-Correlation

Vertical Height ft (m)	$C_{z(lat)} = C_z$	Cross-Correlation			
		$V_h - y_h$	$V_h - F_{Vh}$	$F_{Vh} - y_h$	$V_h - \sigma_x$
60 (18.3)	0	0.940	0.985	0.960	-0.940
	10	0.878	0.984	0.892	-0.852
	$+\infty$	0.834	0.977	0.860	-0.797
80 (24.4)	0	0.477	0.986	0.488	-0.490
	10	0.484	0.984	0.495	-0.468
	$+\infty$	0.381	0.985	0.386	-0.344
100 (30.5)	0	0.329	0.986	0.337	-0.346
	10	0.364	0.988	0.363	-0.351
	$+\infty$	0.269	0.990	0.273	-0.234
120 (36.6)	0	0.347	0.986	0.349	-0.370
	10	0.340	0.989	0.343	-0.330
	$+\infty$	0.337	0.984	0.336	-0.298
140 (42.7)	0	0.154	0.976	0.169	-0.170
	10	0.342	0.987	0.347	-0.332
	$+\infty$	0.165	0.990	0.167	-0.124

(c): Lateral Time Histories Cross-Correlation

Table 6-5 (cont.): 3-D Wind Flow Cross-Correlation

Generally, as the height of the structure increases, the cross-correlation between all time series decreases as expected with the exception being the cross-correlation between the wind speed and the wind-induced loading at the top of the structure. The assumed parameter $C_{z(long)} = +\infty$ and $C_{z(lat)} = +\infty$ also consistently produce the lowest cross-correlation between the time series of interest. From Table 6-5 (a), the cross-correlation between the along-wind (longitudinal) and across-wind (lateral) wind flows at the top of the structure are also well correlated. Even though the two time series were generated independently, all parameters in their simulation were held constant for both directions with the exception of the spectral density functions considered in Section 3.1. Thus, as expected both time series are well correlated for all structures. Perhaps the most interesting result is the cross-correlation between the across-wind (lateral) direction flow and the bending stress time history σ_x from Table 6-5 (c). Strong negative correlation is observed for 60 ft (18.3 m) structures. Whereas, weak negative correlation is observed for 140 ft (42.7 m) structures. At this point, it can be reasoned that the along-wind (longitudinal) wind flow has more of a direct impact on the bending stress σ_x than the across-wind (lateral) wind flow due to the use of the forcing function given considered in the across-wind (lateral) direction. Further investigation is needed for this result.

Chapter Seven

Vortex Shedding

7.1 Setup and Procedure

The numerical investigation of vortex shedding also considers several variations in wind speed, structure properties such as vertical height, outside diameter, and wall thickness, and vortex shedding model parameters as outlined in Section 4.2. The primary goal of this study is to determine the effects of vortex shedding on slender structural systems. A consequence of this study will result in a better understanding of the incorporation of a vortex shedding model into a dynamic, time-domain finite element analysis routine for aeroelastic sensitive structures as considered in this study. Changes to the resultant loading and response of the structure are also of interest.

As given in Chapter Four, the vortex shedding model can be divided into two forcing function components: forced vibration and aerodynamic damping. The forced vibration term derived in Section 4.2 is given in Equation (4-12) as

$$\frac{1}{2}\rho_{air}U^2DC_L(k)\sin(\omega_s t+\phi) \tag{7-1}$$

where the circular frequency of vortices being shed in the wake of the structure ω_s is given as a function of the Strouhal number, St, as

$$\frac{\omega_s D}{U}=2\pi\,\mathrm{St} \tag{7-2}$$

where the Strouhal number and the lift coefficient, $C_L(k)$, are detailed in Section 4.2.

The aerodynamic damping term derived in Section 4.2 is given in Equation (4-8) and repeated here as

$$2\omega_1\rho_{air}D^2K_{a0}\left(\frac{U}{U_{cr}}\right)\left[1-\left(\frac{y}{\lambda D}\right)^2\right]\dot{y} \tag{7-3}$$

where the term

$$K_{a0}\left(\frac{U}{U_{cr}}\right) \tag{7-4}$$

is defined as an aerodynamic coefficient and is further detailed in Section 4.2. Within Equation (7-3) the parameter λ defines the limiting displacement for the aerodynamic damping term. For the case when the across-wind (lateral) displacement, y, equals or exceeds λD, where D is the outside diameter of the structure, the aerodynamic damping term vanishes such that the structure no longer experiences any aeroelastic effects (Simiu and Scanlan, 1986).

For this study, two cases of the forcing function of the vortex shedding model will be considered. First, the forcing function will only consist of the forced vibration term given in Equation (7-1). Within this term, there are no empirical parameters that may be varied to determine their effects on the response of the structure. Thus, the primary results from this study will be used to differentiate the results from the second numerical investigation where the aerodynamic damping term given in Equation (7-3) is included with the forced vibration term. In this latter study, the parameter defining the limiting displacement, λ, which controls the magnitude of the forcing function will be considered to vary in order to determine its effects on the response of the structure.

Both cases of forcing function models for vortex shedding will consider the same variations in the properties of the example structure as first discussed in Chapter Two. The variations in the properties of the example structure are outlined in Table 7-1. There are three vertical height variations, two outside diameter variations, and two wall thickness variations representing 12 total variations in the example structure properties. Each structure variation is discretized using finite elements of 2 ft (610 mm) in length.

Property	Value
Vertical Height	60, 100, 140 ft (18.3, 30.5, 42.7 m)
Outside Diameter	2.0 and 2.5 ft (610 and 762 mm)
Wall Thickness	¼ and ½ in (6.35 and 12.7 mm)

Table 7-1: Variations in Example Structure Properties for Vortex Shedding

In both cases, a three-dimensional wind flow will be considered. The three-dimensional wind flow is comprised of both the along-wind (longitudinal) and across-wind (lateral) turbulence components u' and v', respectively, and the mean wind velocity $\overline{U}$. Both turbulence components u' and v' are independently generated for each nodal point of the structure over a time duration of 3 minutes or 180 seconds. The mean wind velocity $\overline{U}$ is constant in time but varies along the height of the structure according the logarithmic law defining the mean wind velocity profile given in Equation (3-6).

As in Chapter Six, it is necessary to consider the spatial correlation of wind turbulence. The goal, however, of the present study is not to determine the effects of spatial correlation of wind turbulence. Thus, the three-dimensional wind flow will consider variations in the exponential decay coefficient, C_z, within the root-coherence function of Chapter Three in a limited fashion. Table 7-2 provides a summary of the changes to the exponential decay coefficients $C_{z(long)}$ and $C_{z(lat)}$ for the u' and v' turbulence components, respectively, for the simulation of wind speed time series for three-dimensional flow. The example structure property variations of Table 7-1 are also considered to vary for each of the variations listed in Table 7-2. Also as noted in Table 7-2, variations in the mean wind speed at 32.8 ft (10 m) above the ground are considered. There are nine variations in mean wind speed, three variations in the assumed spatial correlation of the u' and v' turbulence components, and 12 variations in the example structure properties. Thus, there are 324 separate analyses for both forcing function models for vortex shedding in this numerical investigation. This number, however, does not include variations in the limiting displacement parameter within the aerodynamic damping term considered in Section 7.3.

Property	Value
Mean Wind Speed at 32.8 ft (10 m)	2, 4, 6, 8, 10, 15, 20, 25, 50 MPH (0.89, 1.79, 2.68, 3.58, 4.47, 6.71, 8.94, 11.2, 22.4 m/s)
Along-Wind (Longitudinal) and Across-Wind (Lateral) Exponential Decay Coefficient $C_{z(long)}$ and $C_{z(lat)}$	$C_{z(long)} = C_{z(lat)} = 0$ $C_{z(long)} = C_{z(lat)} = 10$ $C_{z(long)} = C_{z(lat)} = +\infty$

Table 7-2: Variations in Wind Flow Properties for Vortex Shedding

The variations in the forcing function terms of the vortex shedding model are outlined in Sections 7.2 and 7.3 for the forced vibration term only and for both the forced vibration and aerodynamic damping terms, respectively.

7.2 Forced Vibration Results

The first study of vortex shedding considers only the forced vibration term of the vortex shedding model. Hence, no effects due to the aerodynamic damping term are considered in this first study. Because the forced vibration term given by Equation (7-1) does not have any empirical parameters that may be varied to determine its effects on the response of the structure, this first study consists of only variations in the example structure properties of Table 7-1 and the wind flow properties of Table 7-2. Hence, a total of 324 separate analyses will be performed to determine the effects of the forced vibration term of the vortex shedding model on the response of the structure. This study will help to serve as the basis for determining the effects of the complete vortex shedding model of Section 7.3 that includes both the forced vibration and aerodynamic damping terms.

Results of Analysis

The results for the forced vibration study are presented and discussed using two primary components. First, the response of the structure considering the forced vibration term of the vortex shedding model is investigated. Within this investigation, complete time-domain examples of the along-wind (longitudinal) and across-wind (lateral) responses are presented graphically. Only a few examples may be presented, but these offer a representative description of other analyses conducted for this study. The second component consists of an investigation of the vortex shedding load due to the forced vibration term. As for the response, graphical results are used for investigation of the vortex shedding model induced loading. Similar to Chapter Six, supplemental maximum structure response data generated are also considered.

Figures 7-1 through 7-3 provide an illustrative representation of the resulting time-domain dynamic analysis of the structure considered. Each figure provides the time-history of the along- and across-wind displacements for the top node of the structure. A two-dimensional plot of the movement of the top node between 80 and 90 seconds of the time history is also provided. Dashed lines on the along- and across-wind time histories denote the starting and stopping points for 80 and 90 seconds, respectively. Figure 7-1 considers a structure having a vertical height of 60 ft (18.3 m) and mean wind speeds at 32.8 ft (10 m) of 8 MPH (3.58 m/s) and 25 MPH (11.2 m/s) for sub-figures (a) and (b), respectively. Figure 7-2 considers a structure having a vertical height of 100 ft (30.5 m) and mean wind speeds of 6 MPH (2.68 m/s) and 25 MPH (11.2 m/s). Finally, Figure 7-3 considers a 140 ft (42.7 m) structure with mean wind speeds of 4 MPH (1.79 m/s) and 25 MPH (11.2 m/s). These various mean wind speeds, relatively low and high, for each vertical height variation demonstrate the variation of the forced vibration loading term considered in this study. Each figure considered has the same cross-sectional properties, outside diameter of 2.5 ft (762 mm) and wall thickness of ¼ in (6.35 mm), and full spatial correlation ($C_z = 0$) of the three-dimensional wind flow. Note, however, that far more variations in mean wind speed, structure properties, and spatial correlation were considered as given in Table 7-1 and 7-2, but are not fully provided by Figures 7-1 through 7-3 in the interest of brevity. Also, as in Chapter Six, a linear ramp-up of wind speed during the first five seconds of the analysis is employed. This ensures numerical stability at the beginning of the dynamic analysis.

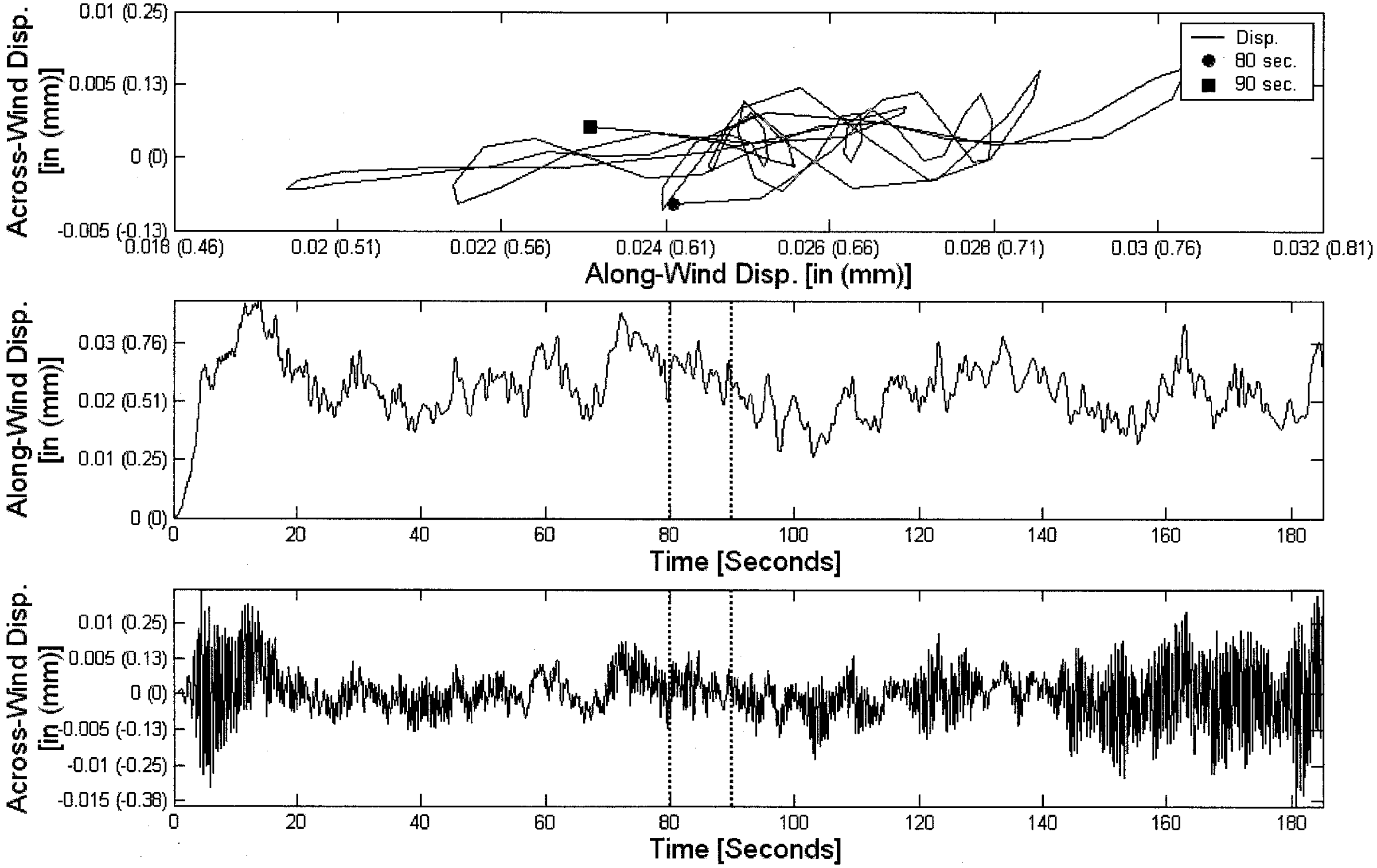

(a): Mean Wind Speed = 8 MPH (3.58 m/s)

Figure 7-1: Forced Vibration Vortex Shedding Response Time History of Analysis – Vertical Height = 60 ft (18.3 m)

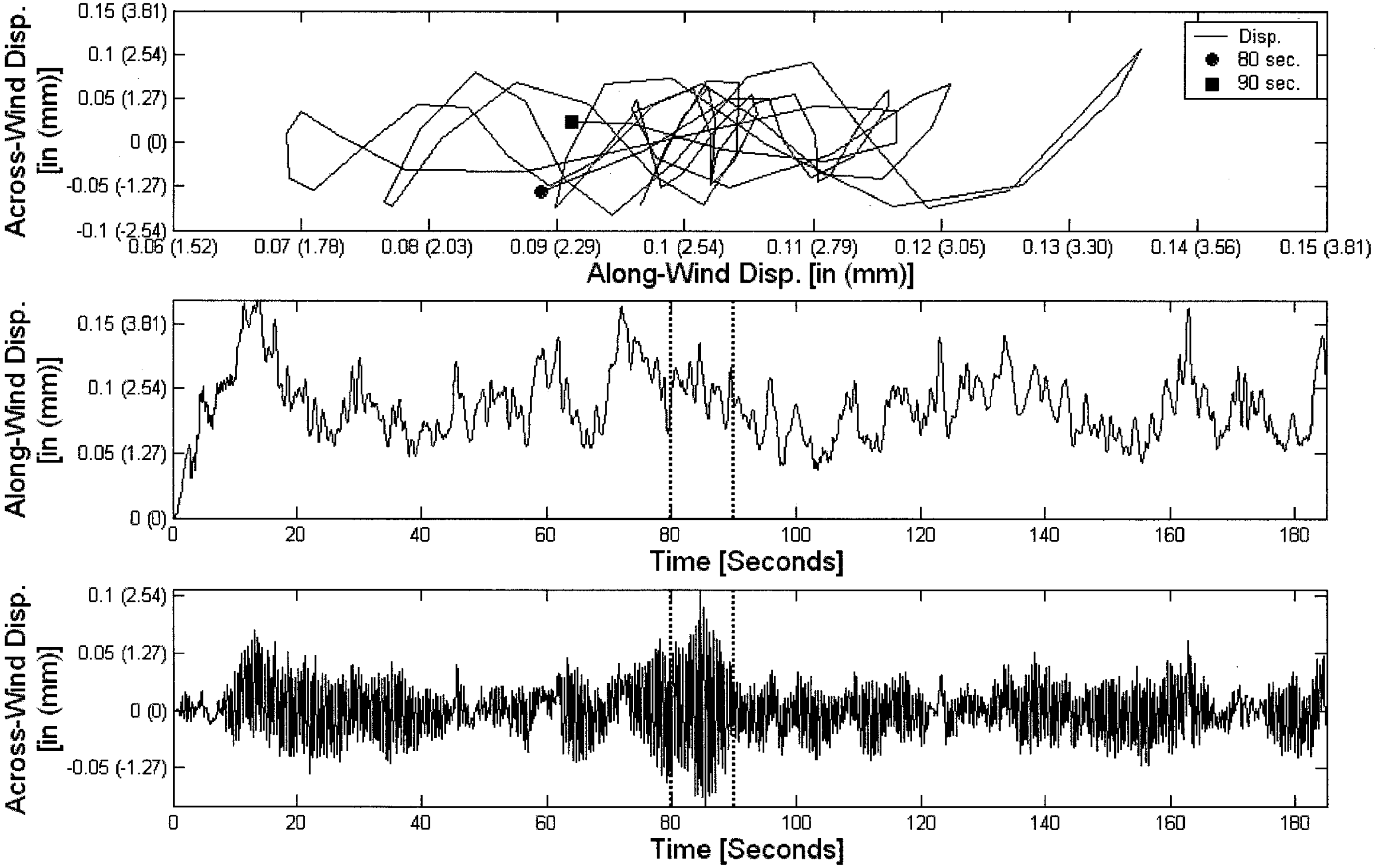

(b): Mean Wind Speed = 25 MPH (11.2 m/s)

Figure 7-1 (cont.): Forced Vibration Vortex Shedding Response Time History of Analysis – Vertical Height = 60 ft (18.3 m)

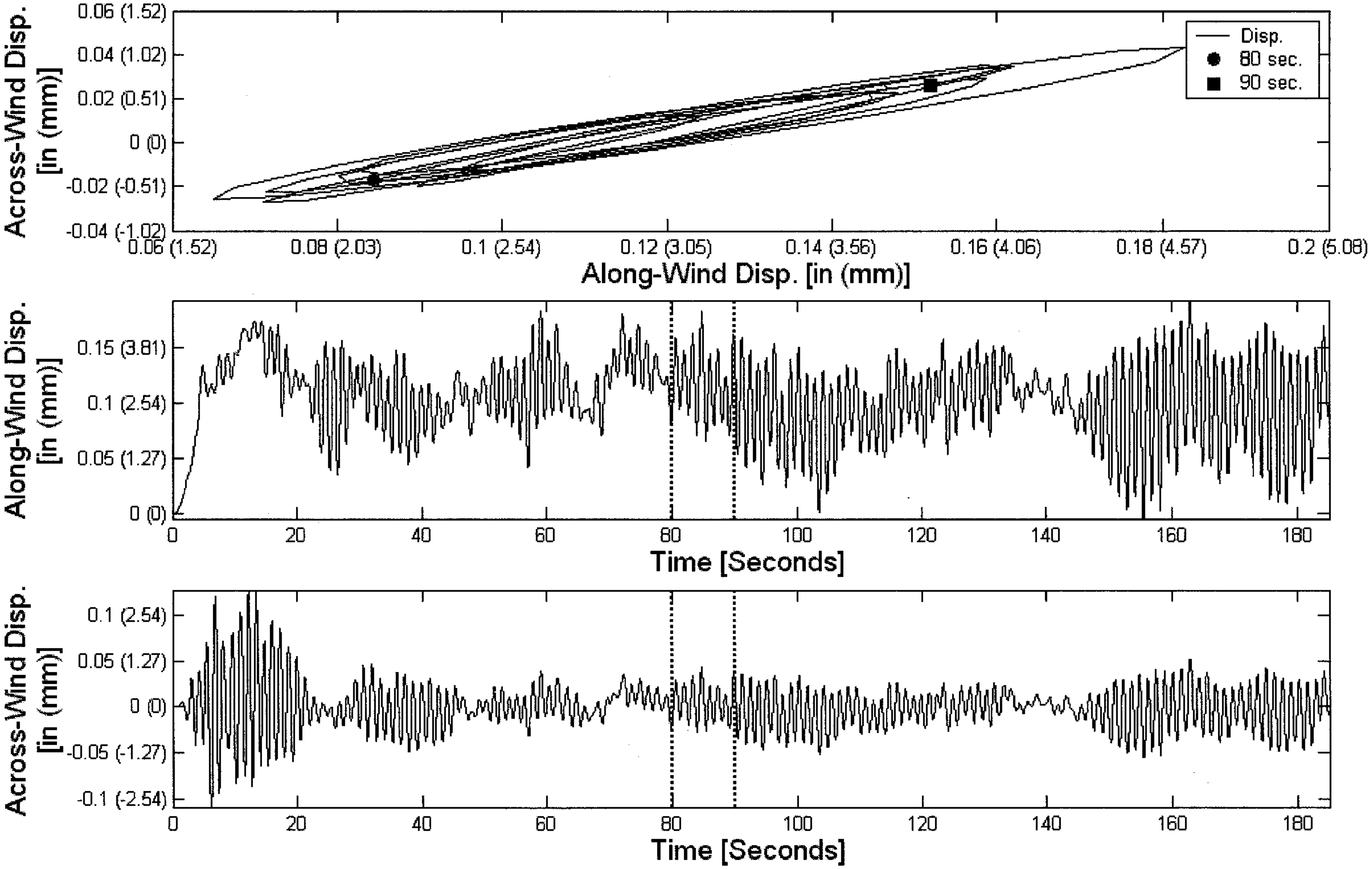

(a): Mean Wind Speed = 6 MPH (2.68 m/s)

Figure 7-2: Forced Vibration Vortex Shedding Response Time History of Analysis – Vertical Height = 100 ft (30.5 m)

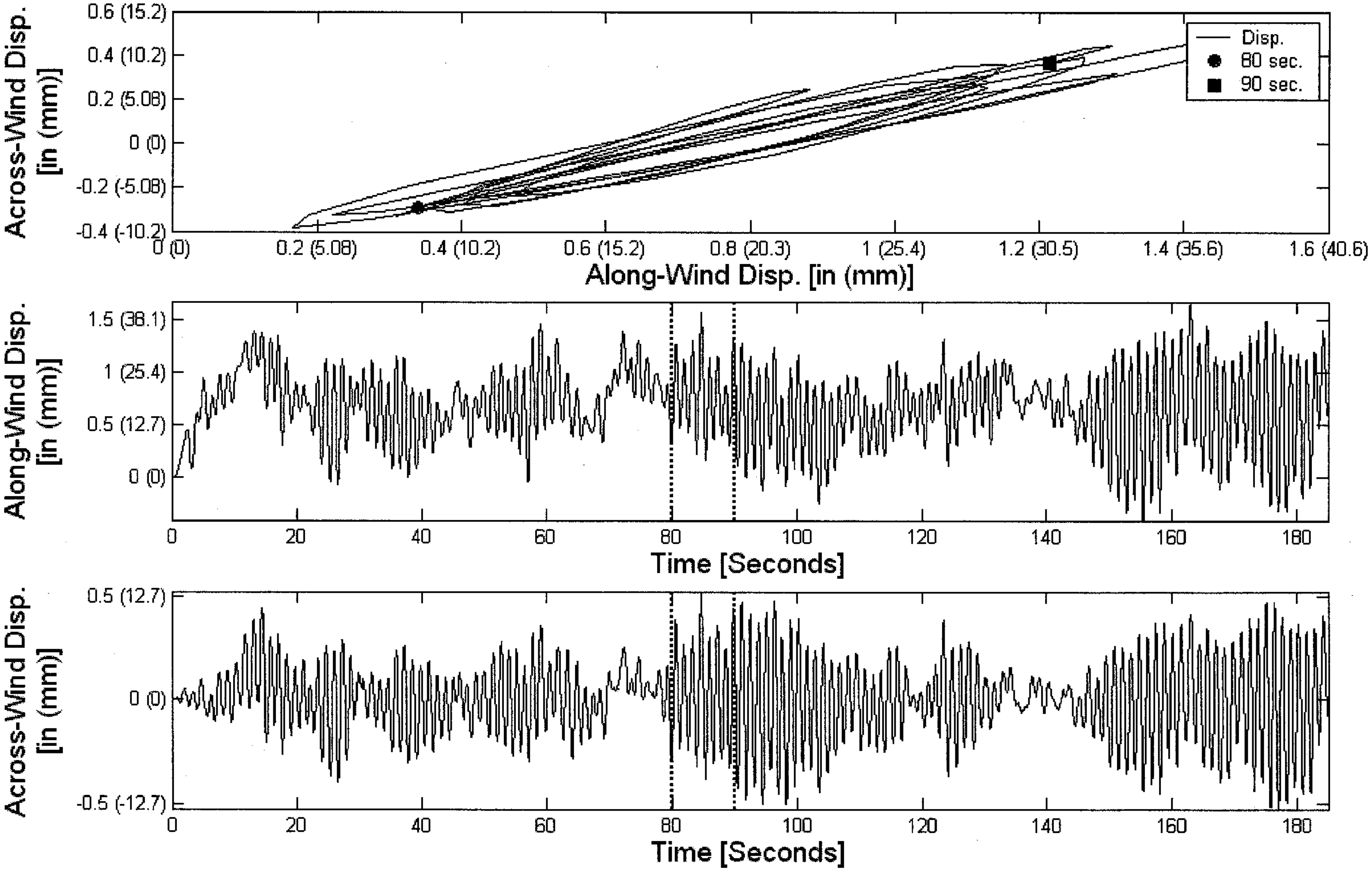

(b): Mean Wind Speed = 25 MPH (11.2 m/s)

Figure 7-2 (cont.): Forced Vibration Vortex Shedding Response Time History of Analysis – Vertical Height = 100 ft (30.5 m)

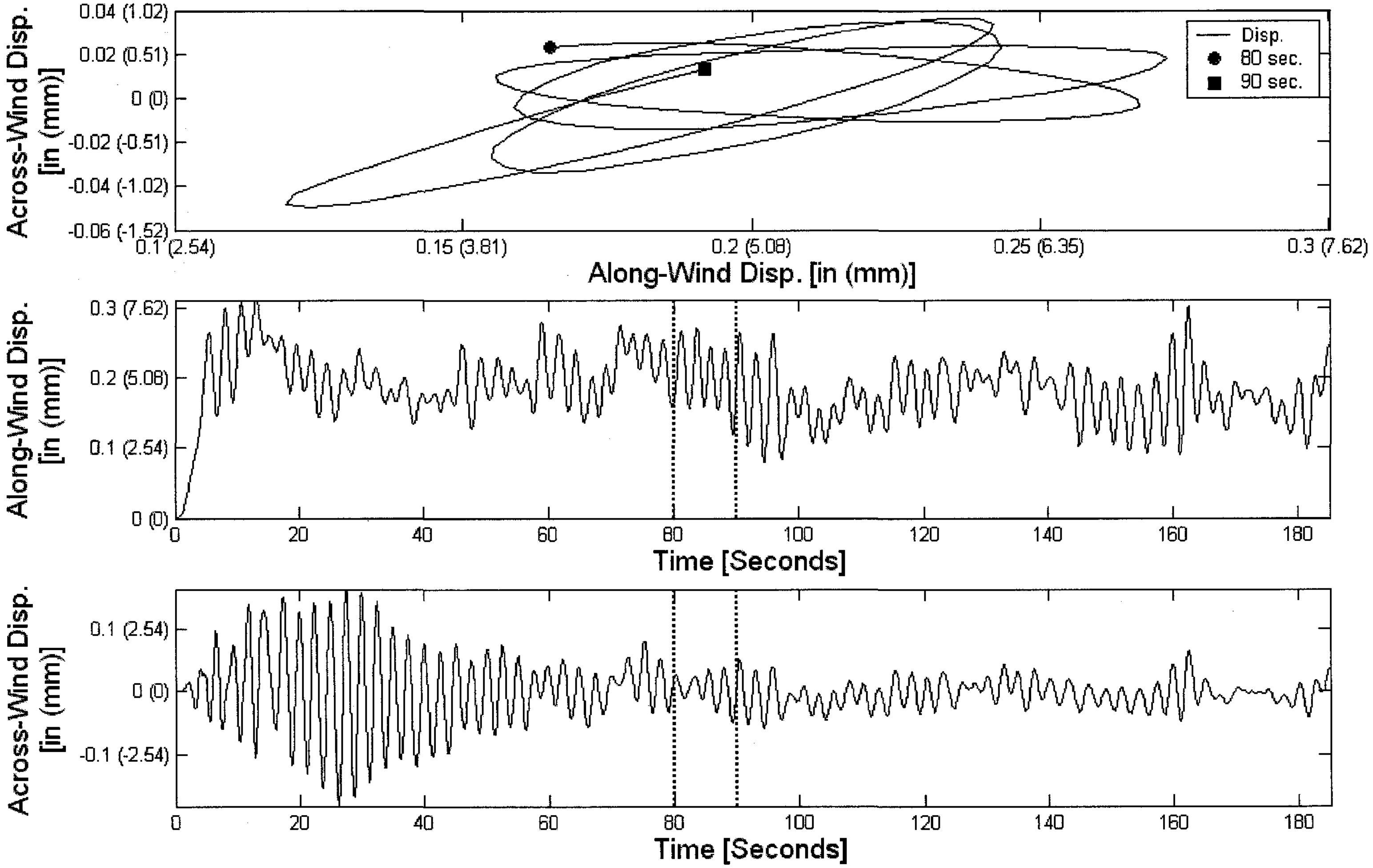

(a): Mean Wind Speed = 4 MPH (1.79 m/s)

Figure 7-3: Forced Vibration Vortex Shedding Response Time History of Analysis – Vertical Height = 140 ft (42.7 m)

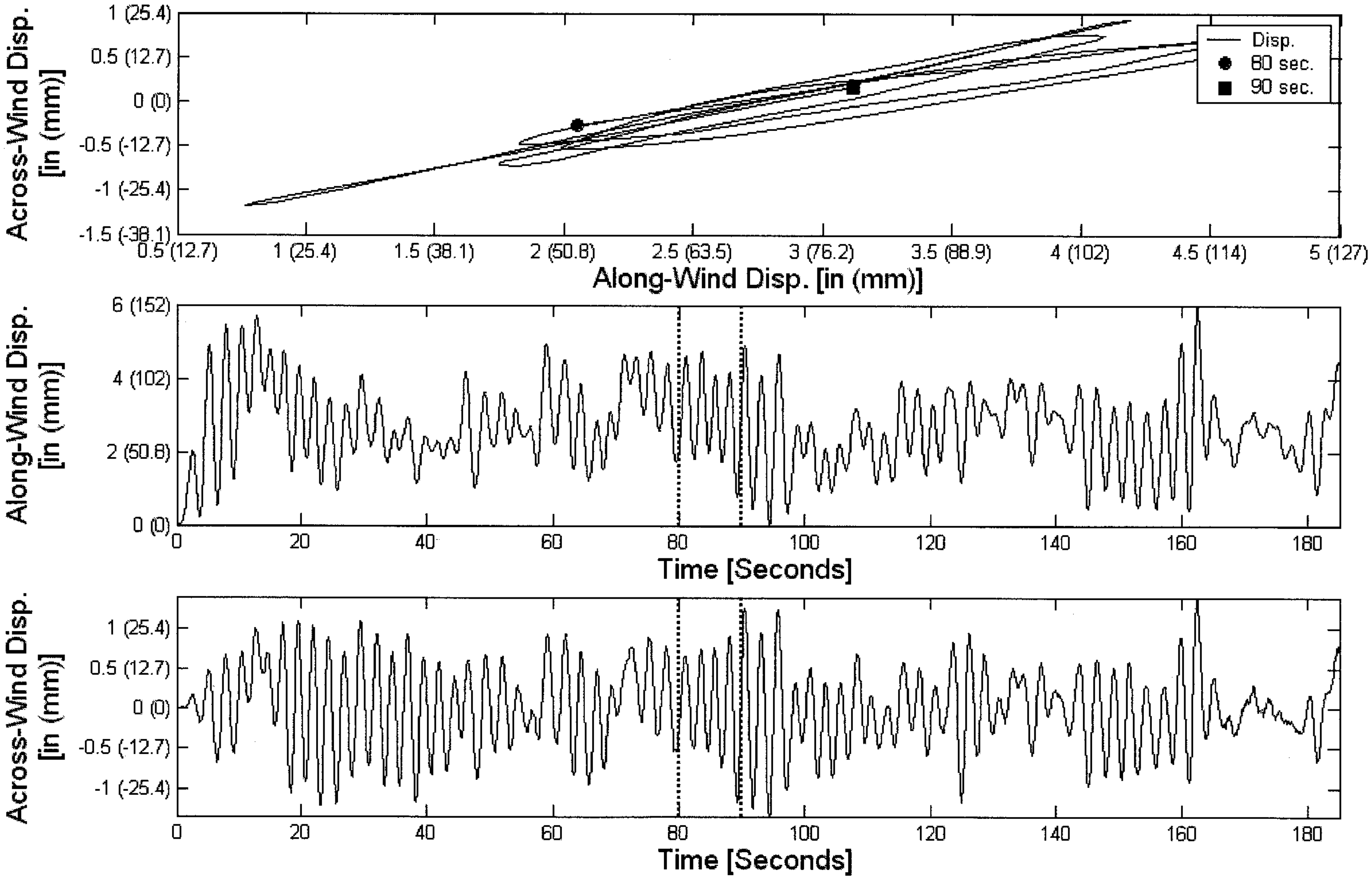

(b): Mean Wind Speed = 25 MPH (11.2 m/s)

Figure 7-3 (cont.): Forced Vibration Vortex Shedding Response Time History of Analysis – Vertical Height = 140 ft (42.7 m)

Based on the information presented in Figures 7-1 through 7-3, several important observations can be derived. First, the response of the 60 ft (18.3 m) structure appears to be much more erratic than the other two structures. This is particularly evident when considering the time interval between 80 and 90 seconds. The across-wind (lateral) response of the 60 ft (18.3 m) structure has a higher frequency component in comparison to the larger structures as expected.

The across-wind (lateral) response of all structures is relatively small in magnitude compared to the along-wind (longitudinal) response. However, the peaks of both displacements appear to act in unison. Thus, it can be reasoned that the effects of the forced vibration term of the vortex shedding model appear to have little effect on the across-wind (lateral) response. The response is particularly controlled by the across-wind (lateral) loading function as provided in Chapter Four. Thus, based on the conclusions of Simiu and Scanlan (1986) regarding the ability to neglect the forced vibration term appears to be a correct assumption. Analysis of the forced vibration resultant load will provide more evidence of the validity of this assumption.

Figures 7-4 through 7-6 provide an illustrative representation of the resulting time-domain dynamic analysis of the structure considered. Each figure provides the time history of the across-wind (lateral) displacement and the forced vibration loading term of the vortex shedding model for the top node of the structure. A two-dimensional plot of the movement of the top node between 80 and 90 seconds of the time history is also provided containing the same information from Figures 7-1 through 7-3. Dashed lines on the displacement and load time histories denote the starting and stopping points for 80 and 90 seconds, respectively. The analyses considered for Figure 7-4 through 7-6 are the same as those considered for Figures 7-1 through 7-3.

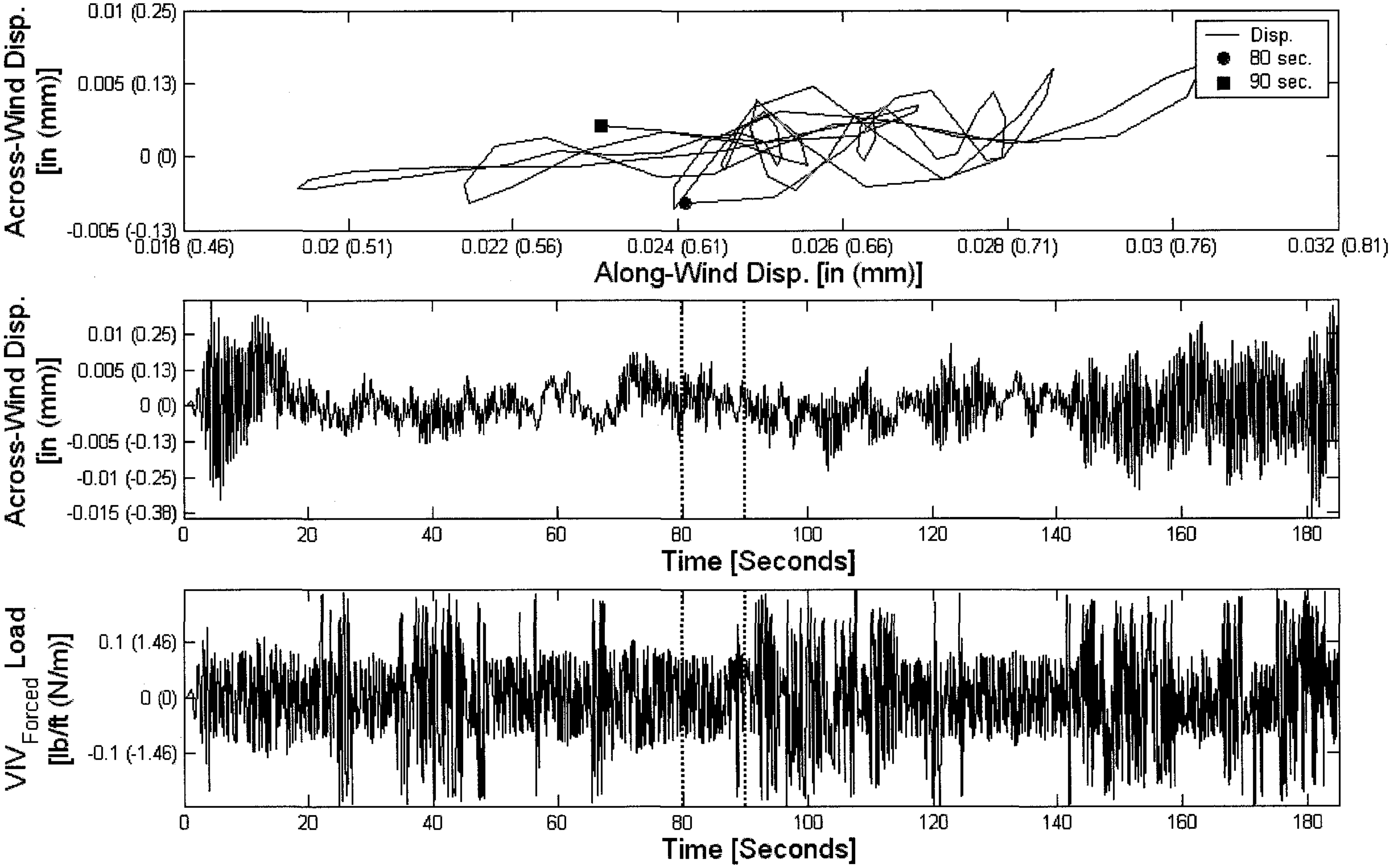

(a): Mean Wind Speed = 8 MPH (3.58 m/s)

Figure 7-4: Forced Vibration Vortex Shedding Load Time History of Analysis – Vertical Height = 60 ft (18.3 m)

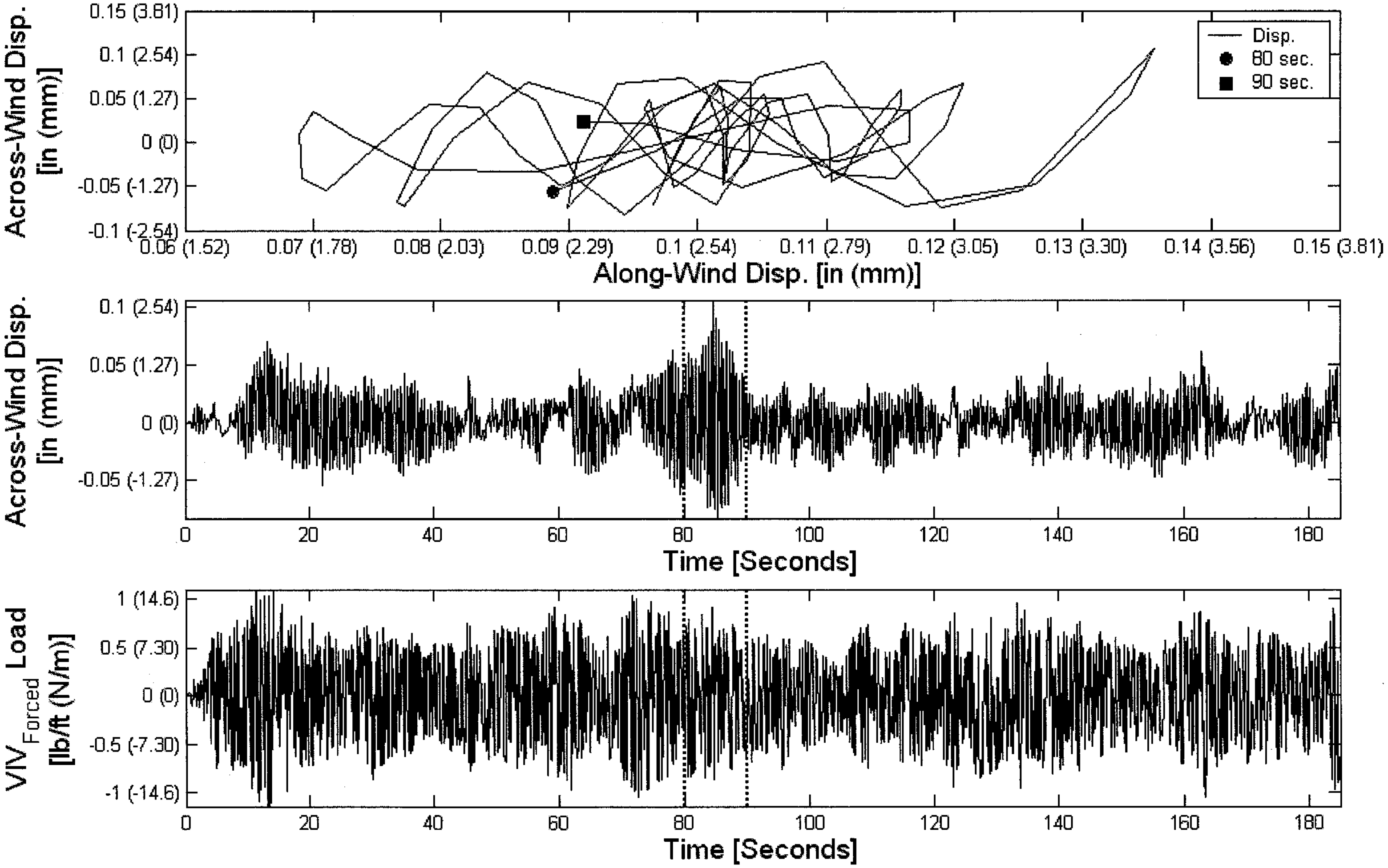

(b): Mean Wind Speed = 25 MPH (11.2 m/s)

Figure 7-4 (cont.): Forced Vibration Vortex Shedding Load Time History of Analysis – Vertical Height = 60 ft (18.3 m)

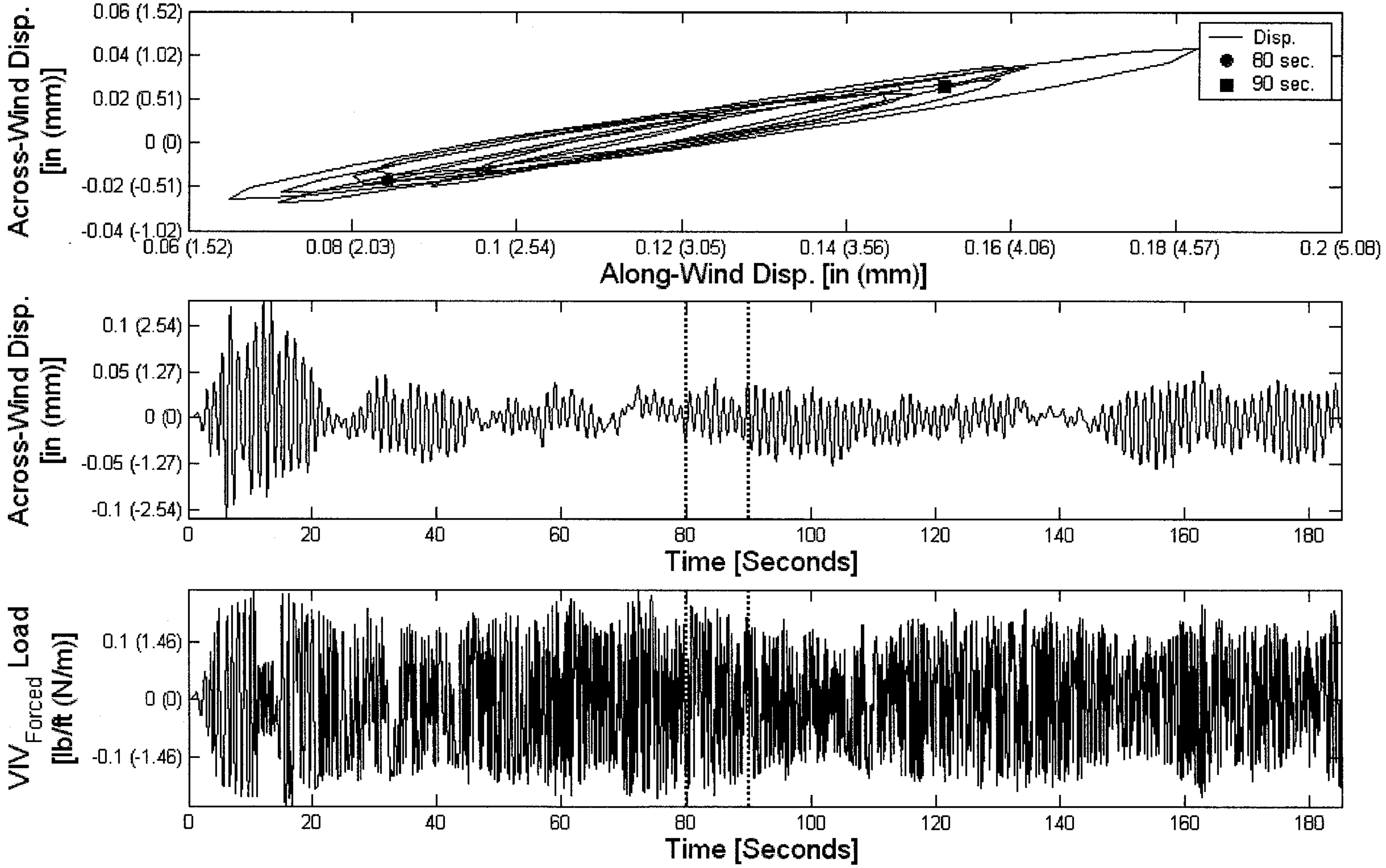

(a): Mean Wind Speed = 6 MPH (2.68 m/s)

Figure 7-5: Forced Vibration Vortex Shedding Load Time History of Analysis – Vertical Height = 100 ft (30.5 m)

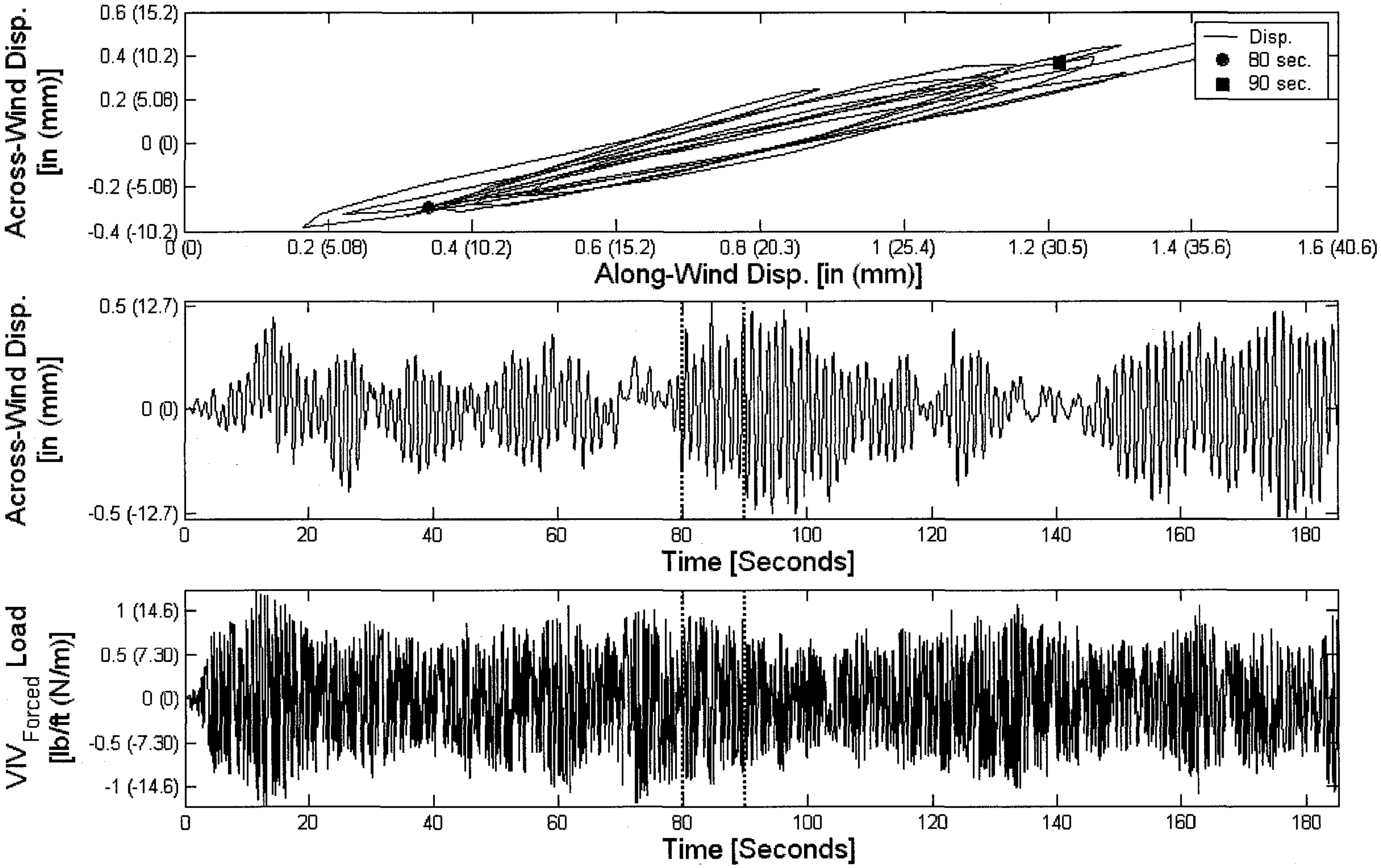

(b): Mean Wind Speed = 25 MPH (11.2 m/s)

Figure 7-5 (cont.): Forced Vibration Vortex Shedding Load Time History of Analysis – Vertical Height = 100 ft (30.5 m)

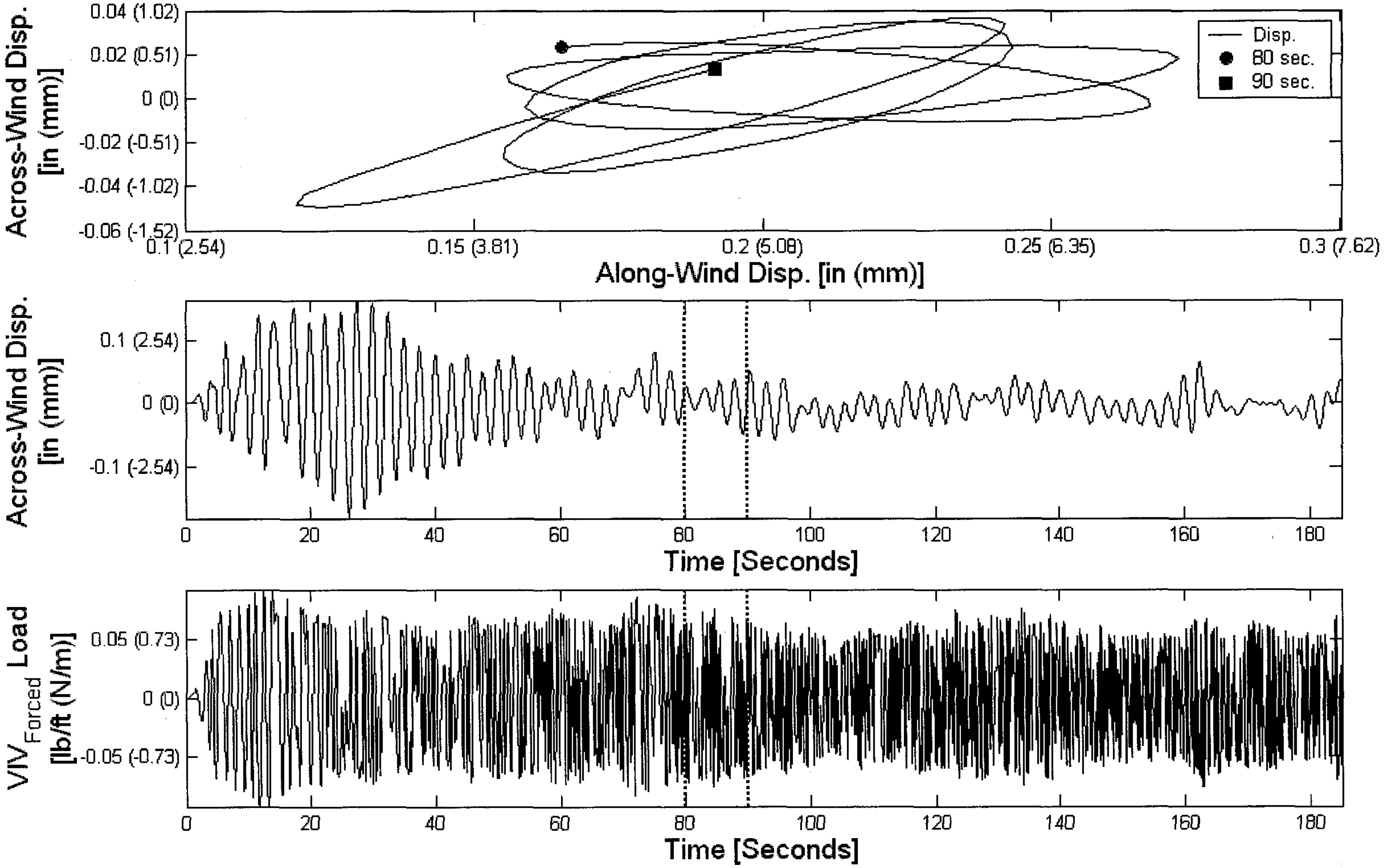

(a): Mean Wind Speed = 4 MPH (1.79 m/s)

Figure 7-6: Forced Vibration Vortex Shedding Load Time History of Analysis – Vertical Height =140 ft (42.7 m)

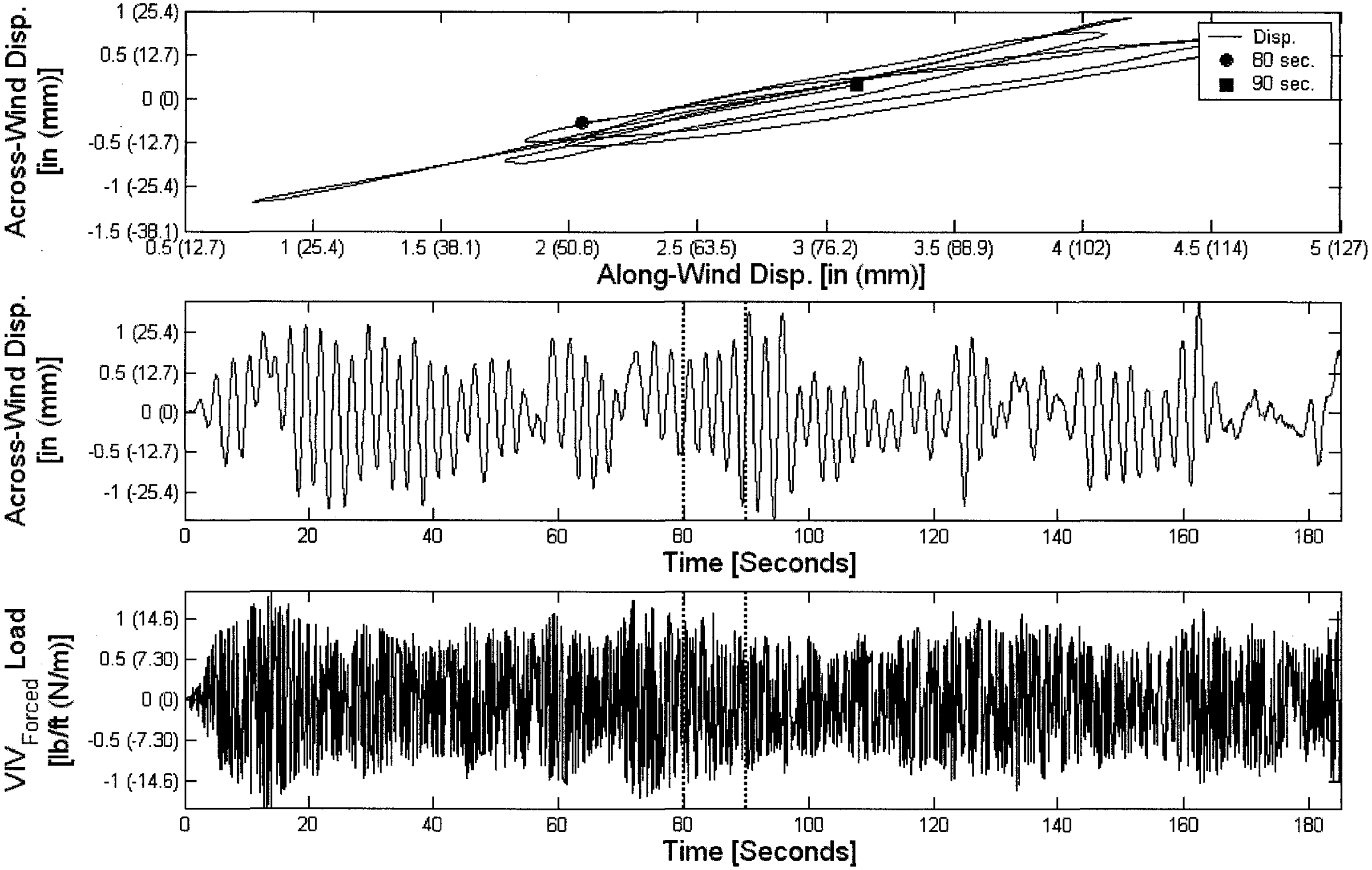

(b): Mean Wind Speed = 25 MPH (11.2 m/s)

Figure 7-6 (cont.): Forced Vibration Vortex Shedding Load Time History of Analysis – Vertical Height =140 ft (42.7 m)

Based on the information presented in Figures 7-4 through 7-6, several important observations can be noted. First, the forced vibration loading term of the vortex shedding model has a higher frequency component throughout the duration of the time history. However, the range of the loading term for the 100 ft (30.5 m) and 140 ft (42.7 m) structures appear more uniform throughout the time-domain for both relatively low and high mean wind speeds. The magnitude of the force vibration load on the 140 ft (42.7 m) structure at the top node is approximately half of the magnitude of the 100 ft (30.5 m) structure for relatively low wind speeds. Whereas, for relatively high wind speeds the magnitudes of the forced vibration loads are nearly equivalent. Finally, the 60 ft (18.3) structure appears to have a uniform range of approximately 0.1 lb/ft at the top node, but it also contains intermittent spikes in the forced vibration load for a mean wind speed of 8 MPH (3.58 m/s).

In regards to Simiu and Scanlan's (1986) conclusion about the ability to neglect the forced vibration term, this assumption appears to have a high degree of validity. Consider the resultant across-wind (lateral) load from the figures of Chapter Six for the three-dimensional study. These loads are substantially higher than the loads presented in Figures 7-4 through 7-6 due to the forced vibration term of the vortex shedding model. Thus, the effects of the forced vibration term are nearly negligible due to their relatively small load resultant magnitudes.

Figure 7-7 provides the maximum structure response in the across-wind (lateral) direction due to the inclusion of the forced vibration term of the vortex shedding model. The three spatial correlations assumed based on the exponential decay parameter C_z are provided. The same characteristics that were provided in Figures 7-1 through 7-3 and Figures 7-4 through 7-6 are again repeated for Figure 7-7.

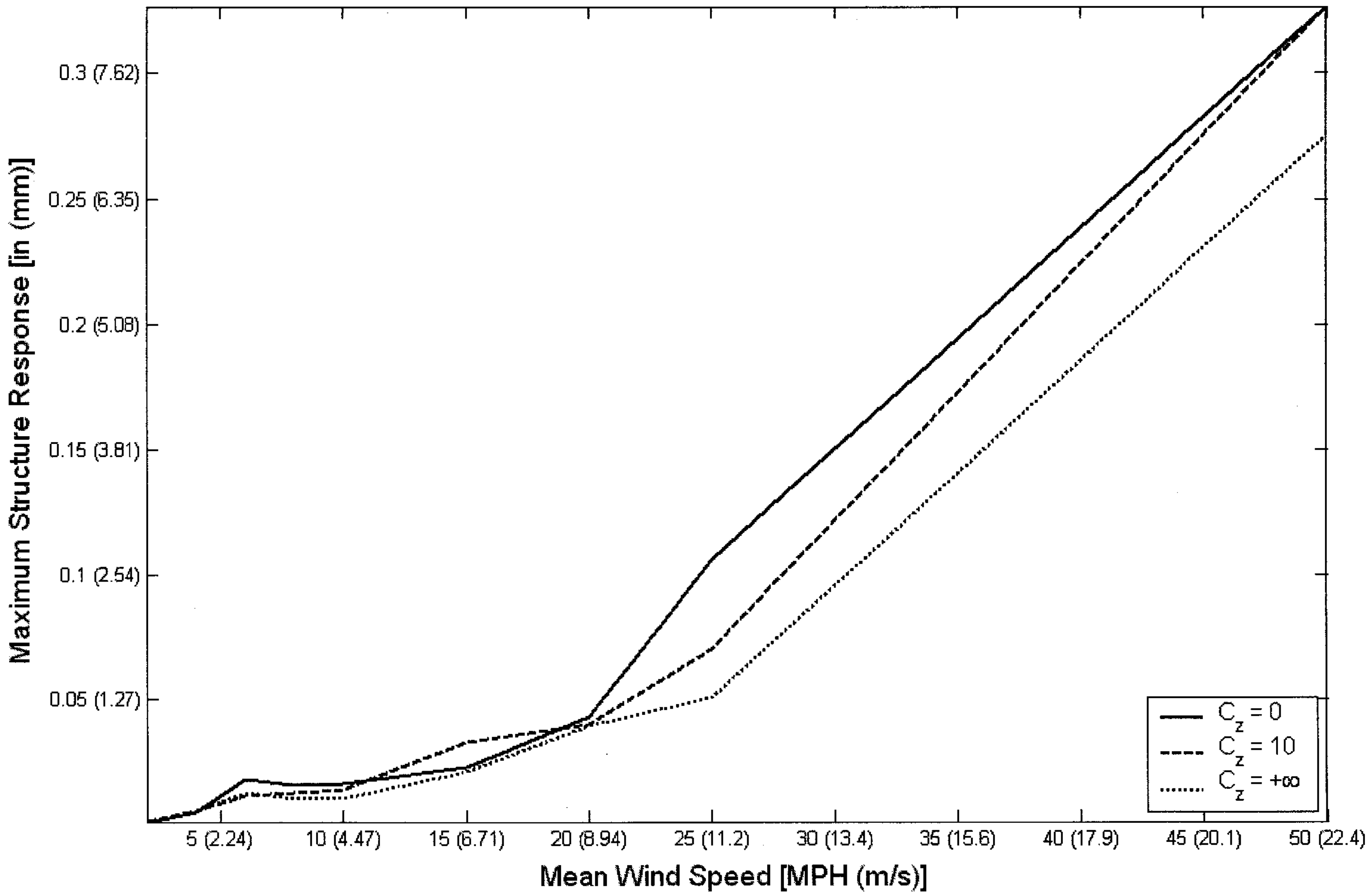

(a): Vertical Height = 60 ft (18.3 m)

Figure 7-7: Forced Vibration Vortex Shedding Maximum Structure Response

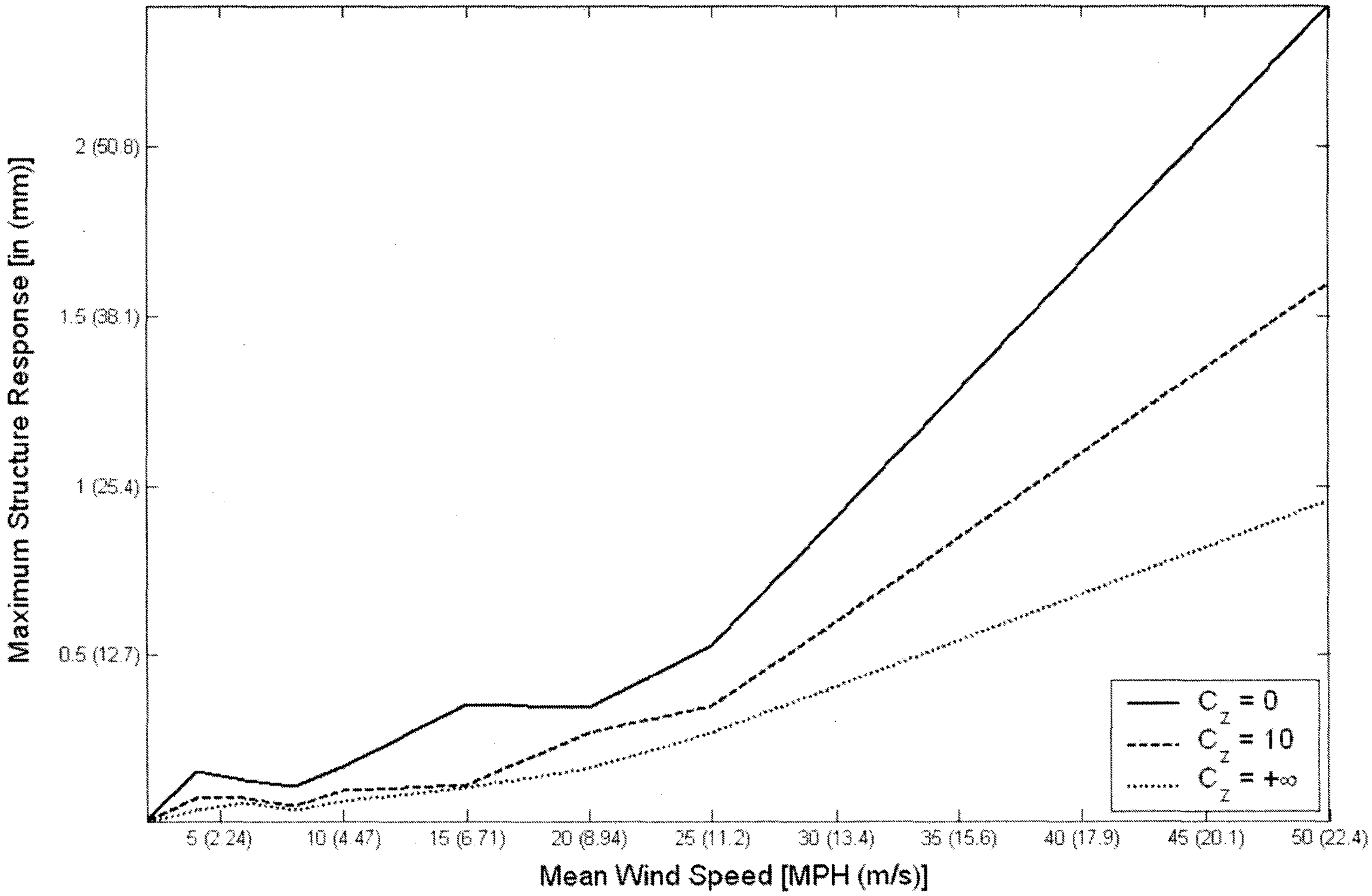

(b): Vertical Height = 100 ft (30.5 m)

Figure 7-7 (cont.): Forced Vibration Vortex Shedding Maximum Structure Response

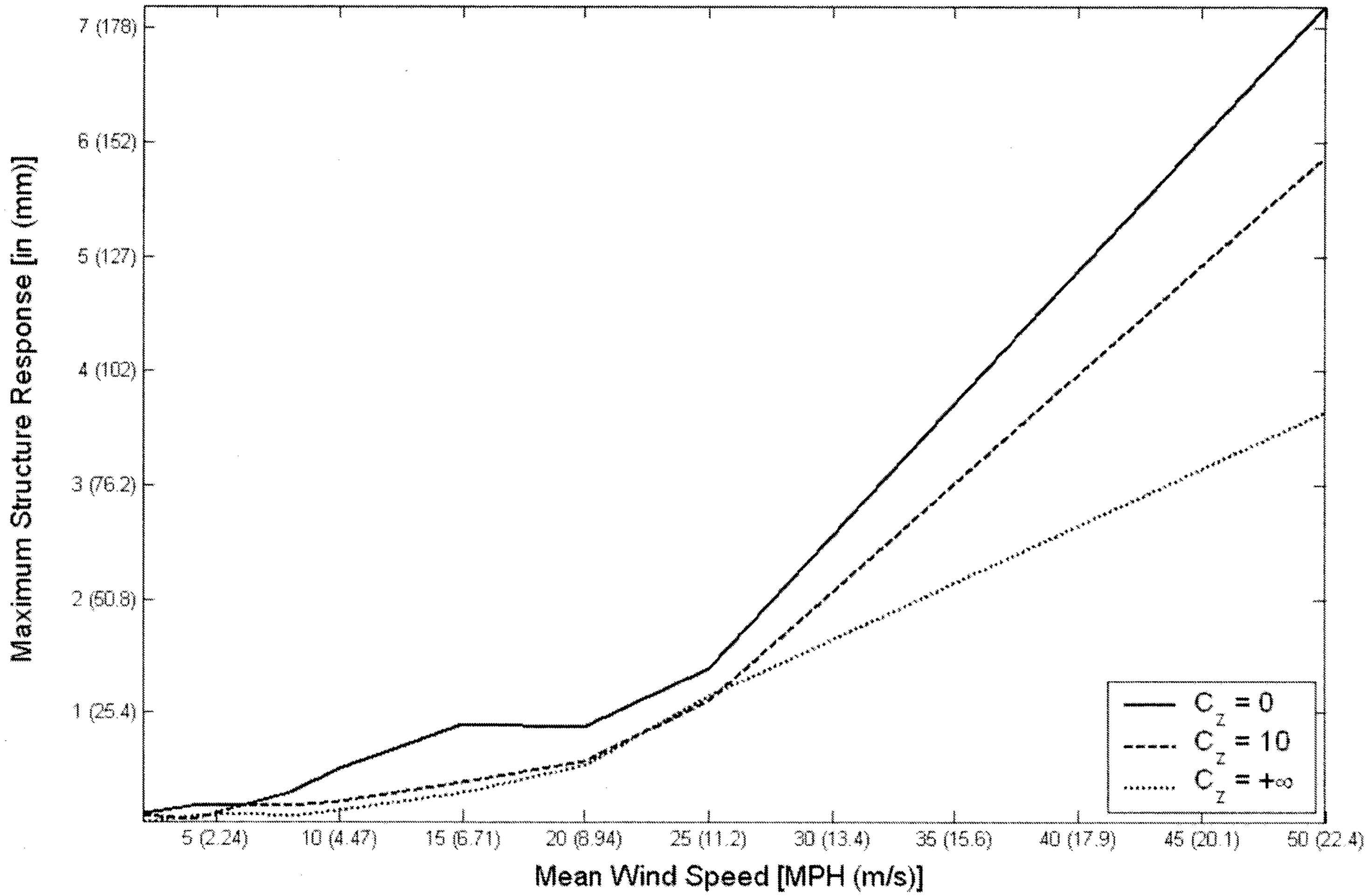

(c): Vertical Height = 140 ft (42.7 m)

Figure 7-7 (cont.): Forced Vibration Vortex Shedding Maximum Structure Response

For all structural height variations, at relatively high wind speeds the fully correlated wind flows consistently produce the largest structural response. At relatively lower wind speeds, depending on the structure height, the effects of the forced vibration term of the vortex shedding model are more clearly seen. At such wind speeds, the resultant across-wind (lateral) loading is not distinctly larger than the resultant loading due to the forced vibration term. Thus, jumps in the maximum response are seen at these lower wind speeds. Consider the 60 ft (18.3 m) structure as an example. For all three spatial correlation properties of the wind flow provided, there is a slight jump in the maximum structure response at a wind speed of 6 MPH (2.68 m/s). This phenomenon also occurs for the other structures at varying wind speeds as illustrated.

7.3 Aerodynamic Damping Results

The second numerical investigation of vortex shedding considers the complete vortex shedding model including both the forced vibration and aerodynamic damping terms of Equations (7-1) and (7-3), respectively. Hence, effects due to the aerodynamic damping term are considered in this second study. Because the forced vibration term does not have any empirical parameters that may be varied to determine its effects on the response of the structure, there are no changes to this term throughout all of the analyses of this study. The aerodynamic damping term, however, does contain an empirical parameter λ that will be considered to vary for this study.

Within Equation (7-3) the parameter λ defines the limiting displacement for the aerodynamic damping term. For the case when the across-wind (lateral) displacement equals or exceeds λD, the aerodynamic damping term vanishes such that the structure no longer experiences any aeroelastic effects (Simiu and Scanlan, 1986). Thus, Table 7-3 provides a summary of the changes to the parameter λ considered for the aerodynamic damping term. The example structure property variations of Table 7-1 and the wind flow property variations of Table 7-2 are also considered to vary for each of the variations listed in Table 7-3. Thus, including the seven variations in the parameter λ for the aerodynamic damping term and the 324 total variations of the example structural properties and wind flow properties, there are 2,268 separate analyses to determine the effects of the complete vortex shedding model for this study.

Property	Value
Limiting Displacement Parameter, λ	0.01, 0.5, 1.0, 1.5, 2.0, 5.0, 10.0

Table 7-3: Variations in Aerodynamic Damping Properties for Vortex Shedding

Results of Analysis

The results of the aerodynamic damping study are presented and discussed using two primary components similar to the forced vibration study. First, the response of the structure considering both the forced vibration and aerodynamic damping terms of the vortex shedding model is investigated. Within this investigation, complete time-domain examples of the along-wind (longitudinal) and across-wind (lateral) responses are presented graphically. Only a few examples are presented, but these offer a representative description of other analyses conducted for this study. The second component consists of an investigation of the vortex shedding load due to both the forced vibration and aerodynamic damping terms. As for the response, graphical results are used for investigation of the vortex shedding loading. Again, supplemental maximum structure response data generated are also presented.

Figures 7-8 through 7-10 provide an illustrative representation of the resulting time-domain dynamic analysis of the structure considered. Each figure provides the time-history of the along- and across-wind displacements for the top node of the structure. A two-dimensional plot of the movement of the top node between 80 and 90 seconds of the time history is also provided. Figure 7-8 considers a structure having a vertical height of 60 ft (18.3 m) and mean wind speeds at 32.8 ft (10 m) of 8 MPH (3.58 m/s) and 25 MPH (11.2 m/s) for sub-figures (a) and (b), respectively. Figure 7-9 considers a structure having a vertical height of 100 ft (30.5 m) and mean wind speeds of 6 MPH (2.68 m/s) and 25 MPH (11.2 m/s). Finally, Figure 7-10 considers a 140 ft (42.7 m) structure with mean wind speeds of 4 MPH (1.78 m/s) and 25 MPH (11.2 m/s). Each figure considered has the same cross-section parameters, outside diameter of 2.5 ft (762 mm) and wall thickness of ¼ in (6.35 mm), full spatial correlation (C_z = 0) of the three-dimensional wind flow, and limiting displacement parameter λ = 1.0 for the aerodynamic damping term. With the exception of the aerodynamic damping term, these are the same variations as presented in Figures 7-1 through 7-3 for the forced vibration study. More variations in mean wind speed, structure properties, spatial correlation, and limiting displacement parameter were considered as given in Tables 7-1, 7-2, and 7-3, but are not fully provided by Figures 7-8 through 7-10 in the interest of brevity.

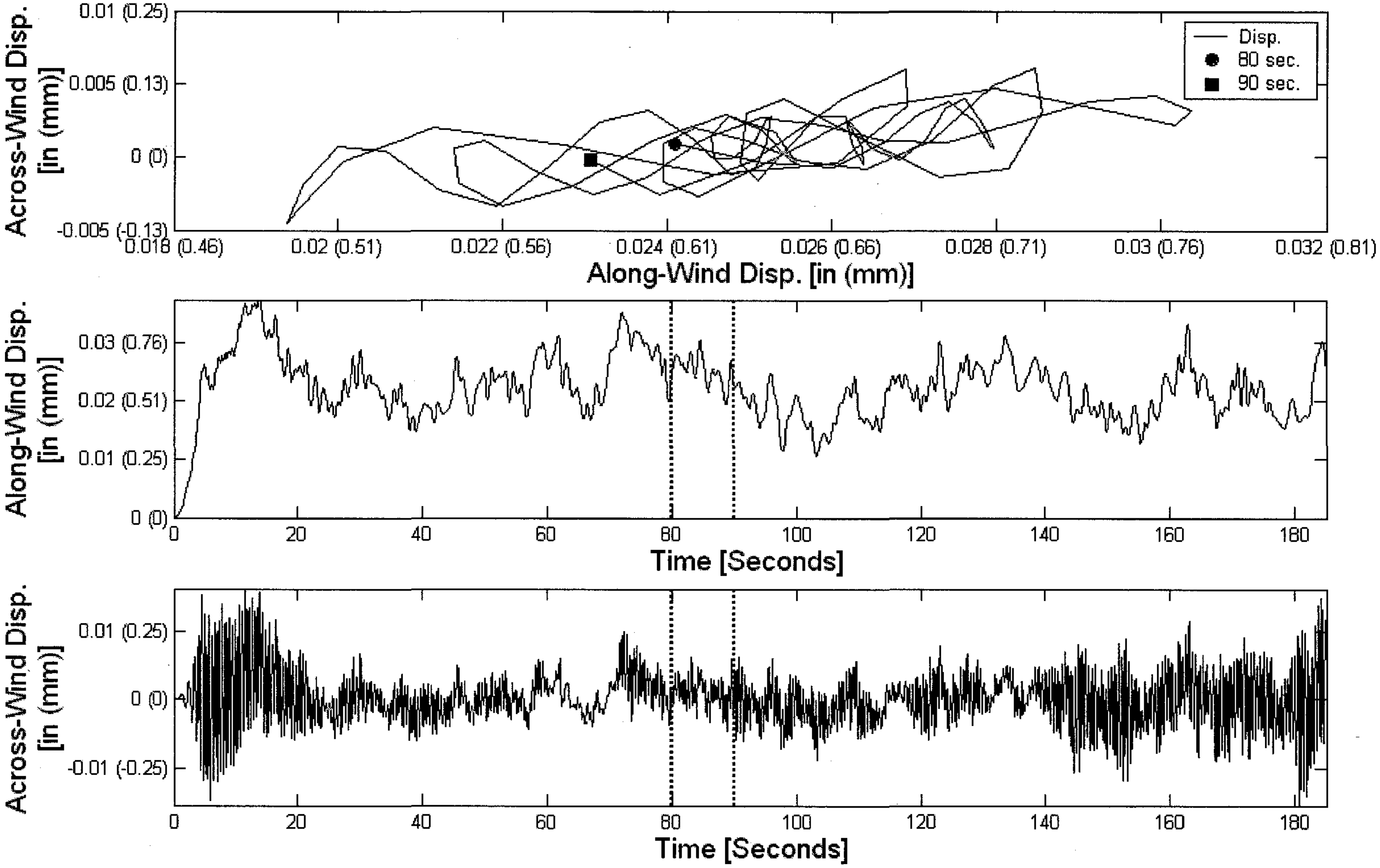

(a): Mean Wind Speed = 8 MPH (3.58 m/s)

Figure 7-8: Aerodynamic Damping Vortex Shedding Response Time History of Analysis – Vertical Height = 60 ft (18.3 m)

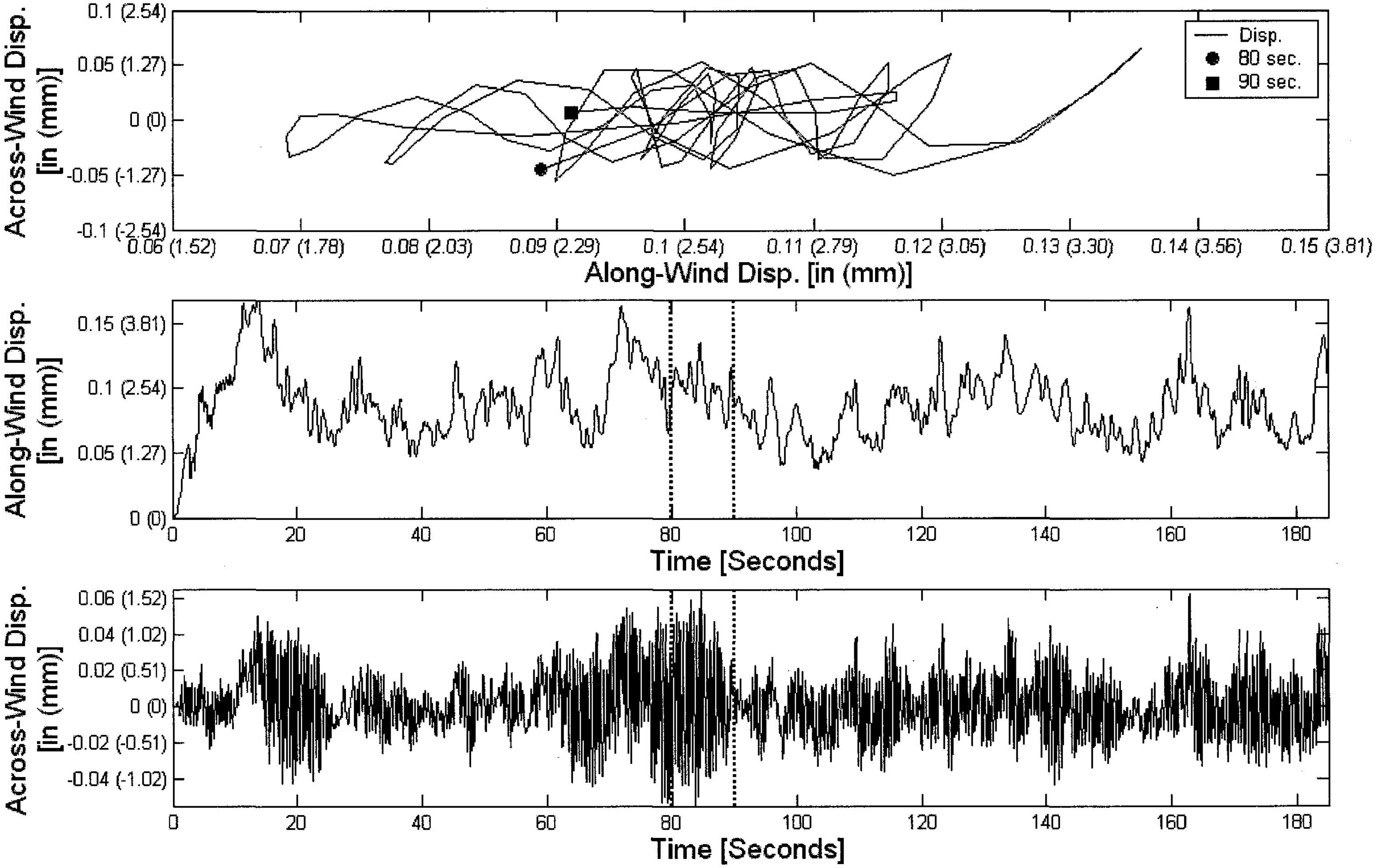

(b): Mean Wind Speed = 25 MPH (11.2 m/s)

Figure 7-8 (cont.): Aerodynamic Damping Vortex Shedding Response Time History of Analysis – Vertical Height = 60 ft (18.3 m)

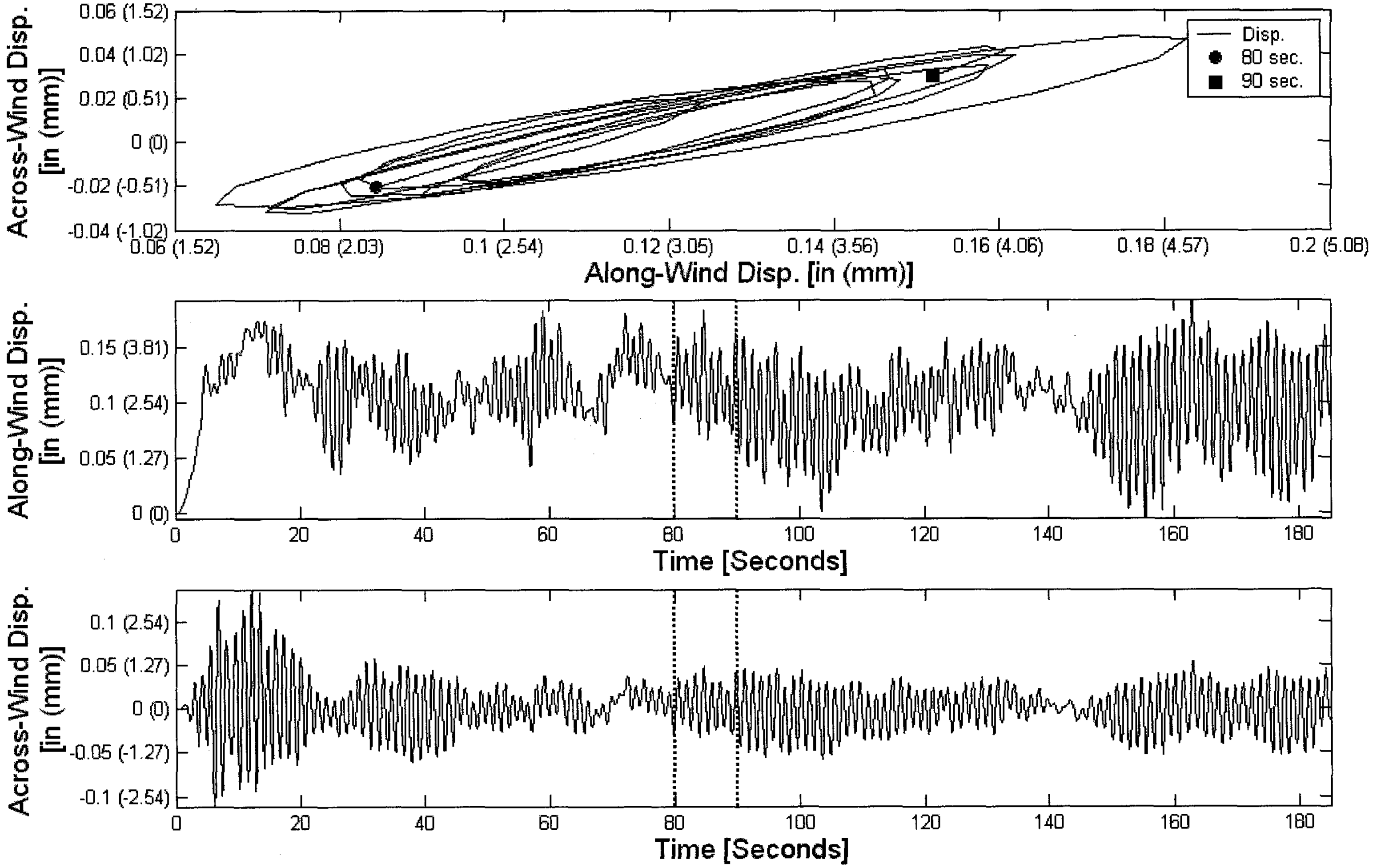

(a): Mean Wind Speed = 6 MPH (2.68 m/s)

Figure 7-9: Aerodynamic Damping Vortex Shedding Response Time History of Analysis – Vertical Height = 100 ft (30.5 m)

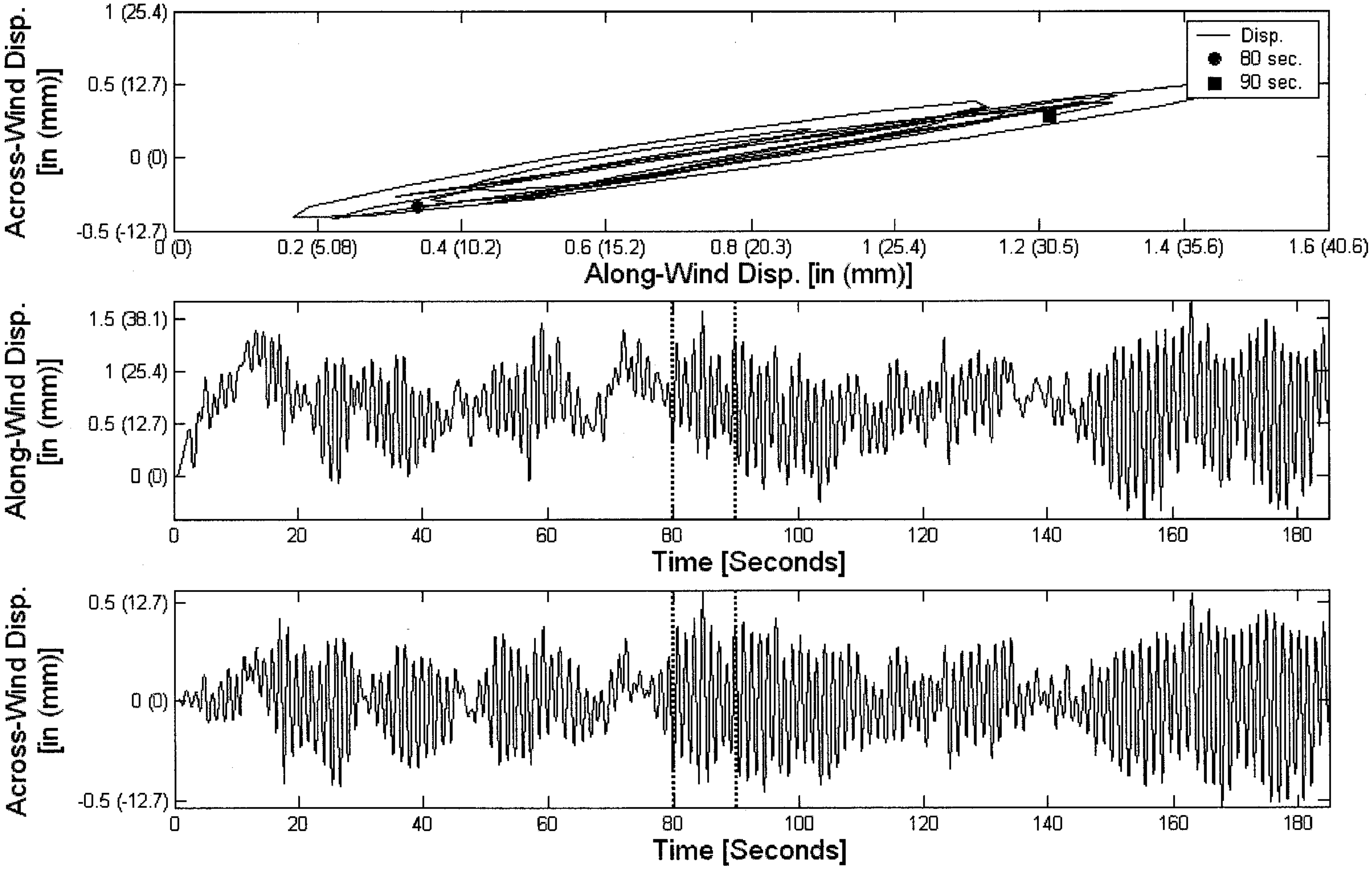

(b): Mean Wind Speed = 25 MPH (11.2 m/s)

Figure 7-9 (cont.): Aerodynamic Damping Vortex Shedding Response Time History of Analysis – Vertical Height = 100 ft (30.5 m)

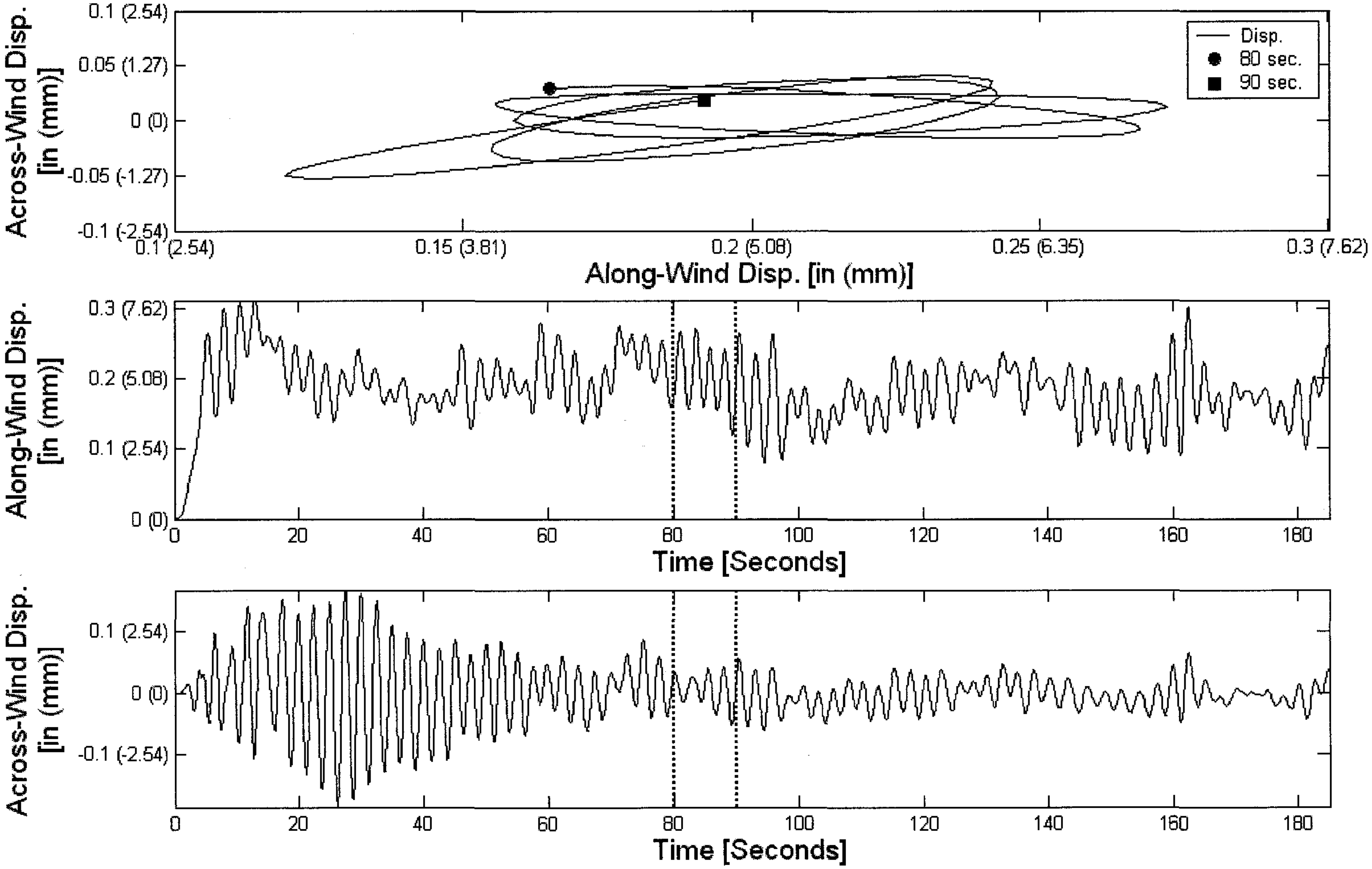

(a): Mean Wind Speed = 4 MPH (1.79 m/s)

Figure 7-10: Aerodynamic Damping Vortex Shedding Response Time History of Analysis – Vertical Height = 140 ft (42.7 m)

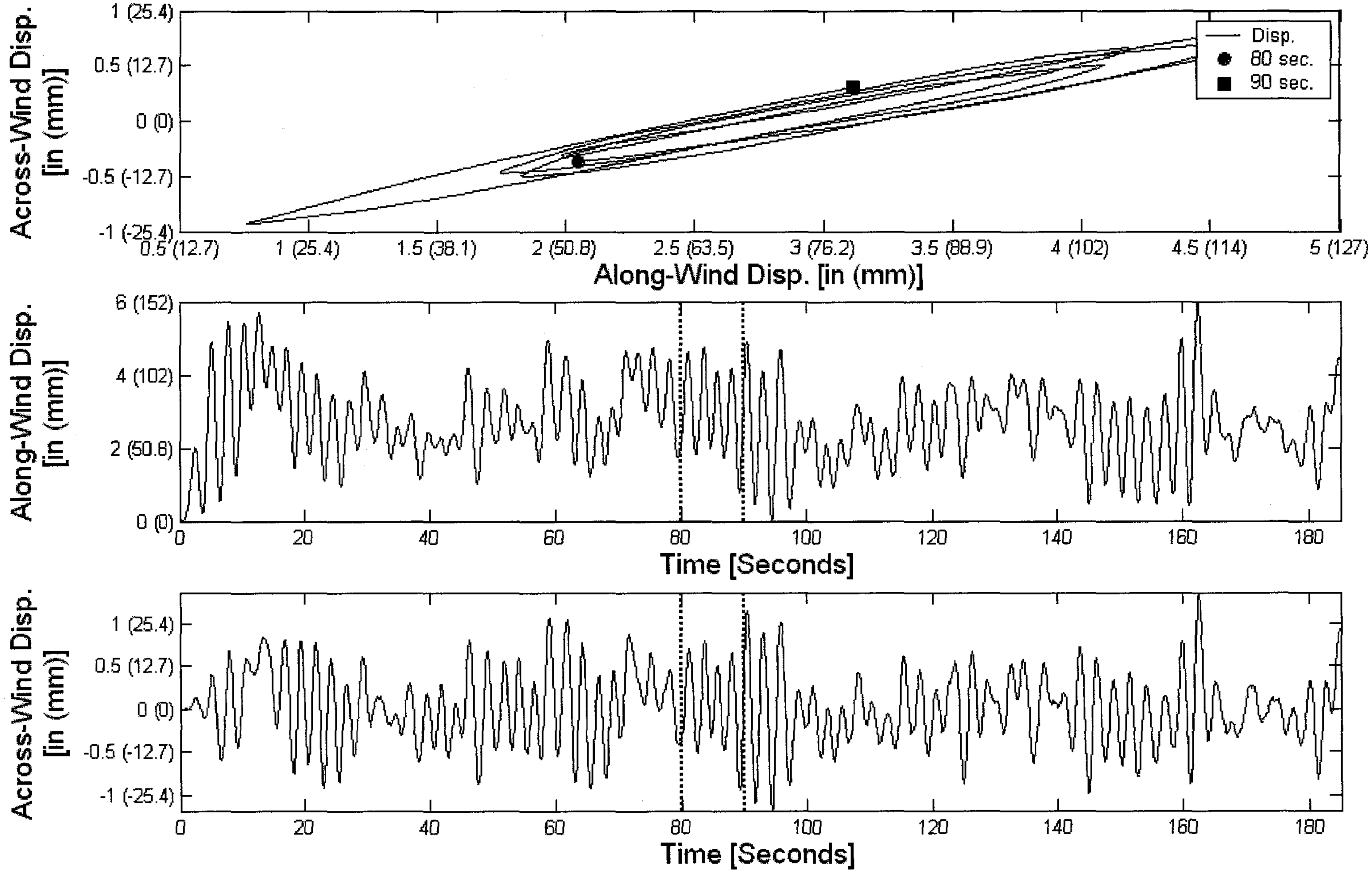

(b): Mean Wind Speed = 25 MPH (11.2 m/s)

Figure 7-10 (cont.): Aerodynamic Damping Vortex Shedding Response Time History of Analysis – Vertical Height = 140 ft (42.7 m)

As was seen in Figure 7-1, the response of the 60 ft (18.3) structure in Figure 7-8 appears to be much more erratic than the other two structures. In comparing the forced vibration only figures from Figures 7-1 through 7-3 where all parameters are the same except for the inclusion of the aerodynamic damping term in Figures 7-8 through 7-10, a few interesting observations may be made. For the 60 ft (18.3 m) structure, the across-wind (lateral) response slightly increases with the aerodynamic damping term. This increase is particularly seen in an increase in the peaks of the across-wind (lateral) response time history. The comparison of the 100 ft (30.5 m) and 140 ft (42.7 m) structures show negligible changes in the response characteristics when the aerodynamic damping term is included in the vortex shedding model. This can be primarily attributed to the displacement of the top node exceeding λD thus forcing the aerodynamic damping term to zero.

As was seen for the forced vibration study, inclusion of both the aerodynamic damping and forced vibration terms in the vortex shedding model appears to have little effect on the response of the structure at this point. Again, notice the peaks of the along-wind (longitudinal) and across-wind (lateral) displacements acting in near unison with each other. This again indicates that the across-wind (lateral) forcing function is primarily responsible for the response. This is particularly valid for the higher mean wind speeds illustrated in Figures 7-8 through 7-10.

Figures 7-11 through 7-13 provide an illustrative representation of the resulting time-domain analysis of the structure considered. Each figure provides the time-history of the across-wind (lateral) displacements and the forced vibration and aerodynamic damping loading terms of the vortex shedding model for the top node of the structure. A two-dimensional plot of the movement of the top node between 80 and 90 seconds of the time history is also provided containing the same information from Figures 7-8 through 7-10. The analyses considered for Figures 7-11 through 7-13 are the same as those considered for Figures 7-8 through 7-10. These analyses are also the same as those considered for Figures 7-4 through 7-6 with the exception of the aerodynamic damping term.

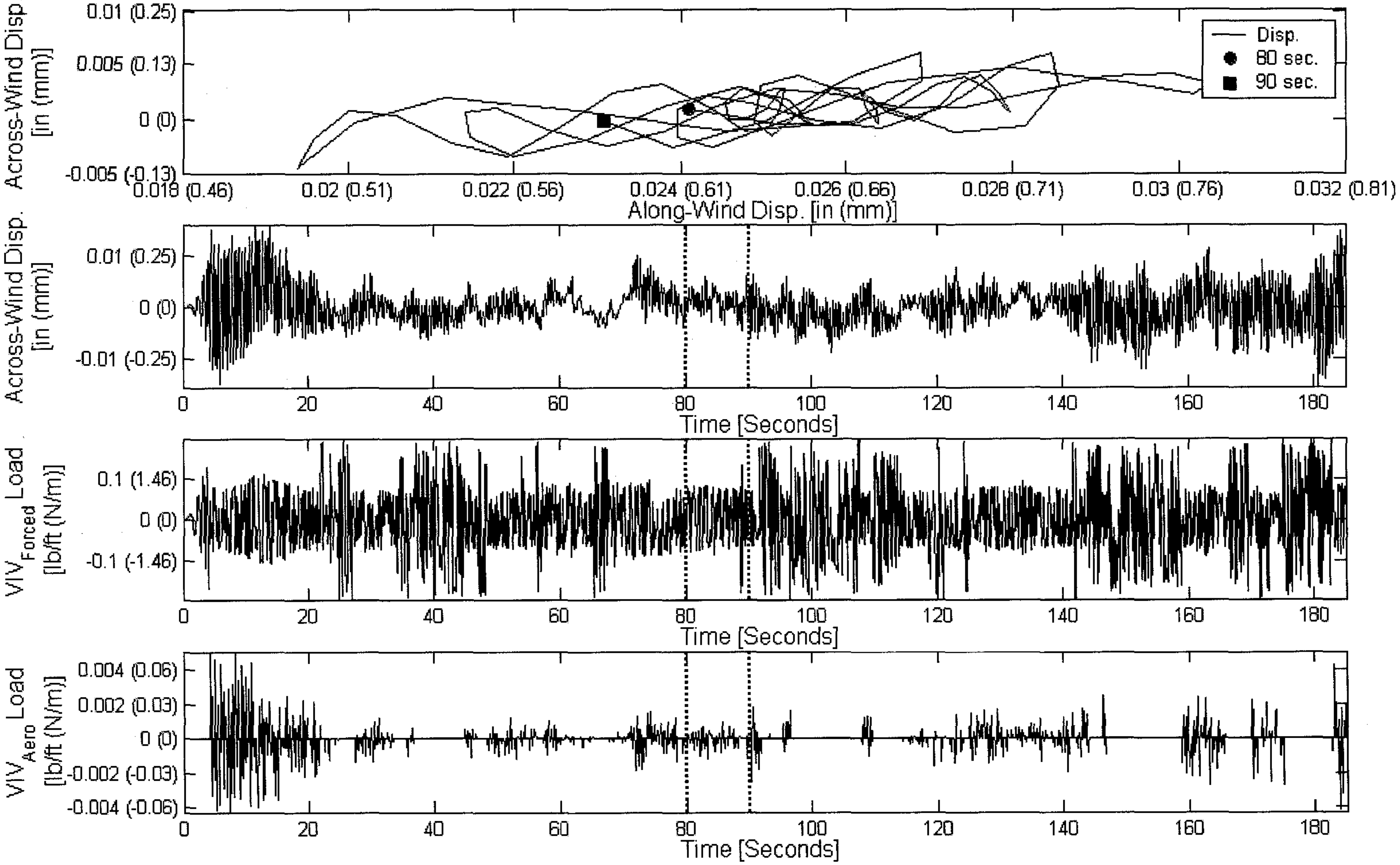

(a): Mean Wind Speed = 8 MPH (3.58 m/s)

Figure 7-11: Aerodynamic Damping Vortex Shedding Load Time History of Analysis – Vertical Height = 60 ft (18.3 m)

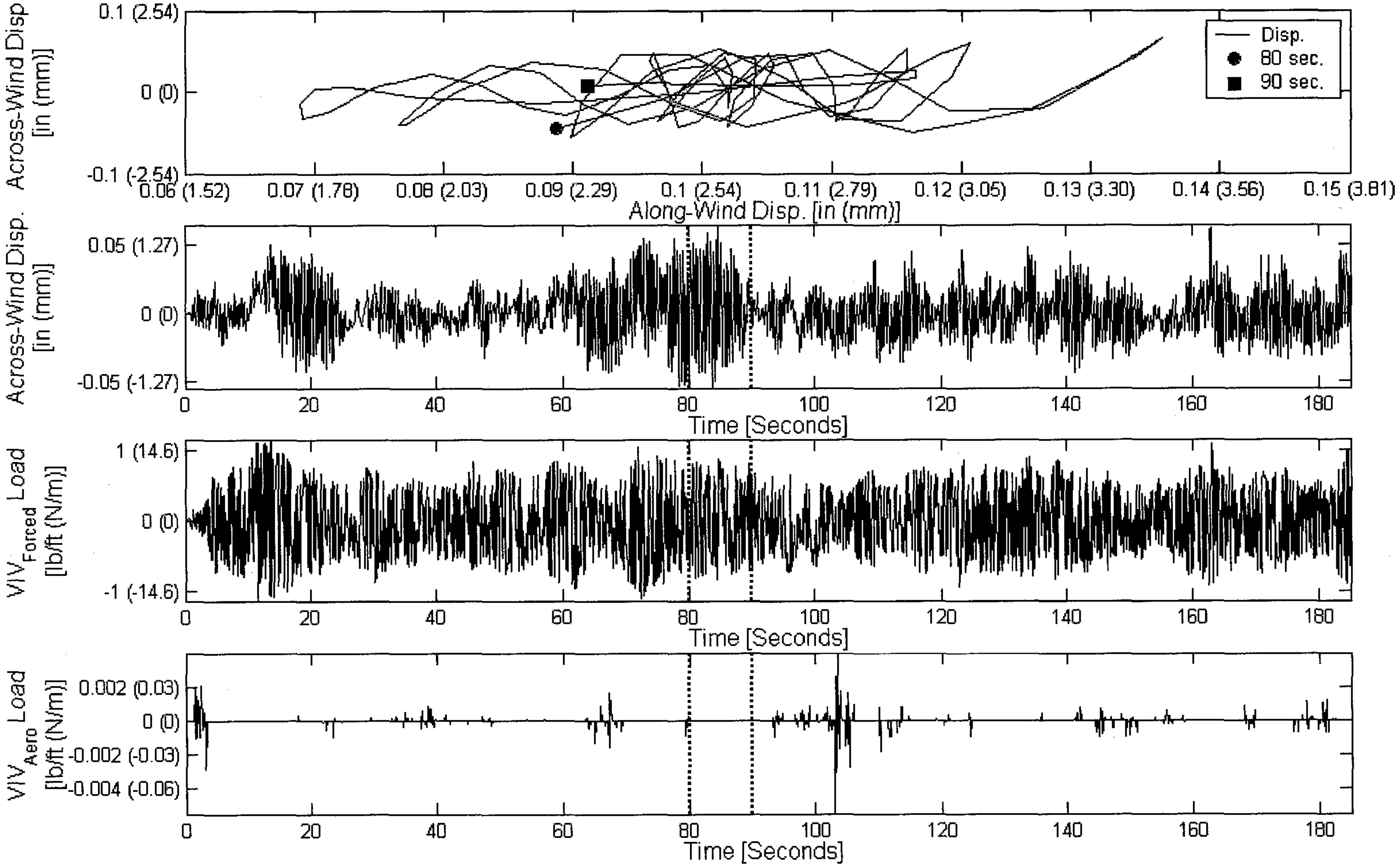

(b): Mean Wind Speed = 25 MPH (11.2 m/s)

Figure 7-11 (cont.): Aerodynamic Damping Vortex Shedding Load Time History of Analysis – Vertical Height = 60 ft (18.3 m)

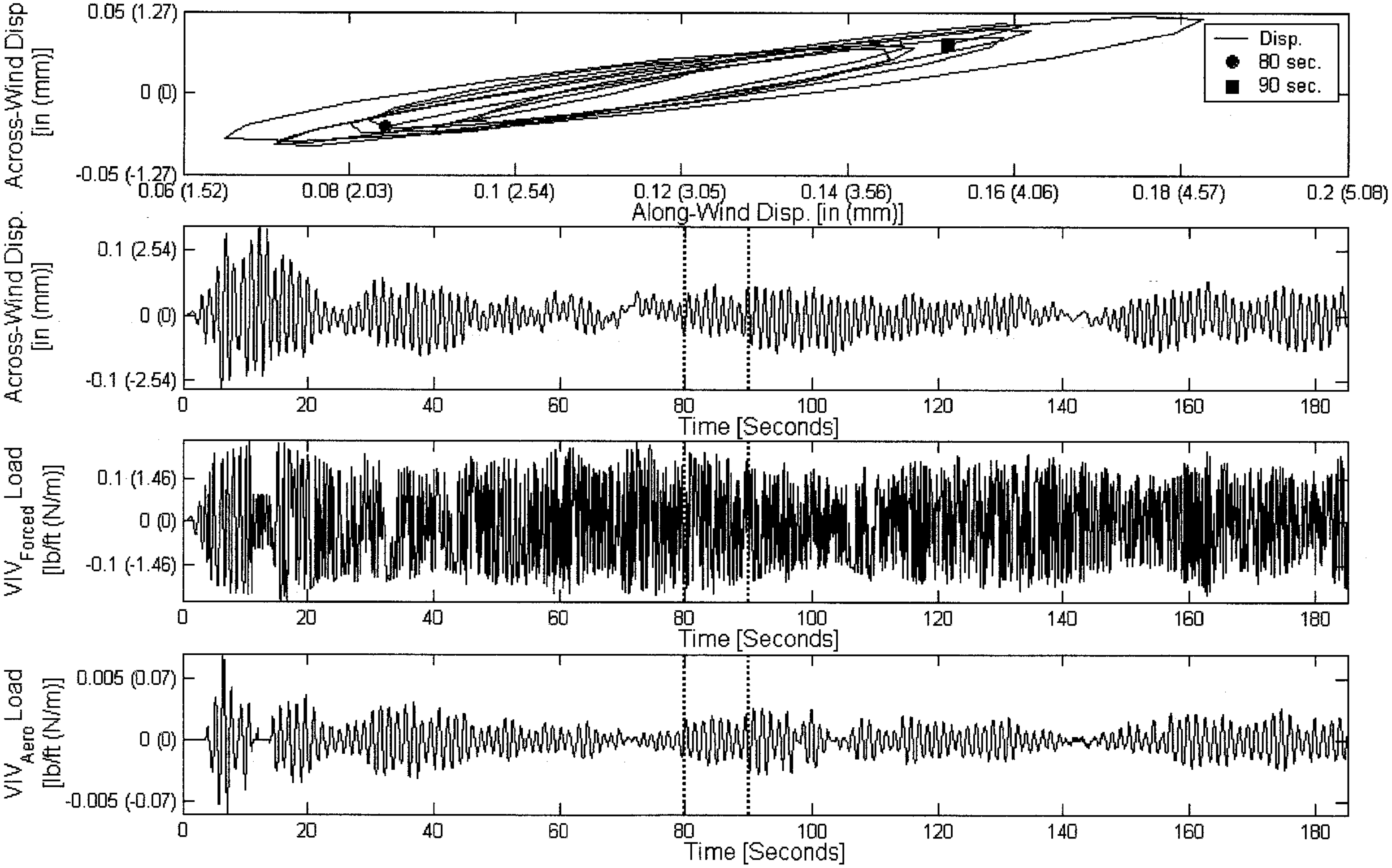

(a): Mean Wind Speed = 6 MPH (2.68 m/s)

Figure 7-12: Aerodynamic Damping Vortex Shedding Load Time History of Analysis – Vertical Height = 100 ft (30.5 m)

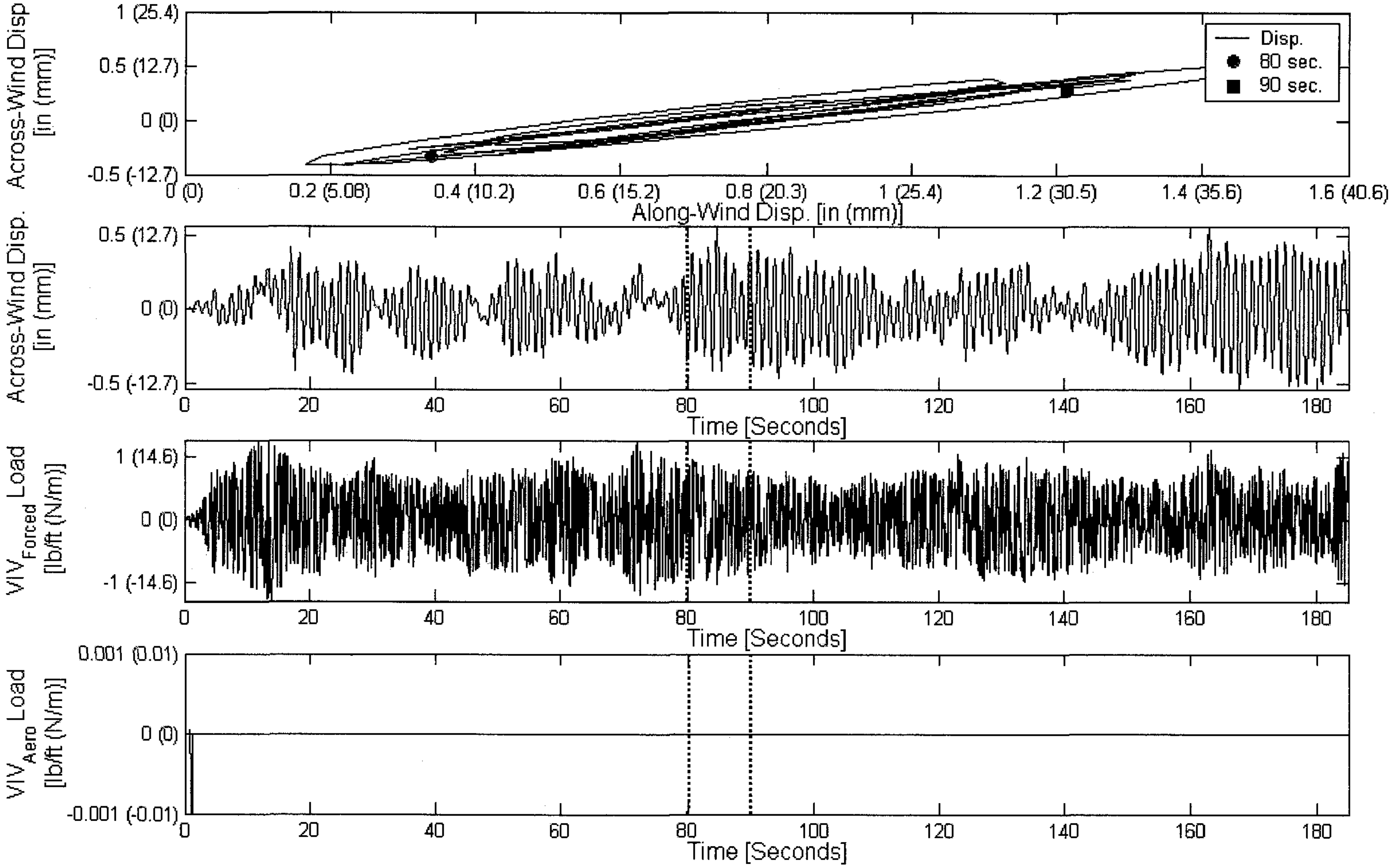

(b): Mean Wind Speed = 25 MPH (11.2 m/s)

Figure 7-12 (cont.): Aerodynamic Damping Vortex Shedding Load Time History of Analysis – Vertical Height = 100 ft (30.5 m)

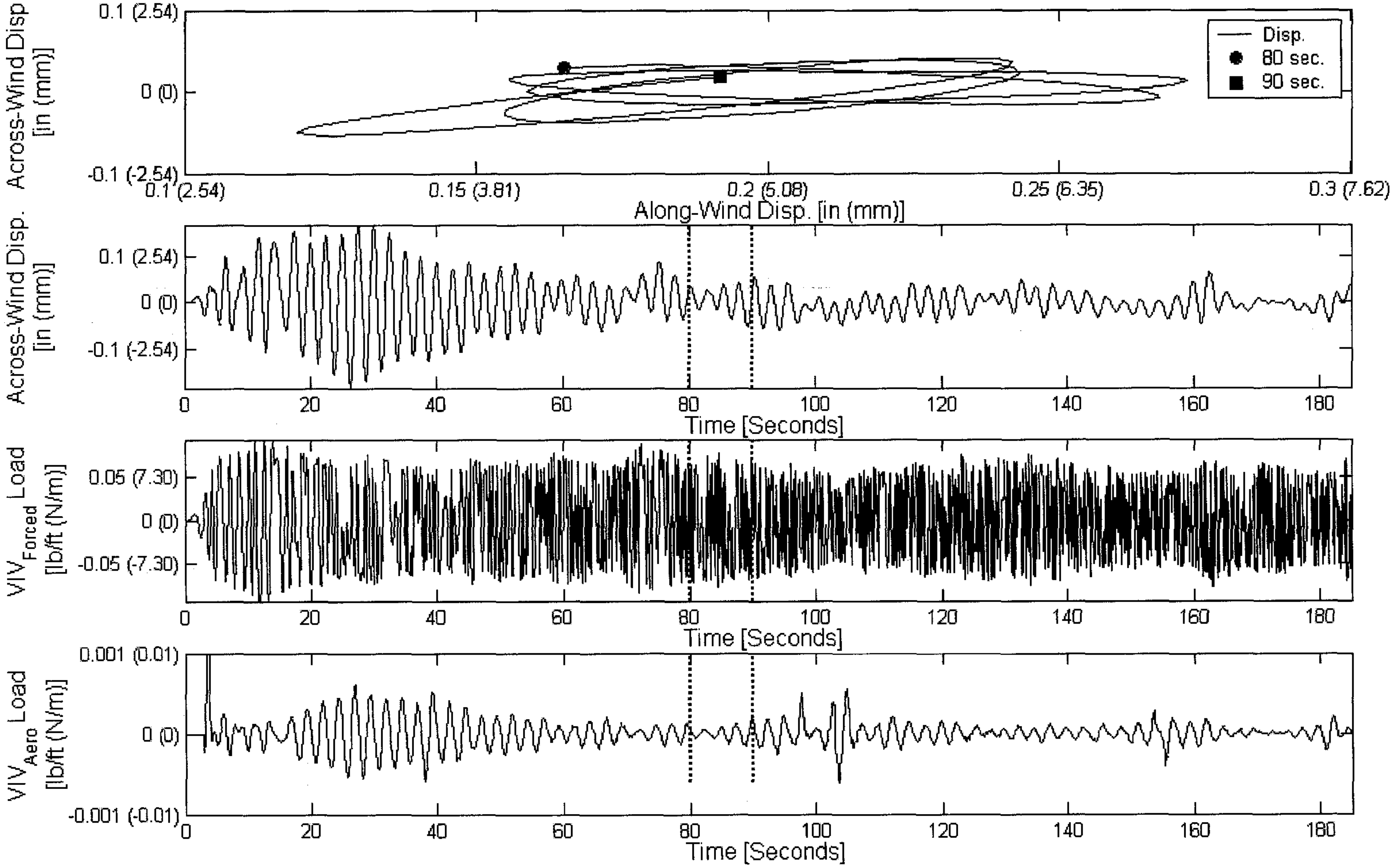

(a): Mean Wind Speed = 4 MPH (1.79 m/s)

Figure 7-13: Aerodynamic Damping Vortex Shedding Load Time History of Analysis – Vertical Height = 140 ft (42.7 m)

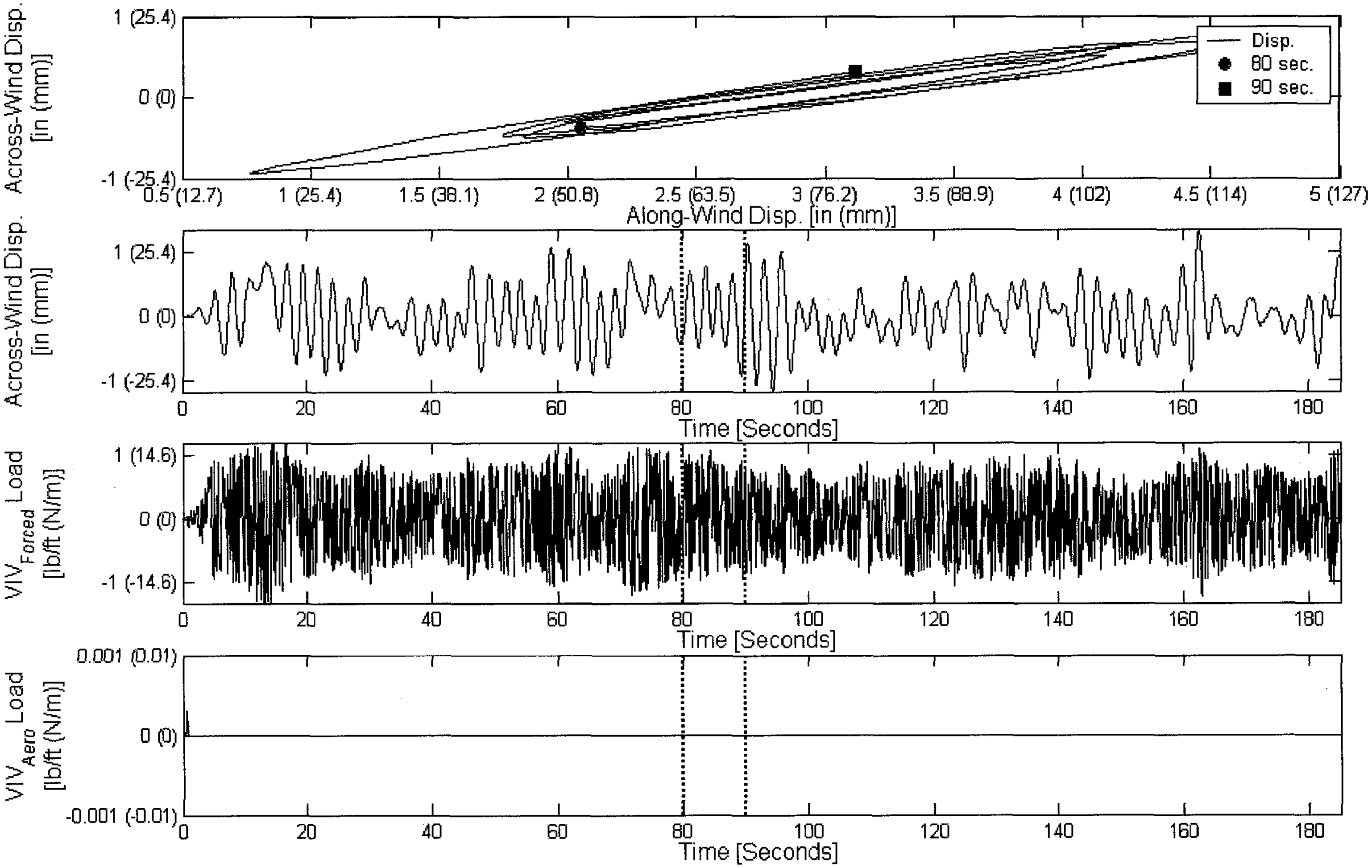

(b): Mean Wind Speed = 25 MPH (11.2 m/s)

Figure 7-13 (cont.): Aerodynamic Damping Vortex Shedding Load Time History of Analysis – Vertical Height = 140 ft (42.7 m)

Based on the information presented in Figures 7-11 through 7-13, several important observations can be noted. As for the forced vibration study, Figures 7-4 through 7-6, the forced vibration load time history has a high frequency component. The range of the forced vibration load for the 100 ft (30.5 m) and 140 ft (42.7 m) structures appear uniform with the magnitude of the load for the 140 ft (42.7 m) structure approximately half of the load for the 100 ft (30.5 m) structure. The aerodynamic damping load for the 60 ft (18.3 m) structure, though substantially smaller in magnitude than the forced vibration load, displays characteristics of intermittent lock-in for which the effect of the loading term can be observed. The aerodynamic damping term is largest in magnitude for the 100 ft (30.5 m) structure, but again appears to be small in comparison to the forced vibration load. At this point, it can be reasoned that the consideration of only the first natural frequency of the structure does not produce significant vortex shedding effects related to the resulting across-wind (lateral) load produced.

Figure 7-14 provides the maximum structure response in the across-wind (lateral) direction due to the complete vortex shedding model including both the forced vibration and aerodynamic damping terms. Comparisons are made for all variations of the limiting displacement parameter λ of the aerodynamic damping term and the forced vibration term only marked as “Forced”. The same characteristics that were provided in Figures 7-8 through 7-10 and Figures 7-11 through 7-13 are again repeated for Figure 7-14.

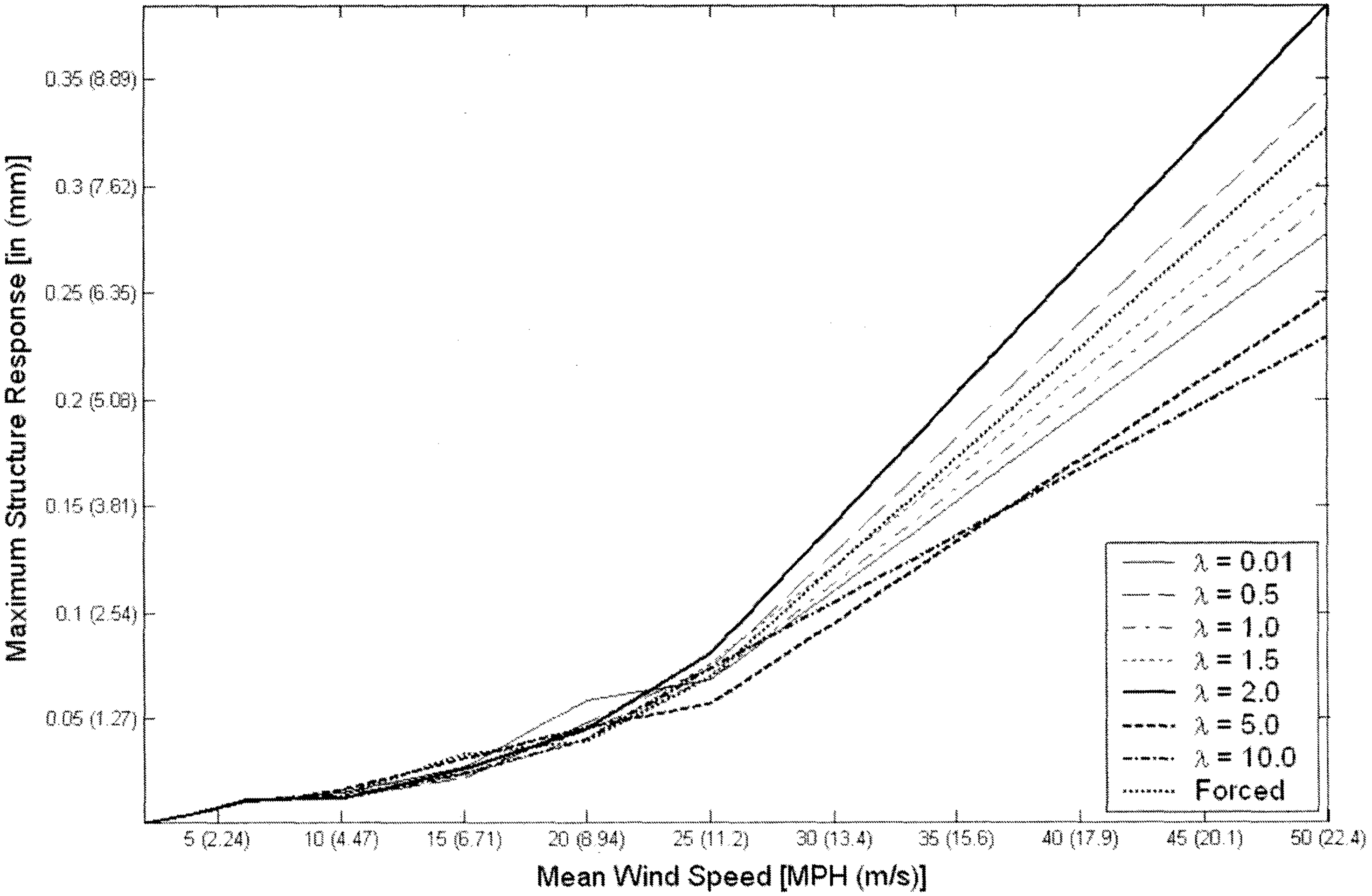

(a): Vertical Height = 60 ft (18.3 m)

Figure 7-14: Aerodynamic Damping Vortex Shedding Maximum Structure Response

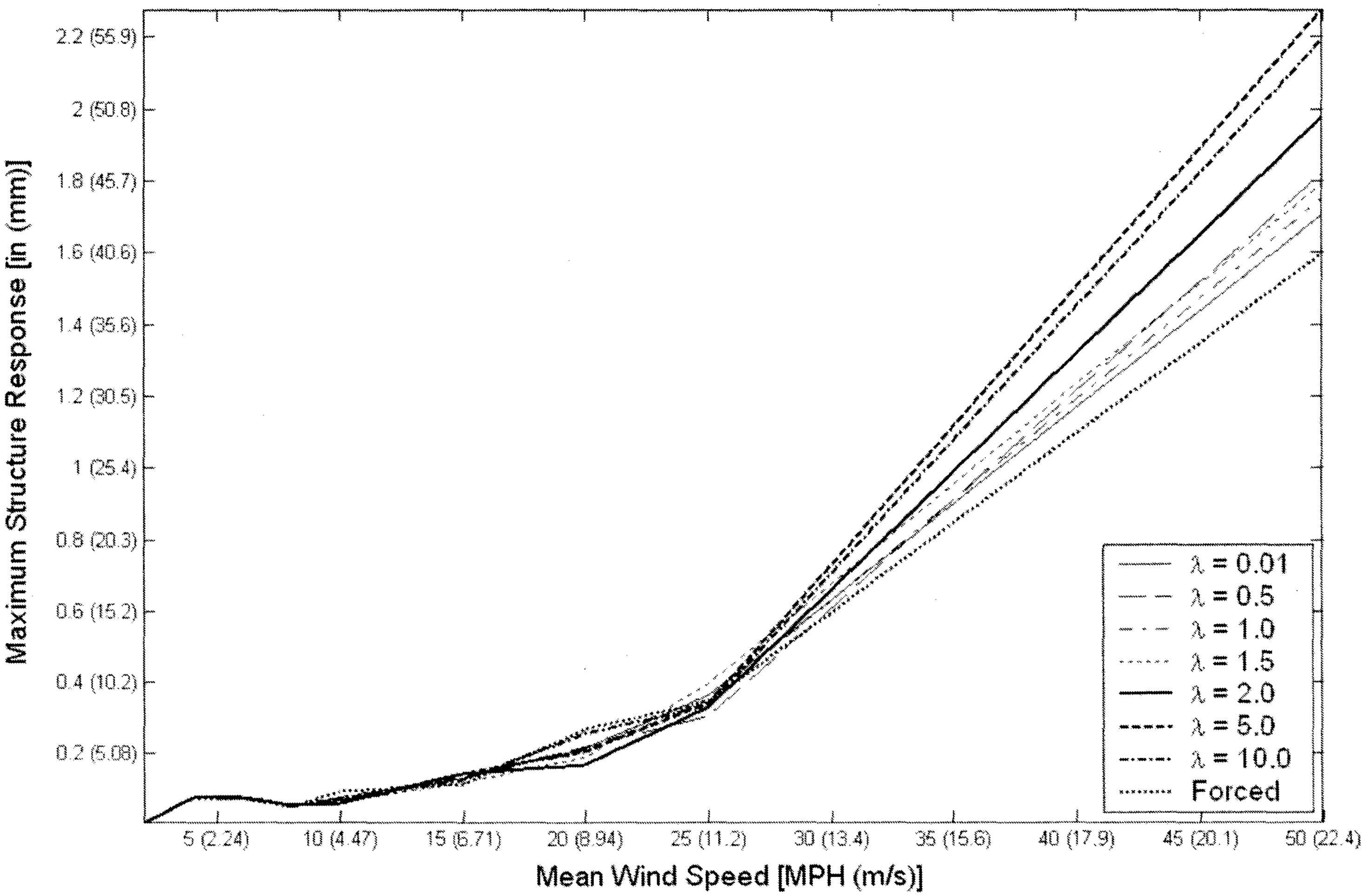

(b): Vertical Height = 100 ft (30.5 m)

Figure 7-14 (cont.): Aerodynamic Damping Vortex Shedding Maximum Structure Response

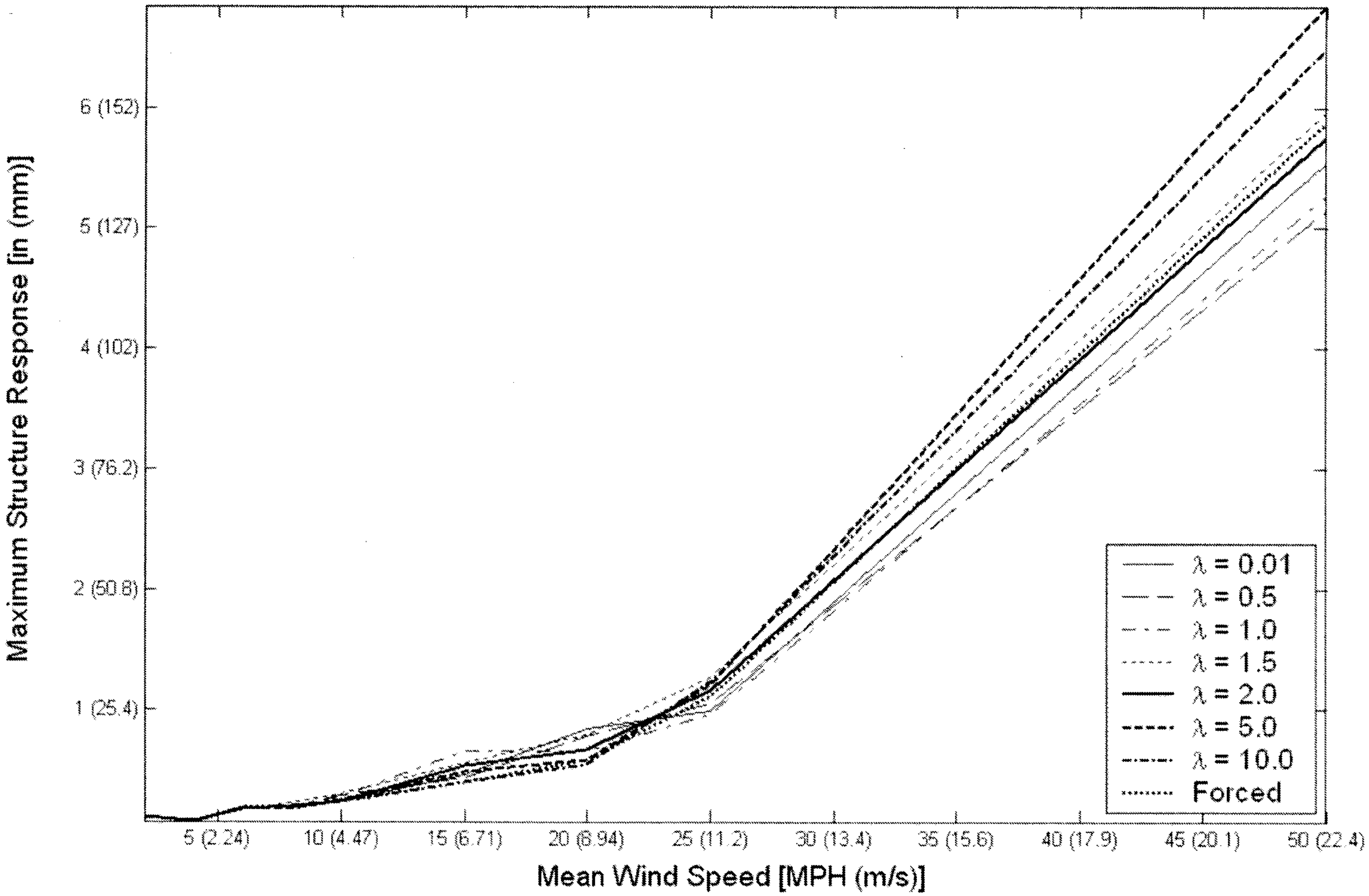

(c): Vertical Height = 140 ft (42.7 m)

Figure 7-14 (cont.): Aerodynamic Damping Vortex Shedding Maximum Structure Response

For all structural height variations, at relatively low wind speeds the effect of including the aerodynamic damping term is regarded as negligible in comparison to the use of only the forced vibration term of the vortex shedding model. The same jumps in maximum response that were seen for the maximum response of the forced vibration study provided in Figure 7-7 are again seen for Figure 7-14. At relatively high wind speeds, though, the difference in including the aerodynamic damping term is clearly seen. Larger values of the limiting displacement parameter λ allow for the aerodynamic damping term to produce across-wind (lateral) vortex shedding loads. Thus, lower values of λ are closer to the maximum response characteristics of the forced vibration study at these higher wind speeds.

Chapter Eight

Fatigue Life

8.1 Setup and Procedure

The numerical investigation study of fatigue life considers several variations in lifetime wind speed distribution, structure properties, spatial correlation of wind turbulence, and vortex shedding modeling. Variations in structure properties include the use of a generalized structure such as the example structure of Chapter Two and the use of a representative high-mast lighting (HML) structural support as considered by Goode and van de Lindt (2006). The primary goal of this study is to determine the effects of these variations on the estimated fatigue life. The classification of the stress process as being narrow-banded or wide-banded and its effects on the estimated fatigue life is also of interest.

The estimation of the fatigue life of a slender structure, as derived in Chapter Five, centers on the classification of the stress process. A narrow-band stress process was used by Crandall and Mark (1963) in their random vibration approach to estimate fatigue life. This type of stress process is characterized by zero or mean-level stress crossings between peaks. Or, as Holmes (2001) states, a narrow-band stress process means that the resulting stress variations can be regarded as quasi-sinusoidal with randomly varying amplitudes. Following Crandall and Mark (1963), the expected damage caused by a narrow-band stress process is given in Equation (5-8) as

$$E[D(T)] = \frac{\nu_0^+}{c}\left(2\sqrt{2}\sigma_y\right)^b \Gamma\left(1+\frac{b}{2}\right) \tag{8-1}$$

where σ_y is the standard deviation of the stress process as a function of time and the parameters b and c are fatigue constants related to the material of the structure for a particular stress category. The fatigue constants are empirical parameters that are determined from the fatigue (S-N) curve as

$$NS^b = c \tag{8-2}$$

where N is the number of cycles at stress amplitude S.

To determine the estimated fatigue life of a structure, the Palmgren-Miner rule is employed such that

$$F_{life} = \frac{1}{\sum_{i=1}^{n} F_i P_{0i}} \tag{8-3}$$

where F_{life} is the estimated fatigue life, F_i is the expected damage determined from Equation (8-1) for the i^{th} wind speed of the lifetime wind speed distribution, i.e. $F_i = E[D(T)]$, and P_{0i} is the probability of occurrence of the wind force for the i^{th} wind speed.

The use of Equation (8-1) for the expected damage is for the consideration of a narrow-band stress process. Indeed, however, this type of stress process is usually not the case for wind-induced loading particularly when multi-mode excitation of the structure is induced by the loading function. The stress process is then characterized by a wide-band stress process that is defined as random vibrations consisting of contributions over a broad range of frequencies (Holmes, 2001). A key feature of this stress process is the lack of zero or mean-level stress crossings between peaks of the stress variation.
Wirsching and Light (1980) developed an empirical approach to determine the fractional fatigue damage or expected damage due to a wide-band stress process. Holmes (2001) outlines this approach and states that the damage is determined by Equation (5-11) as

$$D = \lambda D_{nb} \tag{8-4}$$

where D is the fatigue damage, D_{nb} is the damage calculated for a narrow-band stress process assumption as given by Equation (8-1), and λ is an empirical parameter. The empirical parameter is estimated based on the fatigue parameters of the fatigue (S-N) curve given in Equation (8-2) and a spectral bandwidth parameter of the actual stress process detailed in Section 5.2.

The value of the empirical parameter λ produces upper and lower limits of the fatigue damage and resulting estimated fatigue life. For a narrow-band stress process, the spectral bandwidth parameter approaches zero and the empirical parameter λ approaches unity thus producing an upper limit on fatigue damage and a lower limit on the estimated fatigue life. However, as the spectral bandwidth parameter approaches its upper limit of unity, the empirical parameter λ approaches its lower limit defined by a constant that is a function of the fatigue constants given in Equation (8-2). This scenario produces a lower limit on fatigue damage and an upper limit on the estimated fatigue life. As such, both the upper and lower limits of the estimated fatigue life due to the estimated fatigue damage from the use of Equations (8-1) and (8-4) will be reported for this study of fatigue life.

This study of fatigue life considers variations in the lifetime wind speed distribution as presented in Section 5.3. In order to estimate the fatigue life using Crandall and Mark's (1963) random vibration approach, it is necessary to procure the wind speed statistical distribution information. Statistics for specific locations are not easily accessible and thus it is often difficult to determine the appropriate distribution to use in the determination of fatigue life. This study will thus consider two lifetime wind speed distributions: an assumed distribution based on national data for the contiguous United States and a distribution based on recorded data from a weather station located near the Denver Metropolitan Area in Colorado.

The first lifetime wind speed distribution is an assumed distribution based on a reasonable fit for data developed by the National Oceanographic and Atmospheric Administration (NOAA) for the contiguous United States. The distribution utilized for this fit is the two-parameter lognormal distribution that has a corresponding probability density function (PDF) of the wind speed, u, given in Equation (5-18) as

$$f_U(u) = \frac{1}{\sqrt{2\pi}\,\zeta\,u} \exp\left[-\frac{1}{2}\left(\frac{\ln u - \lambda}{\zeta}\right)^2\right] \tag{8-5}$$

where ζ and λ are the shape and scale parameters, respectively, and are related to the mean wind speed, μ, and standard deviation of wind speed, σ, of the distribution as given in Equation (5-19).

The second lifetime wind speed distribution makes use of data recorded at the former site of the airport near Denver, Colorado called Stapleton. Traditionally, the lifetime wind speed distribution, also known as the parent wind speed distribution, is assumed to behave according to a two-parameter Weibull distribution (Holmes, 2001). The PDF of the Weibull distribution of wind speed, u, is given in Equation (5-21) as

$$f_U(u) = \frac{\kappa u^{\kappa-1}}{\lambda^{\kappa}} \exp\left[-\left(\frac{u}{\lambda}\right)^{\kappa}\right] \tag{8-6}$$

where κ and λ are the shape and scale parameters, respectively, and are related to the mean wind speed, μ, and standard deviation of wind speed, σ, of the distribution as given in Equation (5-22).

The properties of both lifetime wind speed distributions are outlined in Table 8-1. These distributions will both be utilized in this study for fatigue life. The properties of the lognormal distribution are assumed and the properties of the Weibull distribution are derived from a statistical fit of approximately 47 years of data recorded at Stapleton near Denver, Colorado. The data from the Stapleton weather station was obtained from the National Climatic Data Center located in Asheville, North Carolina (NOAA).

Property	Lognormal Distribution	Weibull Distribution
Mean Wind Speed, μ	10 MPH (4.47 m/s)	9.33 MPH (4.17 m/s)
Standard Deviation, σ	2.50 MPH (1.12 m/s)	4.92 MPH (2.20 m/s)
Shape Parameter	0.246	1.98
Scale Parameter	2.27 MPH (1.01 m/s)	10.53 MPH (4.71 m/s)

Table 8-1: Lifetime Wind Speed Distribution Properties for Fatigue Life

As discussed in Chapter Five, the estimation of the fatigue life is obtained by subdividing the lifetime wind speed distribution into equal width bins to determine the damage associated with the i^{th} wind speed. Each bin is then treated as an individual wind event with the midpoint value of the bin being treated as the mean wind speed for the generation of a wind speed time series for dynamic analysis. As was considered in

Chapters Six and Seven, it is necessary to incorporate the spatial correlation of wind turbulence and vortex shedding to determine their effects on the estimated fatigue life. As such, this study considers four primary analyses with additional variations of the appropriate empirical parameter for each analysis as outlined in Table 8-2. All four of these analyses consider both the example structure and HML structural support. Additionally, these analyses including the two structure variations consider both the assumed lognormal lifetime wind speed distribution and the Weibull lifetime wind speed distribution fit to data obtained from the Stapleton weather station.

Analysis Number	Wind Flow Type	Vortex Shedding	Empirical Parameter Variations
1	Two-Dimensional Wind Flow	None	Along-Wind (Longitudinal) Turbulence Component $C_{z(long)} = 0, 10, +\infty$
2	Three-Dimensional Wind Flow	None	Along-Wind (Longitudinal) & Across-Wind (Lateral) Turbulence Components $C_{z(long)} = C_{z(lat)} = 0, 10, +\infty$
3	Three-Dimensional Wind Flow	Forced Vibration Term Only	Along-Wind (Longitudinal) & Across-Wind (Lateral) Turbulence Components $C_{z(long)} = C_{z(lat)} = 10$
4	Three-Dimensional Wind Flow	Forced Vibration and Aerodynamic Damping Terms	Along-Wind (Longitudinal) & Across-Wind (Lateral) Turbulence Components $C_{z(long)} = C_{z(lat)} = 10$ Limiting Displacement Parameter, $\lambda = 0.01, 1, 10$

Table 8-2: Variations in Wind Flow and Vortex Shedding Properties for Fatigue Life

The results of all the analyses of this chapter are presented in tabular format with supplemental graphical figures for illustrative purposes. Within each table, the estimated fatigue life is calculated based on conditions outlined in Tables 8-1 and 8-2. The properties of the structure are further outlined in Sections 8.2 and 8.3 for the example structure and HML structural support, respectively.

The resulting bending stress at the base of the structure is the primary source of the fatigue damage. A three-dimensional dynamic finite element computer program is used to obtain the two, orthogonal bending stresses due to a bending moment in the along-wind (longitudinal) direction and a bending moment in the across-wind (lateral) direction as shown in Figure 8-1.

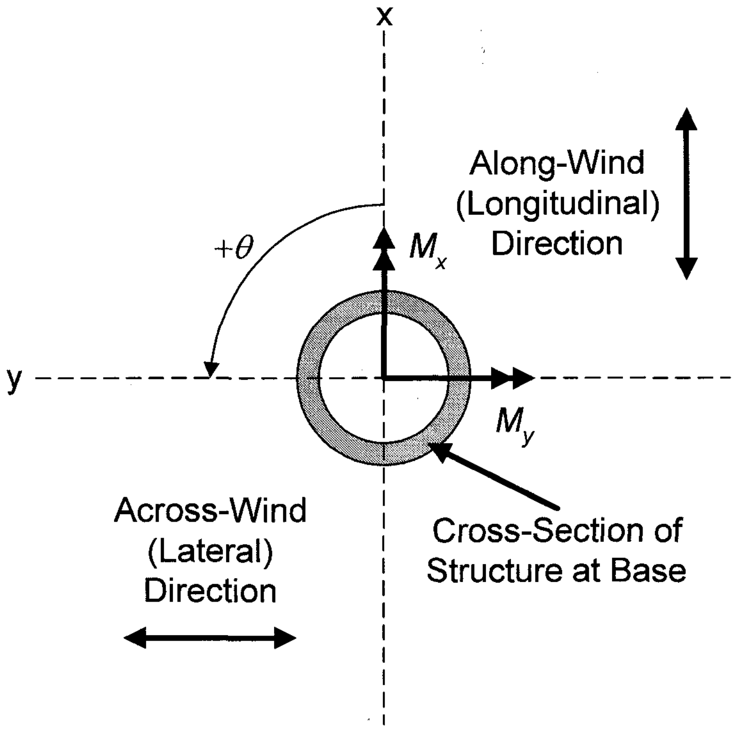

Figure 8-1: Orthogonal Bending Moments

When the angle from the positive *x*-axis to the positive *y*-axis, *θ*, is at 0°, the stress process for estimating the fatigue life is solely defined by the bending stress caused by the bending moment at the base of the structure about the y-axis, M_y. At $\theta = 180^\circ$, the stress process is equal in magnitude, but opposite in sign. Similarly, when $\theta = 90^\circ$, the stress process for estimating the fatigue life is solely defined by the bending stress caused by the bending moment at the base of the structure about the x-axis, M_x. At $\theta = -90^\circ$ or 270°, the stress process is equal in magnitude, but opposite in sign.

At points in between $\theta = 0^\circ$ and $\theta = 90^\circ$, the stress process is caused by an interaction of the bending moments M_x and M_y. By taking the components perpendicular and parallel to a line going from the center of the cross-section to the outer fiber of the cross-section for maximum bending stress at an angle θ, the stress process at the outer fiber of every angle can be determined around the entire cross-section. Then, the bending stress is easily calculated from mechanics as

$$\sigma = \frac{My}{I} \tag{8-7}$$

where y is half the outside diameter at the base of the structure and I is the centroidal moment of inertia of the cross-section. Due to the doubly symmetric cross-section, y and I are equal for all angles θ. Thus, the following sections present the fatigue life estimates at 5° angle increments from 0° to 90° based on the stress process determined as described previously. Based on these values, all other points around the cross-section of the circular cylinder may also be obtained.

For each angle described above, each of the generated data tables in the following sections incorporate three separate fatigue life estimates. Following the approach of Chapter Five and outlined previously in this section, the damage due to any given stress process is determined based on a random vibration approach. For a narrow-band stress process, an upper limit is achieved for the predicted damage. Because the fatigue life is based on the inverse of the predicted damage, a narrow-band stress process creates a lower limit (LL) for the estimated fatigue life. Alternatively, based on the empirical method for estimating the expected damage due to a wide-band stress process, an upper limit (UL) for the estimated fatigue life can also be obtained. Finally, the applied use of the aforementioned empirical method can also produce the estimated fatigue life based on a wide-band stress process. This third estimate of fatigue life is the wide-band (WB) estimate of fatigue life. Thus, the three fatigue life estimates are given in the data tables as: lower limit (LL), wide-band (WB), and upper limit (UL).

Sections 8.2 and 8.3 consider the two variations of the structure separately. Section 8.2 considers a single variation of the example structure presented in Chapter Two. Section 8.3 considers a representative HML structural support as considered by Goode and van de Lindt (2006).

8.2 Example Structure Results

The first study of fatigue life considers only one variation of the example structure from Chapter Two. The properties of the structure considered in this study are outlined in Table 8-3. For the estimation of fatigue life, the base connection must be classified based on an AASHTO detail category. For the purposes of this study, the example structure base connection is assumed to be classified as an AASHTO E detail category (AASHTO, 2001). The details of this category are provided in Table 2-4 of Chapter Two.

Property	Value
Vertical Height	100 ft (30.5 m)
Outside Diameter	2.0 ft (610 mm)
Wall Thickness	¼ in (6.35 mm)
AASHTO Base Connection Detail Category	E

Table 8-3: Example Structure Properties for Fatigue Life

This first study considers the structure outlined in Table 8-3 for variations in the lifetime wind speed distribution, wind flow properties, and vortex shedding properties. The variations in the lifetime wind speed distribution are outlined in Table 8-1. The variations in the wind flow and vortex shedding properties are outlined in Table 8-2.

Results of Analysis

Fatigue life estimates were first obtained for two-dimensional wind flow with variations in the spatial correlation parameter $C_{z(long)}$ as given in Table 8-2. The stress process at the base of the structure is the source of the fatigue damage. Diving the lifetime wind speed distribution into 25 equal width bins produces 25 separate analyses that result in a stress process that has a probability of occurrence equal to the area of the bin. Figure 8-2 provides the stress process for one such bin (bin number 20) with full spatial correlation of the two-dimensional wind flow. A linear ramp-up in wind speed from zero to five seconds is repeated in all such analyses as was done in the studies of Chapters Six and Seven. This time range is indicated by the vertical dashed line at five seconds. The horizontal dashed line represents the mean level for the stress process beyond the initial ramp-up time range. In the determination of the variance of the stress process needed to determine the expected damage associated with the stress process, the initial five seconds of the stress process within the linear ramp-up range is not included.

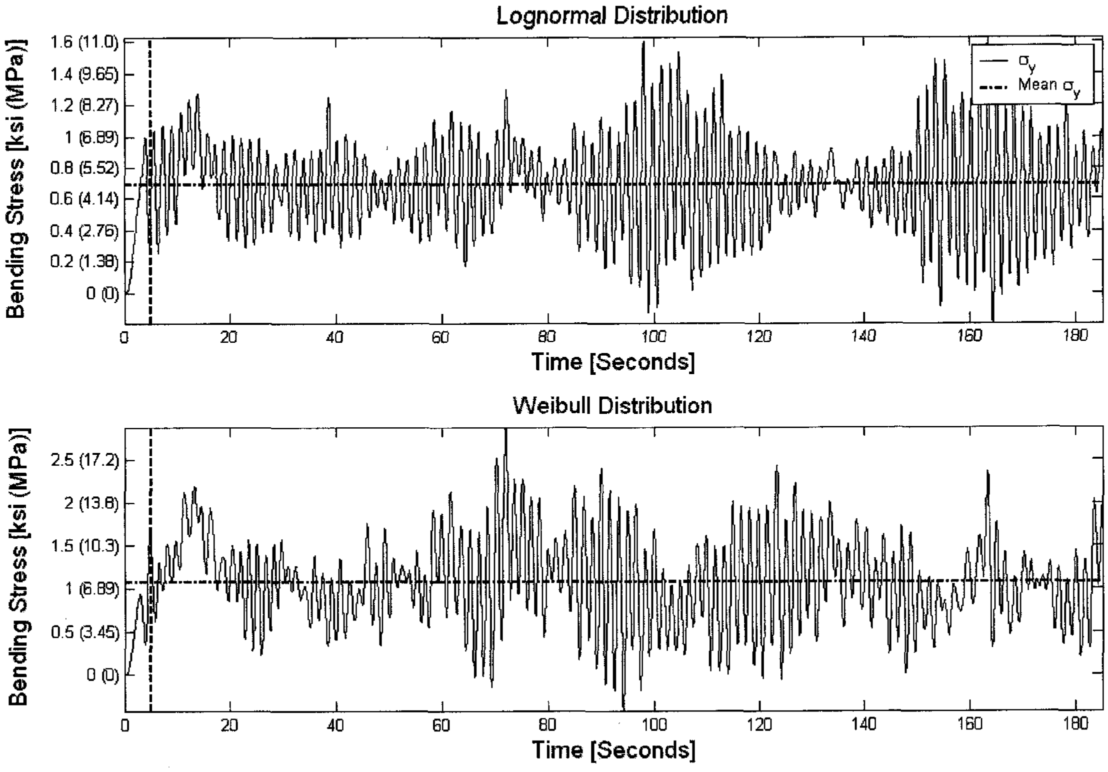

Figure 8-2: 2-D Wind Flow Stress Process – Example Structure

Recall that one of the main features of a wide-band process is the lack of mean level crossings between peaks. From Figure 8-2 it can be determined that both stress processes illustrated are to some degree a wide-band stress process. As will be seen, the estimated fatigue life is closer to the upper limit for a wide-band stress process rather than the lower limit for estimated fatigue life characterized by a narrow-band stress process.

Table 8-4 provides the results of this first study. For the case of $C_{z(long)} = 0$, there is strong spatial correlation of the simulated wind speed time series. Alternatively, when $C_{z(long)} = +\infty$, there is weak spatial correlation of the simulated wind speed time series. Both the lognormal and Weibull distributions given in Table 8-1 are utilized to estimate the fatigue life of the structure. For this section, the structure properties are as given for the example structure in Table 8-3. The lowest wide-band (WB) stress process estimate of fatigue life is indicated in **bold** type in Table 8-4.

Angle $+\theta$	Fatigue Life	Example Structure – Fatigue Life (Years)					
		Lognormal Distribution			Weibull Distribution		
		$C_{z(long)}$			$C_{z(long)}$		
		0	10	$+\infty$	0	10	$+\infty$
0	LL	333	2,739	12,518	158	1,195	5,111
	WB	**400**	**3,286**	**15,016**	**189**	**1,434**	**6,131**
	UL	401	3,292	15,047	189	1,436	6,143
5	LL	337	2,769	12,655	159	1,208	5,167
	WB	404	3,322	15,180	191	1,450	6,198
	UL	405	3,328	15,211	192	1,452	6,210
10	LL	348	2,861	13,076	165	1,248	5,339
	WB	418	3,433	15,686	198	1,498	6,405
	UL	419	3,439	15,718	198	1,501	6,417
15	LL	368	3,023	13,818	174	1,319	5,642
	WB	442	3,628	16,576	209	1,583	6,768
	UL	442	3,634	16,609	209	1,586	6,781
20	LL	398	3,270	14,946	188	1,427	6,102
	WB	478	3,924	17,929	226	1,713	7,321
	UL	478	3,930	17,965	226	1,715	7,335
25	LL	441	3,625	16,569	209	1,582	6,765
	WB	530	4,350	19,876	250	1,899	8,116
	UL	530	4,357	19,916	251	1,901	8,131
30	LL	502	4,126	18,861	238	1,801	7,701
	WB	603	4,952	22,625	285	2,161	9,238
	UL	604	4,960	22,671	286	2,164	9,256
35	LL	589	4,836	22,102	278	2,110	9,024
	WB	706	5,803	26,514	334	2,533	10,826
	UL	707	5,812	26,567	335	2,536	10,847
40	LL	712	5,853	26,755	337	2,554	10,923
	WB	855	7,024	32,094	404	3,066	13,105
	UL	856	7,036	32,159	405	3,070	13,130
45	LL	895	7,354	33,612	423	3,209	13,723
	WB	1,074	8,824	40,320	508	3,851	16,463
	UL	1,076	8,839	40,401	509	3,857	16,495
50	LL	1,175	9,650	44,109	555	4,211	18,009
	WB	1,410	11,580	52,912	667	5,054	21,605
	UL	1,412	11,599	53,018	668	5,062	21,646
55	LL	1,625	13,352	61,028	769	5,826	24,916
	WB	1,950	16,022	73,207	923	6,993	29,892
	UL	1,953	16,049	73,355	924	7,003	29,949
60	LL	2,403	19,745	90,249	1,137	8,616	36,847
	WB	2,884	23,693	108,261	1,364	10,341	44,204
	UL	2,889	23,733	108,478	1,366	10,356	44,290
65	LL	3,881	31,883	145,729	1,835	13,912	59,498
	WB	4,657	38,259	174,813	2,203	16,699	71,379
	UL	4,665	38,323	175,165	2,206	16,723	71,516
70	LL	7,093	58,271	266,343	3,354	25,427	108,743
	WB	8,512	69,924	319,500	4,027	30,519	130,456
	UL	8,525	70,041	320,142	4,032	30,563	130,708
75	LL	15,696	128,958	589,437	7,423	56,273	240,656
	WB	18,838	154,747	707,077	8,911	67,541	288,708
	UL	18,867	155,006	708,498	8,922	67,639	289,266
80	LL	48,951	402,170	1,838,228	23,150	175,492	750,514
	WB	58,748	482,595	2,205,102	27,791	210,636	900,371
	UL	58,839	483,405	2,209,532	27,826	210,940	902,110
85	LL	349,100	2,868,115	13,109,492	165,094	1,251,540	5,352,358
	WB	418,968	3,441,675	15,725,891	198,194	1,502,169	6,421,077
	UL	419,615	3,447,447	15,757,485	198,442	1,504,339	6,433,483
90	LL	$+\infty$	$+\infty$	$+\infty$	$+\infty$	$+\infty$	$+\infty$
	WB	$+\infty$	$+\infty$	$+\infty$	$+\infty$	$+\infty$	$+\infty$
	UL	$+\infty$	$+\infty$	$+\infty$	$+\infty$	$+\infty$	$+\infty$

Table 8-4: 2-D Wind Flow Fatigue Life – Example Structure

As expected, the lowest fatigue life occurs when $C_{z(long)} = 0$ providing strong spatial correlation of the simulated wind speed time series. A significant observation can also be made in regards to the assumption of a two-dimensional wind flow. In this assumption, only along-wind (longitudinal) wind speed time series are utilized to estimate the fatigue life. As the angle θ is increased from the along-wind (longitudinal) axis at 0°, the estimated fatigue life increases slowly. As the angle θ approaches the across-wind (lateral) axis at 90°, the estimated fatigue life increases quickly eventually obtaining infinite fatigue life. Figure 8-3 illustrates this observation for spatial correlation parameters $C_{z(long)} = C_z = 0$, 10 and $+\infty$ for the along-wind (longitudinal) turbulence component u'.

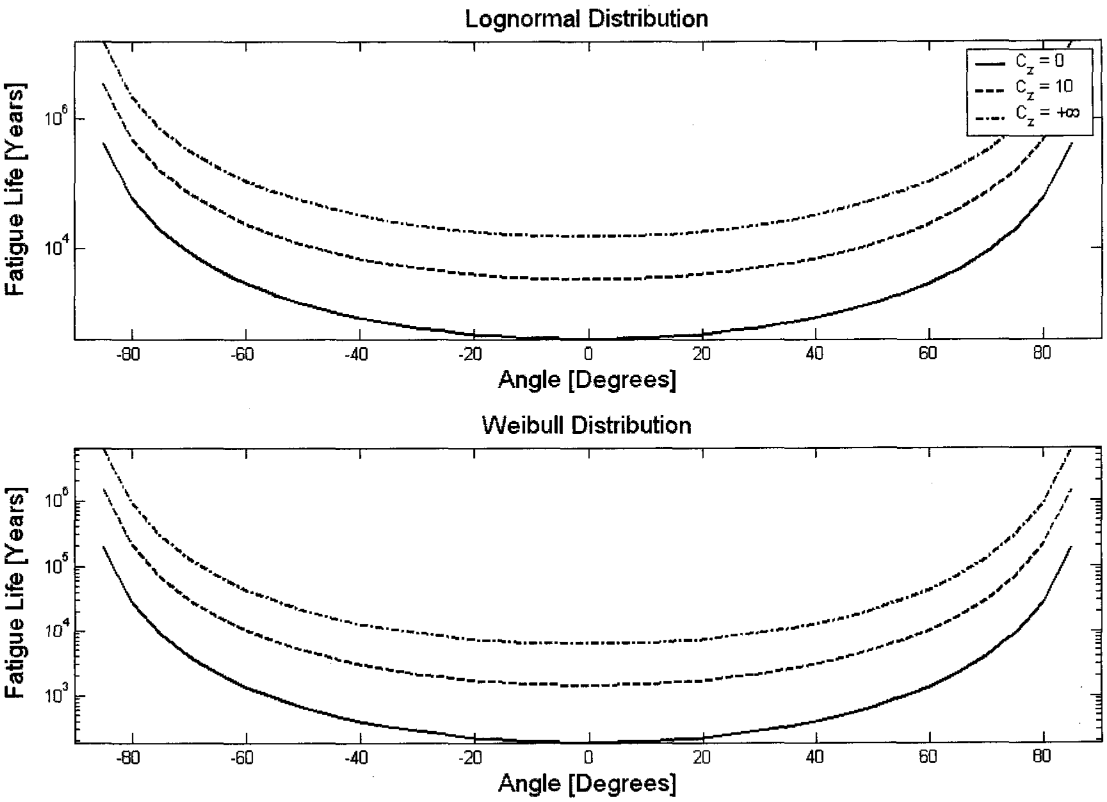

Figure 8-3: 2-D Wind Flow Fatigue Life – Example Structure

Comparisons of the lower limit (LL), wide-band (WB), and upper limit (UL) fatigue life estimates also yield interesting results. The lower limit (LL) fatigue life estimate is approximately 15 – 20% lower than the wide-band (WB) fatigue life estimate. Alternatively, the wide-band (WB) and upper limit (UL) fatigue life estimates are consistently close in magnitude to each other. Thus, the stress process used to estimate the fatigue life is indeed a wind-band stress process.

Finally, a comparison of the lifetime wind speed distributions also yield interesting results. The lognormal distribution based on an assumed mean wind speed and coefficient of variation (COV) produced higher fatigue life estimates than the Weibull distribution based on data from the Stapleton weather station. However, the COV of the Stapleton data is approximately 50%, whereas the COV of the assumed distribution is only 25%. Thus, the high wind tail of the Weibull distribution has a higher probability of occurrence than the lognormal distribution. The expected damage due to these high winds will then occur with a higher probability of occurrence thus reducing the estimated fatigue life.

Following Table 8-2, fatigue life estimates were next obtained for three-dimensional wind flow with variations in the spatial correlation parameters $C_{z(long)}$ and $C_{z(lat)}$. Figure 8-4 provides the stress process associated with one bin (bin number 20) of the divided lifetime wind speed distribution with full spatial correlation of both the along-wind (longitudinal) and across-wind (lateral) turbulence components u' and v', respectively, for the three-dimensional wind flow. The stress process σ_y about the across-wind (lateral) direction y-axis is responsible for fatigue damage in the along-wind (longitudinal) direction. The stress process σ_x about the along-wind (longitudinal) direction x-axis is responsible for fatigue damage in the across-wind (lateral) direction.

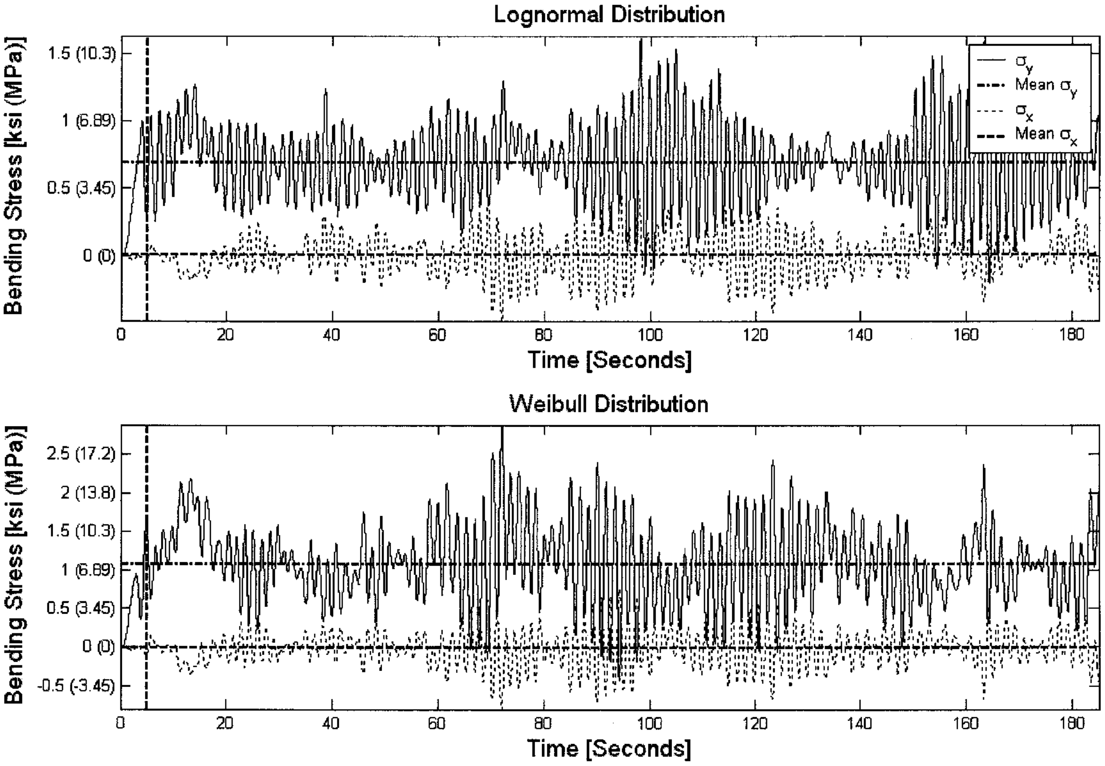
Lognormal Distribution

Weibull Distribution

Figure 8-4: 3-D Wind Flow Stress Process – Example Structure

From Figure 8-4 it can be determined that all stress processes illustrated are to some degree a wide-band stress process.

Table 8-5 provides the estimated fatigue life for three-dimensional wind flow with variations in the spatial correlation parameters $C_{z(long)}$ and $C_{z(lat)}$ as given in Table 8-2. For the case of $C_{z(long)} = C_{z(lat)} = 0$, there is strong spatial correlation of the simulated wind speed time series. Alternatively, when $C_{z(long)} = C_{z(lat)} = +\infty$, there is weak spatial correlation of the simulated wind speed time series. Both the lognormal and Weibull distributions given in Table 8-1 are utilized to estimate the fatigue life of the structure. The structure properties of the example structure are given in Table 8-3. The lowest wide-band (WB) stress process estimate of fatigue life is indicated in **bold** type in Table 8-5.

Angle $+\theta$	Fatigue Life	Example Structure – Fatigue Life (Years)					
		Lognormal Distribution			Weibull Distribution		
		($C_{z(long)}$, $C_{z(lat)}$)			($C_{z(long)}$, $C_{z(lat)}$)		
		(0,0)	(10,10)	(+∞,+∞)	(0,0)	(10,10)	(+∞,+∞)
0	LL	333	2,739	12,518	158	1,195	5,111
	WB	**400**	**3,286**	**15,016**	**189**	**1,434**	**6,131**
	UL	401	3,292	15,047	189	1,436	6,143
5	LL	359	2,890	13,152	163	1,233	5,399
	WB	431	3,468	15,777	195	1,480	6,477
	UL	432	3,474	15,809	196	1,483	6,489
10	LL	395	3,108	14,135	170	1,289	5,825
	WB	475	3,730	16,955	205	1,548	6,987
	UL	475	3,736	16,990	205	1,550	7,001
15	LL	442	3,407	15,504	181	1,374	6,393
	WB	530	4,088	18,598	218	1,650	7,669
	UL	531	4,095	18,636	218	1,652	7,684
20	LL	505	3,798	17,356	196	1,507	7,205
	WB	606	4,558	20,819	236	1,808	8,643
	UL	606	4,565	20,862	236	1,811	8,660
25	LL	578	4,353	20,032	215	1,662	8,306
	WB	694	5,224	24,028	259	1,995	9,963
	UL	695	5,233	24,078	259	1,998	9,983
30	LL	681	5,119	23,707	241	1,880	9,818
	WB	818	6,143	28,436	289	2,257	11,777
	UL	819	6,153	28,496	290	2,260	11,801
35	LL	808	6,089	28,818	276	2,187	11,870
	WB	971	7,308	34,566	331	2,625	14,239
	UL	972	7,319	34,639	332	2,629	14,268
40	LL	980	7,549	36,025	321	2,588	14,900
	WB	1,177	9,060	43,210	386	3,106	17,872
	UL	1,178	9,074	43,302	386	3,111	17,910
45	LL	1,193	9,515	46,597	377	3,126	19,167
	WB	1,433	11,420	55,889	453	3,753	22,990
	UL	1,434	11,438	56,009	454	3,758	23,039
50	LL	1,465	12,280	62,197	454	3,920	25,680
	WB	1,760	14,739	74,599	545	4,705	30,801
	UL	1,761	14,760	74,761	546	4,711	30,867
55	LL	1,823	16,040	86,663	556	5,038	35,319
	WB	2,190	19,253	103,940	668	6,048	42,362
	UL	2,191	19,280	104,168	668	6,056	42,453
60	LL	2,287	21,137	125,052	695	6,589	50,304
	WB	2,747	25,371	149,979	835	7,910	60,333
	UL	2,749	25,406	150,312	836	7,920	60,465
65	LL	2,830	28,762	185,268	889	8,748	74,217
	WB	3,400	34,525	222,194	1,068	10,502	89,014
	UL	3,402	34,571	222,690	1,068	10,515	89,209
70	LL	3,346	39,406	268,080	1,134	12,069	107,464
	WB	4,019	47,303	321,509	1,363	14,490	128,889
	UL	4,022	47,365	322,230	1,364	14,507	129,171
75	LL	3,489	51,308	345,595	1,413	16,424	136,735
	WB	4,191	61,592	414,485	1,697	19,720	164,007
	UL	4,194	61,671	415,403	1,698	19,742	164,354
80	LL	3,116	55,487	348,740	1,588	20,355	141,110
	WB	3,744	66,618	418,310	1,908	24,442	169,291
	UL	3,746	66,695	419,182	1,909	24,467	169,612
85	LL	2,473	48,740	285,982	1,594	21,644	118,155
	WB	2,970	58,534	343,162	1,915	25,994	141,815
	UL	2,972	58,585	343,748	1,916	26,016	142,021
90	LL	1,880	37,115	206,267	1,410	19,444	87,720
	WB	2,257	44,587	247,704	1,693	23,359	105,348
	UL	2,259	44,612	247,931	1,695	23,372	105,439

Table 8-5: 3-D Wind Flow Fatigue Life – Example Structure

Similar to the study considering only two-dimensional wind flow, the lowest fatigue life occurs when $C_{z(long)} = C_{z(lat)} = 0$ providing strong spatial correlation of the three-dimensional simulated wind speed time series. The three-dimensional wind flow, however, utilized both the along-wind (longitudinal) and across-wind (lateral) wind speed time series to estimate the fatigue life. As shown in Figure 8-4 there is a non-zero stress process in the across-wind (lateral) direction. The stress process in the across-wind (lateral) direction for the two-dimensional wind flow case from Figure 8-2 was zero. Thus, as the angle θ is increased from 0° the estimated fatigue life reaches a maximum before it reaches 90°. Indeed, the estimated fatigue life maximum occurs between 60° and 80° depending on the stress process characterization as given in Table 8-5. Figure 8-5 illustrates this observation for spatial correlation parameters $C_{z(long)} = C_{z(lat)} = C_z = 0$, 10 and $+\infty$ for the along-wind (longitudinal) and across-wind (lateral) turbulence components u' and v', respectively. For comparison purposes, one data set from the two-dimensional wind flow study is included for $C_z = 0$.

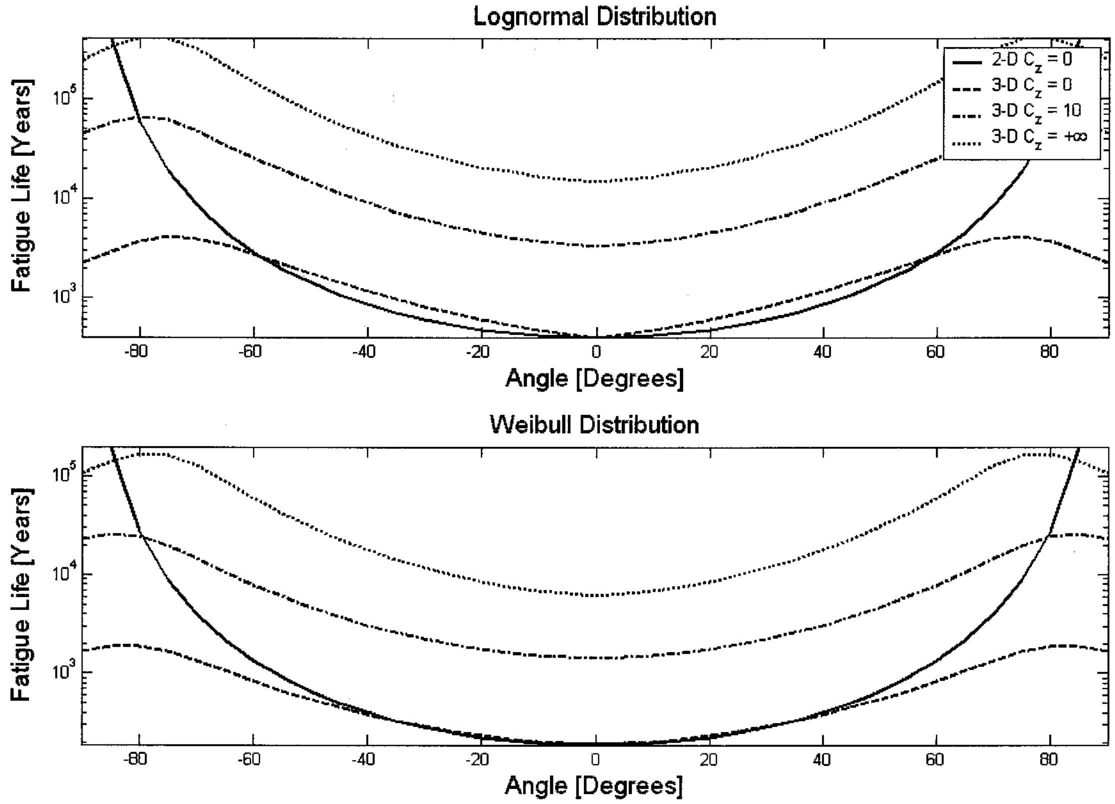

Figure 8-5: 3-D Wind Flow Fatigue Life – Example Structure

As can be seen from Table 8-5 and Figure 8-5, the estimated fatigue life in the across-wind (lateral) direction at $\theta = 90^\circ$ is much larger than in the along-wind (longitudinal) direction at $\theta = 0^\circ$. This can be attributed to the relatively small magnitude of the stress process for the across-wind (lateral) fatigue life estimate compared to the stress process for the along-wind (longitudinal) fatigue life estimate. However, the inclusion of the across-wind (lateral) simulated wind speed time series significantly reduces the fatigue life at angles near 90° in comparison to the two-dimensional wind flow where this time series is not considered.

The next progression provided in Table 8-2 states that fatigue life estimates were next obtained for three-dimensional wind flow including the effects of the forced vibration term in the vortex shedding model. Figure 8-6 provides the stress process associated with one bin (bin number 20) of the divided lifetime wind speed distribution.

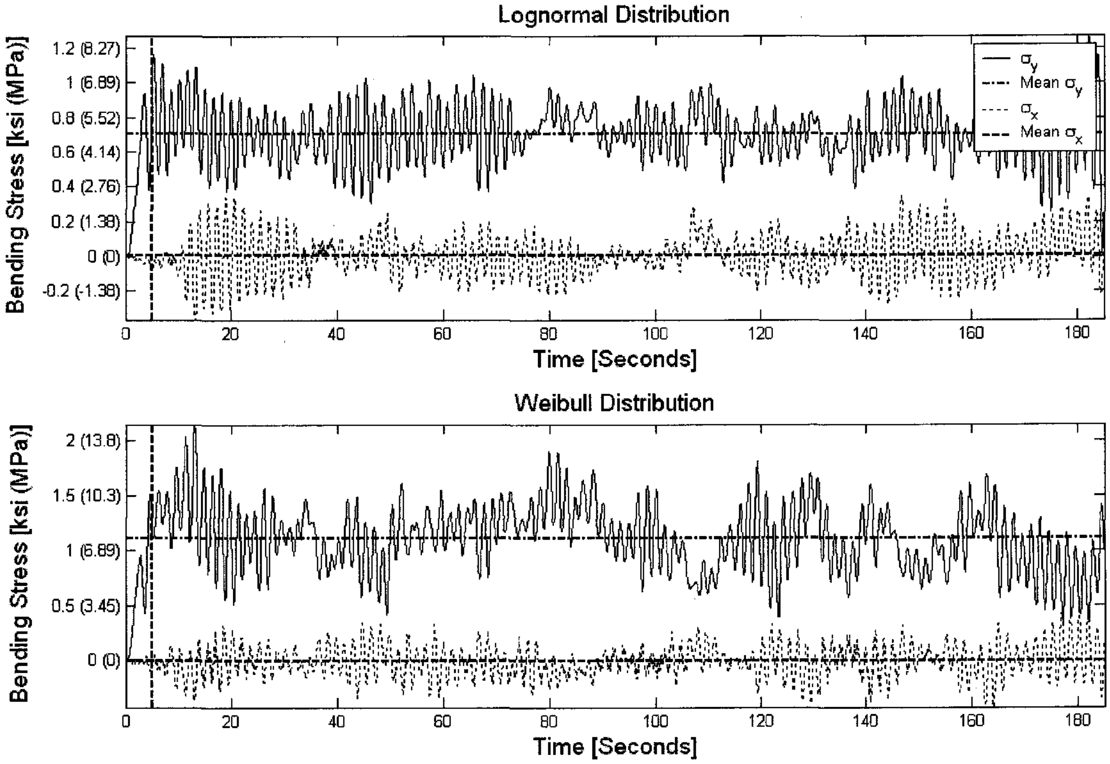
Lognormal Distribution

Weibull Distribution

Figure 8-6: Forced Vibration Vortex Shedding Stress Process – Example Structure

From Figure 8-6 it can be determined that all stress processes illustrated are to some degree a wide-band stress process.

Table 8-6 provides the estimated fatigue life for forced vibration vortex shedding with a single variation in the spatial correlation parameters $C_{z(long)}$ and $C_{z(lat)}$ as given in Table 8-

2. There is no empirical parameter within the forced vibration loading term of the vortex shedding model. Both lognormal and Weibull distributions given in Table 8-1 are utilized to estimate the fatigue life of the structure. For this section, the structure properties are as given for the example structure in Table 8-3. The lowest wide-band (WB) stress process estimate of fatigue life is indicated in **bold** type in Table 8-6.

Angle $+\theta$	Fatigue Life	Example Structure – Fatigue Life (Years)	
		Lognormal Distribution	Weibull Distribution
0	LL	2,739	1,195
	WB	**3,286**	**1,434**
	UL	3,292	1,436
5	LL	2,855	1,241
	WB	3,426	1,490
	UL	3,432	1,492
10	LL	3,045	1,307
	WB	3,654	1,569
	UL	3,660	1,571
15	LL	3,270	1,396
	WB	3,924	1,675
	UL	3,930	1,678
20	LL	3,553	1,503
	WB	4,264	1,803
	UL	4,271	1,806
25	LL	3,859	1,644
	WB	4,630	1,973
	UL	4,639	1,976
30	LL	4,355	1,820
	WB	5,225	2,185
	UL	5,235	2,188
35	LL	4,970	2,068
	WB	5,962	2,481
	UL	5,973	2,485
40	LL	5,629	2,365
	WB	6,753	2,838
	UL	6,766	2,843
45	LL	6,542	2,762
	WB	7,847	3,313
	UL	7,863	3,320
50	LL	7,763	3,265
	WB	9,310	3,916
	UL	9,331	3,925
55	LL	9,106	3,898
	WB	10,919	4,675
	UL	10,945	4,685
60	LL	11,200	4,653
	WB	13,427	5,580
	UL	13,463	5,593
65	LL	13,548	5,497
	WB	16,237	6,588
	UL	16,285	6,607
70	LL	15,713	6,462
	WB	18,823	7,742
	UL	18,887	7,767
75	LL	17,442	7,136
	WB	20,880	8,544
	UL	20,965	8,577
80	LL	17,445	7,388
	WB	20,866	8,839
	UL	20,968	8,880
85	LL	15,952	7,103
	WB	19,069	8,493
	UL	19,174	8,537
90	LL	13,717	6,505
	WB	16,397	7,777
	UL	16,488	7,819

Table 8-6: Forced Vibration Vortex Shedding Fatigue Life – Example Structure

Inclusion of the forced vibration loading term of the vortex shedding model for the estimation of fatigue life had significant effects in the across-wind (lateral) direction stress process. However, at angles near θ = 0°, the additional loading due to vortex shedding did not effect the stress process. Hence, the estimated fatigue life at 0° was also unaffected. As the angle θ is increased from 0°, the estimated fatigue life reaches a maximum between 75° and 80° as shown in Figure 8-7. For comparison purposes, one data set from both the two-dimensional and three-dimensional wind flow studies is included for $C_z = 10$.

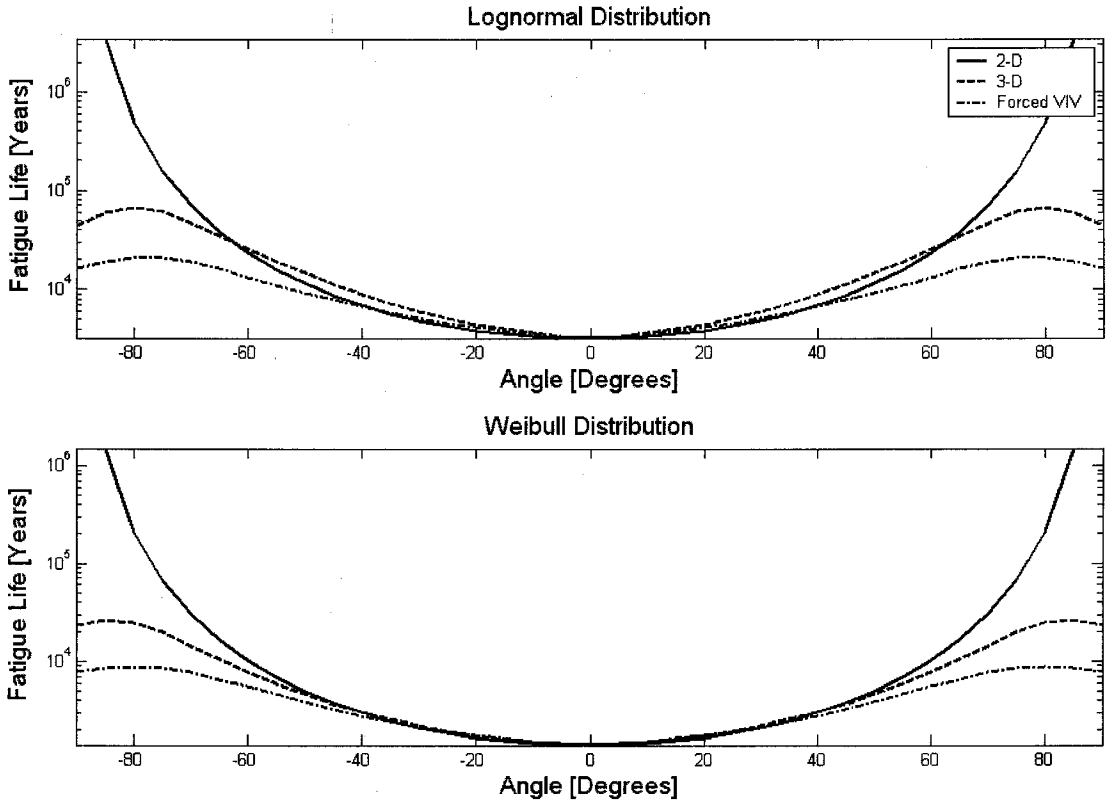

Figure 8-7: Forced Vibration Vortex Shedding Fatigue Life – Example Structure

Increasing θ beyond the range producing the maximum fatigue life estimates, substantial reductions in fatigue life are produced due to vortex shedding. Including the forced vibration term of the vortex shedding model increases the across-wind (lateral) stress process such that the estimated fatigue life is reduced. As provided in Figure 8-7, the across-wind (lateral) stress process for the two-dimensional case is zero because of the lack of wind loading in that direction. In the across-wind (lateral) direction where $\theta = 90^\circ$, the estimated fatigue life is reduced near 62% for the lognormal lifetime wind speed distribution when compared to the three-dimensional wind flow fatigue life estimates when vortex shedding is not considered. For the Weibull distribution, having a more well-defined tail and thus a higher probability of occurrence for larger forced vibration effects due to vortex shedding, the fatigue life is reduced nearly 66% when compared to the three-dimensional wind flow fatigue life estimates. These are substantial reductions and their importance should be noted.

The final fatigue life study for the example structure from Table 8-2 estimates the fatigue life for three-dimensional wind flow including the effects of the forced vibration and aerodynamic damping terms of the vortex shedding model. Variations in the limiting displacement parameter λ contained within the aerodynamic damping term are also included in this study. Figure 8-8 provides the stress process associated with one bin (bin number 20) of the divided lifetime wind speed distribution.

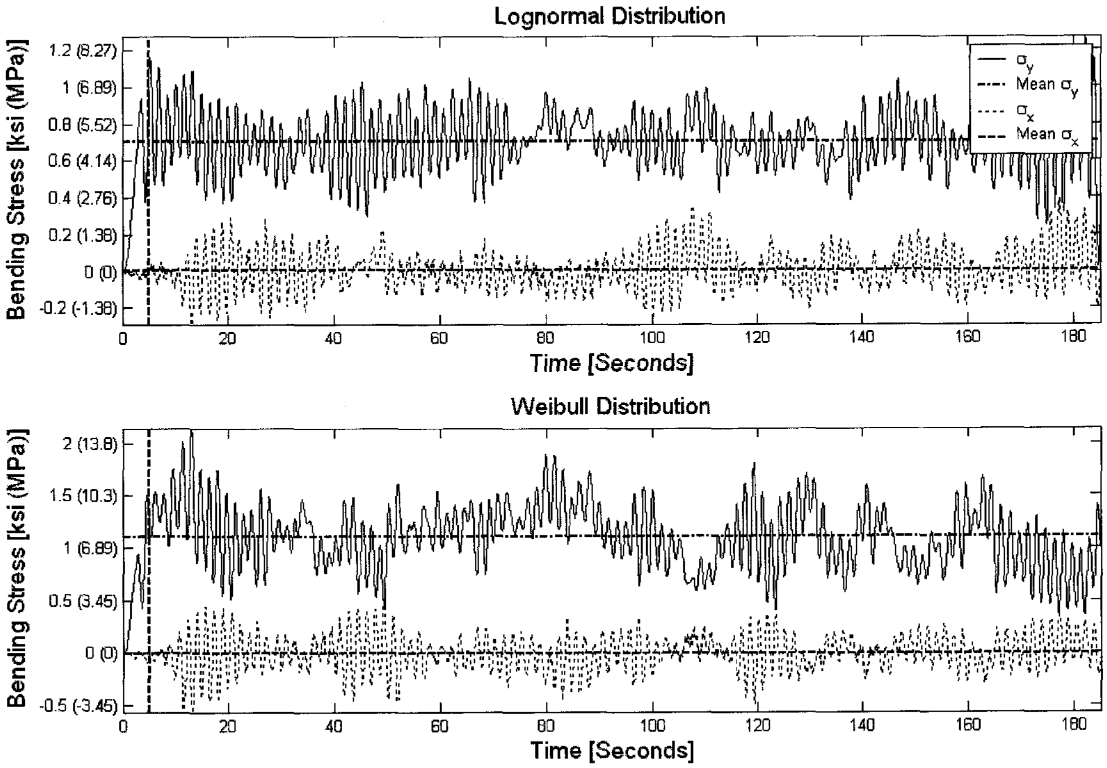

Figure 8-8: Aerodynamic Damping Vortex Shedding Stress Process – Example Structure

From Figure 8-8 it can be determined that all stress processes illustrated are to some degree a wide-band stress process.

Table 8-7 provides the estimated fatigue life for aerodynamic damping vortex shedding with a single variation in the spatial correlation parameters $C_{z(long)}$ and $C_{z(lat)}$ and multiple variations of the limiting displacement parameter λ as given in Table 8-2. The limiting displacement parameter is contained within the aerodynamic damping loading term of the vortex shedding model. The forced vibration loading term is also included in the vortex shedding model. Both the lognormal and Weibull distributions given in Table 8-1 are utilized to estimate the fatigue life of the structure. The structure properties of the example structure are as given in Table 8-3. The lowest wide-band (WB) stress process estimate of fatigue life is indicated in **bold** type in Table 8-7.

Angle $+\theta$	Fatigue Life	Example Structure – Fatigue Life (Years)					
		Lognormal Distribution			Weibull Distribution		
		Limiting Displacement Parameter, λ			Limiting Displacement Parameter, λ		
		0.01	1.0	10.0	0.01	1.0	10.0
0	LL	2,739	2,739	2,739	1,195	1,195	1,195
	WB	**3,286**	**3,286**	**3,286**	**1,434**	**1,434**	**1,434**
	UL	3,292	3,292	3,292	1,436	1,436	1,436
5	LL	2,885	2,868	2,870	1,224	1,237	1,239
	WB	3,462	3,442	3,444	1,469	1,485	1,487
	UL	3,468	3,448	3,449	1,471	1,487	1,489
10	LL	3,114	3,074	3,065	1,278	1,292	1,296
	WB	3,737	3,689	3,678	1,533	1,551	1,555
	UL	3,744	3,695	3,685	1,536	1,553	1,557
15	LL	3,358	3,336	3,302	1,321	1,363	1,382
	WB	4,029	4,003	3,962	1,586	1,636	1,659
	UL	4,036	4,010	3,969	1,588	1,639	1,662
20	LL	3,695	3,647	3,616	1,417	1,475	1,474
	WB	4,434	4,376	4,339	1,700	1,770	1,769
	UL	4,441	4,384	4,346	1,703	1,773	1,772
25	LL	4,147	4,005	4,018	1,542	1,608	1,609
	WB	4,976	4,805	4,820	1,850	1,930	1,932
	UL	4,985	4,813	4,829	1,853	1,933	1,935
30	LL	4,620	4,436	4,484	1,702	1,777	1,776
	WB	5,542	5,323	5,379	2,042	2,133	2,131
	UL	5,553	5,333	5,389	2,045	2,136	2,135
35	LL	5,222	4,960	5,182	1,905	1,998	2,017
	WB	6,264	5,950	6,216	2,286	2,397	2,420
	UL	6,277	5,961	6,228	2,290	2,401	2,424
40	LL	5,985	5,736	5,977	2,137	2,257	2,315
	WB	7,179	6,881	7,170	2,564	2,708	2,777
	UL	7,194	6,895	7,185	2,569	2,713	2,783
45	LL	7,015	6,766	7,007	2,455	2,610	2,649
	WB	8,413	8,116	8,404	2,945	3,131	3,177
	UL	8,432	8,133	8,422	2,951	3,137	3,184
50	LL	8,362	8,032	8,112	2,847	3,082	3,103
	WB	10,028	9,633	9,728	3,415	3,697	3,722
	UL	10,051	9,655	9,750	3,422	3,705	3,730
55	LL	10,017	9,618	9,723	3,316	3,694	3,808
	WB	12,011	11,534	11,658	3,977	4,430	4,566
	UL	12,041	11,561	11,687	3,986	4,440	4,577
60	LL	12,136	11,709	11,754	3,900	4,426	4,666
	WB	14,547	14,037	14,089	4,676	5,307	5,595
	UL	14,587	14,074	14,128	4,688	5,320	5,609
65	LL	14,180	14,271	14,330	4,607	5,353	5,765
	WB	16,992	17,103	17,171	5,522	6,416	6,910
	UL	17,044	17,154	17,224	5,537	6,434	6,930
70	LL	16,312	16,459	16,924	5,346	6,251	6,965
	WB	19,537	19,717	20,269	6,406	7,488	8,344
	UL	19,607	19,784	20,342	6,426	7,513	8,372
75	LL	17,387	17,492	18,392	5,879	6,955	7,851
	WB	20,812	20,941	22,013	7,040	8,327	9,400
	UL	20,899	21,025	22,107	7,066	8,360	9,437
80	LL	16,862	17,193	17,960	6,390	7,282	8,245
	WB	20,170	20,571	21,479	7,647	8,713	9,864
	UL	20,268	20,666	21,587	7,681	8,753	9,910
85	LL	14,889	15,088	16,389	6,340	7,085	7,983
	WB	17,801	18,043	19,588	7,582	8,472	9,545
	UL	17,897	18,135	19,700	7,620	8,516	9,596
90	LL	12,701	12,448	13,836	5,857	6,580	7,285
	WB	15,186	14,888	16,537	7,002	7,867	8,709
	UL	15,266	14,962	16,630	7,040	7,909	8,756

Table 8-7: Aerodynamic Damping Vortex Shedding Fatigue Life – Example Structure

This final fatigue life study of the example structure includes the complete vortex shedding model with both the forced vibration and aerodynamic damping loading terms. This study also had significant effects on the estimated fatigue life when compared to the three-dimensional wind flow study where vortex shedding effects were not considered. As for the previous study where only the forced vibration term of the vortex shedding model was considered, there were no effects on the estimated fatigue life at $\theta = 0^\circ$ because the stress process at this angle only considers bending about the across-wind (lateral) axis. However, as the angle θ is increased from 0°, the effects of vortex shedding become more pronounced. Again, the maximum fatigue life estimate is obtained between 75° and 80° as was seen for the forced vibration term only. Figure 8-9 illustrates the fatigue life for various angles θ. For comparison purposes, one data set from both the two-dimensional and three-dimensional wind flow studies in included for $C_z = 10$. Additionally, the data set from the forced vibration study is also included in Figure 8-9.

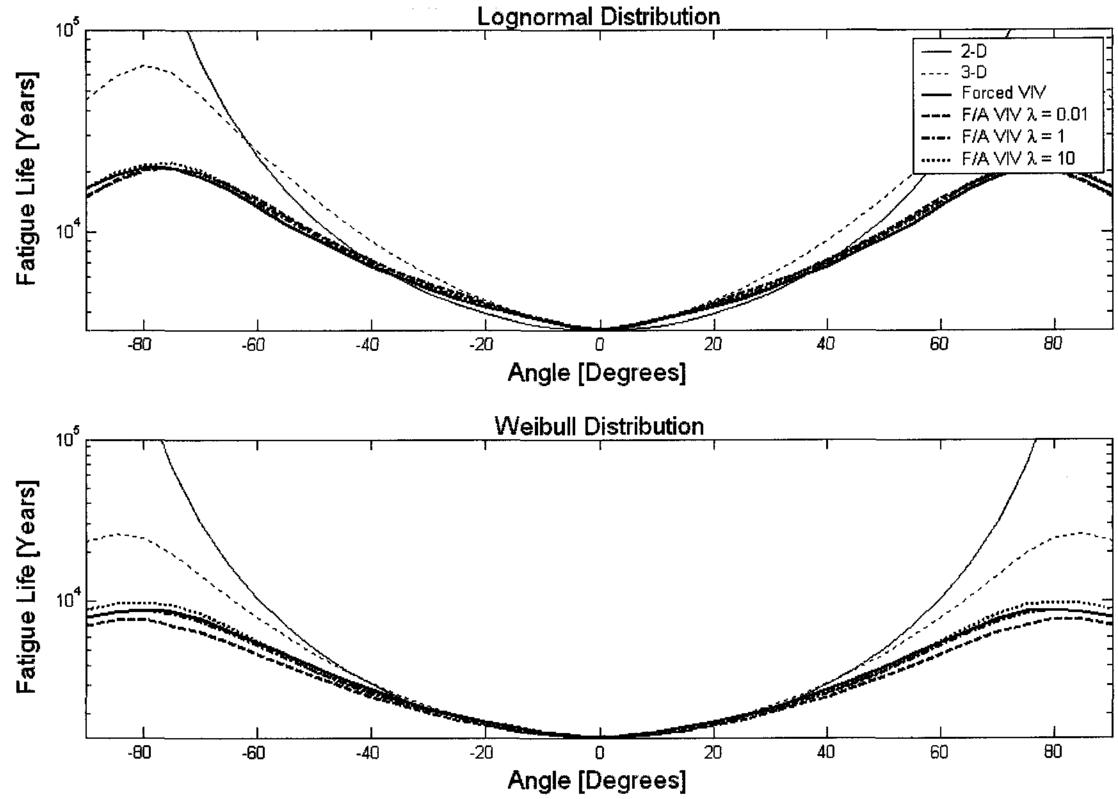

Figure 8-9: Aerodynamic Damping Vortex Shedding Fatigue Life – Example Structure

Increasing θ beyond the range producing the maximum fatigue life estimates, again, produce substantial reductions in fatigue life due to vortex shedding. In the across-wind (lateral) direction where $\theta = 90°$, the estimated fatigue life is reduced nearly 65% on average for the lognormal lifetime wind speed distribution when compared to the three-dimensional wind flow fatigue life estimates when vortex shedding is not considered. For the Weibull distribution, the fatigue life is reduced nearly 69% on average. These are substantial reductions and their importance should also be noted. However, these comparisons are made between a three-dimensional wind flow where vortex shedding was not considered and a three-dimensional wind flow where both the forced vibration and aerodynamic damping terms were included in the vortex shedding model.

Comparisons between the two vortex shedding models for their effects on fatigue life are equally as important. Inclusion of the aerodynamic damping term reduced the across-wind (lateral) fatigue life estimates by 9% and 10% on average for the lognormal and Weibull distributions, respectively. These reductions are much less than the reductions seen in comparing the effects of a vortex shedding model versus no vortex shedding. In regards to the limiting displacement parameter λ, an empirical value greater than unity produces the smallest fatigue life estimates. This observation is expected based on the vortex shedding model used for the aerodynamic damping term. Small values of λ will force the aerodynamic damping term to vanish at even small amplitudes of motion. Thus, the larger values of λ will allow for a greater range of structure motion for which the aerodynamic damping term will not be forced to zero.

8.3 High-Mast Lighting Structural Support Results

The second numerical investigation study of fatigue life considers a representative high-mast lighting (HML) structural support. The properties of the HML structural support must be considered in more detail. Figure 8-10 depicts schematically an HML structural support as considered by Goode and van de Lindt (2006). The properties of this structure are detailed in Table 8-8. The material properties of this structure are the same as those provided for the example structure of Chapter Two. The primary difference between the two structures is the tapered cross-section of the HML structural support. It should also be noted that there are two regions of overlapping lap joints between sections of this structure. In these regions, the stiffness of the cross-section is increased because of the joint construction. For the estimation of fatigue life, the base connection must be classified based on an AASHTO detail category. For the purposes of this study, the HML structural support base connection is assumed to be classified as an AASHTO E′ detail category. The details of this category are provided in Table 2-4 of Chapter Two.

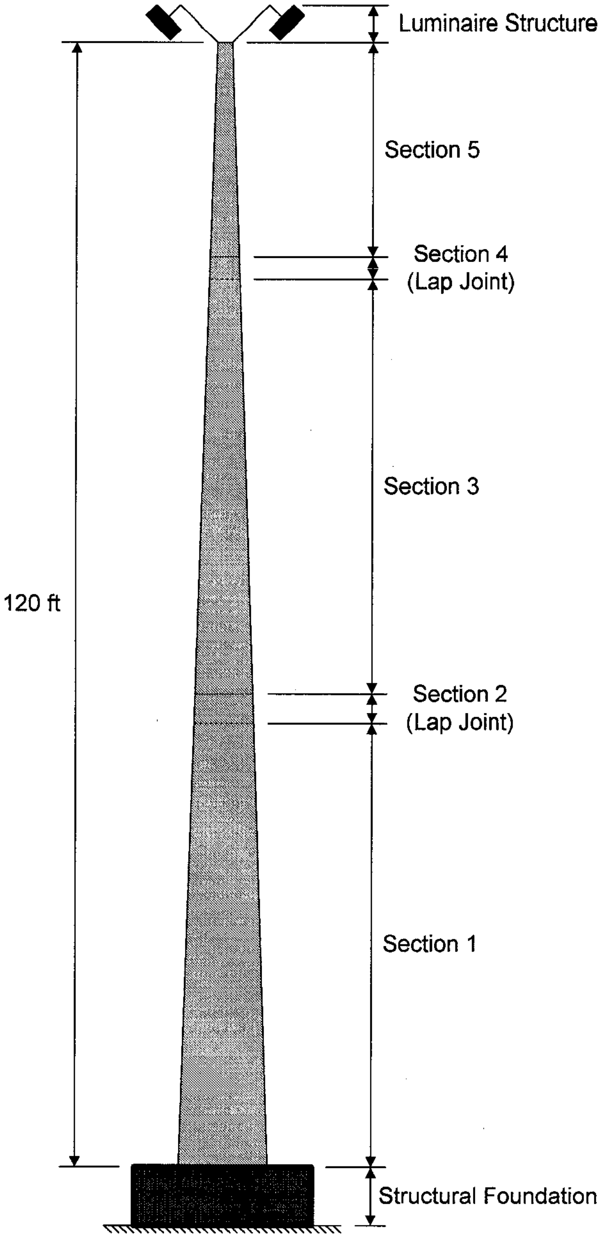

Figure 8-10: HML Structural Support

Property		Value
Number of Sections		5
Section 1	Length of Section	50 ft (15.24 m)
	Outside Diameter: Bottom/Top	26 in (660 mm) / 18.99 in (483 mm)
	Wall Thickness	0.375 in (9.53 mm)
Section 2 (Lap Joint)	Length of Section	3.49 ft (1,064 mm)
	Outside Diameter: Bottom/Top	19.5 in (495 mm) / 19.01 in (483 mm)
	Wall Thickness	0.625 in (15.88 mm)
Section 3	Length of Section	46.35 ft (14.13 m)
	Outside Diameter: Bottom/Top	19.01 in (483 mm) / 12.525 in (318 mm)
	Wall Thickness	0.25 in (6.35 mm)
Section 4 (Lap Joint)	Length of Section	2.68 ft (816 mm)
	Outside Diameter: Bottom/Top	13 in (330 mm) / 12.625 in (321 mm)
	Wall Thickness	0.489 in (12.42 mm)
Section 5	Length of Section	17.48 ft (5.33 mm)
	Outside Diameter: Bottom/Top	12.625 in (321 mm) / 10.18 in (259 mm)
	Wall Thickness	0.239 in (6.07 mm)
Luminaire Structure Weight		666 lb (302 kg)
Luminaire Structure Projected Area: Along-Wind / Across-Wind		11.5 ft^2 (1.07 m^2) / 11.5 ft^2 (1.07 m^2)
AASHTO Base Connection Detail Category		E′

Table 8-8: HML Structural Support Properties for Fatigue Life

This second study considers the structure outlined in Figure 8-10 and Table 8-8 for variations in the lifetime wind speed distribution, wind flow properties, and vortex shedding properties. The variations in the lifetime wind speed distribution are outlined in Table 8-1. The variations in the wind flow and vortex shedding properties are outlined in Table 8-2.

Results of Analysis

Fatigue life estimates were first obtained for two-dimensional wind flow with variations in the spatial correlation parameter $C_{z(long)}$ as given in Table 8-2. The stress process at the base of the structure is the source of the fatigue damage. Dividing the lifetime wind speed distribution into 25 equal width bins produces 25 separate analyses that result in a stress process that has a probability of occurrence equal to the area of the bin. Figure 8-11 provides the stress process for one such bin (bin number 20) with full spatial correlation of the two-dimensional wind flow. As for the example structure study, the vertical dashed line indicates the time range for the linear ramp-up and the horizontal line represents the mean level for the stress process beyond the initial ramp-up time range. In the determination of the variance of the stress process needed to determine the expected damage associated with the stress process, the initial five seconds of the stress process within the linear ramp-up range is not included.

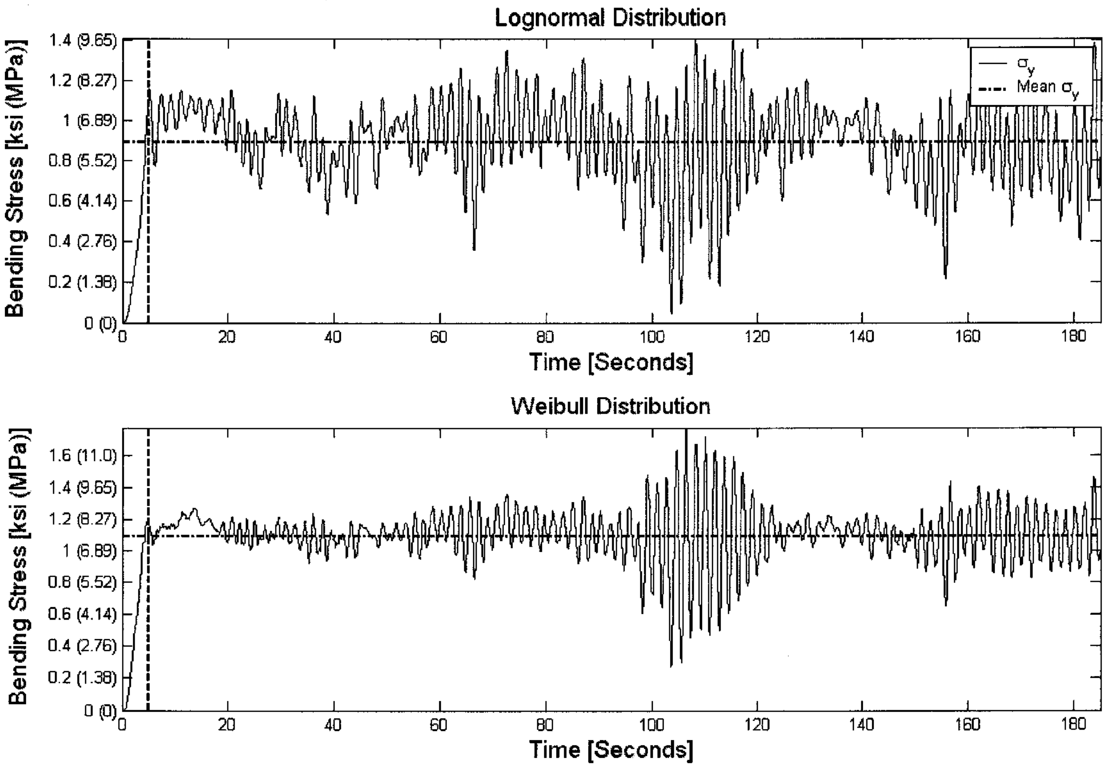
Lognormal Distribution

Weibull Distribution

Figure 8-11: 2-D Wind Flow Stress Process – HML Structural Support

From Figure 8-11 it can be determined that both stress processes illustrated are to some degree a wide-band stress process. As will be seen, the estimated fatigue life is closer to the upper limit for a wide-band stress process rather than the lower limit for estimated fatigue life characterized by a narrow-band stress process.

Table 8-9 provides the results of this first study. For the case of $C_{z(long)} = 0$, there is strong spatial correlation of the simulated wind speed time series. Alternatively, when $C_{z(long)} = +\infty$, there is weak spatial correlation of the simulated wind speed time series. Both the lognormal and Weibull distributions given in Table 8-1 are utilized to estimate the fatigue life of the structure. For this section, the structure properties are as given for the HML structural support in Figure 8-10 and Table 8-8. The lowest wide-band (WB) stress process estimate of fatigue life is indicated in **bold** type in Table 8-9.

Angle $+\theta$	Fatigue Life	High-Mast Lighting Structure – Fatigue Life (Years)					
		Lognormal Distribution			Weibull Distribution		
		$C_{z(long)}$			$C_{z(long)}$		
		0	10	$+\infty$	0	10	$+\infty$
0	LL	1,299	7,620	73,516	705	3,008	17,072
	WB	**1,569**	**9,203**	**88,778**	**852**	**3,633**	**20,617**
	UL	1,570	9,214	88,895	853	3,637	20,643
5	LL	1,313	7,708	74,362	714	3,043	17,268
	WB	1,587	9,309	89,799	862	3,675	20,854
	UL	1,588	9,320	89,917	863	3,679	20,880
10	LL	1,360	7,978	76,971	739	3,149	17,874
	WB	1,643	9,636	92,950	892	3,804	21,586
	UL	1,644	9,647	93,072	893	3,808	21,613
15	LL	1,441	8,456	81,574	783	3,338	18,943
	WB	1,741	10,212	98,508	946	4,031	22,877
	UL	1,742	10,224	98,638	947	4,036	22,905
20	LL	1,565	9,184	88,598	850	3,625	20,574
	WB	1,891	11,091	106,991	1,027	4,379	24,847
	UL	1,892	11,105	107,131	1,028	4,383	24,878
25	LL	1,744	10,236	98,753	948	4,041	22,932
	WB	2,107	12,363	119,254	1,145	4,880	27,695
	UL	2,109	12,378	119,411	1,146	4,886	27,729
30	LL	1,999	11,732	113,184	1,086	4,631	26,283
	WB	2,415	14,169	136,681	1,312	5,594	31,742
	UL	2,417	14,186	136,861	1,313	5,600	31,781
35	LL	2,362	13,864	133,746	1,283	5,472	31,058
	WB	2,854	16,743	161,511	1,550	6,610	37,508
	UL	2,857	16,764	161,724	1,552	6,617	37,555
40	LL	2,889	16,951	163,535	1,569	6,691	37,976
	WB	3,490	20,472	197,484	1,896	8,082	45,862
	UL	3,493	20,497	197,744	1,898	8,091	45,919
45	LL	3,673	21,553	207,928	1,995	8,508	48,284
	WB	4,437	26,030	251,093	2,410	10,276	58,312
	UL	4,441	26,061	251,424	2,413	10,287	58,385
50	LL	4,889	28,692	276,797	2,656	11,325	64,277
	WB	5,907	34,651	334,259	3,209	13,679	77,626
	UL	5,912	34,693	334,699	3,212	13,695	77,723
55	LL	6,881	40,381	389,570	3,738	15,940	90,465
	WB	8,313	48,769	470,443	4,516	19,253	109,252
	UL	8,320	48,828	471,062	4,520	19,274	109,389
60	LL	10,388	60,959	588,090	5,643	24,062	136,564
	WB	12,550	73,621	710,175	6,817	29,064	164,925
	UL	12,561	73,710	711,109	6,824	29,096	165,131
65	LL	17,202	100,947	973,871	9,345	39,847	226,149
	WB	20,782	121,915	1,176,043	11,289	48,129	273,114
	UL	20,800	122,064	1,177,590	11,300	48,182	273,456
70	LL	32,453	190,447	1,837,308	17,631	75,176	426,654
	WB	39,207	230,005	2,218,727	21,299	90,800	515,258
	UL	39,242	230,286	2,221,645	21,319	90,901	515,903
75	LL	74,887	439,469	4,239,710	40,684	173,473	984,532
	WB	90,473	530,752	5,119,859	49,148	209,528	1,188,993
	UL	90,552	531,400	5,126,594	49,194	209,760	1,190,481
80	LL	247,952	1,455,088	14,037,729	134,705	574,370	3,259,797
	WB	299,558	1,757,326	16,951,912	162,729	693,748	3,936,769
	UL	299,820	1,759,470	16,974,212	162,883	694,519	3,941,697
85	LL	1,960,924	11,507,523	111,017,030	1,065,308	4,542,387	25,780,019
	WB	2,369,046	13,897,764	134,063,770	1,286,937	5,486,490	31,133,839
	UL	2,371,120	13,914,724	134,240,130	1,288,154	5,492,586	31,172,813
90	LL	$+\infty$	$+\infty$	$+\infty$	$+\infty$	$+\infty$	$+\infty$
	WB	$+\infty$	$+\infty$	$+\infty$	$+\infty$	$+\infty$	$+\infty$
	UL	$+\infty$	$+\infty$	$+\infty$	$+\infty$	$+\infty$	$+\infty$

Table 8-9: 2-D Wind Flow Fatigue Life – HML Structural Support

Similar observations can be made for the HML structure as were made for the example structure for the two-dimensional wind flow study for fatigue life. As expected, the lowest fatigue life occurs when $C_{z(long)} = 0$ providing strong spatial correlation of the simulated wind speed time series. A significant observation can also be made in regards to the assumption of a two-dimensional wind flow. In this assumption, only along-wind (longitudinal) wind speed time series are utilized to estimate the fatigue life. As the angle θ is increased from the along-wind (longitudinal) axis at 0°, the estimated fatigue life increases slowly. As the angle θ approaches the across-wind (lateral) axis at 90°, the estimated fatigue life increases quickly eventually obtaining infinite fatigue life. Figure 8-12 illustrates this observation for spatial correlation parameters $C_{z(long)} = C_z = 0$, 10, and $+\infty$ for the along-wind (longitudinal) turbulence component u'.

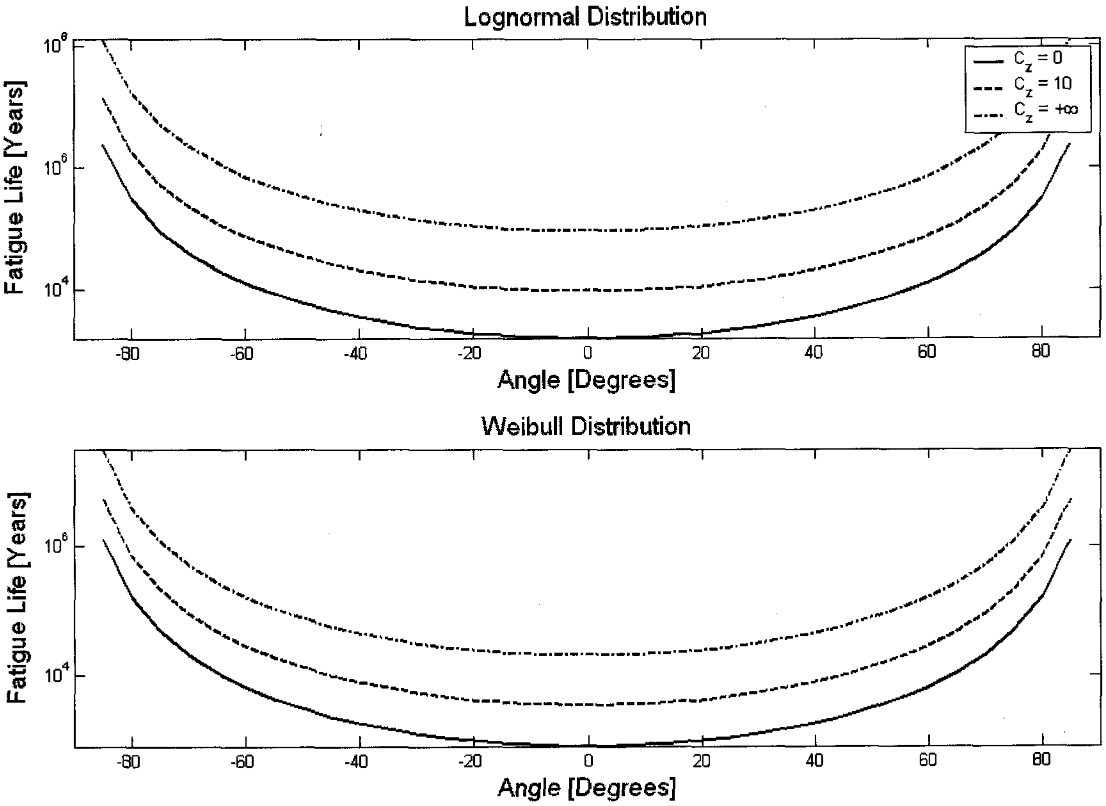

Figure 8-12: 2-D Wind Flow Fatigue Life – HML Structural Support

Comparisons of the lower limit (LL), wide-band (WB), and upper limit (UL) fatigue life estimates also yield interesting results. The lower limit (LL) fatigue life estimate is approximately 15 – 20% lower than the wide-band (WB) fatigue life estimate. Alternatively, the wide-band (WB) and upper limit (UL) fatigue life estimates are consistently close in magnitude to each other. Thus, the stress process used to estimate the fatigue life is indeed a wind-band stress process.

Finally, a comparison of the lifetime wind speed distributions also yield interesting results. The lognormal distribution based on an assumed mean wind speed and coefficient of variation (COV) produced higher fatigue life estimates than the Weibull distribution based on data from the Stapleton weather station. However, the COV of the Stapleton data is approximately 50%, whereas the COV of the assumed distribution is only 25%. Thus, the high wind tail of the Weibull distribution has a higher probability of occurrence than the lognormal distribution. The expected damage due to these high winds will then occur with a higher probability of occurrence thus reducing the estimated fatigue life.

Following Table 8-2, fatigue life estimates were next obtained for three-dimensional wind flow with variations in the spatial correlation parameters $C_{z(long)}$ and $C_{z(lat)}$. Figure 8-13 provides the stress process associated with one bin (bin number 20) of the divided lifetime wind speed distribution with full spatial correlation of both the along-wind (longitudinal) and across-wind (lateral) turbulence components u' and v', respectively, for the three-dimensional wind flow. The stress process σ_y about the across-wind (lateral) direction y-axis is responsible for fatigue damage in the along-wind (longitudinal) direction. The stress process σ_x about the along-wind (longitudinal) direction x-axis is responsible for fatigue damage in the across-wind (lateral) direction.

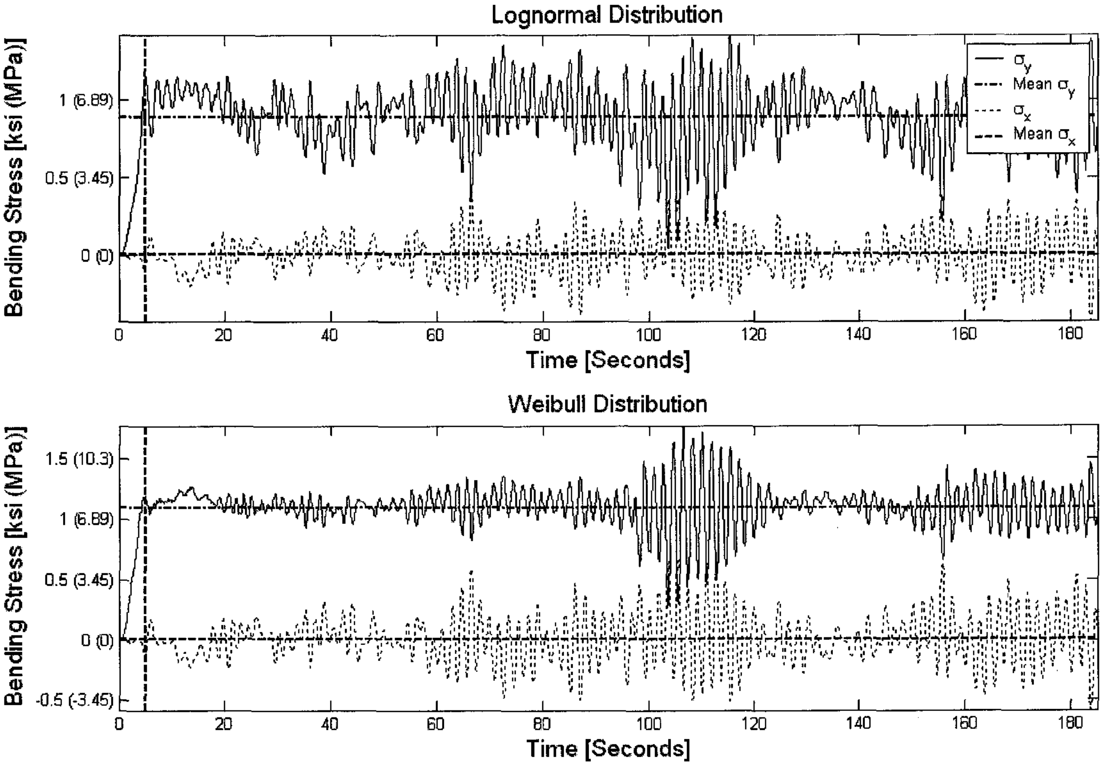

Lognormal Distribution

Weibull Distribution

Figure 8-13: 3-D Wind Flow Stress Process – HML Structural Support

From Figure 8-13 it can be determined that all stress processes illustrated are to some degree a wide-band stress process.

Table 8-10 provides the estimated fatigue life for three-dimensional wind flow with variations in the spatial correlation parameters $C_{z(long)}$ and $C_{z(lat)}$ as given in Table 8-2. For the case of $C_{z(long)} = C_{z(lat)} = 0$, there is strong spatial correlation of the simulated wind speed time series. Alternatively, when $C_{z(long)} = C_{z(lat)} = +\infty$, there is weak spatial correlation of the simulated wind speed time series. Both the lognormal and Weibull distributions given in Table 8-1 are utilized to estimate the fatigue life of the structure. The structure properties of the HML structural support are given in Figure 8-10 and Table

8-8. The lowest wide-band (WB) stress process estimate of fatigue life is indicated in **bold** type in Table 8-10.

Angle $+\theta$	Fatigue Life	High-Mast Lighting Structure – Fatigue Life (Years)					
		Lognormal Distribution			Weibull Distribution		
		($C_{z(long)}$, $C_{z(lat)}$)			($C_{z(long)}$, $C_{z(lat)}$)		
		(0,0)	(10,10)	(+∞,+∞)	(0,0)	(10,10)	(+∞,+∞)
0	LL	1,299	7,620	73,516	705	3,008	17,072
	WB	**1,569**	**9,203**	**88,778**	**852**	**3,633**	**20,617**
	UL	1,570	9,214	88,895	853	3,637	20,643
5	LL	1,514	8,581	86,232	835	3,419	19,660
	WB	1,829	10,363	104,132	1,009	4,130	23,742
	UL	1,831	10,376	104,270	1,010	4,135	23,772
10	LL	1,819	10,150	104,628	1,014	3,973	23,227
	WB	2,198	12,258	126,345	1,225	4,799	28,050
	UL	2,200	12,274	126,514	1,226	4,804	28,085
15	LL	2,249	12,411	130,773	1,274	4,781	28,608
	WB	2,717	14,988	157,916	1,539	5,774	34,548
	UL	2,719	15,007	158,129	1,541	5,781	34,593
20	LL	2,902	15,611	169,794	1,679	5,899	36,237
	WB	3,506	18,852	205,033	2,029	7,125	43,760
	UL	3,510	18,877	205,313	2,031	7,133	43,818
25	LL	3,942	20,761	230,825	2,323	7,647	47,828
	WB	4,762	25,071	278,726	2,806	9,235	57,756
	UL	4,766	25,104	279,110	2,810	9,246	57,833
30	LL	5,742	29,725	338,734	3,422	10,325	66,061
	WB	6,936	35,895	409,023	4,133	12,470	79,773
	UL	6,944	35,943	409,592	4,138	12,484	79,880
35	LL	8,874	45,385	526,298	5,316	14,638	95,668
	WB	10,718	54,804	635,496	6,421	17,679	115,524
	UL	10,730	54,879	636,391	6,428	17,700	115,680
40	LL	14,968	77,235	913,783	8,982	22,226	146,923
	WB	18,077	93,261	1,103,361	10,847	26,844	177,414
	UL	18,099	93,392	1,104,933	10,860	26,875	177,657
45	LL	28,643	154,386	1,801,527	16,640	34,956	241,467
	WB	34,592	186,414	2,175,244	20,095	42,220	291,573
	UL	34,635	186,681	2,178,379	20,121	42,269	291,978
50	LL	70,223	344,814	4,234,117	34,039	55,101	422,247
	WB	84,800	416,337	5,112,377	41,105	66,555	509,859
	UL	84,912	416,944	5,119,831	41,160	66,627	510,575
55	LL	198,335	821,865	11,186,176	53,296	79,776	729,311
	WB	239,488	992,329	13,506,306	64,366	96,363	880,622
	UL	239,823	993,787	13,526,156	64,445	96,464	881,872
60	LL	423,868	1,073,808	14,573,527	49,129	97,644	1,085,475
	WB	511,826	1,296,526	17,596,135	59,345	117,950	1,310,662
	UL	512,535	1,298,433	17,622,091	59,406	118,070	1,312,540
65	LL	327,901	908,537	8,731,537	31,835	102,539	1,165,801
	WB	396,019	1,097,016	10,542,604	38,461	123,865	1,407,664
	UL	396,493	1,098,589	10,558,044	38,494	123,988	1,409,669
70	LL	133,339	668,696	4,077,996	18,437	90,425	811,202
	WB	161,083	807,509	4,924,103	22,279	109,238	979,553
	UL	161,231	808,577	4,931,052	22,294	109,341	980,893
75	LL	54,309	405,248	1,861,024	10,711	66,827	457,836
	WB	65,632	489,484	2,247,419	12,946	80,740	552,921
	UL	65,670	490,019	2,250,322	12,952	80,806	553,608
80	LL	25,233	210,440	945,449	6,404	44,600	255,218
	WB	30,502	254,272	1,142,006	7,741	53,899	308,293
	UL	30,511	254,460	1,143,223	7,743	53,929	308,606
85	LL	13,823	121,051	534,879	4,091	29,587	150,468
	WB	16,712	146,320	646,355	4,946	35,766	181,832
	UL	16,715	146,373	646,768	4,947	35,776	181,944
90	LL	8,275	73,195	337,604	2,756	19,747	95,989
	WB	10,003	88,487	408,082	3,331	23,870	116,010
	UL	10,005	88,506	408,225	3,332	23,877	116,069

Table 8-10: 3-D Wind Flow Fatigue Life – HML Structural Support

Similar to the study considering only two-dimensional wind flow, the lowest fatigue life occurs when $C_{z(long)} = C_{z(lat)} = 0$ providing strong spatial correlation of the three-dimensional simulated wind speed time series. The three-dimensional wind flow, however, utilized both the along-wind (longitudinal) and across-wind (lateral) wind speed time series to estimate the fatigue life. Thus, as the angle θ is increased from 0° the estimated fatigue life reaches a maximum before it reaches 90°. Indeed, the estimated fatigue life maximum occurs between 60° and 80° depending on the stress process characterization. Figure 8-14 illustrates this observation for spatial correlation parameters $C_{z(long)} = C_{z(lat)} = C_z = 0$, 10, and $+\infty$ for the along-wind (longitudinal) and across-wind (lateral) turbulence components u' and v', respectively. For comparison purposes, one data set from the two-dimensional wind flow study is included for $C_z = 0$.

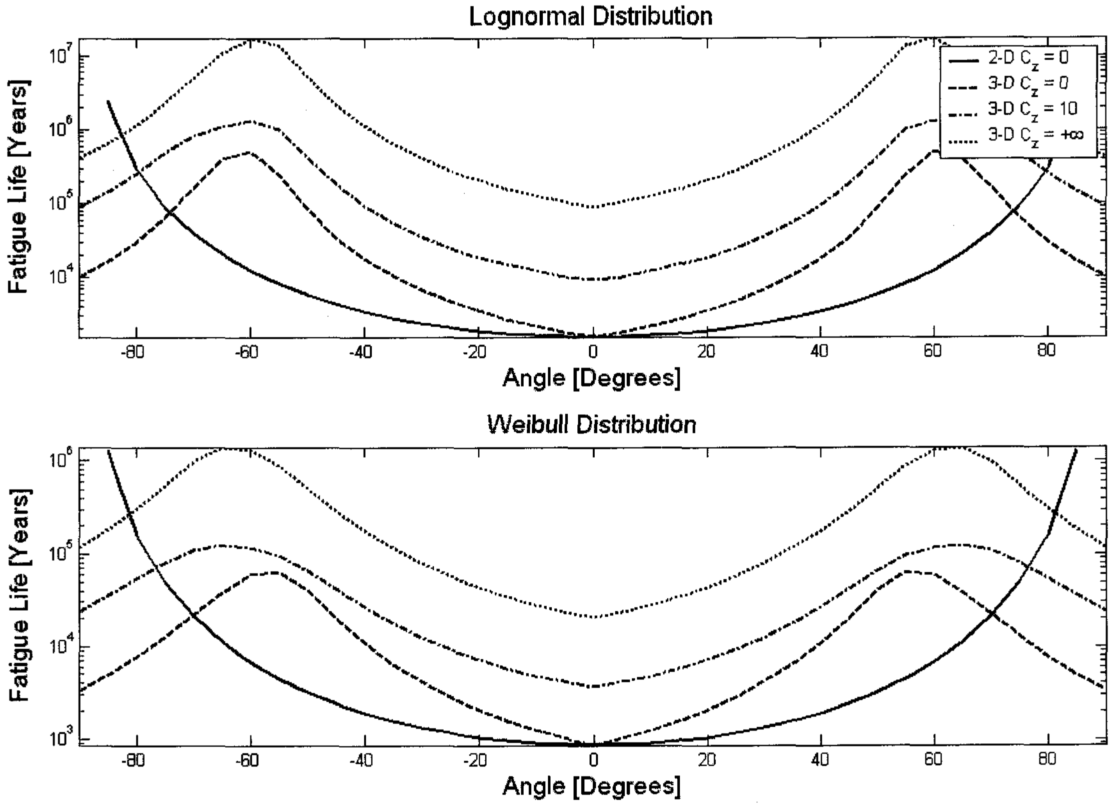

Figure 8-14: 3-D Wind Flow Fatigue Life – HML Structural Support

As can be seen from Table 8-10 and Figure 8-14, the estimated fatigue life in the across-wind (lateral) direction at $\theta = 90^\circ$ is much larger than in the along-wind (longitudinal) direction at $\theta = 0^\circ$. This can be attributed to the relatively small magnitude of the stress process for the across-wind (lateral) fatigue life estimate compared to the stress process for the along-wind (longitudinal) fatigue life estimate. However, the inclusion of the across-wind (lateral) simulated wind speed time series significantly reduces the fatigue life at angles near 90° in comparison to the two-dimensional wind flow where this time series is not considered.

The next progression provided in Table 8-2 states that fatigue life estimates were next obtained for three-dimensional wind flow including the effect of the forced vibration term in the vortex shedding model. Figure 8-15 provides the stress process associated with one bin (bin number 20) of the divided lifetime wind speed distribution.

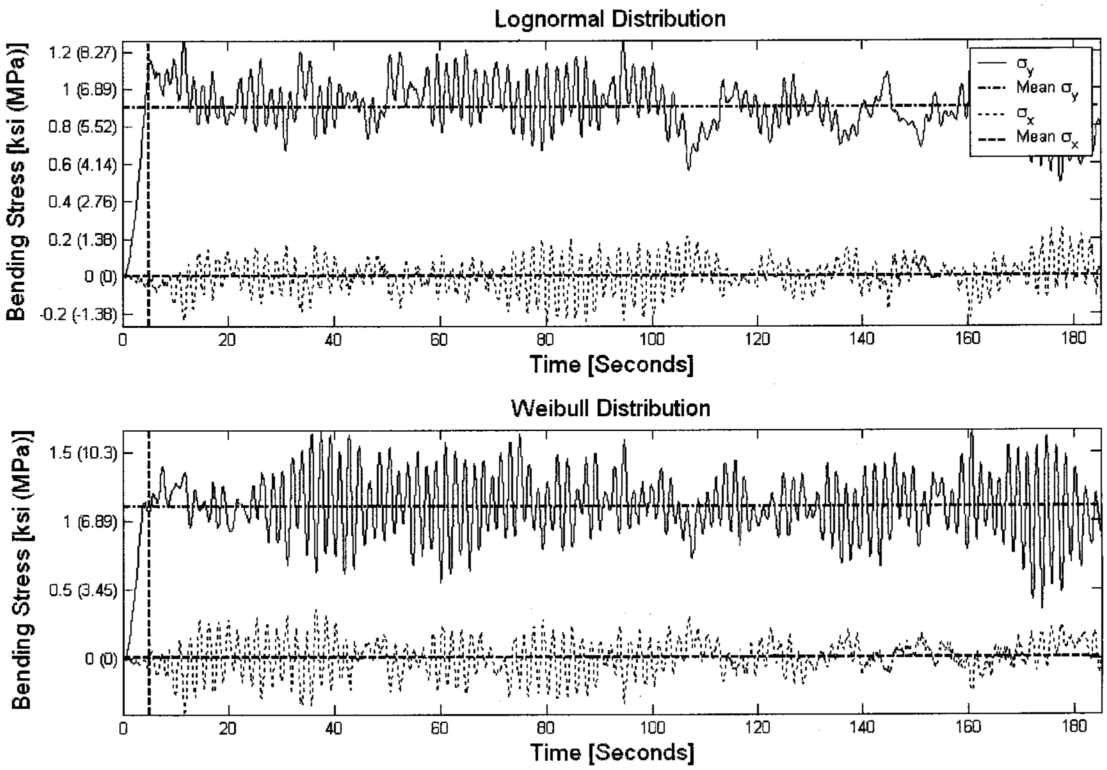

Figure 8-15: Forced Vibration Vortex Shedding Stress Process – HML Structural Support

From Figure 8-15 it can be determined that all stresses illustrated are to some degree a wide-band stress process.

Table 8-11 provides the estimated fatigue life for forced vibration vortex shedding with a single variation in the spatial correlation parameters $C_{z(long)}$ and $C_{z(lat)}$ as given in Table 8-

2. There is no empirical parameter within the forced vibration loading term of the vortex shedding model. Both lognormal and Weibull distributions given in Table 8-1 are utilized to estimate the fatigue life of the structure. For this section, the structure properties are as given for the HML structural support in Figure 8-10 and Table 8-8. The lowest wide-band (WB) stress process estimate of fatigue life is indicated in **bold** type in Table 8-11.

Angle $+\theta$	Fatigue Life	High-Mast Lighting Structure – Fatigue Life (Years)	
		Lognormal Distribution	Weibull Distribution
0	LL	7,620	3,008
	WB	**9,203**	**3,633**
	UL	9,214	3,637
5	LL	8,456	3,398
	WB	10,212	4,104
	UL	10,225	4,109
10	LL	9,538	3,846
	WB	11,518	4,646
	UL	11,533	4,651
15	LL	10,867	4,379
	WB	13,123	5,289
	UL	13,141	5,295
20	LL	12,164	5,104
	WB	14,688	6,164
	UL	14,709	6,172
25	LL	13,928	6,068
	WB	16,816	7,328
	UL	16,841	7,337
30	LL	16,324	7,442
	WB	19,708	8,986
	UL	19,739	8,998
35	LL	18,556	9,005
	WB	22,400	10,872
	UL	22,438	10,889
40	LL	21,373	11,080
	WB	25,796	13,375
	UL	25,843	13,397
45	LL	24,618	13,782
	WB	29,707	16,635
	UL	29,768	16,665
50	LL	28,767	16,699
	WB	34,705	20,151
	UL	34,784	20,192
55	LL	32,045	20,163
	WB	38,649	24,326
	UL	38,748	24,381
60	LL	34,599	23,221
	WB	41,714	28,007
	UL	41,837	28,079
65	LL	34,207	24,592
	WB	41,219	29,649
	UL	41,362	29,737
70	LL	31,150	23,158
	WB	37,511	27,907
	UL	37,666	28,003
75	LL	27,353	19,709
	WB	32,910	23,738
	UL	33,075	23,832
80	LL	22,979	15,683
	WB	27,620	18,879
	UL	27,786	18,963
85	LL	18,984	11,994
	WB	22,800	14,433
	UL	22,955	14,503
90	LL	15,598	9,231
	WB	18,739	11,111
	UL	18,861	11,162

Table 8-11: Forced Vibration Vortex Shedding Fatigue Life – HML Structural Support

Inclusion of the forced vibration loading term of the vortex shedding model for the estimation of fatigue life had significant effects in the across-wind (lateral) direction stress process. However, at angles near θ = 0°, the additional loading due to vortex shedding did not effect the stress process. Hence, the estimated fatigue life at 0° was also unaffected. As the angle θ is increased from 0°, the estimated fatigue life reaches a maximum between 75° and 80° as shown in Figure 8-16. For comparison purposes, one data set from both the two-dimensional and three-dimensional wind flow studies is included for $C_z = 10$.

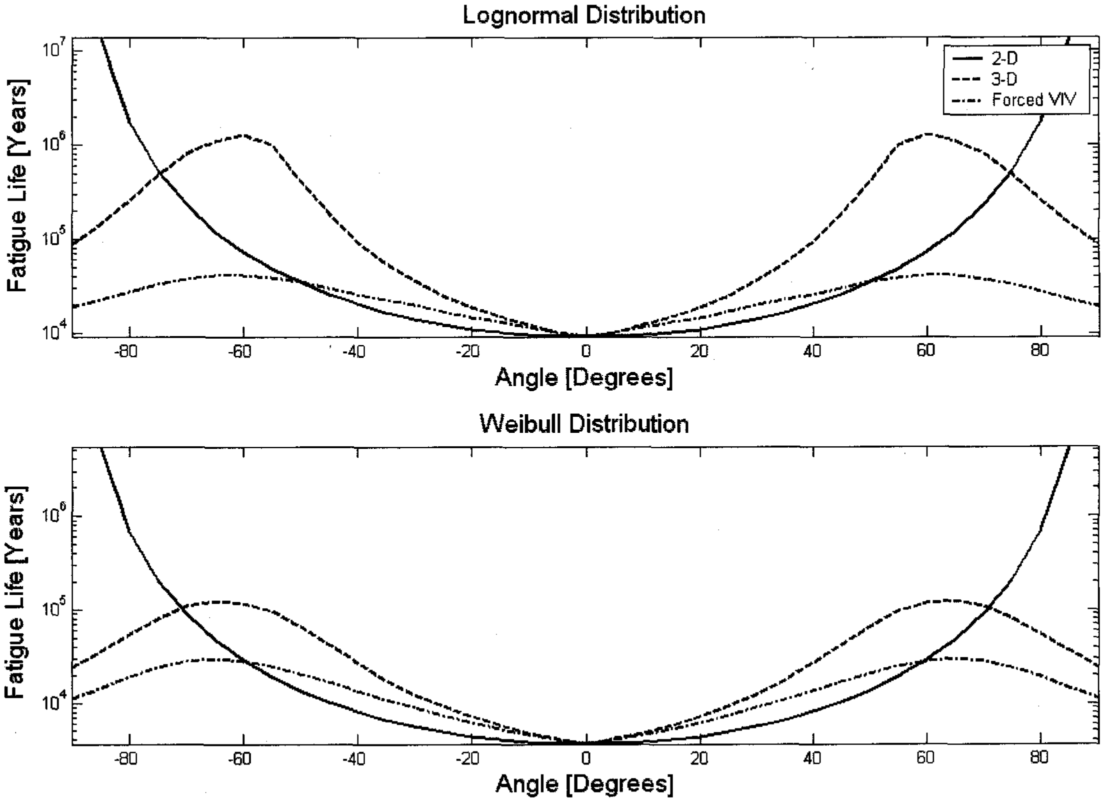

Lognormal Distribution

Weibull Distribution

Figure 8-16: Forced Vibration Vortex Shedding Fatigue Life – HML Structural Support

Increasing θ beyond the range producing the maximum fatigue life estimates, substantial reductions in fatigue life are produced due to vortex shedding. In the across-wind (lateral) direction where $\theta = 90^\circ$, the estimated fatigue life is reduced nearly 76% for the lognormal lifetime wind speed distribution when compared to the three-dimensional wind flow fatigue life estimates when vortex shedding is not considered. For the Weibull distribution the fatigue life is reduced nearly 57% when compared to the three-dimensional wind flow fatigue life estimates. These results are opposite in comparison to the example structure results for forced vibration vortex shedding. Thus, it is believed that the tapered cross-section of the HML structural support does have an effect on the forced vibration forces generated at high wind speeds. These are substantial reductions and their importance should be noted.

The final fatigue life study for the HML structural support from Table 8-2 estimates the fatigue life for three-dimensional wind flow including the effects of the forced vibration and aerodynamic damping terms of the vortex shedding model. Variations in the limiting displacement parameter λ contained within the aerodynamic damping term are also included in this study. Figure 8-17 provides the stress process associated with one bin (bin number 20) of the divided lifetime wind speed distribution.

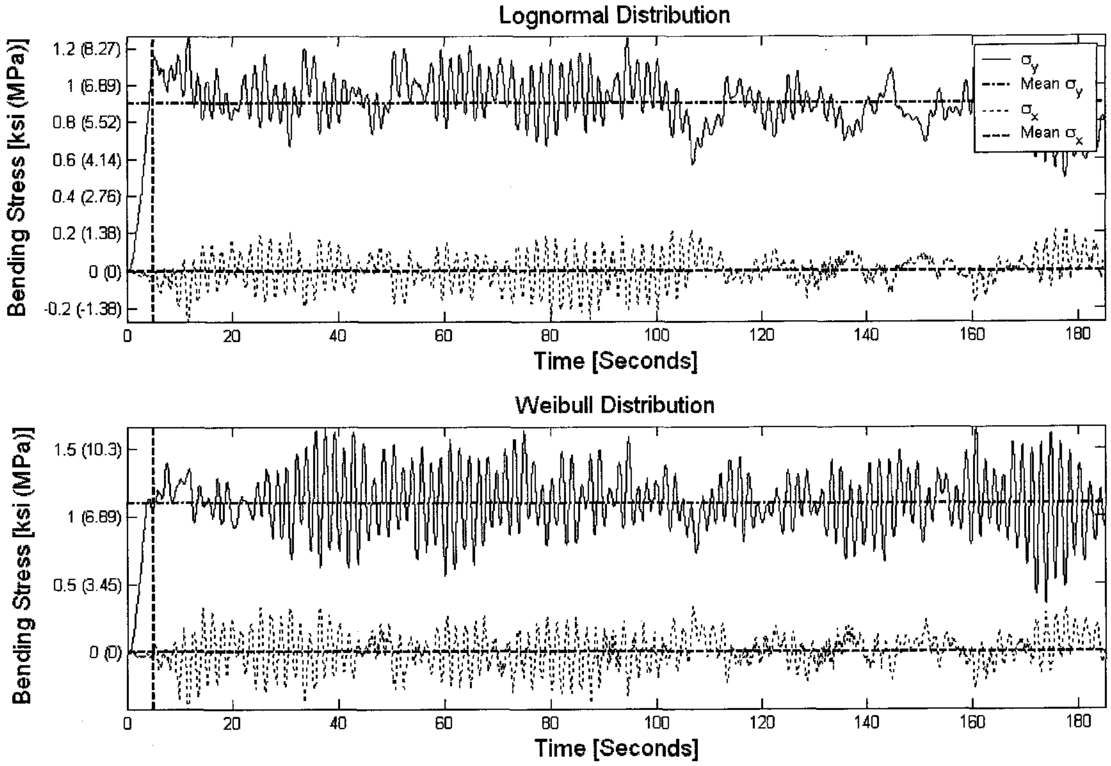

Figure 8-17: Aerodynamic Damping Vortex Shedding Stress Process – HML Structural Support

From Figure 8-17 it can be determined that all stress processes illustrated are to some degree a wide-band stress process.

Table 8-12 provides the estimated fatigue life for aerodynamic damping vortex shedding with a single variation in the spatial correlation parameters $C_{z(long)}$ and $C_{z(lat)}$ and multiple variations of the limiting displacement parameter λ as given in Table 8-2. The limiting displacement parameter is contained within the aerodynamic damping loading term of the vortex shedding model. The forced vibration loading term is also included in the vortex shedding model. Both the lognormal and Weibull distributions given in Table 8-1 are utilized to estimate the fatigue life of the structure. The structure properties of the HML structural support are given in Figure 8-10 and Table 8-8. The lowest wide-band (WB) stress process estimate of fatigue life is indicated in **bold** type in Table 8-12.

Angle $+\theta$	Fatigue Life	High-Mast Lighting Structure – Fatigue Life (Years)					
		Lognormal Distribution			Weibull Distribution		
		Limiting Displacement Parameter, λ			Limiting Displacement Parameter, λ		
		0.01	1.0	10.0	0.01	1.0	10.0
0	LL	7,620	7,620	7,620	3,008	3,008	3,008
	WB	**9,203**	**9,203**	**9,203**	**3,633**	**3,633**	**3,633**
	UL	9,214	9,214	9,214	3,637	3,637	3,637
5	LL	8,486	8,446	8,447	3,423	3,405	3,411
	WB	10,248	10,200	10,201	4,134	4,113	4,119
	UL	10,261	10,212	10,214	4,139	4,118	4,124
10	LL	9,489	9,492	9,477	3,881	3,869	3,891
	WB	11,459	11,463	11,445	4,687	4,673	4,699
	UL	11,474	11,478	11,460	4,692	4,678	4,704
15	LL	10,733	10,777	10,762	4,443	4,452	4,482
	WB	12,960	13,014	12,996	5,365	5,376	5,413
	UL	12,978	13,031	13,013	5,372	5,383	5,419
20	LL	12,332	12,204	12,328	5,133	5,144	5,290
	WB	14,891	14,736	14,886	6,199	6,212	6,388
	UL	14,912	14,757	14,907	6,207	6,220	6,397
25	LL	13,873	13,827	13,929	6,165	6,047	6,289
	WB	16,750	16,695	16,818	7,445	7,303	7,594
	UL	16,775	16,719	16,843	7,455	7,312	7,604
30	LL	16,110	16,209	16,024	7,426	7,284	7,638
	WB	19,449	19,569	19,345	8,967	8,795	9,222
	UL	19,480	19,600	19,376	8,979	8,807	9,235
35	LL	18,463	18,647	18,784	9,136	8,882	9,346
	WB	22,287	22,509	22,675	11,030	10,724	11,284
	UL	22,325	22,547	22,713	11,047	10,741	11,301
40	LL	21,146	21,147	21,577	11,281	11,002	11,413
	WB	25,522	25,523	26,042	13,619	13,281	13,777
	UL	25,569	25,571	26,090	13,641	13,303	13,800
45	LL	24,387	24,799	24,589	13,687	13,175	13,823
	WB	29,427	29,925	29,671	16,521	15,902	16,685
	UL	29,488	29,987	29,732	16,550	15,931	16,715
50	LL	28,464	28,742	28,778	16,628	16,024	16,514
	WB	34,339	34,674	34,719	20,067	19,337	19,928
	UL	34,418	34,754	34,798	20,106	19,376	19,968
55	LL	32,068	32,016	32,213	20,270	19,514	20,067
	WB	38,675	38,613	38,851	24,456	23,544	24,210
	UL	38,776	38,713	38,951	24,511	23,596	24,265
60	LL	34,224	34,788	34,622	23,176	22,399	22,667
	WB	41,261	41,940	41,740	27,953	27,016	27,339
	UL	41,384	42,066	41,865	28,024	27,085	27,408
65	LL	33,739	34,355	35,001	24,545	22,983	23,069
	WB	40,655	41,396	42,175	29,594	27,710	27,813
	UL	40,797	41,541	42,323	29,680	27,790	27,894
70	LL	30,737	30,939	32,009	22,888	21,352	21,199
	WB	37,012	37,256	38,543	27,583	25,733	25,548
	UL	37,166	37,411	38,705	27,676	25,818	25,634
75	LL	26,813	27,534	28,044	19,530	18,342	17,946
	WB	32,260	33,127	33,739	23,526	22,095	21,618
	UL	32,421	33,293	33,910	23,616	22,179	21,700
80	LL	23,067	23,102	23,803	15,517	14,545	14,246
	WB	27,725	27,767	28,608	18,681	17,512	17,152
	UL	27,893	27,935	28,782	18,763	17,588	17,226
85	LL	18,678	18,932	19,297	11,961	11,202	10,917
	WB	22,433	22,737	23,175	14,394	13,481	13,139
	UL	22,585	22,892	23,334	14,463	13,545	13,200
90	LL	15,513	15,900	16,093	9,216	8,736	8,360
	WB	18,638	19,102	19,333	11,093	10,516	10,064
	UL	18,758	19,227	19,460	11,144	10,564	10,109

Table 8-12: Aerodynamic Damping Vortex Shedding Fatigue Life – HML Structural Support

This final fatigue life study of the HML structure to include the complete vortex shedding model, forced vibration and aerodynamic damping, also had significant effects on the estimated fatigue life when compared to the three-dimensional wind flow study where vortex shedding effects were not considered. As for the previous study where only the forced vibration term of the vortex shedding model was considered, there were no effects on the estimated fatigue life at $\theta = 0^\circ$ because the stress process at this angle only considers bending about the across-wind (lateral) axis. However, as the angle θ is increased from 0°, the effects of vortex shedding become more pronounced. Again, the maximum fatigue life estimate is obtained between 75° and 80° as was seen from the forced vibration term only. Figure 8-18 illustrates the fatigue life for various angles θ. For comparison purposed, one data set from both the two-dimensional and three-dimensional wind flow studies is included for $C_z = 10$. Additionally, the data set from the forced vibration study is also included in Figure 8-18.

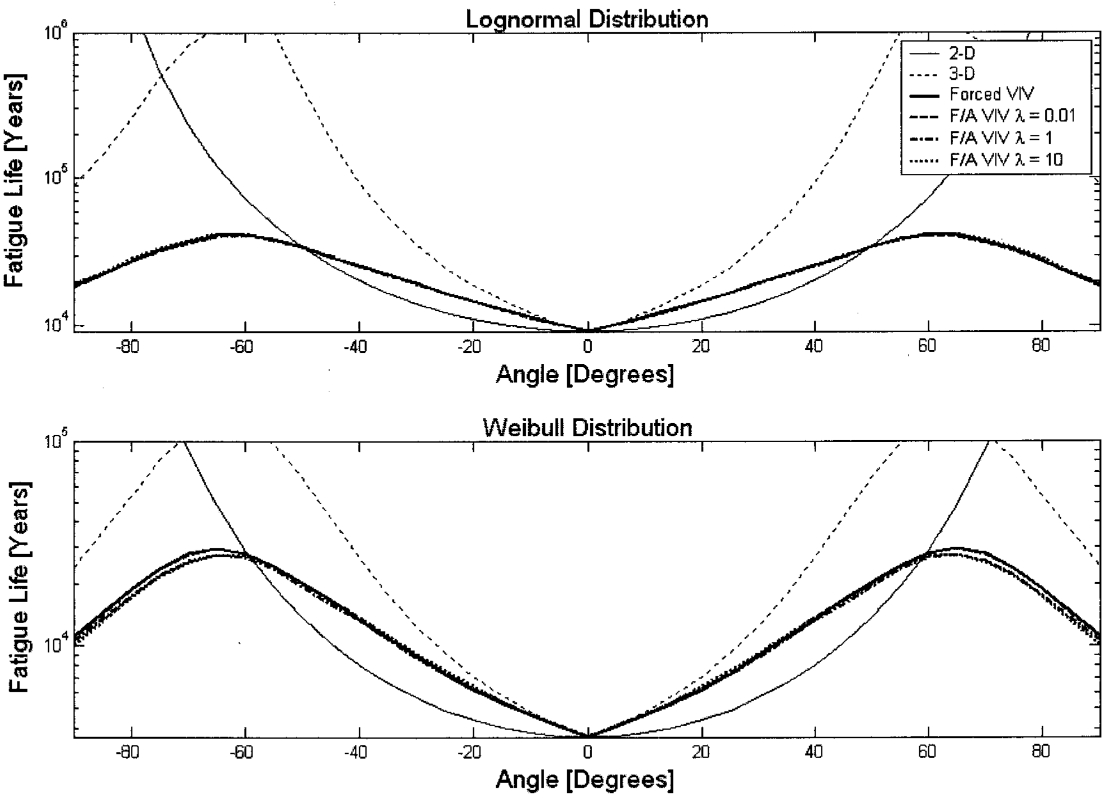

Figure 8-18: Aerodynamic Damping Vortex Shedding Fatigue Life – HML Structural Support

Increasing θ beyond the range producing the maximum fatigue life estimates, again, produces substantial reductions in fatigue life due to vortex shedding. In the across-wind (lateral) direction where $\theta = 90°$, the estimated fatigue life is reduced nearly 76% on average for the lognormal lifetime wind speed distribution when compared to the three-dimensional wind flow fatigue life estimates when vortex shedding is not considered. For the Weibull distribution, the fatigue life is reduced nearly 57% on average. As for the forced vibration vortex shedding comparison between the example structure and HML structural supports, these results are opposite in comparison to the example structure results for forced vibration vortex shedding. Thus, it is believed that the tapered cross-section of the HML structural support does have an effect on the vortex shedding forces generated at high wind speeds. These are substantial reductions and their importance should also be noted. However, these comparisons are made between a three-dimensional wind flow where vortex shedding was not considered and a three-dimensional wind flow where both the forced vibration and aerodynamic damping terms were included in the vortex shedding model.

Comparisons between the two vortex shedding models for their effects on fatigue life are equally as important. Inclusion of the aerodynamic damping term produced negligible effects, less than 1% on average, on the across-wind (lateral) fatigue life estimates for the lognormal and Weibull distributions, respectively. These reductions are significantly less than the reductions seen in comparing the effects of a vortex shedding model versus no vortex shedding. In regards to the limiting displacement parameter λ, an empirical value greater than unity produces the smallest fatigue life estimates for the Weibull distribution. This observation is expected based on the vortex shedding model used for the aerodynamic damping term. Small values of λ will force the aerodynamic damping term to vanish at even small amplitudes of motion. Thus, the larger values of λ will allow for a greater range of structure motion for which the aerodynamic damping term will not be forced to zero. Inconsistent results were seen with varying the empirical parameter λ for the lognormal distribution.

Chapter Nine

Summary, Conclusions, and Recommendations

9.1 Summary and Conclusions

The conclusions and results of this study are focused on two themes based on the studies reported in Chapters Six, Seven, and Eight for spatial correlation, vortex shedding, and fatigue life, respectively. First, the primary objective of this study is the incorporation of all of the models presented in Chapters Two through Five into a seamless, numerical analysis procedure. Second, using the numerical analysis procedure developed, the effects on the structural response of varying the parameters within the semi-empirical models used for spatial correlation and vortex shedding were investigated. As a result of the changes in the empirical parameters, their effects on the estimated fatigue life of the structure where wind fluctuations were deemed as the primary factor in influencing the fatigue performance was subsequently investigated.

Spatial Correlation

The integration of the semi-empirical model for the spatial correlation of wind turbulence in the simulated wind flow, both two- and three-dimensional, proved to be extremely successful. A traditional spectral approach was utilized to generate the necessary wind speed time series with various degrees of spatial correlation among the specified nodal points of the structure in the finite element analysis framework. A frequency dependent random field model given by Simiu and Scanlan (1996) was utilized to determine the root-coherence function. As a result of varying the exponential decay parameter C_z, the spatial correlation of the wind turbulence between points could be easily varied from a fully correlated state when C_z approaches zero to a state of no correlation when C_z approaches $+\infty$. Because the along-wind (longitudinal) and across-wind (lateral) turbulence components u' and v' are generated independently of each other based on assumptions from Asa-Jakobsen and Strømmen (2001), the spatial correlation for each turbulence component can also be set independently of each other, as is demonstrated in the numerical investigations of Chapter Six.

These investigations were initiated to determine the effects of the spatial correlation of wind turbulence on the resultant loading and response of the structure. As expected, some of the results that were observed reaffirmed the models used to derive the wind flow and the numerical analysis procedure. Primary among these results were those that led to fully correlated wind turbulence producing the maximum response of the structure throughout the time range considered. This was the case for all structural variations considered. In general the structural responses increased for increased vertical heights of the structure and mean wind speed. Decreases in the cross-sectional properties such as outside diameter and wall thickness also led to increased structural responses, this increase due to the increased non-linear behavior and increased wind/structure interaction arising from the higher structural flexibility.

To avoid numerical errors at the beginning of the time-domain analysis, a linear ramp-up of the wind speed within the first five seconds of the analysis was successfully employed. The initial results of the studies reported in Chapter Six did not include this ramp-up of wind speed. Significant numerical instabilities associated with the immediate application of the wind flow arose and the resulting wind induced-load time histories were observed to produce an erratic response characteristic. These numerical instabilities were subsequently corrected with the ramp-up procedure, and the data reported in Chapter Six are from these corrected studies.

The measured spatial correlation of a few particular time histories was also examined for both the two- and three-dimensional wind flows. In both cases, when the exponential decay parameter was set to $C_z = 0$, the spatial correlation of the resulting wind flow was nearly fully correlated. Setting $C_z = +\infty$ produced, on average, the expected very low to no spatial correlation of the resulting wind flow. Furthermore, the measured spatial correlation of the resultant drag force loading on the structure was quite similar to the spatial correlation of the wind flow. Based on the loading function used, this outcome between the loading and wind flow was also expected. The spatial correlation of the response time histories produced an outcome that was not necessarily expected from the outset of this study, but logically makes sense because of the continuity of the structure. The spatial correlation of the displacement of the structure was always fully correlated independent of the exponential decay parameter chosen for the wind flow spatial correlation. Finally, in considering the effects of varying the exponential decay parameter, C_z, a range of values was determined for producing strongly and weakly correlated wind flows. When $C_z \leq 10$ the corresponding spatial correlation of the wind flow is strongly correlated. Conversely, setting $C_z > 50$ produces a weakly correlated wind flow.

The cross-correlations of a few particular time histories resulting from the investigations were also considered. As expected, the cross-correlation between any time series decreases with increases in the vertical height of the structure being considered. This can be seen with the shorter structures considered in this study having relatively strong cross-correlation for all time histories considered. The opposite is true for the taller structures considered for this study. Specific to the three-dimensional wind flow, the cross-correlation between the simulated wind flow in both the along-wind (longitudinal) and across-wind (lateral) directions was also strongly correlated. But, the cross-correlation between the across-wind (lateral) flow at the top of the structure and the resulting across-wind (lateral) bending stress σ_x at the base of the structure were negatively correlated. For the shorter structures, this negative correlation was very strong, whereas for the taller structures this negative correlation was relatively weak. Reasons for these phenomena may result from the fact that across-wind displacements and loading are affected by changes in the along-wind direction because of the forcing function used to determine the across-wind loading. Along-wind displacements and loading, however, are not affected by changes in the across-wind direction.

Vortex Shedding

The formulation and incorporation of an adequate vortex shedding model to determine aeroelastic instabilities during the time-domain response of the multi-degree-of-freedom (MDOF) structure proved initially to be difficult but was successfully implemented. The model proposed by Vickery and Basu (1983) and outlined by Simiu and Scanlan (1986) for modeling the effects of vortex shedding for a single degree-of-freedom (SDOF) concrete chimney was adapted into a MDOF structural analysis algorithm for slender structural systems. Based on their SDOF model, Vickery and Basu (1983) investigated the cause of vortex shedding at only one point along the height of the structure. As this is insufficient for the MDOF system considered in this study, the mechanisms for inducing vortex shedding loading, and more specifically lock-in, were investigated for each nodal point of the structure. This allows for points along the height of the structure to independently lock-in based on the aerodynamic damping term of the vortex shedding model. However, as will be discussed in Section 9.3, Simiu and Scanlan (1986) and others note that once lock-in occurs for a particular section of the structure, the forces generated as a result of vortex shedding are strongly correlated. This phenomenon was not specifically investigated within this study. Additionally, only the first or lowest natural frequency of the structure was considered for the critical wind velocity and subsequent lock-in conditions of the vortex shedding model used in this study.

The numerical investigation of Chapter Seven was conducted to determine the effects of the vortex shedding model on the loading and response of the structure. This study investigated two cases of the vortex shedding model. The first case only considered the forced vibration term of the vortex shedding model. Effects due to the aerodynamic damping term of the vortex shedding model were not considered in this first case. The second case considered the complete vortex shedding model which included both the forced vibration and aerodynamic damping terms. This case resulted in additional across-wind (lateral) loading and response of the structure.

For the first case in which only the forced vibration term, as expected, a decrease in the vertical height of the structure yielded a higher frequency component in the response of the structure in the across-wind (lateral) direction. The resultant loading due to the forced vibration term also had a high frequency component for all structures. The range of the loading time history was fairly uniform for all structures. However, the smaller structures also had intermittent spikes in the loading time history due to the forced vibration term. Furthermore, the smaller structure produced a more erratic response whereas the response of the larger structures appeared to be more uniform. For all heights, however, the maximum response of the structure was always produced when the spatial correlation of the wind flow was strong.

Simiu and Scanlan (1986) noted that the forced vibration term of the vortex shedding model can often be neglected because its effects on the loading and response of the structure are often small in magnitude compared to the aerodynamic damping loading and response. Indeed, as was demonstrated in the studies of Chapter Seven, the resultant loading due to the forced vibration term was smaller than the load determined strictly from the buffeting force in the across-wind (lateral) direction. Thus, based on the conclusions of Simiu and Scanlan (1986) the ability to neglect the forced vibration term appears to be a correct assumption.

Noticeable differences were observed when the results of the forced vibration only numerical investigation were compared with those of the complete vortex shedding model where both the forced vibration and aerodynamic damping terms were considered. Again, however, the shorter structure produced a more erratic response compared to the larger structures considered. The response of all structures appeared to only increase at the peaks of the displacement time history with more substantial differences for the smaller structure.

At relatively low wind speeds, the limiting displacement parameter λ had no effect on the response of any of the structures considered because displacements were kept fairly small. At higher wind speeds, however, larger values of λ consistently produced the maximum response of the structure considered. For the smaller structure, intermittent lock-in of the aerodynamic damping load was undeniably seen. The magnitude of this load was significantly lower than the magnitude of the forced vibration load. Thus, it appears that the consideration of only the first natural frequency of the structure does not produce significant effects in regards to the aerodynamic damping term of the vortex shedding model.

An examination of the magnitude of the forced vibration load when the aerodynamic damping term is included showed that it was consistently higher compared to when the aerodynamic damping term is not considered. Considering the aerodynamic damping load, the effects of vortex shedding for the first natural frequency of the structures appeared to be strongest for relatively low wind speeds. Taller structures produced relatively larger aerodynamic damping loads at lower wind speeds than for the short structures. Additionally, increased flexibility of the structures with smaller cross-sectional properties for each vertical height considered produced a narrower range of wind speeds for which lock-in would occur thus producing a relatively significant aerodynamic damping load for all structural heights.

Fatigue Life

The random vibration model for estimating fatigue life based on Miner's Rule developed by Crandall and Mark (1963) was implemented to determine the fatigue performance of the structure due to natural wind fluctuations. First, the structural analysis algorithm from the time-domain, finite element numerical procedure was utilized to determine the expected damage based on the resulting stress process at the base of the structure due from a specified loading event. A procedure developed by Wirsching and Light (1980) and outlined by Holmes (2001) was incorporated to determine upper and lower limits for the expected damage based on the classification of the stress process. The expected damage due to the resulting stress process was determined based on a spectral bandwidth parameter derived from the spectral moments of the stress process for the loading event.

The numerical investigation reported in Chapter Eight was initiated to determine the effects of spatial correlation of wind turbulence and vortex shedding on the estimated fatigue life of the structure. Strong spatial correlation of the simulated wind flow consistently produced the lowest estimate of fatigue life, as would be expected based on the results of the study reported in Chapter Six. The use of the empirical formula to determine the expected damage due to a wide-band stress process also produced fatigue life estimates near the upper limit according to the derivation. Recall, that the lower limit estimate of fatigue life is based on a narrow-band stress process assumption. The results reported in Chapter Eight clearly indicate that the stress process due to the wind event is clearly not a narrow-band process. Finally, the use of the assumed lognormal distribution resulted in a higher estimate of the fatigue life. The Weibull distribution, the preferred distribution in statistically describing the fluctuations of wind speeds for a given area, contained higher probabilities of occurrence for high wind speeds than the lognormal distribution.

The use of a two-dimensional wind flow in which only along-wind displacements are considered produced fatigue life estimates of infinite life in the across-wind (lateral) direction. The lowest fatigue life, as expected, for the two-dimensional wind flow occurred in the along-wind (longitudinal) direction. When the wind flow is expanded to a three-dimensional case, but still without vortex shedding effects, the maximum fatigue life occurred at an angle between 60° and 80° from the along-wind (lateral) direction. There was no change in the lowest fatigue life determined strictly in the along-wind (longitudinal) direction at 0° for the three-dimensional wind flow as compared to the two-dimensional wind flow.

The incorporation of the vortex shedding model produced significant reductions in the estimated fatigue life in the across-wind (lateral) direction. Again, because the loading and response of the structure are decoupled from the along-wind (longitudinal) direction, there was no effect on the estimated fatigue life when compared to both the two- and three-dimensional wind flow estimates of fatigue life. When only the forced vibration term from the vortex shedding model is included, the estimated fatigue life is reduced approximately 65% on average for the example structure compared to the across-wind (lateral) fatigue life estimate for the three-dimensional wind flow without vortex shedding effects. For the HML structural support, the across-wind fatigue life is reduced approximately 76% and 57% for the lognormal and Weibull distributions, respectively. These results are also expected because the lower wind speeds at which the vortex shedding effects are more evident have a higher probability of occurrence with the lognormal distribution than the Weibull distribution for which higher wind speeds have a higher probability of occurrence.

A comparison of the estimated fatigue life change due to the complete vortex shedding model also produced significant effects on the estimated fatigue life in the across-wind (lateral) direction. For the example structure, the complete vortex shedding model reduces the fatigue life estimate by approximately 67% on average compared to the three-dimensional wind flow where the effects of vortex shedding were not included. However, compared to the use of only the forced vibration term, the fatigue life estimate is reduced approximately 10% on average in the across-wind (lateral) direction when the aerodynamic damping term is included in the vortex shedding model. For the HML structural support, the effects of the aerodynamic damping term are not as substantial. When compared to the use of only the forced vibration term, the fatigue life in the across-wind (lateral) direction is only reduced by approximately 1% on average when the aerodynamic damping term is included in the vortex shedding model. Thus, it appears that the tapered section of the HML structural support does help to alleviate the effects of the aerodynamic damping term with respect to the fatigue performance of the structure.

9.2 Contributions

The results of this study represent a substantial step forward with respect to the three-dimensional time-domain modeling of slender structural systems subjected to fluid or wind flow. The incorporation of both spatial correlation of wind turbulence and vortex shedding models into the numerical solution procedure and the use of this solution in numerical investigations represents a very comprehensive study of fluid/structure interaction for this type of structure. Coupled with a random vibration approach, the numerical analysis procedure also constitutes a method by which the fatigue life of the structural system can be estimated based on a statistical distribution representing a loading event over the lifetime of the structure.

Though the structures considered in this study are relatively small in stature and are focused strictly on wind flow, the conclusions and models used in this study may be extrapolated to much larger structural systems with similar characteristics in a general fluid flow environment that are currently usually investigated only in experimental studies at a substantial cost. It is the hope of the author/student that this extension to more complex structures will be the case and provide a step upon which further research and development will be accomplished. Further refinement of the numerical analysis procedure and models used in the implementation of the procedure would be needed, of course, to accommodate a variety of structural system shapes and sizes.

It is also envisioned that such a model will eventually provide a basis for further numerical studies resulting in the review and potential modifications of existing design specifications and design documents. Currently, numerical modeling analyses such as the one developed in this study do not meet design code requirements for acceptability as a design basis from a codified perspective. Furthermore, a greater understanding of various fluid/structure interaction phenomena such as vortex shedding will also lead to a development of efficient and economical mitigation strategies for wind sensitive structural systems.

Based on the conclusions and summary of results presented in Section 9.1 for the numerical investigations of Chapter Six, Seven, and Eight, the effects of the spatial correlation of wind turbulence and vortex shedding on the response, resultant loading, and fatigue performance of the structural system have been provided. From a numerical analysis perspective, these observations have not been previously established. While it is not possible to change the spatial correlation of the wind turbulence for any given location or event, the importance of properly modeling it has been greatly reinforced with this study. Further, the effects of vortex shedding on a slender structural system have also been illustrated in this study based on the changes in response, resultant loading, and fatigue performance in the across-wind (lateral) direction found in the numerical investigations.

9.3 Recommendations

The development of the comprehensive numerical analysis procedure for modeling the spatial correlation of wind turbulence and vortex shedding effects on the response, resultant loading, and fatigue performance of a slender structural system provides a foundation and opportunity for further development of these techniques and their applications. The numerical investigations of Chapters Six, Seven, and Eight considered the effects of parameter changes in a fairly general way. Thus, a refinement of the analysis model and a more detailed investigation of these effects are needed both from a modeling and results point of view.

The modeling of the spatial correlation of wind turbulence was simplified by neglecting the cross-spectral quantities described in Section 3.1. To simulate the wind speed time history used in the analysis of the structural system, a traditional spectral approach was employed. To improve the numerical modeling capabilities and accuracy, it would be necessary to consider the cross-spectral quantities such that variations in the along-wind (longitudinal) spatial correlation and magnitude directly affect the across-wind (lateral) spatial correlation and magnitude. The same would also be true for the across-wind (lateral) characteristics affecting the along-wind (longitudinal) characteristics. Hence, the two wind speed time histories, along-wind (longitudinal) and across-wind (lateral), would have to be generated simultaneously. This leads to the requirement that a more efficient and less memory-intensive procedure be employed to simulate the wind flow. Recent developments in auto-regressive moving averaging (ARMA) methods have shown to be efficient and less memory-intensive (Mignolet and Spanos, 1987; Li and Kareem, 1990; Minh et al, 1999; Cao et al, 2000; Di Paola and Gullo, 2001). Furthermore, these methods can also be used quite effectively to generate records of any length and even appending to the end of a record to extend its length. Other developments in wavelets have also begun to be utilized; however, the author/student is not familiar with these current methods.

The numerical investigation study of the spatial correlation of wind turbulence on the response of the structures considered in this study was also conducted from a broad perspective. The variation in the spatial correlation exponential decay parameter C_z was assumed to be constant along the height of the structure and for varying wind speeds. As noted previously, this is often not the case. Therefore, it would be advantageous to consider varying degrees of spatial correlation based on the parameter C_z along the height of the structure and for different wind speeds. A data collection scheme would be required to obtain typical ranges for these values from field experiments before variations in the C_z parameter can be realistically implemented into a numerical analysis routine. Furthermore, the spatial correlation and cross-correlation of the response and loading of the structure should also be further investigated with these updates to the spatial correlation investigation. At this point, however, an important quantity to consider is the resulting bending stress at the base of the structure, as the bending stress is the primary factor in fatigue performance of these types of structures.

The model used to simulate vortex shedding as developed by Vickery and Basu (1983) appears at this time to be theoretically sound and appropriate to implement into a numerical multi-degree-of-freedom analysis procedure. However, as noted previously, only the first or lowest natural frequency of the system was considered in determining the critical wind velocity and the lock-in phenomenon. Thus, this model should be expanded in its present form to include several natural frequencies of the structure to determine their effects on the response and fatigue performance. A superposition method for determining the across-wind (lateral) loading function could be utilized to combine the effects from each natural frequency. This refinement should produce more substantial effects arising from the vortex shedding model. As noted in Section 9.1, when lock-in occurs, the vortex shedding loads have been observed to be strongly correlated spatially. Thus, when one section of the structure locks-in, other nearby sections of the structure would also lock-in, thereby producing strongly correlated vortex shedding loads near the section that first experienced locked-in. Further investigation of the lock-in phenomenon is needed in the numerical model for vortex shedding.

Similar to the spatial correlation study, the numerical investigation study for vortex shedding was also conducted from a broad perspective. By utilizing the more refined vortex shedding model previously described, the effects of the model would become more substantial and easier to investigate. A refinement in the finite element structural analysis routine could also lend itself to investigating mitigation techniques to avoid the effects of vortex shedding on the structural system. This in itself would be a very substantial step towards code improvements and changes in design standards.

Finally, the model used to investigate the fatigue performance of the structures considered in this study could also be refined or revisited. To determine the stress process at the base of the structure, a simplistic linear mechanics model for determining the stress due to the resulting bending moment was utilized. A more detailed finite element model of the structure and the base connection could help to further isolate and determine the resulting stress process causing fatigue damage. Furthermore, because the response of the structure is determined in the time-domain, a non-linear damage accumulation model or fracture mechanics type of approach may be better suited for a fatigue study given the multi-dimensional stress processes at the base of the structure. A more detailed finite element study of the resulting base connection could be further coupled with the procedure developed herein to obtain better resolution of the stress process resulting in fatigue damage. This would allow for a more detailed investigation of all locations around the base of the structure, including critical junctures that occur in the connection of the pole structure to the base plate. Finally, improvements to the spatial correlation and vortex shedding modeling would also lead to improvements in the prediction of fatigue performance of these structures.

References

AASHTO (2001), *Standard Specifications for Structural Supports for Highway Signs, Luminaires and Traffic Signals*, 4th Edition with interims, American Association of State Highway and Transportation Officials, Washington, D.C.

Aas-Jakobsen, K. and E. Strømmen (2001), "Time Domain Buffeting Response Calculations of Slender Structures", *Journal of Wind Engineering and Industrial Aerodynamics*, Vol. 89, p. 341 – 364.

Ang, A.H-S. and W.H. Tang (1975), *Probability Concepts in Engineering Planning and Design*, Volume 1, John Wiley and Sons, New York.

ASCE 7 (2005), *Minimum Design Loads for Buildings and Other Structures*, American Society of Civil Engineers, Reston, VA.

Basu, R.I. and B.J. Vickery (1983), "Across-Wind Vibrations of Structures of Circular Cross-Section, Part II: Development of a Mathematical Model for Full-Scale Application", *Journal of Wind Engineering and Industrial Aerodynamics*, Vol. 12, p. 75 – 97.

Benfratello, S. and G. Muscolino (1999), "Filter Approach to the Stochastic Analysis of MDOF Wind-Excited Structures", *Probabilistic Engineering Mechanics*, Vol. 14, p. 311 – 321.

Bosch, H.R. and R.M. Guterres (2001), "Wind Tunnel Experimental Investigation on Tapered Cylinders for Highway Support Structures", *Journal of Wind Engineering and Industrial Aerodynamics*, Vol. 89, p. 1311 – 1323.

Bulleit, W.M. and R.A. Chapman (2004), "Characterization of the Correlation Structure of Lumber Strength Properties", *Wood Science and Technology*, Vol. 38, p. 285 – 296.

Cao, Y., Xiang, H. and Y. Zhou (2000), "Simulation of Stochastic Wind Velocity Field on Long-Span Bridges", *Journal of Engineering Mechanics*, Vol. 126, p. 1 – 6.

Celik, I. And F.D. Shaffer (1995), "Long Time-Averaged Solutions of Turbulent Flow Past a Circular Cylinder", *Journal of Wind Engineering and Industrial Aerodynamics*, Vol. 56, p. 185 – 212.

Chen, X. and A. Kareem (2001), "Aeroelastic Analysis of Bridges under Multicorrelated Winds: Integrated State-Space Approach", *Journal of Engineering Mechanics*, Vol. 127, p. 1124 – 1134.

Chopra, A.K. (2001), *Dynamics of Structures*, 2nd Edition, Prentice Hall, Upper Saddle River, NJ.

Crandall, S.H. and W.D. Mark (1963), *Random Vibration of Mechanical Systems*, Academic Press, New York and London.

D'Asdia, P. and S. Noe (1998), "Vortex Induced Vibration of Reinforced Concrete Chimneys In Situ Experimentation and Numerical Previsions", *Journal of Wind Engineering and Industrial Aerodynamics*, Vol. 74-76, p. 765 – 776.

Deoliya, R. and T.K. Datta (2001), "Fatigue Reliability Analysis of Microwave Antenna Towers Due to Wind", *Journal of Structural Engineering*, Vol. 127, p. 1221 – 1230.

Di Paola, M. and I. Gullo (2001), "Digital Generation of Multivariate Wind Field Processes", *Probabilistic Engineering Mechanics*, Vol. 16, p. 1 – 10.

Dul, F.A. and J.A. Pietrucha (1996), "Numerical Analysis of Continuous Models of Structures in Non-Linear Wind Flow Using the Time-Marching Approach", *Journal of Wind Engineering and Industrial Aerodynamics*, Vol. 65, p. 321 – 334.

Flaga, A. (1997), "Nonlinear Amplitude Dependent Self-Limiting Model of Lock-In Phenomenon at Vortex Excitation", *Journal of Wind Engineering and Industrial Aerodynamics*, Vol. 69-71, p. 331 – 340.

Fujisawa, N., Asano, Y., Arakawa, C. and T. Hashimoto (2005), "Computational and Experimental Study on Flow Around a Rotationally Oscillating Circular Cylinder in a Uniform Flow", *Journal of Wind Engineering and Industrial Aerodynamics*, Vol. 93, p. 137 – 153.

Goode, J.S. and J.W. van de Lindt (2006), "Development of a Semi-Prescriptive Reliability-Based Fatigue Selection Procedure for High Mast Lighting Structural Supports", *Journal of the Performance of Constructed Facilities, In-Press*.

Goswami, I., Scanlan, R.H., and N.P. Jones (1993), "Vortex-Induced Vibration of Circular Cylinders I: Experimental Data", *Journal of Engineering Mechanics*, Vo. 119, p. 2270 – 2287.

Goswami, I., Scanlan, R.H., and N.P. Jones (1993), "Vortex-Induced Vibration of Circular Cylinders II: New Model", *Journal of Engineering Mechanics*, Vol. 119, p. 2288 – 2302.

Harrison IV, B.F. and P.N. Roschke (2000), "Laboratory Simulation of Wind Vibrations in Roadside Structures", *Journal of Structural Engineering*, Vol. 126, p. 1238 – 1245.

Holmes, J.D. (2001), *Wind Loading of Structures*, Spon Press, New York.

Kareem, A. (1997), "Correlation Structure of Random Pressure Fields", *Journal of Wind Engineering and Industrial Aerodynamics*, Vol. 69-71, p. 507 – 516.

Kiya, M., Ishikawa, H. and H. Sakamoto (2001), "Near-Wake Instabilities and Vortex Structures of Three-Dimensional Bluff Bodies: A Review", *Journal of Wind Engineering and Industrial Aerodynamics*, Vol. 89, p. 1219 – 1232.

Kondo, K., Murakami, S. and A. Mochida (1997), "Generation of Velocity Fluctuations for Inflow Boundary Condition LES", *Journal of Wind Engineering and Industrial Aerodynamics*, Vol. 67/68, p. 51 – 64.

Kwon, Y.W. and H. Bang (2000), *The Finite Element Method Using MATLAB*, 2nd Edition, CRC Press, New York.

Lakshmanan, N., Arunachalam, S., Selvi Rajan, S., Ramesh Babu, G. and J. Shanmugasundaram (2002), "Correlations of Aerodynamic Pressures for Prediction of Across Wind Response of Structures", *Journal of Wind Engineering and Industrial Aerodynamics*, Vol. 90, p. 941 – 960.

Li, Y. and A. Kareem (1990), "ARMA Representation of Wind Field", *Journal of Wind Engineering and Industrial Aerodynamics*, Vol. 36, p. 415 – 427.

Li, Y. and A. Kareem (1995), "Stochastic Decomposition and Application to Probabilistic Dynamics", *Journal of Engineering Mechanics*, Vol. 121, p. 162 – 174.

Lumley, J.L. and H.A. Panofsky (1964), *The Structure of Atmospheric Turbulence*, Interscience Monographs and Texts in Physics and Astronomy, Vol. XII, John Wiley and Sons, New York.

Mann, J. (1998), "Wind Field Simulation", *Probabilistic Engineering Mechanics*, Vol. 13, p. 269 – 282.

Meneghini, J.R. and P.W. Bearman (1997), "An Investigation of the Effect of Vortex Shedding of a Sudden Transverse Disturbance Applied to a Circular Cylinder", *Journal of Wind Engineering and Industrial Aerodynamics*, Vol. 69-71, p. 229 – 238.

Mignolet, M.P. and P.D. Spanos (1987), "Recursive Simulation of Stationary Multivariate Random Processes – Part I", *Journal of Applied Mechanics*, Vol. 54, p. 674 – 680.

Miner, M.A. (1945), "Cumulative Damage in Fatigue", *Journal of Applied Mechanics*, 12, p. 159.

Minh, N.N., Miyata, T., Yamada, H. and Y. Sanada (1999), "Numerical Simulation of Wind Turbulence and Buffeting Analysis of Long-Span Bridges", *Journal of Wind Engineering and Industrial Aerodynamics*, Vol. 83, p. 301 – 315.

Morison, J.R., O'Brien, M.P., Johnson, J.W. and S.A. Schaaf (1950), "The Force Exerted by Surface Waves on Piles", *AIME Petroleum Transactions*, 189, p. 149-157.

Nagao, F., Utsunomiya, H., Noda, M. and Y. Oshima (2003), "Basic Study on Spatial Correlation of Fluctuating Lifts Acting on Plates", *Journal of Wind Engineering and Industrial Aerodynamics*, Vol. 91, p. 1349 – 1362.

Newland, D.E. (1975), *Random Vibrations and Spectral Analysis*, Longman Group Ltd., London.

Newmark, N.M. (1959), "A Method of Computation for Structural Dynamics", *Transactions of the American Society of Civil Engineers (ASCE)*, American Society of Civil Engineers, 109, p. 111.

NOAA (2001), National Oceanographic and Atmospheric Administration, National Climatic Data Center, Data Set TD-6421, "Enhanced Hourly Wind Station Data for the Contiguous United States", Asheville, North Carolina.

Ohkuma, T., Marukawa, H., Yoshie, K., Niwa, H., Teramoto, T. and H. Kitamura (1995), "Simulation Method of Simultaneous Time-Series of Multi-Local Wind Forces on Tall Buildings by Using Dynamic Balance Data", *Journal of Wind Engineering and Industrial Aerodynamics*, Vol. 54/55, p. 115 – 123.

Paz, M. and W. Leigh (2004), *Structural Dynamics*, 5th Edition, Kluwer Academic Publishers, Boston.

Piccardo, G. and G. Solari (1998), "Close Form Prediction of 3-D Wind-Excited Response of Slender Structures", *Journal of Wind Engineering and Industrial Aerodynamics*, Vol. 74-76, p. 697 – 708.

Piccardo, G. and G. Solari (2000), "3D Wind-Excited Response of Slender Structures: Closed-Form Solution", *Journal of Structural Engineering*, Vol. 126, p. 936 – 943.

Piccardo, G. and G. Solari (2002), "3-D Gust Effect Factor for Slender Vertical Structures", *Probabilistic Engineering Mechanics*, Vol. 17, p. 143 – 155.

Repetto, M.P. and G. Solari (2001), "Dynamic Alongwind Fatigue of Slender Vertical Structures", *Engineering Structures*, Vol. 23, p. 1622 – 1633.

Repetto, M.P. and G. Solari (2002), "Dynamic Crosswind Fatigue of Slender Vertical Structures", *Wind and Structures*, Vol. 5, p. 527 – 542.

Repetto, M.P. and G. Solari (2004), "Directional Wind-Induced Fatigue of Slender Vertical Structures", *Journal of Structural Engineering*, Vol. 130, p. 1032 – 1040.

Repetto, M.P. and G. Solari (2006), “Bimodal Alongwind Fatigue of Structures”, *Journal of Structural Engineering*, Vol. 132, p. 899 – 908.

Rocchi, D. and A. Zasso (2002), “Vortex Shedding from a Circular Cylinder in a Smooth and Wired Configuration: Comparison Between 3D LES Simulation and Experimental Results”, *Journal of Wind Engineering and Industrial Aerodynamics*, Vol. 90, p. 475 – 489.

Ruscheweyh, H., Hortmanns, M. and C. Schnakenberg (1996), “Vortex-Excited Vibrations and Galloping of Slender Elements”, *Journal of Wind Engineering and Industrial Aerodynamics*, Vol. 65, p. 347 – 352.

Sen, Z. (2000), “Stochastic Wind Energy Calculation Formulation”, *Journal of Wind Engineering and Industrial Aerodynamics*, Vol. 84, p. 227 – 234.

Seong, S. H. and J.A. Peterka (1997), “Computer Simulation of Non-Gaussian Multiple Wind Pressure Time Series”, *Journal of Wind Engineering and Industrial Aerodynamics*, Vol. 72, p. 95 – 105.

Simiu, E. and R.H. Scanlan (1986), *Wind Effects on Structures*, 2nd Edition, John Wiley and Sons, New York.

Simiu, E. and R.H. Scanlan (1996), *Wind Effects on Structures*, 3rd Edition, John Wiley and Sons, New York.

Solari, G. and G. Piccardo (2001), “Probabilistic 3-D Turbulence Modeling for Gust Buffeting of Structures”, *Probabilistic Engineering Mechanics*, Vol. 16, p. 73 – 86.

Spanos, P.D. and M.P. Mignolet (1987), “Recursive Simulation of Stationary Multivariate Random Processes – Part II”, *Journal of Applied Mechanics*, Vol. 54, p. 681 – 687.

Stoyanoff, S. (2001), "A Unified Approach for 3D Stability and Time Domain Response Analysis with Application of Quasi-Steady Theory", *Journal of Wind Engineering and Industrial Aerodynamics*, Vol. 89, p. 1591 – 1606.

Toriumi, R., Katsuchi, H. and N. Furuya (2000), "A Study on Spatial Correlation of Natural Wind", *Journal of Wind Engineering and Industrial Aerodynamics*, Vol. 87, p. 203 – 216.

van de Lindt, J.W. and J.S. Goode (2006), *Development of a Reliability-Based Design Procedure for High-Mast Lighting Structural Supports in Colorado*, CDOT Research Report.

Vanmarcke, E.H. (1983), *Random Fields: Analysis and Synthesis*, MIT Press, Cambridge, MA.

Vickery, B.J. and R.I. Basu (1983), "Across-Wind Vibrations of Structures of Circular Cross-Section, Part I: Development of a Mathematical Model for Two-Dimensional Conditions", *Journal of Wind Engineering and Industrial Aerodynamics*, Vol. 12, p. 49 – 73.

Wilcox, D.C. (2000), *Basic Fluid Mechanics*, 2nd Edition, DCW Industries, La Cañada, CA.

Wirsching, P.H. and Light, M.C. (1980), "Fatigue Under Wide Band Random Stresses", *Journal of the Structural Division*, ASCE, Vol. 106, p.1593 – 1607.

Yamamoto, C.T., Meneghini, J.R., Saltara, F., Fregonesi, R.A., and J.A. Ferrari Jr. (2004), "Numerical Simulations of Vortex-Induced Vibrations on Flexible Cylinders", *Journal of Fluids and Structures*, Vol. 19, p. 467 – 489.

Zhou, C.Y. and J.M.R. Graham (2000), "A Numerical Study of Cylinder in Waves and Currents", *Journal of Fluids and Structures*, Vol. 14, p. 403 – 428.